Dispersive approach to the calculation of isospin–breaking corrections to $\pi\pi$–scattering and $\tau^- \to \pi^-\pi^0\nu$

Inaugural dissertation
at the Faculty of Science,
University of Bern

presented by

Martina Cottini

from Italy

Supervisor of the doctoral thesis
Prof. Dr. Gilberto Colangelo

Institute for Theoretical Physics
Albert Einstein Center for Fundamental Physics,
University of Bern

Dispersive approach to the calculation of isospin–breaking corrections to $\pi\pi$–scattering and $\tau^- \to \pi^-\pi^0\nu$

Inaugural dissertation
at the Faculty of Science,
University of Bern

presented by

Martina Cottini

from Italy

Supervisor of the doctoral thesis
Prof. Dr. Gilberto Colangelo

Institute for Theoretical Physics
Albert Einstein Center for Fundamental Physics,
University of Bern

Accepted by the Faculty of Science.

Bern, 08.12.2025

The Dean
Prof. Dr. Jean-Louis Reymond

Abstract

The theoretical uncertainty of the anomalous magnetic moment of the muon Standard Model (SM) prediction, a_μ, is dominated by hadronic inputs, more precisely by the hadronic vacuum polarization (HVP) contribution. The increased tension between the $e^+e^- \to \pi^+\pi^-$ measurements as well as the discrepancy between the data–driven approach and the lattice QCD result requires further investigation. On one side, a model independent approach for the isospin–breaking (IB) effects in the $\pi\pi$–scattering amplitude can help clarifying the current situation. In this work, we derive the modifications to the Roy equations for $\pi\pi$–scattering due to the charged–neutral pion mass difference, which is a first step towards a full dispersive calculation of the radiative corrections for the process $e^+e^- \to \pi^+\pi^-$. On the other side, the hadronic τ decay, $\tau \to \pi\pi^0\nu_\tau$, provides an independent way to compute the HVP contribution to a_μ. Here we will present a dispersive approach to the evaluation of the IB corrections relating $\tau \to \pi\pi^0\nu_\tau$ to $e^+e^- \to \pi^+\pi^-$, with a focus on the long–range corrections usually denoted by $G_{\rm EM}(s)$.

Declaration

This thesis is based on the following work to which the author contributed to directly

[1] G. Colangelo, M. Cottini, M. Hoferichter, S. Holz, *Improved calculation of radiative corrections to $\tau \to \pi\pi\nu_\tau$ decays*, 2510.26871

[2] G. Colangelo, M. Cottini, M. Hoferichter, S. Holz, *Radiative corrections to $\tau \to \pi\pi\nu_\tau$*, 2511.07507

[3] G. Colangelo, M. Cottini, J. Ruiz de Elvira, *Isospin-breaking in the $\pi\pi$ scattering amplitude I: Effects due to the pion mass difference*, 2511.08680

Hence, text may be directly copied without reference. The work presented in this thesis has been supported by the Albert Einstein Center for Fundamental Physics (AEC) and by the Swiss National Science Foundation (SNSF).

Contents

Chapter 1

Introduction

The Standard Model (SM) of particle physics is a predictive theory describing three of the four known fundamental forces, i.e., electromagnetic, weak and strong interactions. This theory is one of the most impressive successes achieved in science throughout the second half of the twentieth century and it has been experimentally confirmed by the physics community as the theory of particles physics which best describes a multitude of experiments, which have thoroughly tested it.

The muon anomalous magnetic moment, a_μ or muon $g-2$, is one of the most precisely measured quantities in particle physics and allows one to test Quantum Field Theory (QFT) in depth and with great accuracy. With its electromagnetic, weak and strong interaction contributions, the theoretical prediction of the anomalous magnetic moment of the muon is a very difficult quantity to compute. The comparison between the theoretical and experimental results of the muon $g-2$ sets severe limits on the deviations from standard theory of elementary particles, the Standard Model, and, at the same time, plays an important role to test physics Beyond the Standard Model (BSM). Indeed the current situation regarding the measurement and the SM prediction of a_μ is one of the most intriguing hints of new physics beyond the SM.

On the experimental side, before April 2021, the experimental value was the one obtained at the E821 experiment at the Brookhaven National Laboratory (BNL). The discrepancy with the theoretical SM result was 3.7 σ [4–7]. In April 2021, the new experimental result of the Muon $g-2$ experiment at Fermilab (FNAL) confirmed the BNL value, bringing the combined BNL+FNAL difference between the experimental and SM result to [8, 9]

$$a_\mu^{\rm exp} - a_\mu^{\rm SM} = 251(59) \times 10^{-11} \,, \tag{1.1}$$

with a significance of 4.2 σ, if the leading hadronic contribution is computed via the dispersive method, i.e., the so called data–driven approach. This difference increased up to 5.1 σ when the new result from FNAL (Run 2+3) was presented in 2023 [10]. However, this discrepancy is reduced if the first BMW collaboration lattice QCD result [11] or the one obtained with the standard method but with the CMD–3 $e^+e^- \to$ hadrons data [12] are employed. In June 2025, both the FNAL final experimental result [13] and the theoretical one [14] were released, leading to a considerable decrease of the discrepancy between the two values.

$$a_\mu^{\rm exp} - a_\mu^{\rm SM} = 38(63) \times 10^{-11} \,, \tag{1.2}$$

where the very precise final experimental result reads

$$a_\mu^{\rm exp} = 116\,592\,071.5(14.5) \times 10^{-11} \quad (124\ {\rm ppb})\ . \tag{1.3}$$

However, the theoretical result released in the 2025 White Paper (WP25) [14] is obtained from the exclusive use of the new, published leading–order hadronic vacuum polarization estimates based on lattice QCD calculations. The data–driven estimate based on experimental $e^+e^- \to$ hadrons cross–section measurements was not included due to the increased tension among the experimental inputs [12, 14]. In addition, a completely new low–energy approach to measure the muon $g-2$ is being developed by the E34 collaboration at J–PARC [15–17].

On the theory side, the long–standing discrepancy between the experimental measurement of a_μ and the data–driven SM prediction of the muon anomalous magnetic moment (before 2025) has kept the hadronic corrections under close scrutiny for several years, since this hadronic uncertainty dominates that of the SM value. In the data driven approach, the leading–order hadronic contribution to the muon $g-2$, $a_\mu^{\rm HLO}$, is usually computed via a dispersion integral using hadronic production cross sections in electron–positron annihilation at low energy. One of the main obstacles to reduce the error of the hadronic contribution to a_μ is the discrepancy between the experimental extractions of the pion vector form factor from the cross section of the reaction $e^+e^- \to \pi^+\pi^-$ by using the initial state radiation (ISR) method (BaBar, KLOE and BESIII) or the energy–scan approach (SND, CMD–2, CMD–3). In particular, the systematic error of the hadronic vacuum polarization (HVP) contribution to the magnetic moment of the muon, $a_\mu^{\rm HVP}$, includes a non–negligible effect due to the tension between the high precision experiments BaBar and KLOE. In this scenario, since 2022, we can add the discrepancy between KLOE/BaBar and CMD–3 [12] measurements. At the current level of precision, a deep investigation of radiative corrections for the process $e^+e^- \to \pi^+\pi^-$ [18–20], which are implemented in Monte–Carlo generators used in the experimental analyses, is required. Without going into details here, there are three main approaches used to compute these corrections: scalar QED supplemented by the pion VFF wherever possible (F×sQED) [21], generalized vector meson dominance (GVMD) [22] and dispersive approach [23]. While the first two approaches rely on models, the model–independent dispersive approach put the computation of the radiative corrections to $e^+e^- \to \pi^+\pi^-$ on a more solid ground.
An alternative theoretical result for $a_\mu^{\rm HLO}$ comes from lattice QCD computations which, however, shows tensions with the data–driven one. The differences between these two theoretical results as well as the ones among the different experiments for the $e^+e^- \to$ hadrons cross section measurement, deserve further investigation.

On one side, in view of a better understanding of the $e^+e^- \to \pi^+\pi^-$ cross section, in particular given the recent increased tension among the experimental measurements, an investigation of the $\pi\pi$–scattering amplitude, and of its isospin–breaking (IB) effects, is necessary. The two processes are related due to the Watson theorem, which guarantees that the $e^+e^- \to \pi^+\pi^-$ and the $\pi\pi \to \pi\pi$ scatterings are described by the same phase, once the amplitudes are written in a partial waves expansion and if we consider only $\pi\pi$ intermediate states. Moreover, the understanding of the $\pi\pi$–scattering process is necessary since, for a comprehensive description of the $e^+e^- \to \pi^+\pi^-$ experimental cross section, rescattering effects are important and need to be included. The $\pi\pi$–scattering amplitude is understood at a remarkable level of accuracy, particularly at low energy and in the isospin limit [24–28]. Experimental measurements have provided, on the one hand, necessary input to theoretical calculations [29] and, on the other, have confirmed the predictions for the S–wave scattering lengths [30–33] to the same level of precision. Whenever experimental data are used, as input or for comparison with theoretical calculations done in the isospin

limit, it becomes necessary to remove isospin–breaking effects from the data. The effects that need to be considered are: the emission of real and virtual photons, the up–down quark mass difference and the charged–neutral pion mass difference. These effects can be investigated with a reliable and model–independent approach in the region below 1 GeV. The approach is that of dispersion relations, but with an approximation: intermediate states only up to two pions are considered while the contribution to isospin–breaking effects of three or more pions or heavier states ($K\bar{K}$, $\eta\eta$, etc.) with or without photons is simply neglected. In fact, the $\pi\pi$ intermediate state represent the main channel and the isospin–breaking effects result already in a small correction to the scattering amplitude, meaning that the contribution of higher order states would be further suppressed. The main motivation for this analysis is to provide input for a dispersive treatment of the same isospin–breaking effects for the vector form factor of the pion, an essential input for the calculation of the hadronic vacuum polarization contribution to the muon $g-2$. Dealing with isospin–breaking effects in this reaction, especially of final–state radiation, has so far been based on models, in particular on scalar QED, with form factor effects taken into account in an ad hoc manner. A dispersive approach can do better and provides a model–independent estimate of these effects, but requires the $\pi\pi$–scattering amplitude, including isospin–breaking effects, as input. In this work, as a first step towards a full dispersive calculation of the radiative corrections for the $e^+e^- \to \pi^+\pi^-$ process, we will analyze the effects due to the charged–neutral pion mass difference in the dispersive analysis of the $\pi\pi$ scattering amplitude.

On the other side, the current problematic theoretical situation, i.e., the tension among the different $e^+e^- \to \pi^+\pi^-$ measurements and the discrepancy between the data–driven and the lattice QCD estimates for the muon $g-2$, requires new and more precise computation, both from an experimental and theoretical point of view. In this sense, the study of the τ decay provides an alternative and independent way to compute this observable, since an analysis of the isospin–breaking corrections to this process in a model independent way offers a completely new estimate of the $e^+e^- \to \pi^+\pi^-$ cross section, and, ultimately, the muon anomalous magnetic moment, which can help in clarifying the current situation. In fact, a conserved–vector–current (CVC) relation between electromagnetic and weak form factors allows to relate the differential decay rate for the process $\tau \to \pi\pi^0\nu_\tau$ to the cross section $\sigma(e^+e^- \to \pi^+\pi^-)$ in the isospin limit. In this work, a model–independent dispersive approach to the computations of the isospin–breaking effects in the $\tau \to \pi\pi^0\nu_\tau$ decay, at $\mathcal{O}(e^2p^2)$ in the chiral power counting, is presented, i.e., with virtual and real photons included. In particular, results for the long–range corrections to the hadronic τ–decay, usually denoted by $G_{\mathrm{EM}}(s)$, will be presented. Up to now these effects were computed only on a model–dependent basis [34–37]. Our model–independent approach set the understanding of these isospin–breaking effects on a more solid ground.

The structure of this work is the following: chapter 2 reviews the QED, electroweak and hadronic contributions to the anomalous magnetic moment of the muon, giving also an overview of the current experimental and theoretical situation. The concepts of unitarity and analyticity which, coupled with complex analysis, provide the central tools used in the calculations of this thesis, are introduced in chapter 3. Chapter 4 is a brief introduction to chiral perturbation theory. A detailed analysis of the properties of the $\pi\pi$–scattering amplitude and explicit representations used in this thesis work are given in chapter 5. In chapters 6–8, the model–independent dispersive approach to the $\pi\pi$–scattering is presented. We first describe the formalism in the isospin–limit and then how this change once we consider isospin–breaking effects. Then we explain how to solve Roy equations away from the isospin–limit and in Ch. 8, we show the results. In chapter 10, we introduce the hadronic τ decay as an alternative computation of the muon $g-2$. In particular, we work out the analysis in the χPT formalism. In chapter 11, we describe our dispersive analysis of the virtual contributions to the process $\tau^- \to \pi^-\pi^0\nu_\tau$, while in chapter 12 we

compute the real emission contributions. The results for the muon $g-2$ estimate accounting for isospin breaking effects in the hadronic τ decay are given in chapter 13. In chapter 14, conclusions and outlook about this thesis work are drawn.

Chapter 2

The muon anomalous magnetic moment

In this chapter, we introduce the anomalous magnetic moment of the muon and explain how it is calculated in the Standard Model. We review the current status of the anomaly between its theoretical prediction and its measurement and we investigate all the SM sectors contributing to the theoretical determination of the muon $g-2$, i.e., electromagnetic, weak and strong interactions.

2.1 A brief historical overview

Besides charge, spin, mass and lifetime, leptons have other very interesting properties like the magnetic and the electric *dipole moments*. Classically the dipole moments can arise from either electrical charges or currents. An orbiting particle with electric charge e and mass m exhibits a magnetic dipole moment

$$\boldsymbol{\mu}_L = \frac{e}{2m}\mathbf{L}\,, \tag{2.1}$$

where $\mathbf{L} = m\mathbf{r}\times\mathbf{v}$ is the orbital angular momentum. Both electric and magnetic moments contribute to the Hamiltonian of electromagnetic interactions of the particle:

$$H = -\boldsymbol{\mu}_m\cdot\mathbf{B} - \boldsymbol{d}_e\cdot\mathbf{E}\,, \tag{2.2}$$

where $\mathbf{B}$ and $\mathbf{E}$ are the magnetic and electric field strengths and $\boldsymbol{\mu}_m$ and $\boldsymbol{d}_e$ the magnetic and electric dipole moment operators. On one side, the search for a permanent electric dipole moment (EDM) has been interesting physicists for decades: the detection of such a dipole would be a strong test of the time reversal symmetry (T) since an EDM along the spin axis can exist only if T is violated. On the other side, the magnetic moment is an observable which can be relatively easily studied experimentally from the motion of the lepton in an external magnetic field. In 1925, Goudsmit and Uhlenbeck, in order to explain the anomalous Zeeman effect [38, 39], postulated that the intrinsic angular momentum (or spin) of the electron was equal to $\frac{1}{2}\hbar$ and that, associated to this spin, there is a magnetic dipole moment $\mu_0 = \frac{e\hbar}{2mc}$, the *Bohr magneton*. Usually the magnetic moments are measured in terms of μ_0 and of the *spin operator*, $\mathbf{S} = \frac{\hbar\boldsymbol{\sigma}}{2}$, which replaces the angular momentum operator $\mathbf{L}$:

$$\boldsymbol{\mu}_m = gQ\mu_0\frac{\boldsymbol{\sigma}}{2}\,, \tag{2.3}$$

where σ_i $(i=1,2,3)$ are the Pauli spin matrices, Q is the electric charge in units of e and g is the gyromagnetic ratio (g–factor). Goudsmit and Uhlenbeck imposed this g–factor to be $g=2$ to explain the anomalous Zeeman effect. In the same year, Back and Landé [40], after numerous experimental investi-

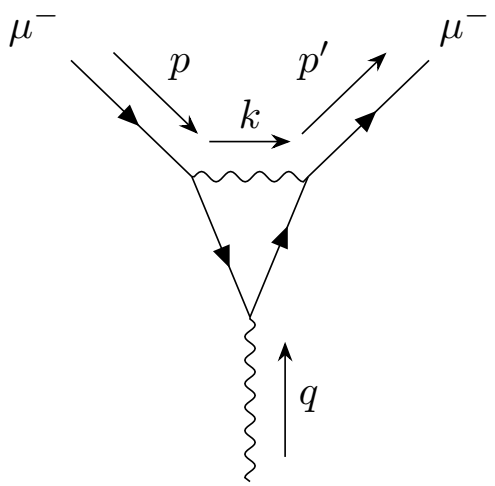

Figure 2.1: 1–loop QED vertex correction diagram

gations on the Zeeman effect, concluded that the magnetic moment of the electron $(\mu_{\rm m})_{\rm e}$ was consistent with the Goudsmit and Uhlenbeck postulate. In 1927, Pauli formulated the quantum mechanical treatment of the electron spin where g remains a free parameter [41]. In 1928, Dirac presented his relativistic theory and predicted $g = 2$ for a free electron [42, 43], twice the value $g = 1$ associated with the orbital angular momentum. In 1947, Nafe, Nelson and Rabi [44] reported an anomalous value by about 0.26% in the hyperfine splitting of hydrogen and deuterium, suggesting a possible anomaly of the magnetic moment of the electron. This brings us to the definition of the lepton *anomalous magnetic moment*

$$a_l \equiv \frac{g_l - 2}{2} \quad \text{where} \quad l = e,\ \mu,\ \tau\ . \tag{2.4}$$

In 1948 Kusch and Foley [45], by studying the hyperfine structure of atomic spectra in a constant magnetic field, presented the first precision determination of the anomalous magnetic moment of the electron $a_e = 0.00119(5)$. In the same year, the theoretical result was computed by Schwinger who, by working on the renormalization of QED, predicted the 1–loop QED (Fig. 2.1) contribution to the anomalous magnetic moment [46]

$$a_l^{\rm QED(1)} = \frac{\alpha}{2\pi} = 0.00116...\ , \tag{2.5}$$

where α is the fine structure constant.

This contribution is due to quantum fluctuations via virtual electron–photon interactions and is universal for all leptons in QED. These theoretical and experimental results provided one of the first tests of the virtual quantum corrections, called *radiative corrections*, predicted by a relativistic QFT.

2.2 The muon anomalous magnetic moment

The theoretical computation of the anomalous magnetic moment of the muon, $a_\mu = \frac{g_\mu - 2}{2}$, has been interesting physicists for over 60 years. On one hand, the anomalous magnetic moment of the electron, a_e, has been computed precisely and its agreement with the experimental result provided one of the early confirmation of QED [47]. Moreover a_e is almost insensitive to strong and weak interactions, provides a stringent test of QED and, until recently, used to lead to the most precise determination of the fine–

structure constant α. In the future, this observable will play an important role to test physics Beyond the Standard Model (BSM) [48]. On the other hand, the long–standing discrepancy between the theoretical computation and experimental measurement of the anomalous magnetic moment of the muon indicates a_μ as a better candidate to study BSM physics. The anomalous magnetic moment of the muon, a_μ, allows one to investigate all the SM sectors (electromagnetic, weak and strong interactions), providing a great candidate to unveil BSM effects. If Λ indicates the scale of BSM, the contribution to the anomalous magnetic moment of a lepton l, a_l, is generally proportional to $\frac{m_l^2}{\Lambda^2}$ [49]. This leads to a $\left(\frac{m_\mu}{m_e}\right)^2 \sim 4\times10^4$ relative enhancement of the sensitivity of the muon versus the electron magnetic moment. Thus the anomalous magnetic moment of the τ would be the best candidate to investigate BSM effects, but the short lifetime of this lepton makes such a measurement very difficult at the moment.

Before April 2021, the experimental value was the one obtained at the E821 experiment at the Brookhaven National Laboratory (BNL) and the discrepancy between the BNL measurement and the theoretical SM result was 3.7 σ. In April 2021, the new experimental result of the Muon g–2 experiment at FermiLab (FNAL) confirmed the BNL result, increasing the combined BNL+FNAL discrepancy with the SM result to 4.2 σ, if the leading hadronic contribution is computed via the traditional dispersive method with $e^+e^- \to$ hadrons data (see later). This discrepancy increased up to 5.1 σ when a new result from FNAL (Run 2+3) was presented in August 2023 [10]. On the other side, the BMW collaboration lattice QCD result in 2021 [11] and the one obtained with the standard method but with the new CMD–3 experimental result for $e^+e^- \to$ hadrons data in 2022 weakened this discrepancy [12]. Between May and June 2025, a new theoretical value [14] and the final experimental result from FNAL [13] for the muon $g-2$ were published, leading to a considerable decrease of the discrepancy between the two results [14]:

$$a_\mu^{\rm exp} - a_\mu^{\rm SM}({\rm WP25}) = 38(63)\times10^{-11} \tag{2.6}$$

In contrast with the theoretical result in the WP20, where the leading–order hadronic vacuum polarization estimate for the muon $g-2$ was obtained from a purely data–driven approach, the one released in the WP25 [14] includes only the new, published lattice–QCD calculations for $a_\mu^{\rm HLO}$, for which the results from different collaborations are in good agreement (see Fig. 2.2). The data–driven estimate of $a_\mu^{\rm HLO}$, computed via a dispersion integral using the hadronic production cross sections in electron–positron annihilation at low energy, was not included due to the increased tension among the experimental inputs [12,14], in particular between KLOE/BaBar and CMD–3 experiments (see Fig. 2.3 for a detailed picture of the current situation of the estimate of $a_\mu^{\rm HLO}$ with the data–driven approach).

In this chapter a review of the theoretical prediction of a_μ in the SM is presented and all the three contributions (QED, electroweak and hadronic) into which $a_\mu^{\rm SM}$ is usually split, are analyzed. For detailed reviews see [9,14,50–52].

2.2.1 QED radiative corrections

The largest contribution to the anomalous magnetic moment is of pure QED origin. The QED contribution to the muon $g-2$ arises only from the interaction of leptons (e, μ, τ) with photons. As a dimensionless quantity, it can be cast in the following general form [53,54]

$$a_\mu^{\rm QED} = A_1 + A_2\left(\frac{m_\mu}{m_e}\right) + A_2\left(\frac{m_\mu}{m_\tau}\right) + A_3\left(\frac{m_\mu}{m_e},\frac{m_\mu}{m_\tau}\right)\ , \tag{2.7}$$

where m_e, m_μ and m_τ are the masses of the electron, muon and tau, respectively. The term A_1, arising from diagrams containing only photons and muons, is mass independent and is therefore universal for all three charged leptons. The contribution A_2 is a function of the indicated mass ratios and only shows up if

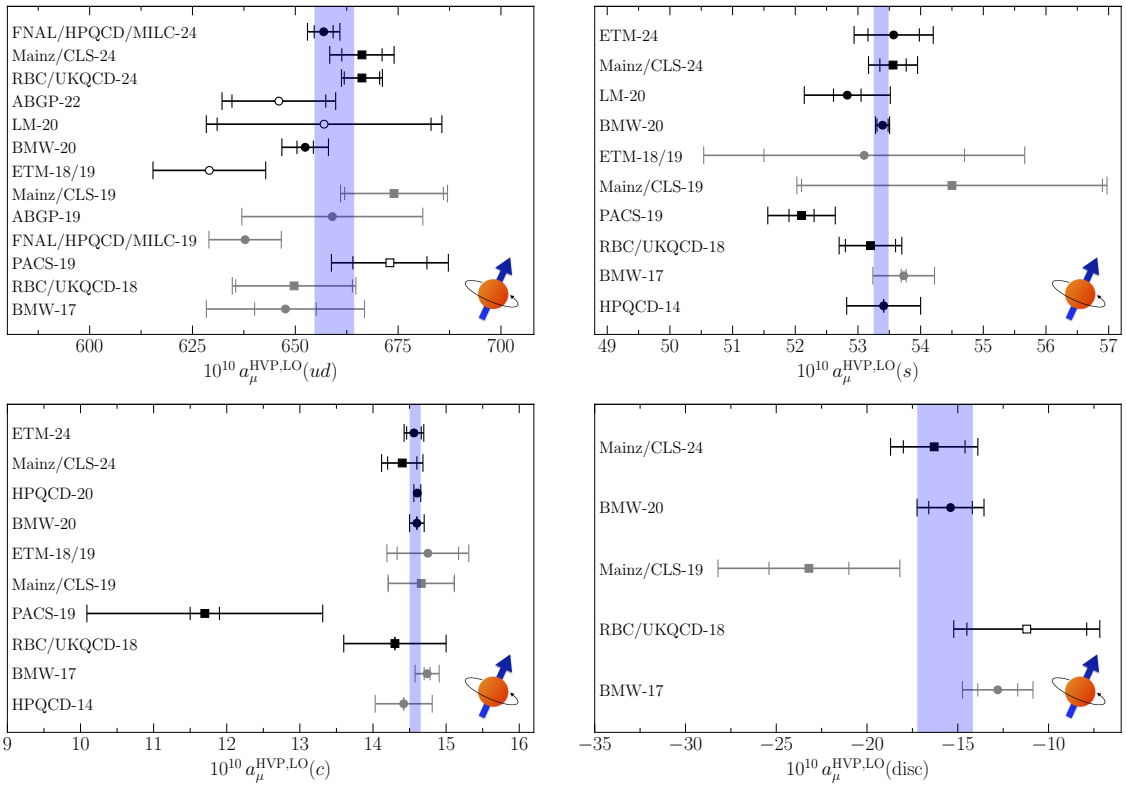

Figure 2.2: Compilation of lattice results for the flavor contributions to a_μ^{HLO}. Upper–left: light–quark connected a_μ^{HLO}. Upper–right: strange–quark connected a_μ^{HLO}. Lower–left: charm–quark connected a_μ^{HLO}. Lower–right: quark disconnected a_μ^{HLO}. The light blue bands correspond to "Avg. A" computed as explained in [14]. Results not included in the average are denoted by unfilled symbols. Figure taken from [14].

an additional lepton loop of a lepton different from the muon is involved. This requires at least two more loops: an additional electron loop $A_2\,(m_\mu/m_e)$ or an additional τ–loop $A_2\,(m_\mu/m_\tau)$. The first produces large logarithms $\propto \ln\,(m_\mu^2/m_e^2)$ and accordingly large effects, while the second, because of the *decoupling* of heavy particles in QED–like theories, produces only small effects $\propto (m_\mu^2/m_\tau^2)$. The renormalizability of QED guarantees that the functions A_i can be expanded as a power series in α/π and computed order by order

$$A_i = A_i^{(2)}\left(\frac{\alpha}{\pi}\right) + A_i^{(4)}\left(\frac{\alpha}{\pi}\right)^2 + A_i^{(6)}\left(\frac{\alpha}{\pi}\right)^3 + A_i^{(8)}\left(\frac{\alpha}{\pi}\right)^4 + \ldots \tag{2.8}$$

One–loop contribution

Only one diagram (Fig. 2.1) is involved in the evaluation of the lowest–order contribution and it provides the famous result obtained by Schwinger $A_1^{(2)} = 1/2$. The Lorentz structure of the vertex correction is given by the three–point function $-ie\Gamma^\mu = \langle\bar{\psi}A^\mu\psi\rangle$, where ψ ($\bar{\psi} = \psi^+\gamma^0$) is the (barred) spinorial representation of the fermion, A is the vectorial representation of the photon and e is the electric charge. As a first step we assign a 4–momentum p to the incoming particle, a 4–momentum p' to the outgoing particle and we define the transferred 4–momentum $q \equiv p' - p$ (Fig. 2.1). This brings us to the spinorial representation $u(p)$ for the incoming particle and $\bar{u}(p')$ for the outgoing one in momentum space. In general, Γ^μ is some expression that involves p, p', γ^μ and constants like the mass of the particle, m, and the electric charge, e. We can narrow down the form of Γ^μ by appealing to Lorentz invariance. Since Γ^μ

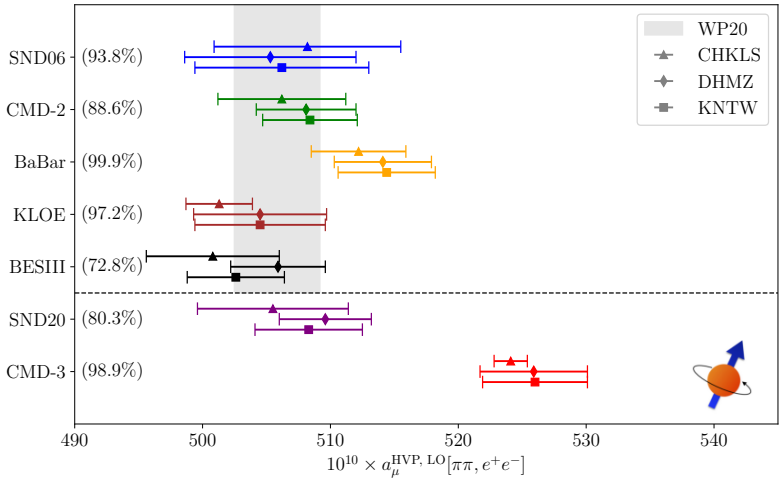

Figure 2.3: Dispersive theoretical predictions for a_μ^{HLO}, based on various measurements of $e^+e^- \to \pi^+\pi^-$ (percentages of the integral covered by each measurement are shown), and for the three approaches "CHKLS," "DHMZ," and "KNTW" (see [14] for details).The gray band indicates the result from WP20, including the error inflation due to the BaBar–KLOE tension. The experiments above the dashed line entered the result for WP20, whilst those below are new measurements since then. Figure taken from [14].

transforms as a vector, it must be a combination of the vectors listed above:

$$-ie\bar{u}(p')\Gamma^\mu u(p) = -ie\bar{u}(p')\left[\gamma^\mu \cdot A + (p'^\mu + p^\mu)\cdot B + (p'^\mu - p^\mu)\cdot C\right] u(p)\,, \tag{2.9}$$

where A, B and C are functions of the transferred squared momentum q^2. From the gauge symmetry of the theory, the Ward identity, $q_\mu \Gamma^\mu = 0$, can be applied and the only term that does not automatically vanish is the one proportional to C, so C must be zero. The last step is to apply the Gordon identity to obtain

$$-ie\bar{u}(p')\Gamma^\mu(p',p)u(p) = -ie\bar{u}(p')\left[\gamma^\mu F_1(q^2) + \frac{i\sigma^{\mu\nu}q_\nu}{2m}F_2(q^2)\right] u(p)\,, \tag{2.10}$$

where $\sigma^{\mu\nu} = \frac{i}{2}\left[\gamma^\mu, \gamma^\nu\right]$ is the spin–1/2 angular momentum tensor, while F_1 and F_2 are unknown functions of q^2 called (electric) Dirac and (magnetic) Pauli form factors, respectively. In the static limit ($q^2 \to 0$) we have

$$F_1(0) = 1 \quad \text{and} \quad F_2(0) = a_l\,. \tag{2.11}$$

The first condition is the *charge renormalization condition*, while the second relation is the finite value of the anomalous magnetic moment of the lepton l.

By explicitly evaluating the one–loop contribution to the muon vertex function we can prove the Schwinger result $A_1^{(2)} = 1/2$. We assign the particle momenta as shown in Fig. 2.1 and by applying the Feynman rules listed in App. A, we obtain

$$\bar{u}(p')\Gamma^\mu(p,p')u(p) = -ie^2\int \frac{\mathrm{d}^4k}{(2\pi)^4}\bar{u}(p')\frac{\gamma^\nu(\not{q}+\not{k}+M)\gamma^\mu(\not{k}+M)\gamma_\nu}{[(k-p)^2+i\epsilon][(q+k)^2-M^2+i\epsilon][(k^2-M^2)+i\epsilon]}u(p)\,, \tag{2.12}$$

where the $+i\epsilon$ terms in the denominator are necessary for proper evaluation of the loop–momentum integral. This integral can be computed using the Feynman parameters technique: squeeze the three denominator factors of Eq. (2.12) into a single quadratic polynomial in k, raised to the third power; shift

k by a constant to complete the square in this polynomial and evaluate the remaining spherically symmetric integral. The price to pay is the introduction of auxiliary parameters to be integrated over. After some lengthy calculation we obtain

$$\begin{aligned}\bar{u}(p')\Gamma^{\mu}(p,p')u(p) = &-ie^2\int\frac{\mathrm{d}^4l}{(2\pi)^4}\int_0^1\mathrm{d}x\,\mathrm{d}y\,\mathrm{d}z\,\delta(x+y+z-1)\frac{2}{D^3}\\ &\times\bar{u}(p')\Bigg[\gamma^{\mu}\cdot\left(-\frac{1}{2}l^2+(1-x)(1-y)q^2+(1-4z+z^2)M^2\right)\\ &+\frac{i}{2M}\sigma^{i\nu}q_{\nu}(2M^2z(1-z))\Bigg]u(p)\,,\end{aligned} \tag{2.13}$$

where $D=l^2-\Delta+i\epsilon$ and $\Delta=-xyq^2+(1-z)^2M^2$. The decomposition into form factors [55] is now manifest and in particular, after performing the integration in d^4l we obtain

$$F_2(q^2)=\frac{\alpha}{2\pi}\int_0^1\mathrm{d}x\,\mathrm{d}y\,\mathrm{d}z\,\delta(x+y+z-1)\left[\frac{2m^2z(1-z)}{m^2(1-z)^2-xyq^2}\right]+\mathcal{O}(\alpha^2)\,, \tag{2.14}$$

and, in order to compute the muon anomalous magnetic moment, we have to set $q^2=0$ and get

$$\begin{aligned}a_{\mu}=F_2(0)&=\frac{\alpha}{2\pi}\int_0^1\mathrm{d}x\,\mathrm{d}y\,\mathrm{d}z\,\delta(x+y+z-1)\left[\frac{2m^2z(1-z)}{m^2(1-z)^2}\right]\\ &=\frac{\alpha}{\pi}\int_0^1\mathrm{d}z\int_0^{1-z}\mathrm{d}y\frac{z}{1-z}=\frac{\alpha}{2\pi}\,.\end{aligned} \tag{2.15}$$

This result, together with the higher–order contributions and the currently best value of the fine structure constant, coming from the electron anomalous magnetic moment a_e [56],

$$\alpha^{-1}(a_e)=137.035\,999\,1496(13)(14)(330)\,, \tag{2.16}$$

leads to the value for the QED contribution to the muon $g-2$ [14]

$$a_{\mu}^{\mathrm{QED}}=116\,584\,718.8(2)\times10^{-11}\,, \tag{2.17}$$

where the higher–order effects are computed up to 5–loops [57] and the error quoted here is obtained by combining the ones from the results of a_{μ}^{QED} computed for three different values of α, i.e., $a_{\mu}^{\mathrm{QED}}[\alpha(Cs)]$, $a_{\mu}^{\mathrm{QED}}[\alpha(a_e)]$ and $a_{\mu}^{\mathrm{QED}}[\alpha(Rb)]$ [14].

2.2.2 Electroweak contribution

The electroweak contribution to the anomalous magnetic moment of the muon is suppressed by a factor $(m_{\mu}/M_W)^2$, where M_W is the mass of the W boson, with respect to the QED contributions.

One–loop contribution

The one–loop electroweak contribution to the muon $g-2$ is due to diagrams shown in Fig. 2.4 and its analytic form is

$$a_{\mu}^{\mathrm{EW}}(1-\mathrm{loop})=\frac{5G_Fm_{\mu}^2}{24\sqrt{2}\pi^2}\left[1+\frac{1}{5}(1-4\sin^2\theta_W)^2+\mathcal{O}\left(\frac{m_{\mu}^2}{M_{Z,W,H}^2}\right)\right]\,, \tag{2.18}$$

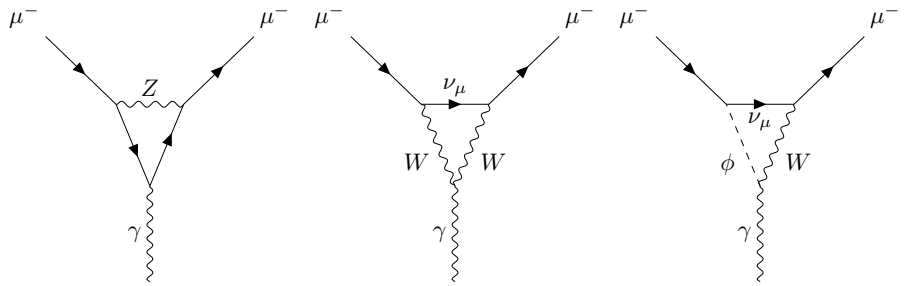

Figure 2.4: Diagrams involved in the computation of the electroweak contribution at one–loop to the muon g–2, where ν_μ is the muon neutrino and ϕ is a scalar.

where $G_F = 1.16637(1) \times 10^{-5}$ GeV^{-2} is the Fermi coupling constant, M_Z, M_W and M_H are the masses of the Z, W and Higgs bosons, respectively, while θ_W is the Weinberg angle. The numerical result is [14]

$$a_\mu^{\rm EW}(1-{\rm loop}) = 194.79(1) \times 10^{-11} \ . \tag{2.19}$$

Higher–order contributions

The two–loop electroweak contribution to a_μ [58, 59] leads to a significant reduction of the one–loop value. This contribution appeared to be of fundamental importance [60] and the correction turned out to be enhanced by a factor $\ln(M_{Z,W}/m_f)$, where m_f is a fermion mass scale much smaller then M_W. In QED, diagrams with an odd number of photons attached to a loop do not contribute due to the Furry's theorem and the $\gamma\gamma\gamma$–amplitude vanishes. In presence of weak interactions, because of parity violation, contributions from the two orientations of the closed fermion loops do not cancel such that the $\gamma\gamma Z$, γZZ and γWW amplitudes do not vanish. The two–loop contributions to $a_\mu^{\rm EW}$ is usually split into a fermionic and a bosonic part: the first one includes all the two–loop EW corrections containing closed fermion loops, whereas all other contributions are grouped into the second one.

Summing up all the results, the electroweak contribution to the muon $g-2$ is [14]

$$a_\mu^{\rm EW} = 154.4(4) \times 10^{-11} \ . \tag{2.20}$$

The updates with respect to the result in [9] are related to more accurate measurements of input parameters entering Feynman diagrams, leading to reduced parametric uncertainties, and to improved determination of hadronic EW contributions [61].

2.2.3 Hadronic contributions

In this section we will analyze the contribution to the muon $g-2$ arising from QED diagrams involving hadrons, which dominate the uncertainty in the SM value [62–64]. The main effect comes from the $\mathcal{O}(\alpha^2)$ hadronic vacuum polarization (HVP) insertion in the internal photon line of the leading one–loop muon vertex diagram (Fig. 2.5), in particular from the $\pi\pi$ intermediate state. It is this contribution that is linked to the pion vector form factor F_π^V and to $\pi\pi$ scattering [65–68]. Similar representations have been used more recently [69–72], in particular on a dispersive approach to hadronic light–by–light (HLbL) scattering [73–78], where the space–like form factor determines the pion–box contribution. Moreover, $\pi\pi$ scattering plays a crucial role in many hadronic quantities that enter HLbL scattering, e.g. in $\gamma^*\gamma^* \to \pi\pi$ [79–82] or the π^0 [83–89] and η, η' [90–95] transition form factors, with recent extension to the $\pi\eta$ system [96, 97].

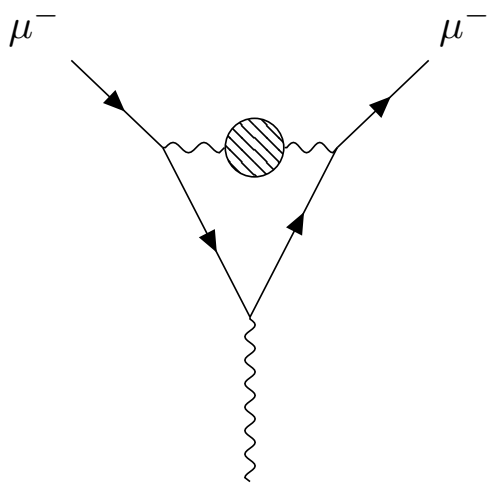

Figure 2.5: HVP contribution to the muon anomalous magnetic moment

Leading–order hadronic contribution

The hadronic leading order (HLO) contribution to the anomalous magnetic moment of the muon, $a_\mu^{\rm HLO}$, is due to the vacuum polarization correction to the internal photon propagator of the one–loop diagram (Fig. 2.5). The computation of this contribution involves low–energy QCD for which the perturbative approach can not be applied. A different approach to perform this evaluation was found by Bouchiat and Michel [98]: using analyticity and unitarity, $a_\mu^{\rm HLO}$ can be computed from hadronic e^+e^- annihilation data via a dispersion integral [98–101] (an introduction to analyticity, unitarity and dispersion relations will be given in the next chapter). The hadronic input for this contribution is encoded in the QCD two–point function of the electromagnetic currents [102]

$$\Pi_h^{\mu\nu} = ie^2 \int {\rm d}^4x\, e^{iq\cdot x} \langle 0|T\{j_{em}^\mu(x) j_{em}^\nu(0)\}|0\rangle = \left(q^2 g^{\mu\nu} - q^\mu q^\nu\right) \Pi_h(q^2)\,, \tag{2.21}$$

where the Lorentz decomposition follows from gauge invariance. The current is defined by

$$j_{em}^\mu := \bar{q} Q \gamma^\mu q\,, \quad q = \begin{pmatrix} u \\ d \\ s \end{pmatrix}\,, \quad Q = \frac{1}{3}\begin{pmatrix} 2 & 0 & 0 \\ 0 & -1 & 0 \\ 0 & 0 & -1 \end{pmatrix}\,, \tag{2.22}$$

and the sign convention is such that the fine–structure constant evolves according to

$$\alpha \to \alpha(q^2) = \frac{\alpha(0)}{1 - [\Pi_h(q^2) - \Pi_h(0)]} = \frac{\alpha(0)}{1 - \Delta\alpha(q^2)}\,, \tag{2.23}$$

where q^2 is the momentum of the internal photon line and $\Delta\alpha(q^2) = -{\rm Re}\bar{\Pi}_h(q^2)$ with $\bar{\Pi}_h(q^2) \equiv \Pi_h(q^2) - \Pi_h(0)$. The renormalized HVP function $\bar{\Pi}_h(q^2)$ is analytic in the complex $s := q^2$ plane and satisfies the dispersion relation

$$\bar{\Pi}_h(s) = \frac{s}{\pi} \int_{s_{\rm thr}}^\infty {\rm d}s\, \frac{{\rm Im}\,\Pi_h(s')}{s'(s'-s)}\,, \tag{2.24}$$

where in pure QCD the integral starts at the two–pion threshold, $s_{\rm thr} = 4M_\pi^2$, since the threshold energy necessary to produce a purely hadronic VP is $(2M_\pi)^2$. In QCD+QED, the $\pi^0\gamma$ final state would be the

first open hadronic channel and should define the lower limit of integration in the dispersion integral. Unitarity also implies the validity of the *optical theorem* thanks to which it is possible to relate $\mathrm{Im}\ \Pi_h(s)$ with the experimentally measured cross section. Up to now, the LO HVP contribution is computed using the cross section for low–energy hadronic e^+e^- annihilation, and this gives the relation

$$\sigma(e^+e^- \to \text{hadrons}) = \frac{4\pi\alpha}{s}\frac{1}{\sigma_e(s)}\left(1+\frac{2m_e^2}{s}\right)\mathrm{Im}\ \Pi_h(s)\ , \tag{2.25}$$

where $\sigma_l(s) = \sqrt{1-\frac{4m_l^2}{s}}$. The HVP contribution to the anomalous magnetic moment of the muon can then be written as [98,100]

$$a_\mu^{\mathrm{HLO}} = \left(\frac{\alpha m_\mu}{3\pi}\right)^2 \int_{s_{\mathrm{thr}}}^{\infty} \frac{\mathrm{d}s}{s^2}\hat{K}(s)R_{\mathrm{had}}(s)\ , \tag{2.26}$$

where the kernel function is

$$\hat{K}(s) = \frac{3s}{m_\mu^2}\left[\frac{x^2}{2}(2-x^2) + \frac{(1+x^2)(1+x)^2}{x^2}\left(\ln(1+x) - x + \frac{x^2}{2}\right) + \frac{1+x}{1-x}x^2\ln x\right]\ , \tag{2.27}$$

with $x = \frac{1-\sigma_\mu(s)}{1+\sigma_\mu(s)}$ and whose behavior is shown in Fig. 2.6, while $R_{\mathrm{had}}(s)$ is related to the hadronic cross section by

$$R_{\mathrm{had}}(s) = \frac{3s}{4\pi\alpha^2}\frac{s\sigma_e(s)}{s+2m_e^2}\sigma(e^+e^- \to \text{hadrons})\ . \tag{2.28}$$

The usual ratio R, defined as the ratio of hadronic to muonic e^+e^- experimental cross sections,

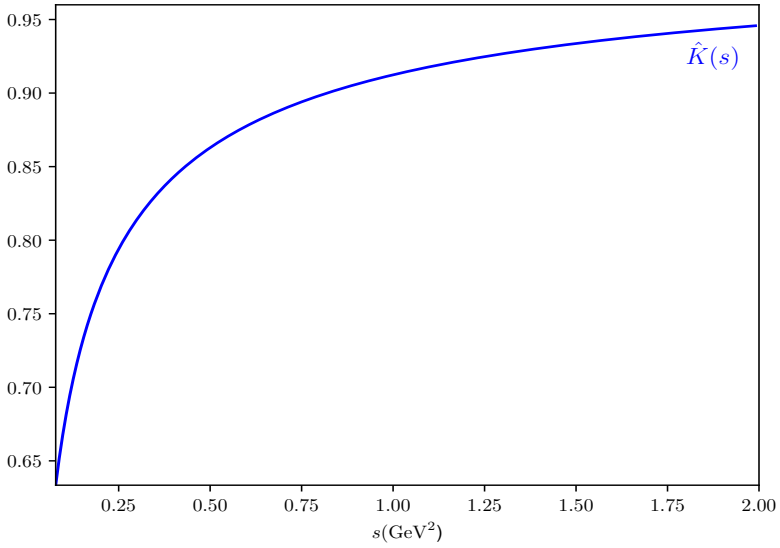

Figure 2.6: Behavior of the function $\hat{K}(s)$ in the interval $s \in [4M_\pi^2, 2\ \mathrm{GeV}^2]$.

$$R(s) = \frac{\sigma(e^+e^- \to \text{hadrons})}{4\pi\alpha(s)^2/3s}\ , \tag{2.29}$$

is not what enters the dispersive representation of the HVP contribution: the representation in Eq. (2.26), with Eqs. (2.27) and (2.28), where $\sigma(e^+e^- \to \text{hadrons})$ depends on the HVP correction function $\Pi_h(s)$, is exact. $R_{\text{had}}(s)$ and $R(s)$ coincide for a tree–level muonic cross section and in the limit $s \gg m_\mu^2$, where of course the electron mass does not play any role but, for clarity, we have provided the expression of the HVP contribution without any approximation. With this dispersive approach it is possible to overcome the issues involving non–perturbative QCD computations appearing in the LO hadronic contribution to a_μ. The ratio $R(s)$, or equivalently Im $\Pi_h(s)$, are obtained from e^+e^- annihilation data, which involves a positive squared momentum transfer and so this is called *time–like* approach.

Before quoting the final result for the HLO contribution to a_μ, let us discuss in more details $\sigma(e^+e^- \to$ hadrons). This cross section can be determined in e^+e^- annihilation, either in *direct scan* mode, where the beam energy is adjusted to provide measurements at different center–of–mass (CM) energies, or by relying on the method of *radiative return*, where a collider is operating at a fixed CM energy. At low energies, the most important channel is the two–pion channel (details in the next section). This final state stems mainly from decays of the ρ meson, with an admixture of the ω. Precise measurements in the ρ region come from CMD–2 and SND experiments but also from the KLOE and BaBar ISR analyses. More recently results with the ISR method in the charm region and large–angle ISR tagging have been obtained by BESIII. Sub–leading contributions arise from decays of the ω and ϕ in the three–pion and two–kaon channels, and from four–pion states with more complicated production mechanisms. The contribution of these channels to the hadronic cross section is obtained from the CMD–2, SND and BaBar experiments. Moreover, even–higher–multiplicity final states (up to six pions) and final states containing pions and kaon or the η have to be included in order to achieve an accurate description of the total hadronic cross section. For energies beyond $\sqrt{s} \sim 2$ GeV, one relies on measurements of the inclusive cross section or, alternatively, for energies above the τ mass and away from flavor threshold, perturbative QCD (pQCD) can provide a good approximation of the total hadronic cross–section. In this case, the annihilation cross section has to be measured inclusively because of the large number of open exclusive channels and precise results in the 2–4.5 GeV range are obtained by BESIII. The distribution of different channel contributions and error squares from different energy regions can be found in Fig. 2.7.

In order to obtain a single estimate for a_μ^{HLO}, a combination of the different data must be performed,

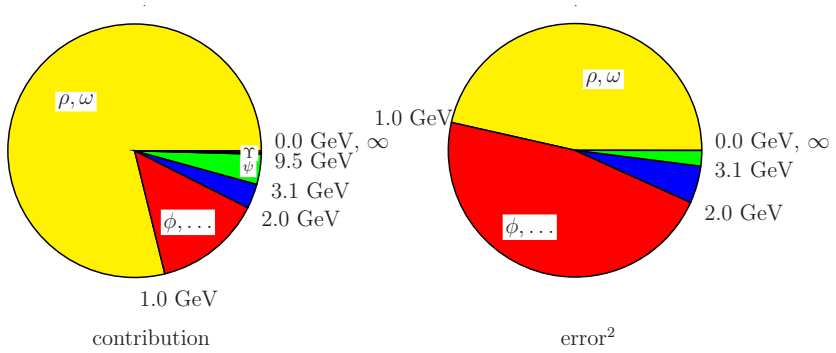

Figure 2.7: Distribution of contribution and error squares from different energy regions. Figure taken from [9].

taking into account the different energy ranges, the different binning, and a possible correlations within and between data sets. The approaches to combine all the different data sets are mainly two: the DHMZ approach uses the software package HVPTools which features an accurate data interpolation, averag-

ing, and integration methods, systematic tests, and a statistical analysis based on the generation of large samples of pseudo–experiments. It allows for a comprehensive treatment of the correlation between the measurements of one experiment, as well as inter–experiment and inter–channel correlations. The KNT [103, 104] approach provides a predominantly data–driven compilation for the hadronic R–ratio, which is then used to predict the HVP contributions to precision observables such as a_μ. Only after combining the different experimental data for $\sigma(e^+e^- \to \text{hadrons})$, the integral for a_μ^{HLO} can be performed and the latest result for the HLO contribution is [9]:

$$a_\mu^{\text{HLO}} = 6931(40) \cdot 10^{-11} \tag{2.30}$$

where the error is mainly due to experimental measurements of hadronic e^+e^- annihilation. This *time–like* approach solves the long–distance QCD problems but it suffers from the experimental uncertainties associated to the hadronic e^+e^- annihilation data. However, as said at the beginning of this chapter, the HLO data–driven contribution to a_μ needs to be investigated further due to the increased tension between the different experimental results for $\sigma(e^+e^- \to \text{hadrons})$.

An alternative evaluation of a_μ^{HLO} can be obtained by lattice QCD calculations. Since the pioneering works of Blum [105] and Aubin and Blum [106], and the seminal paper of ETM in 2011 [107] in two–flavor QCD, many lattice calculations of a_μ^{HLO} have been performed [11, 108–122]. In addition to these, there are now many works giving the individual windows and other contributions [123–131]. The new combined lattice value reads [14]

$$a_\mu^{\text{HLO}} = 7132(61) \cdot 10^{-11} \, . \tag{2.31}$$

This result is the one considered for the final estimate of the muon $g-2$ given in [14].

A few years ago, a new approach has been proposed to determine the leading hadronic contribution to the muon $g-2$, measuring the effective electromagnetic coupling in the *space–like* region via scattering data [132]. This leads to the proposal of a new experiment, MUonE at CERN, to measure the differential cross section of muon–electron elastic scattering as a function of the *space–like* squared momentum transfer $q^2 = t < 0$. The differential cross section of that process provides direct sensitivity to the LO hadronic contribution to a_μ. If we now consider the t–channel process described by the muon–electron elastic scattering, we define the *space–like* squared four momentum as

$$t(x) = \frac{x^2 m_\mu^2}{x-1} < 0 \, , \tag{2.32}$$

where $x \in [0,1]$, and, by recalling the dispersion relation for the hadronic vacuum polarization $\bar{\Pi}_h(q^2)$ in Eq. (2.24), and by imposing $q^2 = t(x) < 0$ we obtain [133]

$$a_\mu^{\text{HLO}} = \frac{\alpha}{\pi} \int_0^1 \mathrm{d}x (x-1) \bar{\Pi}_h[t(x)] = \frac{\alpha}{\pi} \int_0^1 \mathrm{d}x (x-1) \Delta\alpha_h[t(x)] \, . \tag{2.33}$$

Two–pion intermediate state contribution

The contribution of the two–pion intermediate state, which accounts for more then 70% of the total leading order effect, can be expressed in terms of the pion vector form factor (VFF)

$$\langle \pi^\pm(p') | j_{em}^\mu(0) | \pi^\pm(p) \rangle = \pm (p'+p)^\mu F_\pi^V[(p'-p)^2] \, , \tag{2.34}$$

according to

$$\sigma(e^+e^- \to \pi^+\pi^-) = \frac{\pi\alpha^2}{3s} \sigma_\pi^3(s) |F_\pi^V(s)|^2 \frac{s+2m_e^2}{s\sigma_e(s)} \, , \tag{2.35}$$

where $\sigma_\pi(s) = \sqrt{1 - \frac{4M_\pi^2}{s}}$. For a consistent counting of higher orders in α, radiative corrections need to be taken into account, otherwise this would induce corrections at the same order as HVP iterations or hadronic light–by–light (HLbL) scattering. The idea is that the leading–order HVP includes not only the hadronic channels but also the (one–)photon–inclusive ones. In particular, the lowest–lying intermediate state is no longer the two–pion state, but the $\pi^0\gamma$ state so that the HVP input corresponds to infrared–finite photon–inclusive cross sections including both real and virtual corrections. With this convention, the cross section to be inserted in Eq. (2.28) has to be inclusive of final–state radiation (FSR), but both VP and initial–state radiation (ISR) effects need to be subtracted. The expression for the bare cross section then reads

$$\begin{aligned}\sigma^{(0)}(e^+e^- \to \gamma^* \to \text{hadrons}(\gamma)) &= \left|\frac{\alpha(0)}{\alpha(s)}\right|^2 \sigma(e^+e^- \to \gamma^* \to \text{hadrons}(\gamma)) \\ &= \left|1 - \Pi^{\text{SM}}(s)\right|^2 \sigma(e^+e^- \to \gamma^* \to \text{hadrons}(\gamma)) \,, \end{aligned} \tag{2.36}$$

where the running of α is determined by the full renormalized VP function in the SM, e.g. including the lepton–loop contribution

$$\Pi_l(s) = \frac{2\alpha}{\pi} \int_0^1 \mathrm{d}x \; \mathrm{d}(1-x) \ln\left[1 - x(1-x)\frac{s}{m_l^2}\right] . \tag{2.37}$$

While the subtraction of VP effects may be taken into account afterwards thanks to the above equations, the correction of ISR and ISR/FSR interference effects is performed with Monte Carlo generators in the context of each experiment [134–137].

An alternative way to compute the two–pion intermediate state contribution is through the hadronic τ decay, $\tau \to \pi\pi^0\nu_\tau$. Thanks to a conserved–vector–current (CVC) relation between electromagnetic and weak form factors, the differential decay rate $\tau \to \pi\pi^0\nu_\tau$ can be related to the cross section $\sigma(e^+e^- \to \pi^+\pi^-)$ in the isospin limit. In the case of the $e^+e^- \to \pi^+\pi^-$ we have an electromagnetic neutral current and a final state with isospin $(I, I_z) = (1, 0)$, while in the τ decay we have a vector–axial vector charged current and a final state with $(I, I_z) = (1, -1)$. Therefore, in the isospin limit, the purely hadronic cross section for $e^+e^- \to \pi^+\pi^-$ (with QED effects removed) can be related to the $\tau^- \to \pi^-\pi^0\nu_\tau$ differential decay width in this limit by

$$\sigma(e^+e^- \to \pi^+\pi^-)(s) = \frac{1}{\mathcal{N}(s)\Gamma_e^{(0)}} \frac{\mathrm{d}\Gamma(\tau^- \to \pi^-\pi^0\nu_\tau)}{\mathrm{d}s} \,, \tag{2.38}$$

where constants and phase–space factors are collected in

$$\mathcal{N}(s) = \frac{3|V_{ud}|^2}{2\pi\alpha m_\tau^2} s \left(1 - \frac{s}{m_\tau^2}\right)^2 \left(1 + \frac{2s}{m_\tau}\right) \,, \tag{2.39}$$

and further (electroweak) constants appear in

$$\Gamma_e^{(0)} = \frac{G_F^2 m_\tau^5}{192\pi^3} \,. \tag{2.40}$$

Details on this alternative and independent approach will be given later in this work.

Higher-order hadronic contributions

The $\mathcal{O}(\alpha^3)$ contribution to the muon $g-2$ can be divided into two parts:

$$a_\mu^{\mathrm{HHO}} = a_\mu^{\mathrm{HHO}}(\mathrm{VP}) + a_\mu^{\mathrm{HHO}}(\mathrm{LbL}) \ . \tag{2.41}$$

The first term comes from diagrams containing hadronic vacuum polarization insertions into the internal photon line, the second term is the hadronic light–by–light contribution. The results considering the hadronic vacuum polarization insertions, $a_\mu^{\mathrm{HHO}}(\mathrm{VP})$, were computed both at NLO and NNLO, whereas the light–by–light contribution is computed at LO and NLO [14]:

$$a_\mu^{\mathrm{NLO}}(\mathrm{VP}) = -99.6(1.3) \times 10^{-11}, \tag{2.42}$$
$$a_\mu^{\mathrm{NNLO}}(\mathrm{VP}) = 12.4(1) \times 10^{-11}, \tag{2.43}$$
$$a_\mu^{\mathrm{LO}}(\mathrm{LbL}) = 103.3(8.8) \times 10^{-11}, \tag{2.44}$$
$$a_\mu^{\mathrm{NLO}}(\mathrm{LbL}) = 2.6(6) \times 10^{-11} \ . \tag{2.45}$$

For the LbL contribution, in analogy with the VP, the result obtained from lattice QCD needs to be considered [14],

$$a_\mu^{\mathrm{LQCD}}(\mathrm{LbL}) = 122.5(9.0) \times 10^{-11} \ , \tag{2.46}$$

such that the combined (phenomenology + lattice) result for the LbL contribution reads [14]

$$a_\mu(\mathrm{LbL}) = 112.6(9.6) \times 10^{-11} \ . \tag{2.47}$$

2.2.4 SM prediction versus experimental measurement results

On the theory side, a result obtained considering all the contributions listed above was released in 2020 [9]

$$a_\mu^{\mathrm{SM}}(\mathrm{WP20}) = 116\,591\,810(43) \times 10^{-11} \ . \tag{2.48}$$

This result is computed by utilizing the data–driven result for the LO HVP contribution. The experimental inputs for the hadronic cross section were combined thanks to the DHMZ and the KNT methods. Since May 2025 a new theoretical result for the muon $g-2$ is available and it reads [14]

$$a_\mu^{\mathrm{SM}}(\mathrm{WP25}) = 116\,592\,033(62) \times 10^{-11} \ . \tag{2.49}$$

This result is computed by considering only the lattice QCD result for the LO HVP contribution since the increased tension between the different experiments measuring $\sigma(e^+e^- \to \text{hadrons})$ prevent to perform a meaningful combination of the data. The discrepancy between the data–driven and the lattice QCD values shows that resolving the tensions in the data–driven estimations of the HVP contribution is particularly important, and additional results combined with further scrutiny of theory input such as from event generators should provide a path toward this goal.

On the experimental side, the measurement of the anomalous magnetic moment of the muon is obtained by injecting polarized muons into a magnetic storage ring with electric vertical focusing. The measured quantities are then the muon anomalous precession frequency and the magnetic field $\mathbf{B}$ in terms of the proton nuclear magnetic resonance frequency. The first measurement was the one obtained by the E821 experiment at the Brookhaven National Laboratory (BNL) [4–7,138]:

$$a_{\mu^-}^{\mathrm{exp}} = 116\,592\,140(80)(30) \times 10^{-11} \ , \tag{2.50}$$

where the first error is statistical while the second is systematic. This result is in good agreement with the average of the measurements of the muon $g-2$ of positive muons [4–7, 138], $a_{\mu^+}^{\rm exp} = 116\,592\,030(80) \times 10^{-11}$, as predicted by the CPT theorem. By combining these results, the new average is

$$a_\mu^{\rm exp} = 116\,592\,080(60) \times 10^{-11} \quad (0.5\ {\rm ppm})\ . \tag{2.51}$$

The comparison between the experimental measurement in Eq. (2.51) and the SM prediction in Eq. (2.48) shows a discrepancy of $3.7\ \sigma$. On April 2021, the FermiLab Muon $g-2$ experiment revealed a new experimental result for the anomalous magnetic moment of positive muons [8]:

$$a_\mu({\rm FNAL}_{\rm Run\,1}) = 116\,592\,040(54) \times 10^{-11} \quad (0.46\ {\rm ppm})\ . \tag{2.52}$$

This result differs from the SM value in Eq. (2.48) by $3.3\ \sigma$ and agrees with the BNL E821 result. The combined experimental average (BNL+FNAL) is

$$a_\mu^{\rm exp} = 116\,592\,061(41) \times 10^{-11} \quad (0.35\ {\rm ppm})\ . \tag{2.53}$$

The difference, $a_\mu^{\rm exp} - a_\mu^{\rm SM}({\rm WP20}) = (251 \pm 59) \times 10^{-11}$, has a significance of 4.2σ. A new experimental result of the muon $g-2$ was released on August 2023, giving [10]

$$a_\mu({\rm FNAL}_{\rm Run\,2+3}) = 116\,592\,055(24) \times 10^{-11} \quad (0.20\ {\rm ppm})\ . \tag{2.54}$$

and the combined (BNL+FNAL) experimental average became

$$a_\mu^{\rm exp} = 116\,592\,059(22) \times 10^{-11} \quad (0.19\ {\rm ppm})\ . \tag{2.55}$$

yielding a discrepancy of $5.1\ \sigma$ with the data–driven theoretical result $a_\mu^{\rm SM}({\rm WP20})$.
In June 2025, FNAL published the final experimental estimate of the muon $g-2$ [13]

$$a_\mu({\rm FNAL}_{\rm tot}) = 116\,592\,070.5(14.8) \times 10^{-11} \quad (127\ {\rm ppb})\ . \tag{2.56}$$

and the new experimental world average is now

$$a_\mu^{\rm exp} = 116\,592\,071.5(14.5) \times 10^{-11} \quad (124\ {\rm ppb})\ . \tag{2.57}$$

At the current level of precision there is no tension between the latest SM prediction $a_\mu^{\rm SM}({\rm WP25})$ and the experimental world average:

$$a_\mu^{\rm exp} - a_\mu^{\rm SM}({\rm WP25}) = 38(63) \times 10^{-11} \tag{2.58}$$

However, by comparing the uncertainties of Eqs. (2.57) and (2.49) it is apparent that the precision of the SM prediction must be improved by at least a factor four to match the precision of the current experimental average. In this sense, progresses on both data–driven and lattice methods applied to the hadronic contributions are necessary. A plot of the experimental results compared with the current theoretical situation can be found in Fig. 2.8.

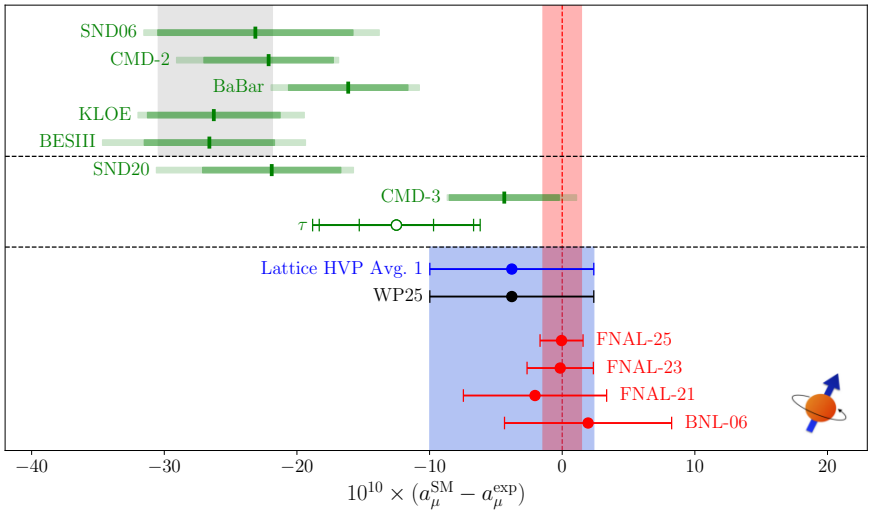

Figure 2.8: Summary of the current SM prediction for a_μ in comparison to experiment (red band and data point). The final WP25 prediction is denoted in black and via the blue band, it derives from the LO HVP result defined by the lattice QCD "Avg.1" shown in blue (see [14] for details). The gray band indicates the WP20 result, based on the e^+e^- experiments above the first dashed line. Figure taken from [14]

.

Chapter 3

Unitarity and Analyticity

Unitarity is a very general property of any quantum field theory: starting from an initial state, the probability of any outcome to happen must always be equal to one. This translates into the unitarity of the so–called S–matrix that relates any initial to any final state of a process. Together with the principle of maximal analyticity, unitarity allows one to determine the analytic structure of a scattering amplitude. Complex analysis can then be used to make predictions even when perturbative methods are not valid, as in the case of QCD at low energy. In this chapter, we introduce the concept of unitarity and analyticity and derive some important tools used in this thesis.

3.1 S–matrix unitarity

Following Peskin and Schröder [139], let us consider a generic scattering process. In the Schrödinger picture, we denote the initial state at time t_i as $|i, t_i\rangle$ while the final state at time t_f as $\langle f, t_f|$. In the Heisenberg picture, the time evolution of the states is collected into an operator, called the S–matrix defined as

$$\langle f|S|i\rangle_H = \langle f, \infty|i, -\infty\rangle_S \, . \tag{3.1}$$

The S–matrix is defined assuming that all the interactions happen in a finite time interval, so that at asymptotic time, $t = \pm\infty$, the states are free of interactions and they are called *asymptotic states*. Using the Born postulate, we can calculate the probability that the system ends up in an arbitrary state $|l\rangle$ in terms of the S–matrix elements:

$$P_l = |\langle l|f\rangle|^2 = |\langle l|S|i\rangle|^2 \, . \tag{3.2}$$

In a free theory, the S–matrix is simply the identity matrix $\mathbb{1}$. Therefore we can write $S = \mathbb{1} + iT$, where T is called the transfer matrix and contains the information about the interaction. Since the S–matrix would vanish unless the initial and final states have the same total 4–momentum, we can write

$$T = (2\pi)^4 \delta^4 \left(\sum p_i^\mu - \sum p_f^\mu \right) \mathcal{M} \, , \tag{3.3}$$

where p_i^μ and p_f^μ are the initial and final particles' momenta, respectively. Then, the non–trivial part of the S–matrix reads

$$\langle f|T|i\rangle = i(2\pi)^4 \delta^4 \left(\sum p_i^\mu - \sum p_f^\mu \right) \mathcal{M}_{fi} \, . \tag{3.4}$$

where $\mathcal{M}_{fi} = \langle f|\mathcal{M}|i\rangle$ is the transition amplitude describing the process $i \to f$.

From the conservation of probability it follows the unitarity of the S–matrix, $S^\dagger S = S S^\dagger = \mathbb{1}$, which

can be written in terms of the transition amplitude as

$$-i(T - T^\dagger) = T^\dagger T \ . \tag{3.5}$$

One of the most important implications of unitarity is the relation between scattering amplitudes and cross sections called the *optical theorem*. Sandwiching the left–hand side of Eq. (3.5) between $\langle f|$ and $|i\rangle$ gives

$$\begin{aligned}\langle f|i(T^\dagger - T)|i\rangle &= i\langle i|T|f\rangle^* - i\langle f|T|i\rangle \\ &= i(2\pi)^4\delta^4\left(\sum p_i^\mu - \sum p_f^\mu\right)\left[\mathcal{M}^*(f \to i) - \mathcal{M}(i \to f)\right] \ .\end{aligned} \tag{3.6}$$

By using the completeness relation

$$\mathbb{1} = \sum_n \int \mathrm{d}\Pi_n |n\rangle\langle n| \ , \tag{3.7}$$

we get

$$\begin{aligned}\langle f|T^\dagger T|i\rangle &= \sum_n \int \mathrm{d}\Pi_n \langle f|T^\dagger|n\rangle\langle n|T|i\rangle \\ &= \sum_n (2\pi)^4\delta^4(p_f - p_n)(2\pi)^4\delta^4(p_i - p_n)\int \mathrm{d}\Pi_n \mathcal{M}(i \to n)\mathcal{M}^*(f \to n) \ .\end{aligned} \tag{3.8}$$

Thus unitarity implies

$$\mathcal{M}(i \to f) - \mathcal{M}^*(f \to i) = i\sum_n \int (2\pi)^4\delta^4(p_i - p_n)\mathcal{M}(i \to n)\mathcal{M}^*(f \to n) \ . \tag{3.9}$$

An important special case is when $|i\rangle = |f\rangle = |A\rangle$, for some state A. Then

$$2i\mathrm{Im}\mathcal{M}(A \to A) = i\sum_n \int \mathrm{d}\Pi_n (2\pi)^4\delta^4(p_a - p_n)|\mathcal{M}(A \to n)|^2 \ . \tag{3.10}$$

If $|A\rangle$ is a two–particle state,

$$\mathrm{Im}\mathcal{M}(A \to A) = 2E_{\mathrm{CM}}|\mathbf{p}_i|\sum_n \sigma(A \to n) \ , \tag{3.11}$$

where E_{CM} and $|\mathbf{p}_i|$ are the total energy of the system and the modulus of the three–momentum of any of the two external particles evaluated in the center–of–mass frame, respectively.

From Eq. (3.10), we see that in order to obtain the imaginary part of a given transition amplitude $\mathcal{M}$, we need to sum over all intermediate states allowed by the symmetries of the process. There might be an infinite number of them so the idea is to identify which intermediate states are dominant in the process. There is only a finite number of them to be considered so we can truncate the series and ignore the rest.

3.2 Partial wave expansion of scattering amplitude

Let us consider the process $\phi_1(p_1)\phi_2(p_2) \to \phi_3(p_3)\phi_4(p_4)$ where the particles ϕ_i have masses m_i and four–momenta $p_i = (E_i, \mathbf{p}_i)$ with $i \in \{1, 2, 3, 4\}$ and, for simplicity, no spin. The four particles are on–shell:

$$p_i^2 = m_i^2 = E_i^2 + \mathbf{p}_i^2, \quad i \in \{1, 2, 3, 4\} \ . \tag{3.12}$$

The kinematic of the process is described by the following Mandelstam variables

$$\begin{aligned} s =&(p_1+p_2)^2 = (p_3+p_4)^2 \,, \\ t =&(p_1-p_3)^2 = (p_2-p_4)^2 \,, \\ u =&(p_1-p_4)^2 = (p_2-p_4)^2 \,. \end{aligned} \tag{3.13}$$

and thanks to the on–shell relation

$$s+t+u = \sum_{i=1}^{4} m_i^2 \,, \tag{3.14}$$

the scattering amplitude depends on two out of three invariant Mandelstam variables in addition to the masses of the particles. We can express the amplitude in terms of the squared center–of–mass energy s and momentum transfer t which depends on the scattering angle θ_s between an incoming and an outgoing particle in the center–of–mass frame of s. Then the relation in Eq. (3.4) becomes

$$\langle \phi_3(p_3)\phi_4(p_4)|T|\phi_1(p_1)\phi_2(p_2)\rangle = (2\pi)^4\delta^{(4)}(p_1+p_2-p_3-p_4)\mathcal{M}(s,t(\theta_s)) \,. \tag{3.15}$$

This scattering amplitude can be expressed as a partial–wave expansion which is based on angular momentum conservation and it is possible because the Legendre polynomials $P_\ell(z)$ form a complete orthogonal set. We can then write the amplitude as

$$\mathcal{M}(s,t(\theta_s)) = \sum_\ell (2\ell+1)P_\ell(\cos\theta_s)f_\ell(s) \,. \tag{3.16}$$

Note that this particular representation includes spinless particles. For particles with arbitrary spins, this relation can be generalized using Wigner $d^J_{mm'}(\theta)$ functions.
The partial waves $f_\ell(s)$ only depend on the centre–of–mass energy squared and they represent transition amplitudes between states of identical angular momentum ℓ. In order to single out a well–defined partial wave, one can simply project the amplitude by integrating over $z_s := \cos\theta_s$:

$$f_\ell(s) = \frac{1}{2}\int_{-1}^{1} \mathrm{d}z_s \mathcal{M}(s,z_s)P_\ell(z_s) \,. \tag{3.17}$$

This relation holds because the Legendre polynomials for an orthogonal basis are normalized as

$$\int_{-1}^{1} \mathrm{d}z_s P_\ell(z_s)P_{\ell'}(z_s) = \frac{2}{2\ell+1}\delta_{\ell\ell'} \,. \tag{3.18}$$

In the elastic region, where the intermediate state is identical to the final state, the unitarity relation of the scattering amplitude can be written as a unitarity relation for the partial waves in a very compacts form. For simplicity, we consider intermediate states with only two particles with masses $m_{n_{1,2}}$. We define the amplitude with initial state $|i\rangle = |\phi_1\phi_2\rangle$ and final state $|f\rangle = |\phi_3\phi_4\rangle$ as $\mathcal{M}_{fi}$, we write the unitarity relation according to the derivation above and we expand the two amplitudes in partial waves:

$$\begin{aligned} \mathrm{Im}\mathcal{M}(s,t) =&(2\pi)^4 \sum_n \frac{1}{2}\int_{\mathbf{k}} \mathrm{d}\Pi_2^n(\mathbf{k})\mathcal{M}_{ni}\mathcal{M}^*_{fn} \\ =&\sum_n \frac{\lambda^{1/2}(s,m_{n_1}^2,m_{n_2}^2)}{64\pi^2 s}\int \mathrm{d}\Omega(\hat{\mathbf{k}})\mathcal{M}_{ni}(s,\hat{\mathbf{p}}_1\cdot\hat{\mathbf{k}})\mathcal{M}^*_{fn}(s,\hat{\mathbf{p}}_3\cdot\hat{\mathbf{k}}) \end{aligned} \tag{3.19}$$

$$= \sum_n \sum_{\ell\ell'} \frac{(2\ell+1)(2\ell'+1)}{64\pi^2} \frac{\lambda^{1/2}(s, m_{n_1}^2, m_{n_2}^2)}{s} f_\ell^{ni} f_{\ell'}^{fn*} \times \int \mathrm{d}\Omega(\hat{\mathbf{k}}) P_\ell(\hat{\mathbf{p}}_1 \cdot \hat{\mathbf{k}}) P_{\ell'}(\hat{\mathbf{p}}_3 \cdot \hat{\mathbf{k}}) \ ,$$

where $\lambda(a,b,c) := a^2 + b^2 + c^2 - 2(ab + bc + ac)$ is the Källen function, $\mathrm{d}\Pi_2^n$ is the 2–body phase space integral of the intermediate state $|n\rangle$ and the partial waves f_ℓ^{ni} correspond to the scattering amplitude $\mathcal{M}_{ni}$. In order to calculate explicitly the phase–space integral, we can expand the Legendre polynomials in spherical harmonics as

$$P_\ell(\hat{\mathbf{p}} \cdot \hat{\mathbf{k}}) = \frac{4\pi}{2\ell+1} \sum_{m=-\ell}^{\ell} Y_{\ell m}(\hat{\mathbf{p}}) Y_{\ell m}(\hat{\mathbf{k}}) \ . \tag{3.20}$$

The orthonormality of the spherical harmonics,

$$\int \mathrm{d}\Omega(\hat{\mathbf{k}}) Y_{\ell m}(\hat{\mathbf{p}}) Y_{\ell m}(\hat{\mathbf{k}}) = \delta_{\ell\ell'} \delta_{mm'} \ , \tag{3.21}$$

allows one to project Eq. (3.19) on the partial wave of interest:

$$\begin{aligned} \mathrm{Im} f_\ell(s) =& \frac{1}{2} \int_{-1}^{1} \mathrm{d}z \mathrm{Im}\mathcal{M}(s, t(z)) P_\ell(z) \\ =& \sum_n \frac{\lambda^{1/2}(s, m_{n_1}^2, m_{n_2}^2)}{16\pi s} f_\ell^{ni} f_\ell^{fn*} \ . \end{aligned} \tag{3.22}$$

3.3 Watson's theorem

An interesting conclusion can be drawn for the amplitude partial wave expansion if only purely elastic final state scattering is considered. Let us write the partial wave expansion of the process $f \to f$ as

$$\mathcal{M}_{ff}(s,z) = \sum_\ell (2\ell+1) t_\ell(s) P_\ell(z) \ . \tag{3.23}$$

Then, assuming $|f\rangle$ to be the only intermediate state in the sum of Eq. (3.22), the imaginary part of a given partial wave is reduced to

$$\mathrm{Im} f_\ell(s) = \frac{\lambda^{1/2}(s, m_3^2, m_4^2)}{16\pi s} f_\ell(s) t_\ell^*(s) \ . \tag{3.24}$$

where m_3 and m_4 are the masses of the two particles composing the state $|f\rangle$.

The imaginary part of the partial wave must be a real quantity which means that the imaginary part of the product $f_\ell(s) t_\ell^*(s)$ must vanish exactly. By writing the partial waves in a complex exponential form

$$\begin{aligned} f_\ell(s) =& |f_\ell(s)| \mathrm{e}^{i\delta_f(s)} \ , \\ t_\ell(s) =& |t_\ell(s)| \mathrm{e}^{i\delta_t(s)} \ , \end{aligned} \tag{3.25}$$

the requirement that $\mathrm{Im} f_\ell(s)$ must be a real quantity implies that $\delta_f(s)$ must be identical to the phase $\delta_t(s)$ up to integer factors of π. This is only true in the limit of purely elastic rescattering and below the inelastic threshold. At higher energies, inelasticities must be accounted for as corrections to this relation.

3.4 Cutting rules

A Feynman diagram yields an imaginary part for $\mathcal{M}$ only when the virtual particles in the diagram go on–shell. For our present purposes, let us define $\mathcal{M}$ by the Feynman rules for perturbation theory. This allows us to consider $\mathcal{M}(s)$ as an analytic function of the complex variable $s = E_{\rm CM}^2$, even though S–matrix elements are defined only for external particles with real momenta. The appearance of an imaginary part of $\mathcal{M}(s)$ always requires a branch cut singularity. Let s_0 be the threshold energy for production of the lightest multiparticle state. For real s below s_0, the intermediate state cannot go on–shell, so $\mathcal{M}(s)$ is real. Thus, for real $s < s_0$, we have the identity

$$\mathcal{M}(s) = [\mathcal{M}(s^*)]^* \ . \tag{3.26}$$

which is exactly the *Schwarz reflection principle*: if Γ is a finite segment of the real axis and D a domain of the complex z–plane whose intersection with the real axis is Γ than any function $f(z)$ which is analytic in D and for which $\mathrm{Im} f(z) = 0$ on Γ must satisfy the equation

$$f(z^*) = f^*(z) \ , \tag{3.27}$$

whenever z and z^* both belong to D. $f(z)$ is said to be a real analytic function in D.

Each side of Eq. (3.26) is an analytic function of s, so it can be analytically continued to the entire complex s plane. In particular, near the real axis for $s > s_0$ we get

$$\begin{aligned} \mathrm{Re}\mathcal{M}(s + i\epsilon) &= \mathrm{Re}\mathcal{M}(s - i\epsilon) \ , \\ \mathrm{Im}\mathcal{M}(s + i\epsilon) &= -\mathrm{Im}\mathcal{M}(s - i\epsilon) \ . \end{aligned} \tag{3.28}$$

There is a branch cut across the real axis, starting at the threshold energy s_0; the discontinuity across the cut is

$$\mathrm{Disc}\mathcal{M}(s) = 2i\mathrm{Im}\mathcal{M}(s + i\epsilon) \ . \tag{3.29}$$

It is possible to prove that the discontinuities arising from a loop diagram give precisely the imaginary part required by Eq. (3.9). Cutkosky showed that the discontinuity of a Feynman diagram across its branch cut is always given by a simple set of *cutting rules* [140]:

- cut through the diagram in any way that can put all the cut propagators on–shell without violating momentum conservation,
- for each cut, replace $\frac{1}{p^2 - m^2 + i\epsilon} \to -2\pi i \delta\left(p^2 - m^2\right)$ and then perform the loop integrals,
- sum over all cuts.

It is important to notice that cuts are directional in the sense that cut particles should have positive energy when flowing from the left to the right side of the diagram.

3.5 Dispersion relations

Let us consider the amplitude $T(s,t,u)$ of the process described in Ch. 3.2 for some fixed real value of t [141], but now we also set $m_i = m$. According to the principle of maximal analyticity, the amplitude is analytic in the whole complex plane, except for the singularities originating from the unitarity relation. From Eq. (3.10), Im $T(s,t,u)$ will be non–zero along the part of the real s–axis from $4m^2$ to $+\infty$. We also suppose that the energy spectrum in the u–channel is the same as that in s, which, in terms of s and for real values of t, this is the part of the real s–axis from $s = -\infty$ to $s = -t$. Thus, unitarity requires that

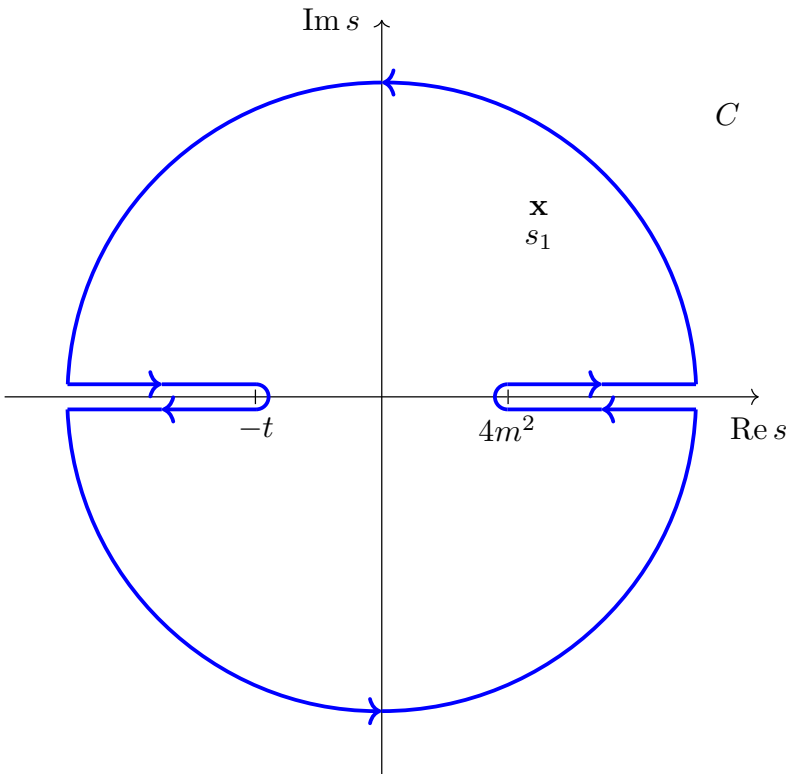

Figure 3.1: Contour of integration in the complex s-plane

on the parts of the real s–axis from $-\infty$ to $-t$ and from $4m^2$ to $+\infty$, Im $T(s,t,u)$ must be non–zero. From the Schwarz reflection principle in Eq. (3.27), if $T(s,t,u)$ has to be analytic in a domain extending both sides of the real s–axis and including the segment of the s–axis on which Im $T(s,t,u)$ is zero, then Im $T(s,t,u)$ must satisfy

$$T(s^*,t) = T^*(s,t)\ , \tag{3.30}$$

provided s and s^* both lie inside the domain of analyticity in s. For a physical process s, t and u will all have real values. The convention adopted to specify the physical amplitude is to give a small positive imaginary part ϵ to whichever of the variables s, t and u is associated with the energy of the physical process and then let ϵ tend to zero. Thus the physical amplitude for an s–channel process is the value of the amplitude $T(s,t,u)$ just above the cut in the s–plane. Since $T(s,t,u)$ is defined in a completely symmetric way, it can be continued from one physical region into that for crossed processes thanks to analyticity.

3.5.1 Single variable dispersion relations

Let s_1 be some fixed point in the s–plane and consider the following function of s

$$F_1(s,s_1) \equiv \frac{f(s)}{(s-s_1)}\ . \tag{3.31}$$

For convenience of notation and to emphasize that $T(s,t)$ is a function of s with t fixed, we have written $T(s,t)$ as $f(s)$. The function $F_1(s,s_1)$ has the same singularities as $f(s)$ with an additional pole, whose residue is $f(s_1)$ at s_1. By considering the contour in Fig. 3.1 and by applying the Cauchy's theorem, we

can write

$$\int_C \mathrm{d}s \frac{f(s)}{s-s_1} = 2\pi i f(s_1) \; . \tag{3.32}$$

The contour C may be separated into two parts, a circle of radius R with center at $s = 0$ and the remainder which is made up of lines parallel to and close to the cuts on the real axis. If we suppose that the contribution from the circle tends to zero, which is the case if $|f(s)| \to 0$ for $|s| \to \infty$, Eq. (3.32) can be written as

$$\int_{-\infty}^{-t} \mathrm{d}s \frac{\mathrm{Im}f(s)}{s-s_1} + \int_{4m^2}^{\infty} \mathrm{d}s \frac{\mathrm{Im}f(s)}{s-s_1} = \pi f(s_1) \; , \tag{3.33}$$

where for real values of s, $\mathrm{Im}f(s) \equiv \mathrm{Im}f(s+i\epsilon) = \frac{1}{2i}\left[f(s+i\epsilon) - f(s-i\epsilon)\right]$. Since $f(s)$ is only defined above or below the axis, we must compute it at $s + i\epsilon$ and by using the relation

$$\frac{1}{s'-s\pm i\epsilon} = \mathbf{P}\frac{1}{s'-s} \mp i\pi\delta(s'-s) \; , \tag{3.34}$$

we obtain [141]

$$\mathrm{Re}f(s) = \frac{1}{\pi}\mathbf{P}\int_{4m^2}^{\infty} \mathrm{d}s' \frac{\mathrm{Im}f(s')}{s'-s} + \frac{1}{\pi}\int_{-\infty}^{-t} \mathrm{d}s' \frac{\mathrm{Im}f(s')}{s'-s} \; , \tag{3.35}$$

where $\mathbf{P}$ denotes the principal value defined by

$$\mathbf{P}\int_{4m^2}^{\infty} \frac{\mathrm{Im}f(s')}{s'-s} ds' \equiv \lim_{\delta\to 0+} \left\{ \int_{4m^2}^{s-\delta} \mathrm{d}s' \frac{\mathrm{Im}f(s')}{s'-s} + \int_{s+\delta}^{\infty} \mathrm{d}s' \frac{\mathrm{Im}f(s')}{s'-s} \right\} \; . \tag{3.36}$$

A relation of the type of Eq. (3.35) is usually referred to as a *dispersion relation*. Remember that $f(s)$ is just the amplitude $T(s,t)$ for some fixed value of t.

3.5.2 Subtraction in dispersion relations

If $|f(s)|$ does not tend to zero sufficiently fast with increasing $|s|$, we cannot use the procedure adopted above to obtain a dispersion relation. However it is still possible to write down a dispersion relation similar to Eq. (3.35) if we suppose that $|s^{-1}f(s)| \to 0$ like some negative power of s. Then we define

$$F_2(s';s,s_1) \equiv \frac{f(s')}{(s'-s)(s'-s_1)} \; , \tag{3.37}$$

where s_1 does not lie on either of the two cuts or coincide with either of the poles. Regarding $F_2(s';s,s_1)$ as a function of s' we see that it possesses the same singularities of $f(s')$ and in addition two simple poles at s and s_1. The difference here from the unsubtracted dispersion relation is that, in order to determine the function $\mathrm{Re}f(s)$, the value of the amplitude at the fixed point s_1, usually called the *subtraction point*, is needed. We then obtain the following dispersion relation:

$$\mathrm{Re}f(s) = f(s_1) + \frac{s-s_1}{\pi}\mathbf{P}\int_{4m^2}^{\infty} \mathrm{d}s' \frac{\mathrm{Im}f(s')}{(s'-s_1)(s'-s)} + \frac{s-s_1}{\pi}\int_{-\infty}^{-t} \mathrm{d}s' \frac{\mathrm{Im}f(s')}{(s'-s_1)(s'-s)} \; . \tag{3.38}$$

which is written for real $s > -t$. For real $s < -t$, the second of the two integrals would have to be written as a principal value integral instead of the first and, of course, for $-t < s < 4m^2$ the $\mathbf{P}$ sign is not necessary for either integral. A dispersion relation of the form shown in Eq. (3.38) is called a *once–subtracted dispersion relation*. In Eq. (3.38), it has been assumed that s_1 does not lie on either of the two cuts but, since this dispersion relation will describe physical quantities, the subtraction point must lie in the physical region, i.e., on one of the two cuts. Of course $f(s)$ is not defined actually on the cut, so we

must specify whether we mean the value just above or just below the cut. Since $f(s_1)$ is to be a physical amplitude, and supposing that it has to correspond to an s–channel process, we choose the subtraction point to be $s_1 + i\epsilon$, where s_1 is real and greater then $4m^2$ while ϵ is small and positive. Because

$$\frac{1}{s' - s_1 - i\epsilon} = \mathbf{P}\frac{1}{s' - s_1} + i\pi\delta(s' - s_1)\,,$$
$$\frac{1}{s' - s - i\epsilon} = \mathbf{P}\frac{1}{s' - s} + i\pi\delta(s' - s)\,, \tag{3.39}$$

we see that

$$\frac{s - s_1}{\pi}\int_{4m^2}^{\infty} \mathrm{d}s' \frac{\mathrm{Im}\ f(s')}{(s' - s_1)(s' - s)} = i[\mathrm{Im}\ f(s) - \mathrm{Im}\ f(s_1)] + \frac{s - s_1}{\pi}\mathbf{P}\int_{4m^2}^{\infty} \mathrm{d}s' \frac{\mathrm{Im}\ f(s')}{(s' - s_1)(s' - s)} \tag{3.40}$$

where $\mathbf{P}$, in this case, means that a principal value of the integral is to be taken at each of the two poles s and s_1. So when the subtraction point $s_1 + i\epsilon$ lies just above the right–hand cut, we obtain [141]

$$\mathrm{Re}f(s) = \mathrm{Re}f(s_1) + \frac{s - s_1}{\pi}\mathbf{P}\int_{4m^2}^{\infty} \mathrm{d}s' \frac{\mathrm{Im}f(s')}{(s' - s_1)(s' - s)} + \frac{s - s_1}{\pi}\int_{-\infty}^{-t} \mathrm{d}s' \frac{\mathrm{Im}f(s')}{(s' - s_1)(s' - s)}\,. \tag{3.41}$$

A particularly important choice is to take the physical threshold as the subtraction point, $s_1 = 4m^2$. Than it is no longer clear what the principal value of the integral at s_1 means. The procedure that has to be adopted in this case is to define the principal value integral at $s_1 = 4m^2$ as the limit, as s_1 approaches $4m^2$ from above, of the principal value integral at s_1:

$$\frac{s - 4m^2}{\pi}\lim_{s_1 \to 4m^{2+}} \mathbf{P}\int_{4m^2}^{\infty} \mathrm{d}s' \frac{\mathrm{Im}f(s')}{(s' - s_1)(s' - s)}\,. \tag{3.42}$$

3.5.3 Double variable dispersion relations–the Mandelstam representation

Let us consider the elastic scattering of spin zero particles of equal mass m and let us assume that unsubtracted dispersion relations are meaningful. To display the symmetry between the s– and the u–channels we rewrite this relation in the form

$$T(s,t) = \frac{1}{\pi}\int_{4m^2}^{\infty} \mathrm{d}s' \frac{\mathrm{Im}\ T(s',t)}{s' - s} + \frac{1}{\pi}\int_{4m^2}^{\infty} \mathrm{d}u' \frac{\mathrm{Im}\ T(t,u')}{u' - u}\,, \tag{3.43}$$

where $u = 4m^2 - s - t$, for a fixed value of t. The dependence of the two integral terms on t comes only through the numerators Im $T(s',t)$ and so the problem becomes that of finding the t–dependence of Im $T(s',t)$. In the s–channel physical region, i.e., for real values of s and t satisfying $s \geq 4m^2$ and $0 \geq t \geq -s + 4m^2$, Im $T(s',t)$ is in fact the imaginary part of the amplitude $T(s,t)$ and is a real function. As we move away from the s–channel physical region one can no longer assume that the continued function is still the imaginary part of the amplitude $T(s,t)$ and in fact it will soon become complex. So we shall write [141]

$$T(s,t) = \frac{1}{\pi}\int_{4m^2}^{\infty} \mathrm{d}s' \frac{D_s(s',t)}{s' - s} + \frac{1}{\pi}\int_{4m^2}^{\infty} \mathrm{d}u' \frac{D_u(t,u')}{u' - u}\,, \tag{3.44}$$

where $D_s(s,t) = \frac{1}{2i}\left[T(s + i\epsilon, t) - T(s - i\epsilon, t)\right]$ is the discontinuity across the s–channel cuts.

By applying unitarity in the s, t and u–channel and then by inserting intermediate states in the t– and u– channels this leads to the definition of the *double spectral functions* ρ_{st}, ρ_{su} and ρ_{tu} and to the

result [141]

$$\begin{aligned} T(s,t) =& \frac{1}{\pi^2}\int_{4m^2}^{\infty} \mathrm{d}s' \int_{b(s')}^{\infty} \mathrm{d}t' \frac{\rho_{st}(s',t')}{(s'-s)(t'-t)} \\ &+ \frac{1}{\pi^2}\int_{4m^2}^{\infty} \mathrm{d}s' \int_{b(s')}^{\infty} \mathrm{d}u' \frac{\rho_{su}(s',u')}{(s'-s)(u'-u)} \\ &+ \frac{1}{\pi^2}\int_{4m^2}^{\infty} \mathrm{d}t' \int_{b(s')}^{\infty} \mathrm{d}u' \frac{\rho_{tu}(s',u')}{(t'-t)(u'-u)} \,, \end{aligned} \tag{3.45}$$

where the double discontinuity is defined as

$$\rho_{st}(s,t) \equiv \frac{1}{2i}\left[D_s(s,t+i\epsilon) - D_s(s,t-i\epsilon)\right] \,, \tag{3.46}$$

and similarly for $\rho_{su}(s,u)$ and $\rho_{tu}(t,u)$. This representation has been obtained by simply using elastic unitarity and all the Cutkosky diagrams considered have been elastic in at least one channel. Clearly above the inelastic threshold we will have additional contributions to the double spectral functions. Notice that Eq. (3.45) involves the assumption that the amplitude has only those singularities that are required by unitarity in each of the three channels and consequently we speak of maximum analyticity of the amplitude.

3.6 Omnès–Muskhelishvili problem

As remarked in Sec. 3.3, in certain cases the phase of an amplitude can be obtained from the Watson theorem. Let us define such an amplitude by $F(s)$ and assume it is analytic on the whole complex plane, except for a branch–cut on the positive real axis. The Omnès–Muskhelishvili method allows one to find the most general solution of this function, provided that its phase is known on the cut. This method has been developed by Omnès [142], based on a previous analysis by Muskhelishvili [143].

The solution to this problem is not unique. Provided that $\Omega(s)$ is a solution normalized at $s = 0$ ($\Omega(0) = 1$), for any function $P(s)$ analytic on the whole complex plane, $F(s) = P(s)\Omega(s)$ is also a solution. One thus needs to add further constraints on $F(s)$ to fix $P(s)$. Let us assume that the cut starts at some branch–point $s_{\rm thr} > 0$. The phase along this cut is given by

$$\mathrm{Arg}(\Omega(s)) = \delta(s) \,, \quad s \in [s_{\rm thr}, \infty] \,. \tag{3.47}$$

There are two different ways to calculate the discontinuity of $\Omega(s)$ on the upper edge of the cut. The first one is to use the formal definition

$$\mathrm{Disc}(\Omega(s)) = \Omega(s+i\epsilon) - \Omega(s-i\epsilon) \,. \tag{3.48}$$

We can also use the direct relation between the discontinuity and the imaginary part of the amplitude along the cut. Moreover, our knowledge of the phase implies that

$$\begin{aligned} \mathrm{Disc}(\Omega(s)) &= 2i|\Omega(s+i\epsilon)| \sin\delta(s) = 2i\Omega(s+i\epsilon)e^{-i\delta(s)}\sin\delta(s) \\ &= \Omega(s+i\epsilon)e^{-i\delta(s)}\left(e^{i\delta(s)} - e^{-i\delta(s)}\right) = \Omega(s+i\epsilon)\left(1 - e^{-2i\delta(s)}\right) \,. \end{aligned} \tag{3.49}$$

By combining the two equations we get

$$\mathrm{Disc}(\log\Omega(s)) = \log\Omega(s+i\epsilon) - \log\Omega(s-i\epsilon) = 2i\delta(s) \,. \tag{3.50}$$

We assume that the phase converges asymptotically to a multiple of π: $\delta(s) \xrightarrow[s\to\infty]{} \alpha\pi =: \delta(\infty)$. Of course, this is an approximation and one could also use an incomplete Omnès–Muskhelishvili method [144,145] to get closer to the reality. However, this goes behind the scope of this thesis. This assumption allows one to write $\Omega(s)$ as a once–subtracted dispersive integral. The subtraction constant is fixed by the normalization condition $\Omega(0) = 1$:

$$\Omega(s) = \exp\left\{\frac{s}{\pi}\int_{s_{\text{thr}}}^{\infty} \mathrm{d}s' \frac{\delta(s')}{s'(s'-s)}\right\} . \tag{3.51}$$

In order to determine the function $P(s)$, we need to know more about the asymptotic behavior of $\Omega(s)$. To that end, we write

$$\begin{aligned}
\Omega(s) &= \exp\left\{\frac{s}{\pi}\int_{s_{\text{thr}}}^{\infty} \mathrm{d}s' \frac{\delta(s')-\delta(s)+\delta(s)}{s'(s'-s)}\right\} \\
&= \exp\left\{\frac{s}{\pi}\int_{s_{\text{thr}}}^{\infty} \mathrm{d}s' \frac{\delta(s')-\delta(s)}{s'(s'-s)} + \frac{\delta(s)}{\pi}\log\frac{s_{\text{thr}}}{s-s_{\text{thr}}} + i\delta(s)\right\} \\
&\xrightarrow{s\to\infty} \exp\left\{-\frac{1}{\pi}\int_{s_{\text{thr}}}^{\infty} \mathrm{d}s' \frac{\delta(s')-\alpha\pi}{s'} + \alpha\log\frac{s_{\text{thr}}}{s} + i\alpha\pi\right\} \\
&\propto \left(\frac{s_{\text{thr}}}{s}\right)^{\alpha} .
\end{aligned} \tag{3.52}$$

Hence, the asymptotic limit of the phase determines the asymptotic behavior of the Omnès solution. For instance, in the case of meson form factors, the Brodsky–Farrar counting rule states that

$$F(s) \overset{s\to\infty}{\lesssim} \frac{C}{s\log s^{\nu}} , \quad \nu > 0 . \tag{3.53}$$

In this case, the only analytic function $P(s)$ that grows slower than exponentially in s is a polynomial.

This method plays a central role in the dispersive definition of the pion vector form factor [102]. In the isospin limit, $F_\pi^V(s)$ is an analytic function of s, apart from a branch cut in the complex s–plane that lies on the real axis, $s \in [4M_\pi^2, \infty)$, and is dictated by unitarity. The form factor is real on the real axis below the branch point $4M_\pi^2$, hence it fulfills the Schwarz reflection principle. The Omnès function alone, with isospin $I = 1$, is the solution for the VFF in the isospin limit and disregarding inelastic contribution to the unitarity relation:

$$F_\pi^V(s) = \Omega_1^1(s) = \exp\left\{\frac{s}{\pi}\int_{s_{\text{thr}}}^{\infty} \mathrm{d}s' \frac{\delta_1^1(s')}{s'(s'-s)}\right\} . \tag{3.54}$$

where $\delta_1^1(s)$ is the isospin $I = 1$ elastic $\pi\pi$ phase shift in the isospin–symmetric limit.

Once the isospin–breaking and inelastic contributions are switched on, the pion VFF can be written as a product of three functions

$$F_\pi^V(s) = \Omega_1^1(s) G_\omega(s) G_{\text{in}}^N(s) , \tag{3.55}$$

where the factor G_ω accounts for ρ–ω mixing, the most important isospin–breaking effect, which becomes enhanced by the small mass difference between the ρ and ω resonances, while G_{in}^N takes into account all further inelastic contributions to the unitarity relation (see [102] for further details). However the $\rho - \omega$ mixing contribution is not the only isospin–breaking effect entering the pion VFF. Corrections due to the charged–neutral pion mass difference or electromagnetic effects are equally important and enter the computation of the elastic $\pi\pi$ phase shift $\delta(s)$. In particular, the contribution due to the charged–neutral pion mass difference will be analyzed in the following.

Chapter 4

Chiral Perturbation Theory

Chiral Perturbation Theory (χPT) can be seen as the low–energy limit of the Standard Model or, to be more precise, the effective quantum field theory describing hadronic interactions according to the SM, below the breaking scale of chiral symmetry ($E \ll \Lambda_\chi \sim$1 GeV). This theory was founded long time ago by the pioneering works of Weinberg [146] and Gasser and Leutwyler [147, 148]. Nowadays χPT is a well–known theory and it allows one to perform loop calculations in the mesonic and baryonic sector at low energy with a very high precision. Moreover the original formulation has been successfully extended in several directions, including heavy quark fields, bound–state dynamics, non–zero temperature effects, etc. In this chapter we will briefly review the properties of χPT and how it is built and then we will focus our attention to its application to the meson fields.

4.1 QCD Lagrangian

Quantum Chromo Dynamics (QCD) is the gauge theory of the strong interactions [149–151], i.e., quarks and gluons interactions, with color $SU(3)$ as the underlying gauge group (for the basic remarks of the $SU(3)$ group see App. B). Quarks are spin–1/2 fermions with six different flavors in addition to their three possible colors. Regarding the so–called current–quark–mass values of the light quarks, one should view the quark mass terms merely as the symmetry breaking parameters with their magnitude providing a measure for the extent to which chiral symmetry is broken [152].

The QCD Lagrangian exhibits a global $SU(3)_L \times SU(3)_R \times U(1)_V \times U(1)_A$ symmetry, where $U(1)_V$ is exactly conserved, its generator is the baryonic number and it survives also in the case of non–vanishing quark masses, $G = SU(3)_L \times SU(3)_R$ is the group of chiral transformation while $U(1)_A$ is not a symmetry at the quantum level due to the Abelian anomaly [153–155], and it reads [156, 157]

$$\mathcal{L}_{\rm QCD} = \sum_{f=u,d,s,c,b,t} \bar{q}_f (i \not{D} - m_f) q_f - \frac{1}{4} \mathcal{G}_{\mu\nu,a} \mathcal{G}^{\mu\nu,a} \ , \tag{4.1}$$

where $\mathcal{G}_{\mu\nu,a} = \partial_\mu \mathcal{A}_{\nu,a} - \partial_\nu \mathcal{A}_{\mu,a} + g f_{abc} \mathcal{A}_{\mu,c} \mathcal{A}_{\nu,c}$ and

$$D_\mu q_f = \left(\partial_\mu - ig \sum_{a=1}^{8} \frac{\lambda_a^C}{2} \mathcal{A}_{\mu,a} \right) q_f \ , \tag{4.2}$$

where λ_a are the Gell–Mann matrices listed in App. B, while the superscript C indicates the action in

color space. The field gauge transformations are

$$q_f \to q'_f = \exp\left[-i\sum_{a=1}^{8}\Theta_a(x)\frac{\lambda_a^C}{2}\right]q_f = U\left[g(x)\right]q_f \ , \tag{4.3}$$

$$\frac{\lambda_a^C}{2}\mathcal{A}_{\mu,a}(x) \to U[g(x)]\frac{\lambda_a^C}{2}\mathcal{A}_{\mu,a}(x)U^\dagger[g(x)] - \frac{i}{g}\partial_\mu U[g(x)]U^\dagger[g(x)] \ , \tag{4.4}$$

$$\mathcal{G}_{\mu\nu} \equiv \frac{\lambda_a^C}{2}\mathcal{G}_{\mu\nu,a} \to U[g(x)]\mathcal{G}_{\mu\nu}U^\dagger[g(x)] \ . \tag{4.5}$$

The six quark flavors are commonly divided into the three light quarks u, d and s and the three heavy flavors c, b and t [158]

$$\begin{pmatrix} m_u = 2.16\,\text{MeV} \\ m_d = 4.70\,\text{MeV} \\ m_s = 93.5\,\text{MeV} \end{pmatrix} \ll 1\ \text{GeV} \leq \begin{pmatrix} m_c = 1.273\,\text{GeV} \\ m_b = 4.183\,\text{GeV} \\ m_t = 172.56\,\text{GeV} \end{pmatrix} \ , \tag{4.6}$$

where the scale of 1 GeV is associated with the masses of the lightest hadrons containing light quarks, e.g. $m_\rho = 770$ MeV, which are not Goldstone bosons resulting from spontaneous symmetry breaking. The scale associated with spontaneous symmetry breaking, $4\pi F_\pi \sim 1170$ MeV, is of the same order of magnitude [159–161].

4.2 Chiral Symmetry

The interactions between quarks and gluons are highly non perturbative at energies below the breaking scale of chiral symmetry. This makes very difficult any description of the low–energy hadronic world in terms of partonic degrees of freedom. On the other hand, the spectrum of the theory at low energies contains only the octet of the Goldstone bosons resulting from spontaneous symmetry breaking: π, K and η. Moreover, from an experimental point of view, at very low energies these pseudoscalar mesons interact weakly, both among themselves and with nucleons. Then QCD can be treated perturbatively even at low energies, if a suitable transformation of degrees of freedom is performed.

By introducing projection operators $P_R = \frac{1}{2}(1+\gamma_5)$ and $P_L = \frac{1}{2}(1-\gamma_5)$, the quark fields can be written as $q_R = P_R q$ and $q_L = P_L q$ and the Lagrangian in the chiral limit ($\{m_u, m_d, m_s\} \to 0$) becomes

$$\mathcal{L}^0_{\text{QCD}} = \sum_{l=u,d,s}\left(\bar{q}_{R,l}i\not{D}q_{R,l} + \bar{q}_{L,l}i\not{D}q_{L,l}\right) - \frac{1}{4}\mathcal{G}_{\mu\nu,a}\mathcal{G}^{\mu\nu,a} \ . \tag{4.7}$$

Due to flavor independence of the covariant derivative, $\mathcal{L}^0_{\text{QCD}}$ is invariant under

$$\begin{aligned}
\begin{pmatrix} u_L \\ d_L \\ s_L \end{pmatrix} &\to U_L \begin{pmatrix} u_L \\ d_L \\ s_L \end{pmatrix} = \exp\left(-i\sum_{a=1}^{8}\Theta_a^L\frac{\lambda_a}{2}\right)e^{-i\Theta^L}\begin{pmatrix} u_L \\ d_L \\ s_L \end{pmatrix} \ , \\
\begin{pmatrix} u_R \\ d_R \\ s_R \end{pmatrix} &\to U_R \begin{pmatrix} u_R \\ d_R \\ s_R \end{pmatrix} = \exp\left(-i\sum_{a=1}^{8}\Theta_a^R\frac{\lambda_a}{2}\right)e^{-i\Theta^R}\begin{pmatrix} u_L \\ d_L \\ s_L \end{pmatrix} \ .
\end{aligned} \tag{4.8}$$

It is now possible to calculate the variation of the QCD Lagrangian under the infinitesimal local form of

Eq. (4.8) [162]

$$\delta\mathcal{L}^0_{\rm QCD} = \bar{q}_R\left(\sum_{a=1}^{8}\partial_\mu\Theta^R_a\frac{\lambda_a}{2}+\partial_\mu\Theta^R\right)\gamma^\mu q_R + \bar{q}_L\left(\sum_{a=1}^{8}\partial_\mu\Theta^L_a\frac{\lambda_a}{2}+\partial_\mu\Theta^L\right)\gamma^\mu q_L\ , \tag{4.9}$$

from which, thanks to the Noether's theorem, it is possible to obtain the conserved currents associated to the transformations of the left–handed or right–handed quarks

$$\begin{aligned} L^{\mu,a} &= \bar{q}_L\gamma^\mu\frac{\lambda^a}{2}q_L,\quad \partial_\mu L^{\mu,a}=0\ ,\\ R^{\mu,a} &= \bar{q}_R\gamma^\mu\frac{\lambda^a}{2}q_R,\quad \partial_\mu R^{\mu,a}=0\ . \end{aligned} \tag{4.10}$$

The eight currents $L^{\mu,a}$ transform under $SU(3)_L\times SU(3)_R$ as an (8, 1) multiplet, i.e., octet and singlet under transformations of the left– and right–handed fields, respectively. Similarly the right–handed currents transform as a (1, 8) multiplet under $SU(3)_L\times SU(3)_R$. Instead of this chiral currents, one often uses linear combinations

$$\begin{aligned} V^{\mu,a} &= R^{\mu,a}+L^{\mu,a} = \bar{q}\gamma^\mu\frac{\lambda^a}{2}q\ ,\\ A^{\mu,a} &= R^{\mu,a}-L^{\mu,a} = \bar{q}\gamma^\mu\gamma_5\frac{\lambda^a}{2}q\ . \end{aligned} \tag{4.11}$$

There are also a conserved singlet vector current associated to a transformation of all left–handed and right–handed quark fields by the same phase

$$V^\mu = \bar{q}_R\gamma^\mu q_R + \bar{q}_L\gamma^\mu q_L = \bar{q}\gamma^\mu q\ , \tag{4.12}$$

and a single axial–vector current from a transformation of all left–handed quark fields with one phase and all right–handed with the opposite phase

$$A^\mu = \bar{q}_R\gamma^\mu q_R - \bar{q}_L\gamma^\mu q_L = \bar{q}\gamma^\mu\gamma_5 q\ . \tag{4.13}$$

The invariance of $\mathcal{L}^0_{\rm QCD}$ under global $SU(3)_L\times SU(3)_R\times U(1)_V$ transformations implies that also the QCD Hamilton operator in the chiral limit satisfy the same symmetry. We can define the *charge operator* as usual

$$\begin{aligned} Q^a_L(t) &= \int d^3x q^\dagger_L(\mathbf{x},t)\frac{\lambda^a}{2}q_L(\mathbf{x},t)\quad a=1,...8\ ,\\ Q^a_R(t) &= \int d^3x q^\dagger_R(\mathbf{x},t)\frac{\lambda^a}{2}q_R(\mathbf{x},t)\quad a=1,...8\ ,\\ Q_V(t) &= \int d^3x q^\dagger(\mathbf{x},t)\frac{\lambda^a}{2}q(\mathbf{x},t)\ , \end{aligned} \tag{4.14}$$

which satisfy the following commutation relations

$$\begin{aligned} \left[Q^a_L,Q^b_L\right] &= if_{abc}Q^c_L\ ,\\ \left[Q^a_R,Q^b_R\right] &= if_{abc}Q^c_R\ , \end{aligned} \tag{4.15}$$

while all the other commutator relations vanish.

4.2.1 Spontaneous Symmetry Breaking

There is evidence, both from phenomenology and from theory that the chiral symmetry is spontaneously broken [163]:

- absence of parity doublets in the hadron spectrum;
- the $N_f - 1$ pseudoscalar mesons are by far the lightest hadrons;
- the vector and axial–vector spectral functions are quite different;
- the anomaly matching conditions [164–166] together with confinement require the spontaneous breaking of the chiral symmetry group for $N_f \geq 3$;
- in vector–like gauge theories like QCD, vector symmetries like the diagonal subgroup $SU(3)_V$ remain unbroken [167, 168];
- there is evidence from lattice gauge theories for a non–vanishing quark condensate.

Considering all these arguments, it is clear that the chiral symmetry G is spontaneously broken to the vectorial subgroup $H = SU(N_f)_V$. If we consider the vector charges $Q_V^a = Q_R^a + Q_L^a$ which satisfy $\left[Q_R^a + Q_L^a, Q_R^b + Q_L^b\right] = i f_{abc} Q_V^c$, the ground state is necessarily invariant under $SU(3)_V \times U(1)_V$ [167, 168] in the chiral limit , i.e., the eight vector charges Q_V^a as well as the baryon number operator $Q_V/3$ annihilate the ground state

$$Q_V^a|0\rangle = Q_V|0\rangle = 0 \; . \tag{4.16}$$

We now consider the linear combinations $Q_A^a = Q_R^a - Q_L^a$ satisfying $\left[Q_A^a, Q_A^b\right] = i f_{abc} Q_V^c$ and $\left[Q_A^a, Q_V^b\right] = i f_{abc} Q_A^c$. Since the parity doubling is not observed for the low–lying states, one assumes that the Q_A^a do not annihilate the ground state

$$Q_A^a|0\rangle \neq 0 \; , \tag{4.17}$$

i.e., the ground state of QCD is not invariant under *axial* transformations. According to Goldstone's theorem [169–173], to each axial generator Q_A^a, which does not annihilate the ground state, corresponds a massless Goldstone boson field $\phi^a(x)$ with spin 0, whose symmetry properties are tightly connected to the generator in question. The Goldstone bosons have the same transformation behavior under parity, $\phi^a(\mathbf{x}, t) \to -\phi^a(-\mathbf{x}, t)$, i.e., they are pseudoscalars and transform under subgroup H, which leaves the vacuum invariant, as an octet

$$\left[Q_V^a, \phi^b(x)\right] = i f_{abc} \phi^c(x) \; . \tag{4.18}$$

From this discussion it is clear that the operator responsible for the spontaneous chiral symmetry breaking in QCD must be a color–singlet, pseudoscalar quark–gluon operator:

$$P_a(x) = i\bar{q}(x)\gamma_5 \lambda_a q(x) \; , \quad a = 1, ...8 \; , \tag{4.19}$$

where, by using $(i)^2 \left[\gamma_5 \frac{\lambda_a}{2}, \gamma_0\gamma_5\lambda_a\right] = \lambda_a^2\gamma_0$, we obtain

$$i\left[Q_A^a(t), P_a(y)\right] = \begin{cases} \bar{u}u + \bar{d}d & a = 1, 2, 3 \\ \bar{u}u + \bar{s}s & a = 4, 5 \\ \bar{d}d + \bar{s}s & a = 6, 7 \\ \frac{1}{3}(\bar{u}u + \bar{d}d + 4\bar{s}s) & a = 8 \end{cases} \; . \tag{4.20}$$

We evaluate Eq. (4.20) for a ground state which is invariant under $SU(3)_V$, i.e., $\langle 0|\bar{u}u|0\rangle = \langle 0|\bar{d}d|0\rangle = \langle 0|\bar{s}s|0\rangle$, and by assuming a non–vanishing singlet scalar quark condensate ($\langle 0|\bar{q}q|0\rangle = \langle \bar{q}q\rangle \neq 0$)

$$\langle 0|i\left[Q_A^a(t), P_a(y)\right]|0\rangle = \frac{2}{3}\langle \bar{q}q\rangle \ , \quad a = 1, ..., 8 \ . \tag{4.21}$$

By inserting a complete set of states into the commutator of Eq. (4.21), both the pseudoscalar density $P_a(y)$ as well as the axial charge operators Q_A^a must have a non–vanishing matrix element between the vacuum and massless one–particle states $|\phi_b\rangle$. In particular, because of Lorentz covariance, the matrix element of the axial–vector current operator between the vacuum and these massless states appropriately normalized, can be written as

$$\langle 0|A_\mu^a(0)|\phi^b(p)\rangle = ip_\mu F\delta^{ab} \ , \tag{4.22}$$

where $F \approx 93$ MeV denotes the *decay* constant of the Goldstone bosons in the chiral limit. Assuming $Q_A^a|0\rangle \neq 0$, a non–zero value of F is a necessary and sufficient condition for the spontaneous chiral symmetry breaking. On the other hand, because of Eq. (4.21), a non–vanishing scalar quark condensate $\langle \bar{q}q\rangle$ is a sufficient (but not a necessary) condition for a spontaneous symmetry breakdown in QCD.

4.2.2 Explicit Symmetry Breaking

The finite u–, d– and s–quark masses in the QCD Lagrangian result in non–zero divergences of the symmetry currents. As a consequence, the charge operators are in general no longer time independent. In order to study the explicit breaking of the chiral symmetry let us consider the quark–mass matrix of the three light quarks and project it on the nine λ matrices [174]

$$M = \begin{pmatrix} m_u & 0 & 0 \\ 0 & m_d & 0 \\ 0 & 0 & m_s \end{pmatrix} = \frac{m_u + m_d + m_s}{\sqrt{6}}\lambda_0 + \frac{(m_u + m_d)/2 - m_s}{\sqrt{3}}\lambda_8 + \frac{m_u - m_d}{2}\lambda_3 \ . \tag{4.23}$$

In particular, the quark mass term mixes left– and right– handed fields

$$\mathcal{L}_M = -\bar{q}Mq = -(\bar{q}_R M q_L + \bar{q}_L M q_R) \ , \tag{4.24}$$

which variation under the transformations of Eq. (4.8)

$$\begin{aligned} \delta\mathcal{L}_M = -i\Bigg[& \sum_{a=1}^{8} \Theta_a^R \left(\bar{q}_R \frac{\lambda_a}{2} M q_L - \bar{q}_L M \frac{\lambda_a}{2} q_R\right) + \Theta^R(\bar{q}_R M q_L + \bar{q}_L M q_R) \\ & \sum_{a=1}^{8} \Theta_a^L \left(\bar{q}_L \frac{\lambda_a}{2} M q_R - \bar{q}_R M \frac{\lambda_a}{2} q_L\right) + \Theta^L(\bar{q}_L M q_R + \bar{q}_R M q_L)\Bigg] \ , \end{aligned} \tag{4.25}$$

gives rise to the following divergences

$$\begin{aligned} \partial_\mu V^{\mu,a} &= i\bar{q}\left[M, \frac{\lambda^a}{2}\right] q \ , \\ \partial_\mu A^{\mu,a} &= i\bar{q}\left\{\frac{\lambda^a}{2}, M\right\}\gamma_5 q \ , \\ \partial_\mu V^\mu &= 0 \ , \\ \partial_\mu A^\mu &= 2i\bar{q}M\gamma_5 q + \frac{3g^2}{32\pi^2}\epsilon_{\mu\nu\rho\sigma}\mathcal{G}_a^{\mu\nu}\mathcal{G}_a^{\rho\sigma} \ , \quad \epsilon_{0,1,2,3} = 1 \ . \end{aligned} \tag{4.26}$$

4.2.3 Non–Linear Realization of Chiral Symmetry

Denoting by V_i the generators of H and by A_i the remaining generators of G, any element of G can be unambiguously decomposed as $g = e^{\xi_i A_i} e^{\eta_i V_i}$. The Goldstone boson fields are associated to the coordinates ξ_i of the coset space G/H. In order to understand how these transform under G we consider the action of a generic element $g \in G$ on $u(\xi_i) = e^{\xi_i A_i}$:

$$g e^{\xi_i A_i} = e^{\xi_i'(g,\xi) A_i} e^{\eta_i'(g,\xi) V_i} \ . \tag{4.27}$$

This transformation provides a non–linear realization of the group G [175,176]. This realization is not linear since V_i's and A_i's do not commute but it becomes linear if restricted to the subgroup H:

$$h_0 e^{\xi_i A_i} = \left[e^{\eta_i^0 V_i} e^{\xi_i A_i} e^{-\eta_i^0 V_i} \right] e^{\eta_i^0 V_i} \ , \quad h_0 = e^{\eta_i^0 V_i} \in H \ . \tag{4.28}$$

In the specific case of chiral symmetry we have that if $g_R : u(\xi_i) \to u(\xi_i')$, $g_L : u(-\xi_i) = u(\xi_i)^\dagger \to u(\xi_i')^\dagger$ and we can write

$$\begin{aligned} u(\xi_i) &\xrightarrow{G} g_R u(\xi_i) h^{-1}(g,\xi_i) = h(g,\xi_i) u(\xi_i) g_L^{-1} \ , \\ u(\xi_i)^\dagger &\xrightarrow{G} g_L u(\xi_i)^\dagger h^{-1}(g,\xi_i) = h(g,\xi_i) u(\xi_i)^\dagger g_R^{-1} \ , \end{aligned} \tag{4.29}$$

where $h(g,\xi_i) = e^{\eta'(g,\xi_i) V}$.

4.3 Effective Lagrangians

Chiral perturbation theory provides a systematic method to discuss the consequences of the global flavor symmetries of QCD at low energies by means of an *effective field theory*. The pseudoscalar mesons are not only the lightest hadrons but also the (pseudo–) Goldstone bosons of the theory. In the chiral limit, the interaction of Goldstone bosons become arbitrarily weak for decreasing energy, no matter how strong the underlying interaction is. This is the basis for a systematic low–energy expansion with an effective chiral Lagrangian that is organized in a derivative expansion.

4.3.1 QCD in the Presence of External Fields

Following [147,148], we introduce into the QCD Lagrangian the couplings of nine vector currents and the eight axial–vector currents as well as the scalar and pseudoscalar quark densities to external c–number fields $v^\mu(x)$, $v_{(s)}^\mu$, $a^\mu(x)$, $s(x)$ and $p(x)$

$$\mathcal{L} = \mathcal{L}_{\rm QCD}^0 + \bar{q}\gamma_\mu \left(v^\mu + \frac{1}{3} v_{(s)}^\mu + \gamma_5 a^\mu \right) q - \bar{q}(s - i\gamma_5 p) q = \mathcal{L}_{\rm QCD}^0 + \mathcal{L}_{\rm ext} \ , \tag{4.30}$$

where the external fields are color–neutral, Hermitian 3×3 matrices

$$v^\mu = \sum_{a=1}^{8} \frac{\lambda_a}{2} v_a^\mu, \ \ a^\mu = \sum_{a=1}^{8} \frac{\lambda_a}{2} a_a^\mu, \ \ s = \sum_{a=0}^{8} \lambda_a s_a, \ \ p = \sum_{a=0}^{8} \lambda_a p_a \ . \tag{4.31}$$

The big advantage is that one can perform all calculations with a (locally) $SU(3)_L \times SU(3)_R$ invariant effective Lagrangian in a manifestly chiral invariant manner. Only at the very end, one inserts the appropriate external fields to extract the Green functions of quark currents or matrix elements of interest. The ordinary three flavor QCD Lagrangian is recovered by setting $v^\mu = v_{(s)}^\mu = a^\mu = p = 0$ and

$s = \mathrm{diag}(m_u, m_d, m_s)$. If one defines the generating functional

$$\exp(i\mathcal{Z}[v,a,s,p]) = \langle 0|T\exp\left[i\int \mathrm{d}^4x\mathcal{L}_{\mathrm{ext}}(x)\right]|0\rangle \ , \tag{4.32}$$

then any Green function consisting of the time–ordered product of color–neutral, Hermitian quadratic forms can be obtained from Eq. (4.32) through a functional derivative with respect to the external fields. The quark fields are operators in the Heisenberg picture and have to satisfy the equation of motion and the canonical anti–commutation relations. The generating functional is related to the vacuum–to–vacuum transition amplitude in the presence of external fields [147,148]

$$\exp[i\mathcal{Z}(v,a,s,p)] = \langle 0_{\mathrm{out}}|0_{\mathrm{in}}\rangle_{v,a,p,s} \ . \tag{4.33}$$

Now we want to study the transformation properties of the external fields under local $SU(3)_L \times SU(3)_R \times U(1)_V$, therefore we write Eq. (4.30) in terms of the left– and right– handed quark fields and we introduce the fields r_μ and l_μ such as

$$v_\mu = \frac{1}{2}(r_\mu + l_\mu) \quad \text{and} \quad a_\mu = \frac{1}{2}(r_\mu - l_\mu) \ . \tag{4.34}$$

The external fields then are subjected to the transformations

$$\begin{aligned} r_\mu &\to V_R r_\mu V_R^\dagger + iV_R\partial_\mu V_R^\dagger \ , \\ l_\mu &\to V_L l_\mu V_L^\dagger + iV_L\partial_\mu V_L^\dagger \ , \\ v_\mu^{(s)} &\to v_\mu^{(s)} - \partial_\mu\Theta \ , \\ s + ip &\to V_R(s+ip)V_L^\dagger \ , \\ s - ip &\to V_L(s-ip)V_R^\dagger \ . \end{aligned} \tag{4.35}$$

4.3.2 Lowest–Order Effective Lagrangian

The choice of coordinates in the coset space G/H is not unique but, in any given set of coordinates, we can introduce a field $u(\xi_i)$ transforming as in Eq. (4.29) [175, 176]. The freedom in the choice of coordinates implies that the parametrization of u in terms of the pseudoscalar meson fields is not unique. In the following we shall adopt the exponential parametrization in the 3×3 flavor space, defined by

$$u^2(x) = U(x) = \exp\left(i\frac{\phi(x)}{F}\right) \ , \quad \phi(x) = \sum_{a=1}^{8}\lambda_a\phi_a(x) \equiv \begin{pmatrix} \pi^0 + \frac{1}{\sqrt{3}}\eta & \sqrt{2}\pi^+ & \sqrt{2}K^+ \\ \sqrt{2}\pi^- & -\pi^0 + \frac{1}{\sqrt{3}}\eta & \sqrt{2}K^0 \\ \sqrt{2}K^- & \sqrt{2}K^0 & -\frac{2}{\sqrt{3}}\eta \end{pmatrix} \ , \tag{4.36}$$

where the parameter F is a dimensional constant that can be related to the decay constant of pseudoscalar mesons. In the absence of external fields, we can only construct trivial operators in terms of u and $u^\dagger$, without their derivatives. Once we have fixed the coupling constant in order to reproduce the correct kinetic term of spinless fields, the most general chiral invariant effective Lagrangian density with the minimal number of derivatives reads [174]

$$\mathcal{L}_{\mathrm{eff}} = \frac{F^2}{4}\langle\partial_\mu U\partial^\mu U^\dagger\rangle \ , \tag{4.37}$$

where the notation $\langle \cdots \rangle$ indicates the trace of the matrices expression inside. This Lagrangian is the chiral realization of $\mathcal{L}^0_{\rm QCD}$ at the lowest order in the derivative expansion and it is invariant under the *global* $SU(3)_L \times SU(3)_R$ transformations

$$\begin{aligned} U &\mapsto RUL^\dagger \,, \\ \partial_\mu &\mapsto \partial_\mu \left(RUL^\dagger\right) = R\partial_\mu U L^\dagger \,, \\ U^\dagger &\mapsto LU^\dagger R^\dagger \,, \\ \partial_\mu U^\dagger &\mapsto L\partial_\mu U^\dagger R^\dagger \,. \end{aligned} \tag{4.38}$$

where $L = \exp\left(i\Theta^L_a \frac{\lambda_a}{2}\right)$ and $R = \exp\left(-i\Theta^R_a \frac{\lambda_a}{2}\right)$. The global $U(1)_V$ invariance is trivially satisfied because the Goldstone bosons have baryon number zero.

Now we want to study the vector and axial–vector currents associated with the global $SU(3)_L \times SU(3)_R$ symmetry of the effective Lagrangian. If we want to compute $J^{\mu,a}_L$, we set $\Theta^R_a = 0$ and choose $\Theta^L_a = \Theta^L_a(x)$. Then to first order in Θ^L_a we obtain

$$\delta\mathcal{L}_{\rm eff} = \frac{F^2}{4}\left\langle Ui\partial_\mu\Theta^L_a\frac{\lambda_a}{2}\partial^\mu U^\dagger + \partial_\mu U\left(-i\partial^\mu\Theta^L_a\frac{\lambda_a}{2}U^\dagger\right)\right\rangle = \frac{F^2}{4}i\partial_\mu\Theta^L_a\langle\lambda_a\partial_\mu U^\dagger U\rangle \,, \tag{4.39}$$

where we used $\partial_\mu U^\dagger U = -U^\dagger\partial_\mu U$ from differentiating $U^\dagger U = 1$. We then obtain an expression for the left current and, with an equivalent procedure, for the right current:

$$J^{\mu,a}_L = \frac{\partial\delta\mathcal{L}_{\rm eff}}{\partial\partial_\mu\Theta^L_a} = i\frac{F^2}{4}\langle\lambda_a\partial^\mu U^\dagger U\rangle \,, \tag{4.40}$$

$$J^{\mu,a}_R = \frac{\partial\delta\mathcal{L}_{\rm eff}}{\partial\partial_\mu\Theta^R_a} = -i\frac{F^2}{4}\langle\lambda_a U\partial^\mu U^\dagger\rangle \,, \tag{4.41}$$

and, from Eqs. (4.40) and (4.41), one can obtain the expression for the vector and axial–vector currents

$$\begin{aligned} J^{\mu,a}_V &= J^{\mu,a}_R + J^{\mu,a}_L = -i\frac{F^2}{4}\langle\lambda_a\left[U,\partial^\mu U^\dagger\right]\rangle \,, \\ J^{\mu,a}_A &= J^{\mu,a}_R - J^{\mu,a}_L = -i\frac{F^2}{4}\langle\lambda_a\left\{U,\partial^\mu U^\dagger\right\}\rangle \,. \end{aligned} \tag{4.42}$$

Moreover, because of the symmetry of $\mathcal{L}_{\rm eff}$ under $SU(3)_L \times SU(3)_R$, both vector and axial–vector currents are conserved ($\partial_\mu J^{\mu,a}_{V,A} = 0$).

So far we have assumed a perfect $SU(3)_L \times SU(3)_R$ symmetry, but we know that an explicit symmetry breaking may lead to finite masses of the Goldstone bosons (Sec. 4.2.2). Although M is a constant matrix and does not transform along with the quark fields, $\mathcal{L}_M$ would be invariant if M transforms as [161]

$$M \mapsto RML^\dagger \,. \tag{4.43}$$

The most general Lagrangian $\mathcal{L}(U, M)$ invariant under Eqs. (4.38) and (4.43) and at lowest order in M is

$$\mathcal{L}_{\rm s.b.} = \frac{F^2 B}{2}\langle MU^\dagger + UM^\dagger\rangle \,, \tag{4.44}$$

where it is possible to prove that the new parameter B is related to the chiral quark condensate. All this analysis concerns the lowest–order effective Lagrangian which respects the global $SU(3)_L \times SU(3)_R$ symmetry. However, the Ward identities originating in the global $SU(3)_L \times SU(3)_R$ symmetry of QCD are obtained from a locally invariant generating functional involving a coupling to external fields. We want

to approximate the generating functional $\mathcal{Z}_{\rm QCD}[v,a,s,p]$ by a sequence $\mathcal{Z}^{(2)}_{\rm eff}[v,a,s,p]+\mathcal{Z}^{(4)}_{\rm eff}[v,a,s,p]+\cdots$, where the effective generating functionals are obtained using the effective field theory. Therefore, we need to promote the global symmetry of the effective Lagrangian to a local one and introduce a coupling to the same external fields v, a, s and p in QCD. Let us define the covariant derivative as

$$D_\mu U \equiv \partial_\mu U - i r_\mu + i U l_\mu \mapsto V_R(D_\mu U)V_L^\dagger \,. \tag{4.45}$$

Since the effective Lagrangian will ultimately contain arbitrarily high powers of derivatives we also need the field strength tensors $f^L_{\mu\nu}$ and $f^R_{\mu\nu}$ corresponding to the gauge fields

$$\begin{aligned} f^R_{\mu\nu} &\equiv \partial_\mu r_\nu - \partial_\nu r_\mu - i[r_\mu, r_\nu] \,, \\ f^L_{\mu\nu} &\equiv \partial_\mu l_\nu - \partial_\nu l_\mu - i[l_\mu, l_\nu] \,, \end{aligned} \tag{4.46}$$

which are traceless. In the chiral counting scheme of chiral perturbation theory the elements are counted as

$$U = \mathcal{O}(p^0) \,, \quad D_\mu U = \mathcal{O}(p) \,, \quad r_\mu, l_\mu = \mathcal{O}(p) \,, \quad f^{L,R}_{\mu\nu} = \mathcal{O}(p^2) \,, \quad \chi = \mathcal{O}(p^2) \,. \tag{4.47}$$

Then the most general locally invariant effective Lagrangian at lowest chiral order is given by

$$\mathcal{L}^{(2)} = \frac{F^2}{4}\langle D_\mu U (D^\mu U)^\dagger\rangle + \frac{F^2}{4}\langle \chi U^\dagger + U\chi^\dagger\rangle \,, \tag{4.48}$$

where [147,148]

$$\chi \equiv 2B_0(s+ip) \,. \tag{4.49}$$

$\mathcal{L}^{(2)}$ is completely determined by chiral symmetry except for the couplings F and B which have to be constrained from experimental data. By differentiating with respect to the external sources we find

$$\langle 0|J^{\mu,a}_A(x)|\phi^b(p)\rangle = \langle 0| - F\partial^\mu\phi_a(x)|\phi^b(p)\rangle = -F\partial^\mu e^{-ip\cdot x}\delta^{ab} = ip^\mu F e^{-ip\cdot x}\delta^{ab} \,, \tag{4.50}$$

$$3F^2B = -\langle\bar{q}q\rangle \,, \tag{4.51}$$

so that the connections between F and the pion decay constant F_π, defined by $\langle 0|\bar{q}\gamma^\mu\gamma_5 q|\pi^+(p)\rangle = i\sqrt{2}F_\pi p^\mu$, and between B and the quark condensate are evident. While F_π is experimentally known from the process $\pi^+ \to \mu^+\nu$, $F_\pi = 92.4$ MeV, the quark condensate is not directly related to any physical observable. It is the product $B\times m_q$ that can be related to the pseudoscalar meson masses:

$$\begin{aligned} M_\pi^2 &= 2mB \,, \\ M_K^2 &= (m+m_s)B \,, \\ M_\eta^2 &= \frac{2}{3}B(m+2M_s) \,, \end{aligned} \tag{4.52}$$

where $m = m_u = m_d$. These results plus the one in Eq. (4.51), are knows as the Gell–Mann, Oakes and Renner relations [177]. Moreover the masses of Eq. (4.52) can be combined to obtained the Gell–Mann–Okubo relation

$$4M_K^2 = 3M_\eta^2 + M_\pi^2 \,, \tag{4.53}$$

which is independent of the value of B.

4.3.3 Effective Lagrangians and Weinberg's Power Counting Scheme

A perturbative description in terms of the most general effective Lagrangian containing all possible terms compatible with assumed symmetry principles yields the most general S–matrix consistent with the fundamental principles of quantum field theory and the assumed symmetry principles [146]. Hence, one needs some scheme to organize the effective Lagrangian and a systematic method of assessing the importance of diagrams generated by the interaction terms of this Lagrangian when calculating a physical matrix element. In the framework of mesonic chiral perturbation theory, the most general chiral Lagrangian describing the dynamics of the Goldstone bosons is organized as a string of terms with an increasing number of derivatives and quark mass terms

$$\mathcal{L}_{\text{eff}} = \mathcal{L}_2 + \mathcal{L}_4 = \mathcal{L}_6 + \cdots \,, \tag{4.54}$$

where the subscripts refer to the order in the momentum and quark mass expansion. With such a counting scheme, the chiral orders in the mesonic sector are always even [$\mathcal{O}(p^{2m})$] because Lorentz indices of derivatives always have to be contracted with either the metric tensor $g^{\mu\nu}$ or the Levi–Civita tensor $\epsilon^{\mu\nu\rho\sigma}$ to generate scalars and the quark mass terms are counted as $\mathcal{O}(p^2)$. Weinberg's power counting scheme [146] analyzes the behavior of a given diagram under a linear rescaling of all the external momenta, $p_i \mapsto t p_i$, and a quadratic rescaling of the light quark masses, $m_q \mapsto t^2 m_q$. The chiral dimension D of a given diagram with amplitude $\mathcal{M}(p_i, m_q)$ is defined by

$$\mathcal{M}(t p_i, t^2 m_q) = t^D \mathcal{M}(p_i, m_q) \,, \tag{4.55}$$

and thus

$$D = 2 + \sum_{n=1}^{\infty} 2(n-1) N_{2n} + 2 N_L \,, \tag{4.56}$$

where N_{2n} is the number of vertices originating from $\mathcal{L}_{2n}$ and N_L is the number of independent loops. While the external three–momenta can be made arbitrarily small (to a certain extent), the re–scaling of the quark masses is a theoretical instrument only and loop diagrams are suppressed due to the term $2N_L$.

4.3.4 Chiral Lagrangian at $\mathcal{O}(p^4)$

The expression of the chiral Lagrangian at $\mathcal{O}(p^4)$ was computed in [147,148] and it reads

$$\begin{aligned}
\mathcal{L}_{p^4} =& L_1 \left[\langle D_\mu U (D^\mu U)^\dagger \rangle\right]^2 + L_2 \langle D_\mu U (D_\nu U)^\dagger \rangle \langle D^\mu U (D^\nu U)^\dagger \rangle \\
&+ L_3 \langle D_\mu U (D^\mu U)^\dagger D_\nu U (D^\nu U)^\dagger \rangle + L_4 \langle D_\mu U (D^\mu U)^\dagger \rangle \langle \chi U^\dagger + U \chi^\dagger \rangle \\
&+ L_5 \langle D_\mu U (D^\mu U)^\dagger (\chi U^\dagger + U \chi^\dagger) \rangle + L_6 \left[\langle \chi U^\dagger + U \chi^\dagger \rangle\right]^2 \\
&+ L_7 \left[\langle \chi U^\dagger - U \chi^\dagger \rangle\right]^2 + L_8 \langle U \chi^\dagger U \chi^\dagger + \chi U^\dagger \chi U^\dagger \rangle \\
&- i L_9 \langle f_{\mu\nu}^R D^\mu U (D^\nu U)^\dagger + f_{\mu\nu}^L (D^\mu U)^\dagger D^\nu U \rangle + L_{10} \langle U f_{\mu\nu}^L U^\dagger f_R^{\mu\nu} \rangle \\
&+ H_1 \langle f_{\mu\nu}^R f_R^{\mu\nu} + f_{\mu\nu}^L f_L^{\mu\nu} \rangle + H_2 \langle \chi \chi^\dagger \rangle \,.
\end{aligned} \tag{4.57}$$

where $\langle \cdots \rangle$ denotes a trace in flavor space. The numerical values of the low–energy coupling constants L_i are not determined by chiral symmetry and they represent the inability to solve the dynamics of QCD in the non–perturbative regime. So far they have either been fixed using empirical input [147,148,178] or theoretically using QCD–inspired models [179–182], meson–resonance saturation [183–187] and lattice QCD [188,189].

The loop graphs with vertices from $\mathcal{L}^{(2)}$ generate divergences, which are absorbed into the renormal-

ization of the low energy constants of $\mathcal{L}^{(4)}$:

$$L_i = L_i^r + \frac{\Gamma_i}{32\pi^2} R \,, \quad i = 1, \cdots, 10 \,, \tag{4.58}$$

$$H_i = H_i^r + \frac{\Delta_i}{32\pi^2} R \,, \quad i = 1, 2 \,, \tag{4.59}$$

where R is defined as

$$R = \frac{2}{d-4} - [\ln(4\pi) - \gamma_E + 1] \,, \tag{4.60}$$

with d the number of space–time dimensions and γ_E the Euler–Mascheroni constant. Γ_i and Δ_i are constants and the renormalized coefficients L_i^r depend on the scale μ introduced by dimensional regularization. Their values at two different scales are related by

$$L_i^r(\mu_2) = L_i^r(\mu_1) + \frac{\gamma_i}{16\pi^2} \ln\left(\frac{\mu_1}{\mu_2}\right) \,. \tag{4.61}$$

4.3.5 Chiral Lagrangian with photons and leptons

In order to describe the radiative corrections in QCD processes like the $\pi\pi$–scattering or the $\tau^\pm \to \pi^\pm\pi^0\nu_\tau$ processes, which are the goals of this thesis, we need to introduce the chiral Lagrangian involving also photons and leptons. Starting from Eq. (4.36), the leading–order Lagrangian in $SU(3)$ reads [190]

$$\mathcal{L}_{\text{eff}} = \frac{F_0^2}{4}\langle u_\mu u^\mu \rangle + \sum_\ell \left[\bar{\ell}(i\partial\!\!\!/ + eA\!\!\!/ - m_\ell)\ell + i\bar{\nu}_{\ell\text{L}}\partial\!\!\!/\nu_{\ell\text{L}}\right] \,, \tag{4.62}$$

where

$$u_\mu = i\left[u_\text{R}^\dagger(\partial_\mu - ir_\mu)u_\text{R} - u_\text{L}^\dagger(\partial_\mu - il_\mu)u_L\right] \,, \tag{4.63}$$

with

$$u_{\text{L/R}} = \exp\left(\mp\frac{i}{2F_0}\sum_{a=0}^{8}\phi_a\lambda_a\right) \,, \tag{4.64}$$

and the currents given by

$$\begin{aligned} l_\mu &= v_\mu - a_\mu - eQ_\text{L}^\text{em}A_\mu + \sum_\ell \left(\bar{\ell}\gamma_\mu\nu_{\ell\text{L}}Q_\text{L}^\text{w} + \bar{\nu}_{\ell\text{L}}\gamma_\mu\ell Q_\text{L}^{\text{w}\dagger}\right) \,, \\ r_\mu &= v_\mu + a_\mu - eQ_\text{R}^\text{em}A_\mu \,, \end{aligned} \tag{4.65}$$

in terms of the external vector and axial–vector currents v_μ and a_μ, and the flavor–space matrices

$$\begin{aligned} Q_{\text{L,R}}^\text{em} \to Q^\text{em} &= \frac{1}{3}\,\text{diag}(2,-1,-1) \,, \\ Q_\text{L}^\text{w} &= -2\sqrt{2}G_F \begin{pmatrix} 0 & V_{ud} & V_{us} \\ 0 & 0 & 0 \\ 0 & 0 & 0 \end{pmatrix} \,. \end{aligned} \tag{4.66}$$

The relevant counterterms of the radiative corrections to $\tau^- \to \pi^-\pi\nu_\tau$ originate from terms in the NLO Lagrangians [190,191]

$$\mathcal{L}_{e^2p^2} = e^2{F_0}^2\left\{\frac{1}{2}K_1\,\langle(\hat{Q}_\text{L}^\text{em})^2 + (\hat{Q}_\text{R}^\text{em})^2\rangle\,\langle u_\mu u^\mu\rangle\, + K_2\,\langle\hat{Q}_\text{L}^\text{em}\hat{Q}_\text{R}^\text{em}\rangle\,\langle u_\mu u^\mu\rangle\right.$$

$$
\begin{aligned}
&- K_3\,[\langle \hat{Q}_{\rm L}^{\rm em} u_\mu\rangle\,\langle \hat{Q}_{\rm L}^{\rm em} u^\mu\rangle + \langle \hat{Q}_{\rm R}^{\rm em} u_\mu\rangle\,\langle \hat{Q}_{\rm R}^{\rm em} u^\mu\rangle] + K_4\,\langle \hat{Q}_{\rm L}^{\rm em} u_\mu\rangle\,\langle \hat{Q}_{\rm R}^{\rm em} u^\mu\rangle \\
&+ K_5\,\langle[(\hat{Q}_{\rm L}^{\rm em})^2 + (\hat{Q}_{\rm R}^{\rm em})^2] u_\mu u^\mu\rangle + K_6\,\langle(\hat{Q}_{\rm L}^{\rm em}\hat{Q}_{\rm R}^{\rm em} + \hat{Q}_{\rm R}^{\rm em}\hat{Q}_{\rm L}^{\rm em}) u_\mu u^\mu\rangle \\
&+ \frac{1}{2} K_7\,\langle(\hat{Q}_{\rm L}^{\rm em})^2 + (\hat{Q}_{\rm R}^{\rm em})^2\rangle\,\langle\chi_+\rangle + K_8\,\langle \hat{Q}_{\rm L}^{\rm em}\hat{Q}_{\rm R}^{\rm em}\rangle\,\langle\chi_+\rangle \\
&+ K_9\,\langle[(\hat{Q}_{\rm L}^{\rm em})^2 + (\hat{Q}_{\rm R}^{\rm em})^2]\chi_+\rangle + K_{10}\,\langle(\hat{Q}_{\rm L}^{\rm em}\hat{Q}_{\rm R}^{\rm em} + \hat{Q}_{\rm R}^{\rm em}\hat{Q}_{\rm L}^{\rm em})\chi_+\rangle \\
&- K_{11}\,\langle(\hat{Q}_{\rm L}^{\rm em}\hat{Q}_{\rm R}^{\rm em} - \hat{Q}_{\rm R}^{\rm em}\hat{Q}_{\rm L}^{\rm em})\chi_-\rangle \\
&- iK_{12}\,\langle[(\hat{\nabla}_\mu \hat{Q}_{\rm L}^{\rm em})\hat{Q}_{\rm L}^{\rm em} - \hat{Q}_{\rm L}^{\rm em}\hat{\nabla}_\mu \hat{Q}_{\rm L}^{\rm em} - (\hat{\nabla}_\mu \hat{Q}_{\rm R}^{\rm em})\hat{Q}_{\rm R}^{\rm em} + \hat{Q}_{\rm R}^{\rm em}\hat{\nabla}_\mu \hat{Q}_{\rm R}^{\rm em}] u^\mu\rangle \\
&+ K_{13}\,\langle(\hat{\nabla}_\mu \hat{Q}_{\rm L}^{\rm em})(\hat{\nabla}^\mu \hat{Q}_{\rm R}^{\rm em})\rangle + K_{14}\,\langle(\hat{\nabla}_\mu \hat{Q}_{\rm L}^{\rm em})(\hat{\nabla}^\mu \hat{Q}_{\rm L}^{\rm em}) + (\hat{\nabla}_\mu \hat{Q}_{\rm R}^{\rm em})(\hat{\nabla}^\mu \hat{Q}_{\rm R}^{\rm em})\rangle\Big\}\,,
\end{aligned}
\tag{4.67}
$$

and

$$
\begin{aligned}
\mathcal{L}_{\rm lept} = e^2 \sum_\ell \Big\{ {F_0}^2 \Big[& X_1 \bar{\ell}\gamma_\mu \nu_{\ell{\rm L}} \langle u^\mu \{\hat{Q}_{\rm R}^{\rm em}, \hat{Q}_{\rm L}^{\rm w}\}\rangle + X_2 \bar{\ell}\gamma_\mu \nu_{\ell{\rm L}} \langle u^\mu [\hat{Q}_{\rm R}^{\rm em}, \hat{Q}_{\rm L}^{\rm w}]\rangle + X_3 m_\ell \bar{\ell}\nu_{\ell{\rm L}} \langle \hat{Q}_{\rm L}^{\rm w}\hat{Q}_{\rm R}^{\rm em}\rangle \\
& + iX_4 \bar{\ell}\gamma_\mu \nu_{\ell{\rm L}} \langle \hat{Q}_{\rm L}^{\rm w}\hat{\nabla}^\mu \hat{Q}_{\rm L}^{\rm em}\rangle + iX_5 \bar{\ell}\gamma_\mu \nu_{\ell{\rm L}} \langle \hat{Q}_{\rm L}^{\rm w}\hat{\nabla}^\mu \hat{Q}_{\rm R}^{\rm em}\rangle + {\rm h.c.}\Big] \\
& + X_6 \bar{\ell}(i\partial\!\!\!/ + eA\!\!\!/)\ell + X_7 m_\ell \bar{\ell}\ell \Big\}\,,
\end{aligned}
\tag{4.68}
$$

where explicit chiral symmetry breaking is induced by

$$
\chi_+ = u_{\rm R}^\dagger \chi u_{\rm L} + u_{\rm L}^\dagger \chi^\dagger u_{\rm R}\,,
\tag{4.69}
$$

with the substitution $\chi \to 2B_0 \mathcal{M}_{\rm quark}$, where $\mathcal{M}_{\rm quark}$ is the (diagonal) quark mass matrix, and

$$
\begin{aligned}
\hat{\nabla}_\mu \hat{Q}_{\rm L}^{\rm em} &= u(D_\mu Q_{\rm L}^{\rm em})u^\dagger\,, \\
\hat{\nabla}_\mu \hat{Q}_{\rm R}^{\rm em} &= u^\dagger(D_\mu Q_{\rm L}^{\rm em})u\,,
\end{aligned}
\tag{4.70}
$$

utilizing the covariant derivative

$$
\begin{aligned}
D_\mu Q_{\rm L}^{\rm em} &= \partial_\mu Q_{\rm L}^{\rm em} - i[l_\mu,\, Q_{\rm L}^{\rm em}]\,, \\
D_\mu Q_{\rm R}^{\rm em} &= \partial_\mu Q_{\rm R}^{\rm em} - i[r_\mu,\, Q_{\rm R}^{\rm em}]\,.
\end{aligned}
\tag{4.71}
$$

The low–energy constants in the Lagrangians of Eqs. (4.67) and (4.68) contain UV–divergences, which, in dimensional regularization, can be separated from the UV–finite parts by

$$
K_i = K_i^r(\mu) + \Sigma_i \Lambda(\mu)\,, \quad i \in \{1, \ldots, 14\}\,,
\tag{4.72}
$$

$$
X_i = X_i^r(\mu) + \Xi_i \Lambda(\mu)\,, \quad i \in \{1, \ldots, 8\}\,,
\tag{4.73}
$$

$$
\Lambda(\mu) = \frac{\mu^{d-4}}{16\pi^2}\left\{\frac{1}{d-4} - \frac{1}{2}\left[\ln 4\pi - \gamma_E + 1\right]\right\}\,,
\tag{4.74}
$$

where the coefficients Σ_i and Ξ_i can be found in [191] and [190], respectively.

4.4 Resonance contribution

From the point of view of chiral symmetry, vector, axial–vector, scalar and pseudoscalar mesons, or any other meson resonances, do not show any particular importance and their presence is manifest indirectly in the values of the low–energy constants L_i^r. We shall therefore investigate the chiral couplings of the vector and axial–vector mesons to Goldstone bosons for the ρ meson couplings, i.e., not considering

them as a gauge bosons of any kind. All resonances carry non–linear realizations of the chiral group $G = SU(3)_L \times SU(3)_R$ depending on their transformation properties under the diagonal subgroup $SU(3)_V$ [183, 184]. We are interested in resonances transforming as octets R and singlets R_1 under $SU(3)_V$:

$$\begin{aligned} R &\xrightarrow{G} h(\psi) R h(\psi)^\dagger \,, \\ R_1 &\xrightarrow{G} R_1 \,, \end{aligned} \tag{4.75}$$

with the usual matrix notation for the octet

$$R = \frac{1}{\sqrt{2}} \sum_{i=1}^{8} \lambda_i R^i \,. \tag{4.76}$$

The non–linear realization of G on the octet field R is local and we have to define the covariant derivative

$$\nabla_\mu R = \partial_\mu R + [\Gamma_\mu, R] \,, \tag{4.77}$$

with

$$\Gamma_\mu = \frac{1}{2} \left\{ u^\dagger \left[\partial_\mu - i \left(v_\mu + a_\mu \right) \right] u + u \left[\partial_\mu - i \left(v_\mu - a_\mu \right) \right] \right\} \,, \tag{4.78}$$

ensuring the proper transformation

$$\nabla_\mu R \xrightarrow{G} h(\psi) \nabla_\mu h(\psi)^\dagger \,. \tag{4.79}$$

We want to discuss the chiral couplings of the meson resonances of the type $V(1^{--})$, $A(1^{++})$, $S(0^{++})$ and $P(0^{++})$ to the pseudoscalar Goldstone fields and to do that we describe the relevant degrees of freedom in terms of antisymmetric tensor fields [147, 148]. To determine the resonance exchange contributions to the effective chiral Lagrangian we need the lowest order couplings in the chiral expansion which are linear in the resonance fields. With the coset element $u(\psi)$ defined by

$$u(\psi) \xrightarrow{G} g_R u(\psi) h(\psi)^\dagger = h(\psi) u(\psi) g_L^\dagger \,, \tag{4.80}$$

we obtain the following terms

$$\begin{aligned} \text{Octet}: \qquad & u_\mu = i u^\dagger D_\mu U u^\dagger = u_\mu^\dagger \,, \\ & u_\mu u_\nu \,, \\ & u_{\mu\nu} = i u^\dagger D_\mu D_\nu U u^\dagger \,, \\ & \chi_\pm = u^\dagger \chi u^\dagger \pm u \chi^\dagger u \,, \\ & f_\pm^{\mu\nu} = u F_L^{\mu\nu} u^\dagger \pm u^\dagger F_R^{\mu\nu} u \,, \end{aligned} \tag{4.81}$$

$$\text{Singlets}: \quad \langle u_\mu u_\nu \rangle \,, \quad \langle u_{\mu\nu} \rangle \,, \quad \langle \chi_\pm \rangle \,. \tag{4.82}$$

Because of P and C invariance, it turns out that all the couplings linear in the fields V, A, S and P start at order p^2. All the resonance couplings can be included in the Lagrangian [183, 184]

$$\mathcal{L}_{\text{res}} = \sum_{R=V,A,S,P} \left[\mathcal{L}_{\text{kin}}(R) + \mathcal{L}_2(R) + \mathcal{L}_4(R) + \cdots \right] \,, \tag{4.83}$$

with kinetic terms

$$\mathcal{L}_{\text{kin}}(R) = -\frac{1}{2}\langle \nabla^\lambda R_{\lambda\mu} \nabla_\nu R^{\nu\mu} - \frac{1}{2} M_R^2 R_{\mu\nu} R^{\mu\nu} \rangle - \frac{1}{2} \partial^\lambda R_{1,\lambda\mu} \partial_\nu R_1^{\nu\mu} + \frac{1}{4} M_{R_1}^2 R_{1,\mu\nu} R_1^{\mu\nu} \ , \tag{4.84}$$

for $R = V,\ A$ and

$$\mathcal{L}_{\text{kin}}(R) = \frac{1}{2}\langle \nabla^\mu R \nabla_\mu R - M_R^2 R^2 \rangle + \frac{1}{2}\left(\partial^\mu R_1 \partial_\mu R_1 - M_{R_1}^2 R_1^2 \right) \ , \tag{4.85}$$

for $R = S,\ P$ and with M_R, M_{R_1} the corresponding masses in the chiral limit. The interactions read

$$\begin{aligned}
\mathcal{L}_2[V(1^{--})] &= \frac{F_V}{2\sqrt{2}} \langle V_{\mu\nu} f_+^{\mu\nu} \rangle = \frac{iG_V}{\sqrt{2}} \langle V_{\mu\nu} u^\mu u^\nu \rangle \ , \\
\mathcal{L}_2[A(1^{++})] &= \frac{F_A}{2\sqrt{2}} \langle A_{\mu\nu} f_-^{\mu\nu} \rangle \ , \\
\mathcal{L}_2[S(0^{++})] &= c_d \langle S u_\mu u^\mu \rangle + c_m \langle S \chi_+ \rangle + \tilde{c}_d S_1 \langle u_\mu u^\mu \rangle + \tilde{c}_m S_1 \langle \chi_+ \rangle \ , \\
\mathcal{L}_2[P(0^{-+})] &= i d_m \langle P \chi_- \rangle + i \tilde{d}_m P_1 \langle \chi_- \rangle \ .
\end{aligned} \tag{4.86}$$

We notice that for V and A only octets can couple whereas both octets and singlets appear for S and P. Moreover there is no coupling that would induce the transitions $V \to P\gamma$ at $\mathcal{O}(p^2)$ in the chiral expansion.

Chapter 5

Pion–pion Scattering

Pion–pion scattering is one of the simplest hadronic reactions that displays many key features of low–energy QCD [25], most prominently approximate chiral symmetry, its spontaneous breaking, and the explicit breaking due to finite up– and down–quark masses. Accordingly, the chiral symmetry constrains the low–energy scattering amplitude, which can be systematically analyzed in χPT [146–148,192] and has been worked out up to two loop order [193]. In addition, the $\pi\pi$–scattering exhibits further remarkable properties that extend beyond the low–energy region where the chiral expansion applies. In this chapter we analyze the main properties of the $\pi\pi$ scattering amplitude and present explicit representations used in the calculation.

5.1 Kinematics

Let us consider the pion–pion scattering process $\pi(p_1)\pi(p_2) \to \pi(p_3)\pi(p_4)$. Each pion can be described by a four–vector $p_i^\mu = (E_i, \mathbf{p}_i)$ and a mass M_{π_i}, where $i = 1, 2, 3, 4$. In the isospin limit all the pions have the same mass

$$p_i^2 = M_\pi^2 = E_i^2 + (\mathbf{p}_i)^2 \ , \quad i \in \{1, 2, 3, 4\} \ . \tag{5.1}$$

The kinematic of the process can be expressed in terms of the Mandelstam variables:

$$\begin{aligned} s &= (p_1 + p_2)^2 = (p_3 + p_4)^2 \ , \\ t &= (p_1 - p_3)^2 = (p_4 - p_2)^2 \ , \\ u &= (p_1 - p_4)^2 = (p_3 - p_2)^2 \ , \end{aligned} \tag{5.2}$$

which satisfy the relation

$$s + t + u = \sum_{i=1}^{4} p_i = \sum_{i=1}^{4} M_i^2 \ , \tag{5.3}$$

where the last equality holds if the pions are on–shell. Then the $\pi\pi$–scattering amplitude depends on two of the three Mandelstam variables and on the pion mass.

5.2 Multipion states

In the isospin limit, the pions form an isospin triplet with total isospin $I = 1$ and its third component $I_3 = -1, 0, 1$. Using the notation $|I, I_3\rangle$ we get

$$\begin{aligned} |\pi^+\rangle &= |1,1\rangle \ , \\ |\pi^0\rangle &= |1,0\rangle \ , \\ |\pi^-\rangle &= |1,-1\rangle \ . \end{aligned} \tag{5.4}$$

An alternative and more convenient basis is the one formed by three elements $|\pi_i\rangle$, $i \in \{1,2,3\}$ so that the physical basis can be rewritten as

$$\begin{aligned} |\pi^+\rangle &= \frac{1}{\sqrt{2}}(|\pi^1\rangle + i|\pi^2\rangle) \ , \\ |\pi^0\rangle &= |\pi^3\rangle \ , \\ |\pi^-\rangle &= \frac{1}{\sqrt{2}}(|\pi^1\rangle - i|\pi^2\rangle) \ . \end{aligned} \tag{5.5}$$

Once the third isospin component of each element of the basis is known, one can construct the two–particle states by taking the direct products of two one–particle states $|\pi^i\pi^j\rangle = |\pi^i\rangle \otimes |\pi^j\rangle$. A product of states $|j_1, m_1\rangle \otimes |j_2, m_2\rangle \equiv |j_1, j_2; m_1, m_2\rangle$ can be expressed in terms of the total isospin $|J, M\rangle$ according to

$$|j_1, j_2; m_1, m_2\rangle = \sum_{J,M} \langle J, M | j_1, j_2; m_1, m_2\rangle |J, M\rangle \ , \tag{5.6}$$

where $\langle J, M | j_1, j_2; m_1, m_2\rangle$ are known as the Clebsch–Gordan coefficients. Then we find

$$\begin{aligned} |\pi^+\pi^-\rangle &= -\sqrt{\frac{1}{6}}|2,0\rangle - \sqrt{\frac{1}{2}}|1,0\rangle - \sqrt{\frac{1}{3}}|0,0\rangle \ , \\ |\pi^-\pi^+\rangle &= -\sqrt{\frac{1}{6}}|2,0\rangle + \sqrt{\frac{1}{2}}|1,0\rangle - \sqrt{\frac{1}{3}}|0,0\rangle \ , \\ |\pi^0\pi^0\rangle &= -\sqrt{\frac{2}{3}}|2,0\rangle - \sqrt{\frac{1}{3}}|0,0\rangle \ , \\ |\pi^+\pi^0\rangle &= -\sqrt{\frac{1}{2}}|2,1\rangle - \sqrt{\frac{1}{2}}|1,1\rangle \ , \\ |\pi^0\pi^+\rangle &= -\sqrt{\frac{1}{2}}|2,1\rangle + \sqrt{\frac{1}{2}}|1,1\rangle \ , \\ |\pi^-\pi^0\rangle &= \sqrt{\frac{1}{2}}|2,-1\rangle - \sqrt{\frac{1}{2}}|1,-1\rangle \ , \\ |\pi^0\pi^-\rangle &= \sqrt{\frac{1}{2}}|2,-1\rangle + \sqrt{\frac{1}{2}}|1,-1\rangle \ , \\ |\pi^-\pi^-\rangle &= |2,-2\rangle \ , \\ |\pi^+\pi^+\rangle &= |2,2\rangle \ . \end{aligned} \tag{5.7}$$

5.3 Isospin amplitudes

Thanks to isospin conservation, a process can be described in terms of the so–called isospin amplitudes $T^I(s,t,u)$. If we consider a scattering process $a+b \to c+d$ in the s–channel we get

$$\begin{aligned}\langle c;d|T_s|a;b\rangle &= \sum_{I,J}\langle c;d|I,m\rangle\langle I,m|T_s|J,m\rangle\langle J,m|a;b\rangle \\ &= (2\pi)^4\delta^4\left(\sum_i p_i\right) c^{I\,*}_{c;d}c^J_{a;b}T^I(s,t,u)\ ,\end{aligned} \tag{5.8}$$

where $c^J_{a;b} = \langle J,m|a;b\rangle$ identify the Clebsch–Gordan coefficients while T_s indicates the T–matrix in the s–channel. Then the physical $\pi\pi$–scattering amplitude can be written in terms of the isospin amplitude

$$\begin{aligned}T^c(s,t,u) &:= T(\pi^+\pi^- \to \pi^+\pi^-) = \frac{1}{6}T^2 + \frac{1}{2}T^1 + \frac{1}{3}T^0\ , \\ T^x(s,t,u) &:= T(\pi^+\pi^- \to \pi^0\pi^0) = -\frac{1}{3}T^2 + \frac{1}{3}T^0\ , \\ T^n(s,t,u) &:= T(\pi^0\pi^0 \to \pi^0\pi^0) = \frac{2}{3}T^2 + \frac{1}{3}T^0\ .\end{aligned} \tag{5.9}$$

There are two further amplitudes, which are related by crossing transformations to the previous ones

$$\begin{aligned}T^{++}(s,t,u) &:= T(\pi^+\pi^+ \to \pi^+\pi^+) = T^c(t,u,s)\ , \\ T^{+0}(s,t,u) &:= T(\pi^+\pi^0 \to \pi^+\pi^0) = T^x(t,u,s)\ .\end{aligned} \tag{5.10}$$

By using an alternative convention for the isospin basis, the $\pi\pi$–scattering amplitude can be written as

$$\langle\pi^a(p_1)\pi^b(p_2)|T|\pi^c(p_3)\pi^d(p_4)\rangle = A(s,t,u)\delta^{ab}\delta^{cd} + B(s,t,u)\delta^{ac}\delta^{bd} + C(s,t,u)\delta^{ad}\delta^{bc}\ , \tag{5.11}$$

where $a,b,c,d \in \{1,2,3\}$. An important feature of the isospin amplitude for the pion–pion scattering process is the crossing symmetry which is due to the fact that in the isospin limit, all of the three physical pions have the same mass. So we obtain the following relations

$$B(s,t,u) = A(t,s,u)\ , \quad C(s,t,u) = A(u,t,s)\ . \tag{5.12}$$

Thanks to Eq. (5.5) we can relate the amplitudes $A(s,t,u)$, $B(s,t,u)$ and $C(s,t,u)$ to physical processes:

$$\begin{aligned}\langle\pi^+\pi^-|\pi^0\pi^0\rangle &= A(s,t,u)\ , \\ \langle\pi^+\pi^0|\pi^+\pi^0\rangle &= B(s,t,u)\ , \\ \langle\pi^0\pi^-|\pi^0\pi^-\rangle &= C(s,t,u)\ ,\end{aligned} \tag{5.13}$$

and, using Eq. (5.9), we can relate them to the isospin amplitudes:

$$\begin{aligned}T^0(s,t) &= 3A(s,t,u) + A(t,u,s) + A(u,s,t)\ , \\ T^1(s,t) &= A(t,u,s) - A(u,s,t)\ , \\ T^2(s,t) &= A(t,u,s) + A(u,s,t)\ .\end{aligned} \tag{5.14}$$

By inserting Eq. (5.14) into Eq. (5.9), one trivially obtains the expression of each of these amplitudes T^i, $i = c,\ x,\ n$ in terms of the isospin–invariant amplitude A:

$$\begin{aligned} T^c(s,t,u) &= A(s,t,u) + A(t,u,s)\ , \\ T^x(s,t,u) &= A(s,t,u)\ , \\ T^n(s,t,u) &= A(s,t,u) + A(t,u,s) + A(u,s,t)\ . \end{aligned} \tag{5.15}$$

5.4 Partial wave representation

By considering elastic $\pi\pi$ scattering in the framework of QCD and in the isospin symmetry limit, where the masses of the up and down quarks are taken equal and the electromagnetic interaction is ignored, the scattering process is described by a single Lorentz invariant amplitude $A(s,t,u)$ (see Eq. (5.11)). The partial wave decomposition then reads

$$T^I(s,t) = 32\pi \sum_\ell (2\ell+1) P_\ell(z)\, t^I_\ell(s)\ , \tag{5.16}$$

where the Legendre polynomials $P_\ell(z)$ depend on the scattering angle θ in the centre of mass frame of s:

$$z = \cos\theta = 1 + \frac{2t}{s - 4M_\pi^2}\ . \tag{5.17}$$

The partial wave amplitude can then be obtained from

$$t^I_\ell(s) = \frac{1}{64\pi} \int_{-1}^{1} \mathrm{d}z\, T^I(s, t(z)) P_\ell(z)\ . \tag{5.18}$$

In the purely elastic case and in the isospin symmetry limit, we only consider a pair of pions in the intermediate state and the unitarity relation in Eq. (3.22) for the $\pi\pi$ scattering partial waves can be written in a very compact form:

$$\mathrm{Im} t^I_\ell(s) = \sigma(s) |t^I_\ell(s)|^2\ , \tag{5.19}$$

where $\sigma(s) = \sqrt{1 - \frac{4M_\pi^2}{s}}$. This shows that there is a diagonal relation between the imaginary part of the partial wave and its modulus squared.

Below the inelasticity threshold, which is the two–kaon threshold in the case of the $\pi\pi$ scattering, the partial waves can be expressed uniquely as a function of their phase–shift, $\delta^I_\ell(s)$:

$$t^I_\ell(s) = |t^I_\ell(s)| \mathrm{e}^{i\delta^I_\ell(s)} = \frac{\mathrm{e}^{2i\delta^I_\ell(s)} - 1}{2i\sigma(s)}\ . \tag{5.20}$$

This relation can be generalized to the inelastic region by introducing an inelasticity function $\eta^I_\ell(s)$, with the property $\eta^I_\ell(s) \leq 1$. The generalization of the partial wave amplitude then reads

$$t^I_\ell(s) = |t^I_\ell(s)| \mathrm{e}^{i\delta^I_\ell(s)} = \frac{\eta^I_\ell(s) \mathrm{e}^{2i\delta^I_\ell(s)} - 1}{2i\sigma(s)}\ . \tag{5.21}$$

In the limit $\eta^I_\ell(s) \to 1$, we recover the elastic relation in Eq. (5.20).

5.4.1 Roy equations

In this section we present a representation for the the partial wave amplitude t_ℓ^I of elastic $\pi\pi$ scattering due to Roy [194]. This is an important result for this thesis work and constitutes the starting point of our model–independent analysis of the isospin–breaking effects due to the pion mass difference in the $\pi\pi$ scattering amplitude (see Chs. 6–8).

Roy's representation for the partial wave amplitude t_ℓ^I of elastic $\pi\pi$ scattering reads

$$t_\ell^I(s) = k_\ell^I(s) + \sum_{I'=0}^{2}\sum_{\ell'=0}^{\infty}\int_{4M_\pi^2}^{\infty} \mathrm{d}s' K_{\ell\ell'}^{II'}(s,s')\mathrm{Im}\; t_{\ell'}^{I'}(s')\;, \tag{5.22}$$

where I and ℓ denote isospin and angular momentum, respectively, and $k_\ell^I(s)$ is the partial wave projection of the subtraction term, which shows up only in the S– and P–waves:

$$k_\ell^I(s) = a_0^I\delta_\ell^0 + \frac{s-4M_\pi^2}{4M_\pi^2}(2a_0^0 - 5a_0^2)\left(\frac{1}{3}\delta_0^I\delta_\ell^0 + \frac{1}{18}\delta_1^I\delta_l^1 - \frac{1}{6}\delta_2^I\delta_\ell^0\right)\;. \tag{5.23}$$

where a_0^0 and a_0^2 are the S–wave scattering lengths. The kernels $K_{\ell\ell'}^{II'}(s,s')$ contain a diagonal singular Cauchy kernel that generates the right hand cut in the partial wave amplitudes, as well as a logarithmically singular piece that accounts for the left hand cut [24]:

$$K_{\ell\ell'}^{II'}(s,s') = \frac{1}{\pi(s'-s)}\delta^{II'}\delta_{\ell\ell'} + \bar{K}_{\ell\ell'}^{II'}(s,s') \tag{5.24}$$

Eqs. (5.22) are consequences of the analyticity properties of the $\pi\pi$ scattering amplitude, of the Froissart bound and of crossing symmetry. They are valid in the interval $-4M_\pi^2 < s < 60M_\pi^2$ [194–196], and, combined with unitarity, they amount to an infinite system of coupled, singular integral equations for the partial waves. The integration is split into a low energy interval $4M_\pi^2 < s' < s_0$ and a remainder, $s_0 < s' < \infty$ where s_0 is defined as the *matching point*, and it is chosen somewhere in the range where the Roy equations are valid. The two S–wave scattering lengths, the elasticity parameter below the matching point and the imaginary parts above that point are treated as an externally assigned input. The mathematical problem consist in solving the Roy's integral equations with this input.

Thanks to several analyses and applications of the Roy equations, it has been shown that, for a given input of S–wave scattering lengths, elasticity parameters and imaginary parts, there are in general many possible solutions to the equations. This non–uniqueness is due to the singular Cauchy kernel on the right hand side of Eqs. (5.22). In order to investigate the uniqueness properties of the Roy system, one may keep only this part of the kernel, so that the integral equations decouple. In this case, a single channel problem is obtained, that is a single partial wave, which, moreover, does not have a left hand cut. By investigating the infinitesimal neighborhood of a given solution, it was found that the multiplicity of the solution increases by one whenever the value of the phase shift at the matching point goes through a multiple of $\pi/2$ [197]. Details on the solution of Roy equations in the isospin limit and for $I \in \{0,1,2\}$, $\ell \in \{0,1,2,3\}$ can be found in [24, 27].

5.5 Electromagnetic corrections to $\pi\pi$–scattering at low energies

We are interested in the computation of the $\pi\pi$–scattering amplitude at next–to–leading order including electromagnetic effects. In this case we switch from the $SU(3)$ Lagrangian formalism described in Ch. 4 to the one in $SU(2)$. At leading order, the effective Lagrangian, considering also the electromagnetic

interaction, reads [184]

$$\mathcal{L}^{(2)} = \frac{F^2}{4}\langle d^\mu U^\dagger d_\mu U + \chi^\dagger U + U^\dagger \chi\rangle - \frac{1}{4}F^{\mu\nu}F_{\mu\nu} - \frac{1}{2a}\left(\partial\cdot A\right)^2 + C\langle Q_R U Q_L U^\dagger\rangle \,, \tag{5.25}$$

where, in order to obtain a consistent expansion scheme, the electric charge e is considered of order p ($e, Q_R, Q_L \sim \mathcal{O}(p)$) and the transformation properties of the various quantities under the chiral $SU(N_f)\times SU(N_f)$ read [191]

$$\begin{aligned} U &\to g_R U g_L^\dagger \\ Q_I &\to g_I Q_I g_I^\dagger \quad \text{with} \quad I = R, L \end{aligned} \tag{5.26}$$

where $g_{R,L} \in SU(N_f)_{R,L}$. To perform this computation we will use a different but equivalent parametrization of the field U:

$$U(x) = \sigma(x) + i\frac{\phi(x)}{F} \,, \tag{5.27}$$

where $\sigma(x) = \sqrt{1 - \frac{\phi^2(x)}{F}}$ and, in the case $N_f = 2$,

$$\phi(x) = \begin{pmatrix} \pi^0 & \sqrt{2}\pi^+ \\ \sqrt{2}\pi^- & -\pi^0 \end{pmatrix} . \tag{5.28}$$

The covariant derivative $d_\mu U$ is defined as

$$d_\mu U = \partial_\mu U - i(v_\mu + Q_R A_\mu + a_\mu)U + iU(v_\mu + Q_L A_\mu - a_\mu) \,, \tag{5.29}$$

and the last term of Eq. (5.25) contain the *spurious* $Q_L^a(x)$ and $Q_R^a(x)$, which play the role of sources for insertions into the QCD Green's functions of the electromagnetic vertex operators $A_\mu \bar{q}_L \frac{\lambda^a}{2}\gamma^\mu q_L$ and $A_\mu \bar{q}_R \frac{\lambda^a}{2}\gamma^\mu q_R$, respectively. The low energy constant C gives an electromagnetic contribution to the charged pseudoscalar masses

$$\begin{aligned} M^2_{\pi^0} &= (m_u + m_d)B \,, \\ M^2_{\pi^\pm} &= (m_u + m_d)B + 2C\cdot\frac{e^2}{F^2} \,, \end{aligned} \tag{5.30}$$

which yields

$$Z \equiv \frac{C}{F^4} = \frac{M^2_{\pi^\pm} - M^2_{\pi^0}}{2e^2F^2} \,. \tag{5.31}$$

Finally the penultimate term of Eq. (5.25) acts as a gauge fixing. At next–to–leading order the generating functional $\mathcal{Z}(v_\mu, a_\mu, s, p, Q_L, Q_R)$ in the presence of electromagnetic interactions, involves one loop graphs with vertices from $\mathcal{L}^{(2)}$, tree graphs with vertices from $\mathcal{L}^{(2)}$ and at most one vertex from the next–to–leading effective Lagrangian

$$\mathcal{L}^{(4)} = \mathcal{L}_{p^4} + \mathcal{L}_{e^2p^2} + \mathcal{L}_{e^4} \,, \tag{5.32}$$

where $\mathcal{L}_{p^4}$ contains the purely QCD low energy interactions among the pseudoscalar mesons at $\mathcal{O}(p^4)$, while $\mathcal{L}_{e^2p^2}$ and $\mathcal{L}_{e^4}$ are the chiral Lagrangians involving also photons and leptons. As previously said, we are now working in the $N_f = 2$ case and the explicit expression for all the terms in Eq. (5.32) with the details about their derivation can be found in [198]. As an explicative example, we can then compute the amplitude for the $\pi^+\pi^- \to \pi^+\pi^-$ scattering process. In the isospin basis, the $\pi^+\pi^- \to \pi^+\pi^-$ scattering

amplitude at leading order is given by

$$\langle \pi^+\pi^-|\pi^+\pi^-\rangle = \frac{1}{4}\Big(\langle \pi^1\pi^1|\pi^1\pi^1\rangle + \langle \pi^1\pi^1|\pi^2\pi^2\rangle + \langle \pi^1\pi^2|\pi^1\pi^2\rangle - \langle \pi^1\pi^1|\pi^2\pi^1\rangle + \{1 \leftrightarrow 2\}\Big) \ . \quad (5.33)$$

Considering the Lagrangian of Eq. (5.25), the tree level scattering amplitude reads

$$A(s,t,u)_{\rm TL} = \frac{s+t-2M_0^2}{F^2} \ . \quad (5.34)$$

where $M_0^2 = 2\hat{m}B$ is the bare mass and can be written in terms of the physical mass according to the expression of $M_{\pi^0}^2$ at next–to–leading order [198]:

$$\begin{aligned} M_{\pi^0}^2 =& 2\hat{m}B\left\{1 + \frac{2M_{\pi^0}^2}{F^2}\ell_3^r(\mu) + e^2\mathcal{K}_{\pi^0}^r(\mu) + \frac{M_{\pi^\pm}^2}{16\pi^2F^2}\ln\frac{M_{\pi^\pm}^2}{\mu^2} - \frac{M_{\pi^0}^2}{32\pi^2F^2}\ln\frac{M_{\pi^0}^2}{\mu^2}\right\} \\ & - 2\frac{B^2}{F^2}(m_d-m_u)^2\ell_7 - \frac{8}{3}B(m_d-m_u)e^2k_7 \ , \end{aligned} \quad (5.35)$$

where

$$\mathcal{K}_{\pi^0}^r(\mu) = -\frac{20}{9}\left[k_1^r + k_2^r - \frac{9}{10}(2k_3^r - k_4^r) - k_5^r - k_6^r - \frac{1}{5}k_7\right] \ . \quad (5.36)$$

ℓ_i and k_i are the low–energy constants equivalent to the one in Eqs. (4.58), (4.72) and (4.73) but in the $SU(2)$ case. At NLO there are four kind of diagrams which contribute to the $\pi^+\pi^- \to \pi^+\pi^-$ scattering amplitude. However we will not consider $\mathcal{O}(e^4)$ contributions, which include two–photon exchange box diagrams and which are expected to be smaller than the other contributions at the same order.

5.5.1 Strong Interaction Diagrams

Considering only the strong sector, the process is described by: 1–loop diagrams with vertices from the Lagrangian in Eq. (5.25) and a tree level diagram with the vertex described by the Lagrangian $\mathcal{L}_{p^4}$.

* π^+, π^-, π^0–loop diagrams.
  The first diagrams at NLO that we consider are the one of the type shown in Fig. 5.1. By computing the amplitude in the s–, t– and u–channels, we get

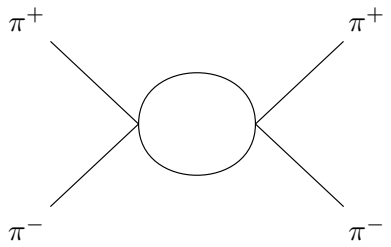

Figure 5.1: π^+, π^-, π^0–loop diagrams for the $\pi^+\pi^- \to \pi^+\pi^-$–scattering amplitude

$$\begin{aligned} A(s,t,u)_{\pi-\text{loop}} =& \frac{(s-M_{\pi^0}^2)}{2F^4}J_{00}(s) \\ & + \frac{1}{2(1-d)F^4}\Big\{\left[4(1-2d)M_{\pi^\pm}^2 + 8(d-1)M_{\pi^0}^2 + (4-3d)s + 2t\right]A(M_{\pi^\pm}^2) \\ & + \Big[8(d-1)M_{\pi^0}^2(4M_{\pi^\pm}^2+s) - d(4M_{\pi^\pm}^2+s)^2 \end{aligned} \quad (5.37)$$

$$- 16(d-1)M_{\pi^0}^4 + 16M_{\pi^\pm}^2 s + 8M_{\pi^\pm}^2 t - 2st\Big] \frac{J_{+-}(s)}{2}\Bigg\}$$
$$+ \frac{1}{2F^4}\left[\left(8M_{\pi^\pm}^2 - 4M_{\pi^0}^2 - u\right) A(M_{\pi^\pm}^2) + \left(2M_{\pi^0}^2 - 4M_{\pi^\pm}^2 + u\right)^2 \frac{J_{+-}(u)}{2}\right]$$
$$+ \{s \leftrightarrow t\}\,, \tag{5.38}$$

where d is the number of space–time dimensions and the loop functions are defined in App.C.

∗ Tadpole Diagrams.
The second type of 1–loop diagram is the tadpole diagram drawn in Fig. 5.2 and the amplitude

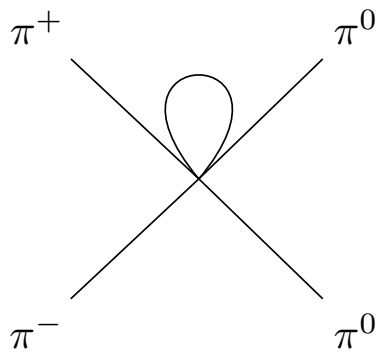

Figure 5.2: Tadpole diagram for the $\pi^+\pi^- \to \pi^+\pi^-$–scattering amplitude

reads

$$A(s,t,u)_{\rm Tad} = -\frac{1}{F^4}\left\{\left[4\left(4M_{\pi^\pm}^2 + s + t\right) - 18M_{\pi^0}^2\right] A(M_{\pi^\pm}^2) + \left(-3M_{\pi^0}^2 + s + t\right) A(M_{\pi^0}^2)\right\}\,. \tag{5.39}$$

∗ $\mathcal{O}(p^4)$ diagram.
Another contribution involving only the strong interactions is the tree level diagram with the vertex from $\mathcal{L}_{p^4}$ and the amplitude is

$$A(s,t,u)_{p^4} = \frac{1}{F^4}\left\{\left[(s-2M_{\pi^\pm}^2)^2 + (t-2M_{\pi^\pm}^2)^2\right](l_1+l_2) + 2(u-2M_{\pi^\pm}^2)^2 l_2\right\}\,. \tag{5.40}$$

∗ Z–correction
The last term in the pure strong amplitude is the wave function renormalization correction or Z–correction which comes from tadpole contributions to the external legs of the pions (Fig. 5.3). This contribution to the $\pi^+\pi^- \to \pi^+\pi^-$ scattering amplitude than reads

$$A(s,t,u)_Z = 2\frac{s+t-2M_{\pi^0}^2}{F^4} A(M_{\pi^\pm}^2)\,. \tag{5.41}$$

5.5.2 Electromagnetic Interaction Diagrams

∗ Vertex Diagram
By introducing the electromagnetic interaction we need to consider loops with virtual photons. This affects the wave function renormalization of the charged pions and introduce a long range component into the scattering amplitude through the vertex correction graph (Fig. 5.4). In order to take care of the infrared divergences, we introduce a fictitious photon mass. In analogy to the

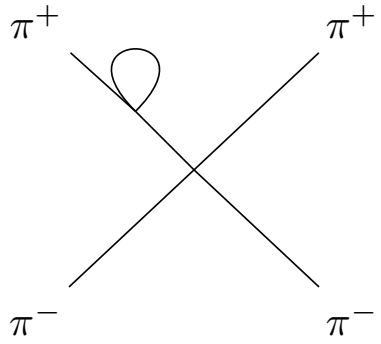

Figure 5.3: Z–correction for the $\pi^+\pi^- \to \pi^+\pi^-$ scattering amplitude

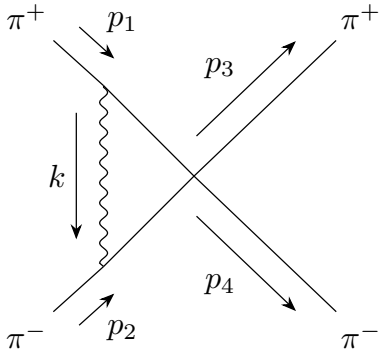

Figure 5.4: Vertex diagram for the $\pi^+\pi^- \to \pi^+\pi^-$–scattering amplitude

contribution from the diagram in Fig. 5.1, we have to consider the s–, t– and u–channel so that the vertex amplitude reads

$$
\begin{aligned}
A(s,t,u)_V =& \frac{e^2}{F^2}\Bigg\{ \left[\frac{2(M_{\pi^\pm}^2 - t)}{M_{\pi^\pm}^2} + \frac{(2M_{\pi^\pm}^2 - u)}{M_{\pi^\pm}^2}\right] A(M_{\pi^\pm}^2) \\
&+ \frac{\left[16M_{\pi^\pm}^4 + 4M_{\pi^0}^2\left(4M_{\pi^\pm}^2 - s\right) - 8M_{\pi^\pm}^2(3s+2t) + s(5s+8t)\right]}{4M_{\pi^\pm}^2 - s} J_{+-}(s) \\
&+ \left(4M_{\pi^\pm}^2 - 2M_{\pi^0}^2 - u\right) J_{+-}(u) \\
&+ \Bigg[\frac{4}{4M_{\pi^\pm}^2 - s}\left(M_{\pi^0}^2\left(2s - 8M_{\pi^\pm}^2\right) + 4M_{\pi^\pm}^2(s+2t) - s(s+3t)\right) \\
&\qquad - 2\left(8M_{\pi^\pm}^2 - 2M_{\pi^0}^2 - 3u\right)\Bigg] J_{\pm\gamma}(M_{\pi^\pm}^2) \\
&+ 4\left(2M_{\pi^\pm}^2 - s\right)\left(s + t - 2M_{\pi^0}^2\right) G_{+-\gamma}(s) \\
&- 2\left[8M_{\pi^\pm}^4 + M_{\pi^0}^2\left(2u - 4M_{\pi^\pm}^2\right) - 6M_{\pi^\pm}^2 u + u^2\right] G_{+-\gamma}(u)\Bigg\} + \{s \leftrightarrow t\}\,,
\end{aligned}
\tag{5.42, 5.43}
$$

where the loop functions are listed in the App. C.

$*$ $\mathcal{O}(e^2p^2)$ diagram

In analogy with the pure strong case we have to consider the tree level diagram coming from the

counterterms Lagrangian $\mathcal{L}_{e^2p^2}$. The amplitude then reads

$$A(s,t,u)^{\rm TL}_{e^2p^2} = -\frac{e^2}{F^2}\Bigg\{ -\frac{20}{9}k_1\,(s+t) + \frac{4}{9}k_2\left[72M^2_{\pi^\pm} - 23\,(s+t)\right] + 2\,(2k_3+k_4)\left[8M^2_{\pi^\pm} - 3\,(s+t)\right] + M^2_{\pi^0}\left(\frac{40}{9}k_5 - \frac{248}{9}k_6 + \frac{8}{9}k_7 - 32k_8\right)\Bigg\}\,. \tag{5.44}$$

In addition to this contribution, the wave function renormalization terms coming from the same Lagrangian of counterterms reads:

$$A(s,t,u)^{\rm WFR}_{e^2p^2} = -\frac{80}{9}\frac{e^2}{F^2}(s+t-2M^2_{\pi^0})\,(k_1+k_2)\ , \tag{5.45}$$

and the terms which depend on k_i coming from the mass renormalization of the neutral pion given in Eq. (5.35).

∗ Born–type diagrams.
By studying the electromagnetic interactions in the $\pi\pi$–scattering we have to consider also tree level diagrams of the type in Fig. 5.5 where the full circles are made explicit in Fig. 5.6 and they are grouped in the pion vector form factor F^π_V. The contribution to the scattering amplitude from

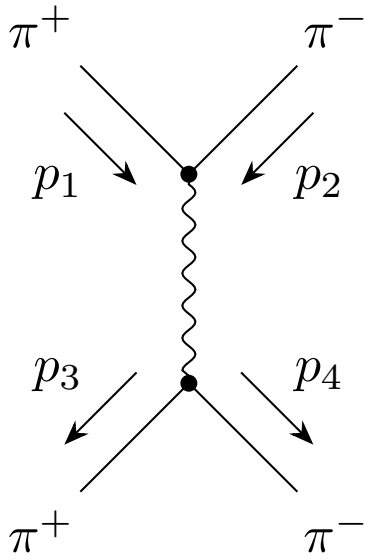

Figure 5.5: Born–type diagram for the $\pi^+\pi^- \to \pi^+\pi^-$–scattering amplitude

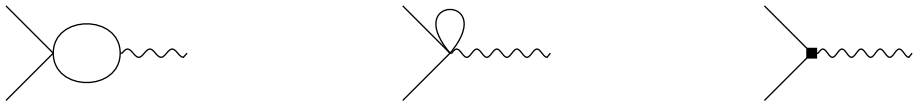

Figure 5.6: The electromagnetic vertex function of a charged pion to one–loop order. The full square takes into account the contribution from the low–energy constants just as the tree contribution including the effect of the wave function renormalization. Diagrams of order $\mathcal{O}(e^3p)$ are discarded.

these diagrams is

$$A(s,t,u)_{\text{Born-type}} = e^2 \left\{ \left(\frac{u-t}{s} \left[F_V^\pi(s) \right]^2 \right) + \left(\frac{u-s}{t} \left[F_V^\pi(t) \right]^2 \right) \right\} . \tag{5.46}$$

∗ Self–Energy Correction
The last contribution comes from the self–energy correction described by the diagram in Fig. 5.7. The scattering amplitude for this contribution is

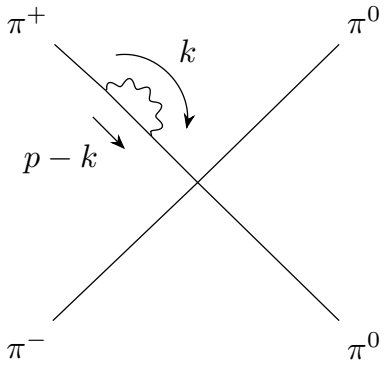

Figure 5.7: Self–energy correction diagram for the $\pi^+\pi^- \to \pi^0\pi^0$–scattering amplitude

$$A(s,t,u)_{\text{SE}} = 4e^2 \frac{s+t-2M_{\pi^0}^2}{F^2} J_{\pm\gamma}(p^2) . \tag{5.47}$$

It is important to underline the fact that, by using the parametrization in Eq. (5.27), we get rid of the contribution from the diagram in Fig. 5.8 since in the expanded Lagrangian there is any term which represents the $4\pi\gamma$ vertex. This diagram has to be taken into account if we consider the exponential parametrization of $U(x)$ (Eq. (4.36) but in the $N_f = 2$ case).

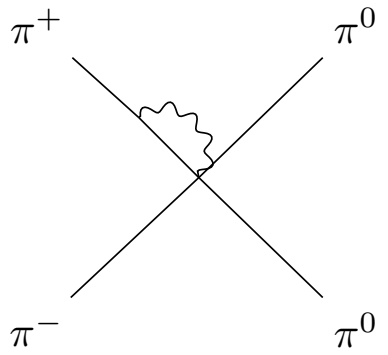

Figure 5.8: $4\pi\gamma$ vertex diagram for the $\pi^+\pi^- \to \pi^+\pi^-$–scattering amplitude

Before giving the final result for the total scattering amplitude, we want to put the attention to an important feature of the $\pi\pi$–scattering at 1–loop. From the detailed analysis just shown it is evident that the contributing diagrams can be separated in two well–defined groups: a contribution which accounts for the pion mass difference, i.e., $M_\pi \neq M_{\pi^0}$, and electromagnetic integration diagrams involving virtual photons. This clear separation turns out to be important for the dispersive analysis of the isospin–breaking effects in the $\pi\pi$–scattering amplitude (see Chs. 6–8) since it allows to ease the study by treating separately

the effects due to the pion mass difference and the one due to virtual and real photons.

5.5.3 Total $\pi^+\pi^- \to \pi^+\pi^-$ Scattering Amplitude

Now that we have all the contributions we can add them all and simplify them. We need to substitute the explicit expression of the space–time dimension d in terms of ϵ

$$\begin{aligned} d &= 4 - 2\epsilon \,, \\ \frac{1}{d-1} &= \frac{1}{3}\left(1 + \frac{2}{3}\epsilon + \frac{4}{9}\epsilon^2\right) \,, \end{aligned} \tag{5.48}$$

and, in order to obtain a finite amplitude, i.e., finite for $\epsilon \to 0$, the constants l_i and k_i of the Lagrangian $\mathcal{L}^{(4)}$ need to be renormalized such that

$$\ell_i^r(\mu^2) = \frac{\gamma_i}{32\pi^2}\left(\bar{\ell}_i + \ln\frac{M_{\pi^\pm}^2}{\mu^2}\right) \,, \tag{5.49}$$

$$k_i^r(\mu^2) = \frac{\sigma_i}{32\pi^2}\left(\bar{k}_i + \ln\frac{M_{\pi^\pm}^2}{\mu^2}\right) \,. \tag{5.50}$$

Moreover we have to consider the correction of $\mathcal{O}(e^2)$ to the mass of the charged pion which are given by the expression of $M_{\pi^\pm}^2$ at NLO:

$$\begin{aligned} M_{\pi^\pm}^2 =& 2\hat{m}B\left\{1 + \frac{e^2}{4\pi^2} + \frac{2M_{\pi^0}^2}{F^2}\ell_3^r(\mu) + e^2\mathcal{K}_{\pi^\pm}^r(\mu) + \frac{M_{\pi^0}^2}{32\pi^2F^2}\ln\frac{M_{\pi^0}^2}{\mu^2}\right\} \\ &+ 2e^2F^2\left\{Z\left(1 + \frac{e^2}{4\pi^2}\right) + e^2\mathcal{K}'^r_{\pi^\pm}(\mu) - (3+4Z)\frac{M_{\pi^\pm}^2}{32\pi^2F^2}\ln\frac{M_{\pi^\pm}^2}{\mu^2}\right\} \\ &- \frac{8}{3}B(m_d - m_u)e^2k_7 \,, \end{aligned} \tag{5.51}$$

with

$$\begin{aligned} \mathcal{K}_{\pi^\pm}^r &= -\frac{20}{9}\left[k_1^r + k_2^r - k_5^r - \frac{1}{5}\left(23k_6^r + k_7 + 18k_8^r\right)\right] \,, \\ \mathcal{K}'^r_{\pi^\pm} &= -\frac{10}{9}\left[2Z(k_1^r + k_2^r) - \frac{1}{2}k_{13}^r - k_{14}^r\right] \,. \end{aligned} \tag{5.52}$$

The final amplitude for the $\pi^+\pi^- \to \pi^+\pi^-$ scattering process is conveniently written in the following $s \leftrightarrow t$ symmetric decomposition [199]

$$\begin{aligned} A^{+-;+-}(s,t,u) = \Bigg\{ &\frac{s - M_{\pi^0}^2}{F^2} + B^{+-;+-}(s,t,u) + C^{+-;+-}(s,t,u) \\ &+ e^2\left(\frac{u-t}{s}\left[F_V^\pi(s)\right]^2\right)\Bigg\} + \{s \leftrightarrow t\} \,, \end{aligned}$$

where $B^{+-;+-}(s,t,u)$ collects the unitarity pieces arising from the diagrams of type drawn in Fig. 5.1 and Fig. 5.4:

$$B^{+-;+-}(s,t,u) = \frac{1}{2F^4}\left(s - M_{\pi^0}^2\right)^2\bar{J}_{00}(s)$$

$$
\begin{aligned}
&+\frac{1}{F^4}\left[\frac{s^2}{4}-\frac{1}{12}(u-t)(s-4M_{\pi^\pm}^2)+2s\Delta_\pi+4\Delta_\pi^2\right]\bar{J}_{+-}(s)\\
&+\frac{1}{4F^4}(u-2M_{\pi^\pm}^2-2\Delta_\pi)(u-2M_{\pi^\pm}^2-2\Delta_\pi-4e^2F^2)\bar{J}_{+-}(u)\\
&+\frac{2e^2}{F^2}(u-2M_{\pi^\pm}^2-2\Delta_\pi)\left[2(s-2M_{\pi^\pm}^2)G_{+-\gamma}(s)-(u-2M_{\pi^\pm}^2)G_{+-\gamma}(u)\right]\\
&-\frac{e^2}{F^2}\left[s+4\Delta_\pi-4(s-2M_{\pi^\pm}^2)\left(\frac{t-u}{t+u}\right)\right]\bar{J}_{+-}(s)\,. \qquad (5.53)
\end{aligned}
$$

The function $C^{+-;+-}(s,t,u)$ represents the contributions from tadpoles as well as from the strong [147, 148] and electromagnetic [198] low–energy constants

$$
\begin{aligned}
C^{+-;+-}(s,t,u)=&\frac{s-M_{\pi^0}^2}{F^2}\frac{e^2}{32\pi^2}\left[-18-8\left(1+\ln\frac{m_\gamma^2}{M_{\pi^\pm}^2}\right)+\frac{1}{2}(\mathcal{K}^{+-;+-}-\mathcal{K}^{+-;+-})\right]\\
&+\frac{e^2M_{\pi^0}^2}{32\pi^2F^2}\left[10+\frac{1}{2}(\mathcal{K}^{+-;+-}+\mathcal{K}^{+-;+-})\right]-\frac{e^2}{2\pi^2F^2}(s-2M_{\pi^\pm}^2)\left(\frac{t-u}{t+u}\right)\\
&+\frac{1}{48\pi^2F^4}\left[(s-2M_{\pi^\pm}^2)^2(\bar{l}_1+\bar{l}_2)+(u-2M_{\pi^\pm}^2)^2\bar{l}_2\right]-\frac{M_{\pi^0}^4}{32\pi^2F^4}\bar{l}_3 \qquad (5.54)\\
&+\frac{1}{16\pi^2F^4}\left(-\frac{5}{18}u^2-\frac{13}{18}s^2+\frac{2}{3}uM_{\pi^0}^2+\frac{19}{6}u\Delta_\pi+\frac{5}{18}M_{\pi^0}^4-\frac{58}{9}M_{\pi^0}^2\Delta_\pi\right)\\
&-\frac{1}{96\pi^2F^4}\frac{\Delta_\pi}{M_{\pi^0}^2}\left(-3s^2+16sM_{\pi^0}^2+2uM_{\pi^0}^2-23M_{\pi^0}^4\right)\,,
\end{aligned}
$$

where all the logarithms of the pion mass ratio are expanded as

$$
\ln\frac{M_{\pi^\pm}^2}{M_{\pi^0}^2}=\frac{\Delta_\pi}{M_{\pi^0}^2}+\cdots\,, \qquad (5.55)
$$

and

$$
\begin{aligned}
\mathcal{K}^{+-;+-}&=\left(3+\frac{4Z}{9}\right)\bar{k}_1-\frac{40Z}{9}\bar{k}_2-9\bar{k}_3+4Z\bar{k}_4+4(1+8Z)\bar{k}_6+2(1-8Z)\bar{k}_8\,,\\
\mathcal{K}^{++;++}&=-\left(3+\frac{4Z}{9}\right)\bar{k}_1-\frac{248Z}{9}\bar{k}_2+9\bar{k}_3-20Z\bar{k}_4+4(1+8Z)\bar{k}_6+2(1-8Z)\bar{k}_8\,. \qquad (5.56)
\end{aligned}
$$

Chapter 6

Isospin–breaking effects due to the pion mass difference in $\pi\pi$ scattering

In the previous chapter we computed in detail the radiative corrections to $\pi\pi$ scattering in the chiral representation. Now we want to evaluate isospin–breaking effects with the model–independent dispersive approach, i.e., by means of Roy equations. In particular, we will compute radiative corrections due to the charged–neutral pion mass difference, which actually belong to the broad class of effects generated by virtual photon exchanges, but which is well–defined on its own and can be treated separately from all the others.

6.1 Dispersive representation of $\pi\pi$ scattering in the isospin limit

As we showed in Eq. (5.15), the $\pi\pi$ scattering amplitude in the isospin limit and in the charge basis can be written in terms of the single isospin–invariant amplitude $A(s,t,u)$. For small values of s and t, the dominant contribution comes from the S– and P–waves such that the isospin–invariant $\pi\pi$ scattering amplitude can be split in a contributions generated by the imaginary parts of the S– and P–waves below a certain energy $\sqrt{s_2} = 2$ GeV and the rest:

$$A(s,t,u) = A(s,t,u)_{SP} + A(s,t,u)_d \; . \tag{6.1}$$

At energies below the upper limit of validity of the Roy equations, $s_1 = 68M_\pi^2$, the background amplitude $A(s,t,u)_d$, which collects the contribution of the imaginary parts of higher waves as well as of high energies from S– and P–waves, can be well described by a polynomial. Given the nature of this part of the amplitude, we expect it to be little sensitive to the pion mass difference and we will therefore keep it unchanged. As our result will show, although a sensitivity to this mass difference is visible, its size is small compared to the uncertainties with which the background amplitude is currently known.

The amplitude $A(s,t,u)_{SP}$ can be expressed in terms of three functions of a single variable:

$$\begin{aligned} A(s,t,u)_{SP} &= 32\pi \left\{ \frac{1}{3}W^0(s) + \frac{3}{2}(s-u)W^1(t) + \frac{3}{2}(s-t)W^1(u) \right. \\ &\quad \left. + \frac{1}{2}W^2(t) + \frac{1}{2}W^2(u) - \frac{1}{3}W^2(s) \right\} \; , \end{aligned} \tag{6.2}$$

where the functions $W^0(s)$, $W^1(s)$, $W^2(s)$ have only a right–hand cut and admit a simple dispersive representation in terms of the imaginary parts of the S– and P–waves as well as by the two S–wave

scattering lengths a_0^0, a_0^2:

$$\begin{aligned} W^0(s) &= \frac{a_0^0\, s}{4M_\pi^2} + \frac{s(s-4M_\pi^2)}{\pi}\int_{4M_\pi^2}^{s_2} \mathrm{d}s'\, \frac{\mathrm{Im}\, t_0^0(s')}{s'(s'-4M_\pi^2)(s'-s)}\ , \\ W^1(s) &= \frac{s}{\pi}\int_{4M_\pi^2}^{s_2} \mathrm{d}s'\, \frac{\mathrm{Im}\, t_1^1(s')}{s'(s'-4M_\pi^2)(s'-s)}\ , \\ W^2(s) &= \frac{a_0^2\, s}{4M_\pi^2} + \frac{s(s-4M_\pi^2)}{\pi}\int_{4M_\pi^2}^{s_2} \mathrm{d}s'\, \frac{\mathrm{Im}\, t_0^2(s')}{s'(s'-4M_\pi^2)(s'-s)}\ . \end{aligned} \tag{6.3}$$

This representation is valid in the isospin limit, where the imaginary parts have been determined as a solution of the Roy equations below s_1, supplemented by phenomenological input between s_1 and s_2.

The representations of the $\pi\pi$ scattering amplitudes T^n, T^c and T^x in Eq. (5.15), as well as the ones arising from crossing symmetry T^{++} and T^{+0} in Eq. (5.10), inherit from Eq. (6.1) the splitting between the S– and P–waves and the background amplitudes:

$$T^k(s,t,u) = T^k_{SP}(s,t,u) + T^k_d(s,t,u)\ , \tag{6.4}$$

with $k = n, c, x, ++, +0$. As argued above, only the amplitude T^k_{SP} is expected to be sensitive to the pion mass difference, and we will concentrate on this in the following.

6.2 Effects due to $M_\pi - M_{\pi^0}$

In the chiral expansion, taking into account the effects due to the pion mass difference is straightforward, but doing this for the $\pi\pi$ interaction in a dispersive framework that extends beyond the chiral regime is significantly more involved. We will now describe a fully dispersive treatment of these effects, with the approximation of considering only up to two pions intermediate states.

Away from the isospin limit, the Roy equations take a very different form since different processes get contributions from different intermediate states in each channel. Even when considering only S– and P–waves, instead of coupled integral equations for three different partial waves, one ends up with coupled integral equations for seven different partial waves (of the five different channels in Eqs. (5.15) and (5.10), only T^c and T^{+0} admit a P–wave).

To estimate the effect in the region below s_1, we proceed as follows. First, we concentrate only on the T^k_{SP} amplitudes and insert the expression in Eq. (6.2) of A_{SP} in terms of single–variable functions. This provides a dispersive representation of the physical amplitudes, but still in the isospin limit. As a next step, we express the imaginary parts of the fixed–isospin partial waves appearing in the definition of the W^I functions in Eq. (6.3) in terms of the imaginary parts of the physical channels and correspondingly define new single–variable functions labeled accordingly. In the following, we detail this procedure for each amplitude.

The $\pi^0\pi^0 \to \pi^0\pi^0$ amplitude: Let us consider first the T^n amplitude, which is completely crossing–symmetric in the three Mandelstam variables, i.e., in each channel, the same intermediate states, $\pi^0\pi^0$ or $\pi^+\pi^-$, are possible and with the same weight. Doing the steps outlined above, one ends up with the following representation:

$$T^n_{SP}(s,t,u) = 32\pi\left(W_S^{n,00}(s) + W_S^{n,+-}(s) + (s\leftrightarrow t) + (s\leftrightarrow u)\right)\ , \tag{6.5}$$

with

$$\begin{aligned} W_S^{n,00}(s) &= \frac{a_n^{00}\, s}{4M_{\pi^0}^2} + \frac{s(s-4M_{\pi^0}^2)}{\pi}\int_{4M_{\pi^0}^2}^{s_1} \mathrm{d}s' \frac{\mathrm{Im}\, t_S^{n,00}(s')}{s'(s'-4M_{\pi^0}^2)(s'-s)} \,, \\ W_S^{n,+-}(s) &= \frac{s(s-4M_{\pi^0}^2)}{\pi}\int_{4M_\pi^2}^{s_1} \mathrm{d}s' \frac{\mathrm{Im}\, t_S^{n,+-}(s')}{s'(s'-4M_{\pi^0}^2)(s'-s)} \,, \end{aligned} \tag{6.6}$$

where M_π and M_{π^0} denote the charged– and neutral–pion mass, respectively, and the superscripts 00 and $+-$ in the W–functions indicate the charges of the intermediate pions contributing to the imaginary part in the unitarity relation.

The $\pi^+\pi^+ \to \pi^+\pi^+$ amplitude: For this amplitude, the P–wave is again absent in the s channel, but allowed in the t and u channels. We, therefore, need to define the scattering angle (or the cosine thereof, $z_{t,u}$) in the t or u center–of–mass frame:

$$\begin{aligned} s = \frac{1}{2}(t-4M_\pi^2)(z_t-1), \quad u = \frac{1}{2}(t-4M_\pi^2)(-z_t-1) \,, \\ z_t = \frac{s-u}{t-4M_\pi^2} \,. \end{aligned} \tag{6.7}$$

The analogous expression to (6.2) for the T^{++} amplitude reads

$$\begin{aligned} T_{SP}^{++}(s,t,u) &= 32\pi\Big(W_S^{++}(s) + W_S^{c,00}(t) + W_S^{c,+-}(t) + W_S^{c,00}(u) + W_S^{c,+-}(u) \\ &\quad + (u-s)W_P^{c,+-}(t) + (t-s)W_P^{c,+-}(u)\Big) \,, \end{aligned} \tag{6.8}$$

where

$$\begin{aligned} W_S^{++}(s) &= \frac{a^{++}\, s}{4M_\pi^2} + \frac{s(s-4M_\pi^2)}{\pi}\int_{4M_\pi^2}^{s_1} \mathrm{d}s' \frac{\mathrm{Im}\, t_S^{++}(s')}{s'(s'-4M_\pi^2)(s'-s)} \,, \\ W_S^{c,+-}(s) &= \frac{a_c^{+-}\, s}{4M_\pi^2} + \frac{s(s-4M_\pi^2)}{\pi}\int_{4M_\pi^2}^{s_1} \mathrm{d}s' \frac{\mathrm{Im}\, t_S^{c,+-}(s')}{s'(s'-4M_\pi^2)(s'-s)} \,, \\ W_S^{c,00}(s) &= \frac{s(s-4M_\pi^2)}{\pi}\int_{4M_{\pi^0}^2}^{s_1} \mathrm{d}s' \frac{\mathrm{Im}\, t_S^{c,00}(s')}{s'(s'-4M_\pi^2)(s'-s)} \,, \\ W_P^{c,+-}(s) &= \frac{s}{\pi}\int_{4M_\pi^2}^{s_1} \mathrm{d}s' \frac{3\mathrm{Im}\, t_P^{c,+-}(s')}{s'(s'-4M_\pi^2)(s'-s)} \,. \end{aligned} \tag{6.9}$$

Via the crossing relation in Eq. (5.10), Eq. (6.8) also provides a representation for T^c.

The $\pi^+\pi^- \to \pi^0\pi^0$ amplitude: For this amplitude, there is no P–wave in the s channel, because of the two identical particles in the final state, but a P–wave is present in the t and u channels, for the crossed process $\pi^+\pi^0 \to \pi^+\pi^0$. In the t channel, for example, the scattering angle can be expressed in terms of the Mandelstam variables as follows:

$$z_t = \frac{t(s-u) + \Delta_\pi^2}{\lambda(t, M_\pi^2, M_{\pi^0}^2)} \,, \quad \text{with} \quad \Delta_\pi := M_\pi^2 - M_{\pi^0}^2 \,, \tag{6.10}$$

with $\lambda(a,b,c) = a^2 + b^2 + c^2 - 2(a\,b + b\,c + c\,a)$ the Källen function.

We can then derive the expression of the T^x_{SP} amplitude in terms of single–variable functions:

$$\begin{aligned} T^x_{SP}(s,t,u) &= 32\pi \left[W_S^{x,+-}(s) + W_{x,S}^{00}(s) + W_S^{+0}(t) + W_S^{+0}(u) \right. \\ &\quad \left. + \left(t(s-u) + \Delta_\pi^2\right)\, W_P^{+0}(t) + \left(u(s-t) + \Delta_\pi^2\right) W_P^{+0}(u) \right] \,, \end{aligned} \tag{6.11}$$

which are defined as

$$\begin{aligned} W_S^{x,+-}(s) &= \frac{a_1\, s}{4M_\pi^2} + \frac{s(s-4M_\pi^2)}{\pi} \int_{4M_\pi^2}^{s_1} \mathrm{d}s' \frac{\mathrm{Im}\, t_{x,S}^{+-}(s')}{s'(s'-4M_\pi^2)(s'-s)} \,, \\ W_S^{x,00}(s) &= \frac{s(s-4M_\pi^2)}{\pi} \int_{4M_{\pi^0}^2}^{s_1} \mathrm{d}s' \frac{\mathrm{Im}\, t_{x,S}^{00}(s')}{s'(s'-4M_\pi^2)(s'-s)} \,, \\ W_S^{+0}(s) &= \frac{a_2\, s}{4\bar{M}_\pi^2} + \frac{s(s-4\bar{M}_\pi^2)}{\pi} \int_{4\bar{M}_\pi^2}^{s_1} \mathrm{d}s' \frac{\mathrm{Im}\, t_S^{+0}(s')}{s'(s'-4\bar{M}_\pi^2)(s'-s)} \,, \\ W_P^{+0}(s) &= \frac{1}{\pi} \int_{4\bar{M}_\pi^2}^{s_1} \mathrm{d}s' \frac{3\mathrm{Im}\, t_P^{+0}(s')}{\lambda(s', M_\pi^2, M_{\pi^0}^2)(s'-s)} \,, \end{aligned} \tag{6.12}$$

where $\bar{M}_\pi = (M_\pi + M_{\pi^0})/2$ and the two scattering–length–like quantities $a_{1,2}$ are related to the true scattering lengths by

$$a_1 = a_x^{+-} + 2\epsilon_\pi a_2 - 8\Delta_\pi \left[\bar{M}_\pi^2 (1+\epsilon_\pi) f_s^{+0}(-\Delta_\pi) - M_\pi^2 f_p^{+0}(-\Delta_\pi) \right] , \tag{6.13}$$

$$a_2 = \frac{a_c^{+0}}{1+\epsilon_\pi^2} + \Delta_\pi^2 \left(\frac{1-\epsilon_\pi^2}{1+\epsilon_\pi^2} \right) f_s^{+0}(\epsilon_\pi \Delta_\pi), \tag{6.14}$$

and where we have introduced $\epsilon_\pi := \frac{\Delta_\pi}{4M_\pi^2}$ and

$$f_s^{+0}(s) = \frac{1}{\pi} \int_{4\bar{M}_\pi^2}^{\infty} \mathrm{d}s' \frac{\mathrm{Im}\, t_S^{+0}(s')}{s'(s'-4\bar{M}_\pi^2)(s'-s)} \,, \tag{6.15}$$

$$f_p^{+0}(s) = \frac{1}{\pi} \int_{4\bar{M}_\pi^2}^{\infty} \mathrm{d}s' \frac{3\mathrm{Im}\, t_P^{+0}(s')}{\lambda(s', M_\pi^2, M_{\pi^0}^2)(s'-s)} \,. \tag{6.16}$$

The introduction of the parameters a_1 and a_2 is necessary in order to ensure that

$$W_S^{x,+-}(4M_\pi^2) = a_1 \quad \text{and} \quad W_S^{+0}(4\bar{M}_\pi^2) = a_2 \,. \tag{6.17}$$

while

$$t_S^x(4M_\pi^2) = a_x^{+-} \quad \text{and} \quad t_S^{+0}(4\bar{M}_\pi^2) = a_c^{+0} \,. \tag{6.18}$$

6.3 Unitarity relations for $\Delta M_\pi \neq 0$

We now want to estimate the effect of the pion mass difference in each physical channel and shift M_{π^0} to its physical value. This affects the physical ranges of the kinematic variables and, correspondingly, the thresholds of the various processes. Moreover, it is also reflected in the analytic structure of the T^k amplitudes for which, in addition to the branch cut at $4M_\pi^2$ in the s channel, a second one develops at $4M_{\pi^0}^2$, or at $4\bar{M_\pi}^2$ in the t channel, as has been discussed in detail in [200]. Indeed, the expressions obtained above do show these different cuts already, provided one takes for M_{π^0} its physical value.

Nevertheless, in order to solve the integral equations derived in Sec. 6.2, there is still one piece of

information missing: the expression of the imaginary parts of the amplitudes that appear in the dispersive integrals above, as fixed by unitarity. For the S–wave of the $T^{n,x,c}$ amplitudes, we have a coupled–channel problem in the s channel, where the unitarity relation is expressed at best in matrix form [200]:

$$\begin{aligned} \mathrm{Im}T_S(s) &= T_S(s)\Sigma(s)T_S^*(s)\,, \quad \text{with } T_S = \begin{pmatrix} t_S^n(s) & -t_S^x(s) \\ -t_S^x(s) & t_S^c(s) \end{pmatrix}\,, \\ \Sigma(s) &= \begin{pmatrix} \sigma_0(s)\theta(s-4M_{\pi^0}^2) & 0 \\ 0 & 2\sigma(s)\theta(s-4M_\pi^2) \end{pmatrix}\,, \end{aligned} \tag{6.19}$$

with $\sigma(s)=\sqrt{1-\dfrac{4M_\pi^2}{s}}$ and $\sigma_0(s)=\sqrt{1-\dfrac{4M_{\pi^0}^2}{s}}$ the phase–space factors for the charged and neutral pions, respectively.

From this, one can read off the imaginary parts for each of the components (to simplify the notation, we absorb θ–functions in the definition of the σ's):

$$\begin{aligned} \mathrm{Im}\, t_S^n(s) &= \sigma_0(s)|t_S^n(s)|^2 + 2\sigma(s)|t_S^x(s)|^2\,, \\ \mathrm{Im}\, t_S^x(s) &= \sigma_0(s)t_S^n(s)t_S^x(s)^* + 2\sigma(s)t_S^x(s)t_S^c(s)^*\,, \\ \mathrm{Im}\, t_S^c(s) &= \sigma_0(s)|t_S^x(s)|^2 + 2\sigma(s)|t_S^c(s)|^2\,. \end{aligned} \tag{6.20}$$

For the remaining partial waves of relevance here, considering only intermediate pion states, the unitarity relation takes the form of the standard optical theorem: $\mathrm{Im}t = \rho|t|^2$, with ρ the relevant phase space factor. In this way, we obtain the following expressions of the imaginary parts we need to insert in the dispersive integrals.

Amplitude T^n:

$$\mathrm{Im}\, t_S^{n,00}(s) = \sigma_0(s)\,|t_S^n(s)|^2\,, \qquad \mathrm{Im}\, t_S^{n,+-}(s) = 2\sigma(s)\,|t_S^x(s)|^2\,. \tag{6.21}$$

Amplitudes T^c and T^{++}:

$$\begin{aligned} \mathrm{Im}\, t_S^{c,00}(s) =& \sigma_0(s)\,|t_S^x(s)|^2\,, \quad \mathrm{Im}\, t_S^{c,+-}(s) = 2\sigma(s)\,|t_S^c(s)|^2\,, \\ \mathrm{Im}\, t_S^{++}(s) =& \sigma(s)\,\left|t_S^{++}(s)\right|^2\,, \quad \mathrm{Im}\, t_P^{c,+-}(s) = 2\sigma(s)\,|t_P^c(s)|^2\,. \end{aligned} \tag{6.22}$$

Amplitudes $\pi^+\pi^- \to \pi^0\pi^0$ and $\pi^+\pi^0 \to \pi^+\pi^0$:

$$\begin{aligned} \mathrm{Im}t_S^{x,+-}(s) =& 2\sigma(s)t_S^x(s)t_S^c(s)^*, \quad \mathrm{Im}\, t_S^{+0}(s) = \frac{2\,\lambda^{1/2}(s,M_\pi^2,M_{\pi^0}^2)}{s}\,\left|t_S^{+0}(s)\right|^2\,, \\ \mathrm{Im}t_S^{x,00}(s) =& \sigma_0(s)t_S^n(s)t_S^x(s)^*, \quad \mathrm{Im}\, t_P^{+0}(s) = \frac{2\,\lambda^{1/2}(s,M_\pi^2,M_{\pi^0}^2)}{s}\,\left|t_P^{+0}(s)\right|^2\,. \end{aligned} \tag{6.23}$$

6.4 Scattering–lengths: matching with χPT

A crucial step in the procedure just outlined is to provide input values for the subtraction constants, which are all expressed in terms of scattering lengths. Like in the isospin–limit case [25], they will be fixed by matching to χPT at low energy. The $\pi\pi$ scattering amplitudes in the presence of isospin breaking have been calculated in two papers: the amplitude T^x in [198] and later extended to T^c in [199] (the details of the computation of T^c were also worked out in Ch. 5 in this work). These two papers contain both the

effect of the pion–mass difference as well as the effects due to virtual photons, but in a form that allows them to be easily disentangled. Here, we will make this separation explicit while recasting the amplitude in a form that allows for an easy matching to our dispersive representation.

Let us start with the T^n amplitude: the χPT representation of the functions $W_S^{n,00}$ and $W_S^{n,+-}$ up to order p^4 reads:

$$\begin{aligned} W_S^{n,00}(s) &= \frac{s}{4M_{\pi^0}^2}\left[a_n^{00} + b_n^{00}\frac{(s-4M_{\pi^0}^2)}{M_\pi^2}\right] + \frac{1}{64\pi F_\pi^4} D_0^0\left[M_{\pi^0}^4\right](s)\,, \\ W_{n,S}^{+-}(s) &= \frac{1}{32\pi F_\pi^4} D^0\left[(x-M_{\pi^0}^2)^2\right](s)\,, \end{aligned} \tag{6.24}$$

where F_π is the pion decay constant, and a_n^{00} and b_n^{00} denote the scattering length and slope parameter, respectively, in the threshold expansion of the neutral amplitude. The function

$$D_i^j[p(x)](s) := \frac{s^2(s-4M_{\pi^j}^2)}{16\pi^2}\int_{4M_{\pi^i}^2}^\infty \mathrm{d}x \frac{\sigma_i(x)p(x)}{x^2(x-4M_{\pi^j}^2)(x-s)}\,, \quad \text{with} \quad i,j=0,\pm \tag{6.25}$$

is the triply–subtracted dispersive integral (twice at $s=0$ and once at $4M_{\pi^j}^2$ as indicated by the superscript), where the discontinuity is given by the polynomial $p(x)$ multiplied by the two–pion phase space $\sigma_i(s)$. Note that, in the following, the sub– and superscripts referring to charged pions will be omitted, i.e., $D[p] := D_\pm^\pm[p]$, $D^0[p] := D_\pm^0[p]$, and so on.

The explicit expression for the threshold parameters a_n^{00} and b_n^{00} are listed in App. D. Here, we show only the expanded results up to $\mathcal{O}(\delta_\pi^2)$ (after having verified that numerically this is a good approximation):

$$\begin{aligned} a_n^{00} =& \frac{M_\pi^2}{32\pi F_\pi^2}\Bigg\{1-\delta_\pi + \xi\Bigg[\left(4\bar\ell_1 + 8\bar\ell_2 - \frac{3}{2}\bar\ell_3 + 2\bar\ell_4\right)(1-\delta_\pi)^2 + \frac{13}{2} - 4\delta_\pi\left(1+\frac{\delta_\pi}{2}\right) \\ &+ \delta_\pi(1-\delta_\pi)\left(\frac{\bar k_{31}}{9} - \frac{10}{9}\bar k_2 - \bar k_4\right) - 9\pi\sqrt{\delta_\pi}\left(1-\frac{3}{2}\delta_\pi\right)\Bigg]\Bigg\}\,, \\ b_n^{00} =& \frac{M_\pi^2}{32\pi F_\pi^2}\,\xi\left[\frac{4}{3}(\bar\ell_1+2\bar\ell_2)(1-\delta_\pi) + \frac{1}{2} + \frac{1}{6}\delta_\pi(1+2\delta_\pi) - \frac{9\pi}{4}\sqrt{\delta_\pi}\left(1-\frac{\delta_\pi}{2}\right)\right]\,, \end{aligned} \tag{6.26}$$

where

$$\delta_\pi := \frac{\Delta_\pi}{M_\pi^2}\,, \quad \text{and} \quad \xi := \frac{M_\pi^2}{16\pi^2 F_\pi^2}\,. \tag{6.27}$$

The threshold parameters are expressed in terms of the mesonic ℓ_i and electromagnetic k_i low–energy constants (LECs) (see [198]), with k_{31} given by the combination

$$k_{31} = -\frac{5}{9}k_1 + k_3\,. \tag{6.28}$$

The renormalization of the LECs at one–loop order was studied in [198] and is given by

$$\ell_i = l_i^r(\mu) + \gamma_i\lambda\,, \quad k_i = k_i^r(\mu) + \sigma_i\lambda\,, \tag{6.29}$$

where γ_i and σ_i are the corresponding renormalization group β functions [198, 201], μ is the renormalization scale, and λ reads

$$\lambda = \frac{\mu^{d-4}}{32\pi^2}\left(\frac{2}{d-4} - \log(4\pi) + \gamma - 1\right)\,, \tag{6.30}$$

with γ the Euler–Mascheroni constant.

The $\bar{l}_i$ and $\bar{k}_i$ are defined from the renormalized LECs as

$$\ell_i^r = \frac{\gamma_i}{32\pi^2}\left(\bar{\ell}_i + \log\frac{M_\pi^2}{\mu^2}\right) , \quad k_i^r = \frac{\sigma_i}{32\pi^2}\left(\bar{k}_i + \log\frac{M_\pi^2}{\mu^2}\right) , \tag{6.31}$$

so that the combination $\bar{k}_{31}$ reads

$$\bar{k}_{31} := \frac{9}{4Z}\left[\left(3+\frac{4}{9}Z\right)\bar{k}_1 - 3\bar{k}_3\right] . \tag{6.32}$$

The constants σ_i renormalize both photon and pion–mass difference divergences, with the latter encoded in the factor

$$Z := \frac{\Delta_\pi}{2e^2F^2} , \tag{6.33}$$

and, for this work, the relevant σ_i values are

$$\sigma_1 = -\frac{27}{20} - \frac{1}{5}Z , \quad \sigma_2 = 2Z , \quad \sigma_3 = -\frac{3}{4} , \quad \sigma_4 = 2Z; \quad \sigma_6 = \frac{1}{4} + 2Z , \quad \sigma_8 = \frac{1}{8} - Z . \tag{6.34}$$

The combination k_{31} is defined such as $\sigma_{31} = Z/9$, implying that the three counterterms appearing in a_n^{00} in Eq. (6.26)—namely, k_2, k_4, and k_{31}—only renormalize effects due to the pion–mass difference. Of course this does not imply that also the finite parts only contain effects due to the pion mass difference—in other words, that the finite parts would vanish in the limit $Z \to 0$. This is an intrinsic ambiguity of the present calculation which cannot be resolved. However, the analysis presented here only concerns a part of the isospin–breaking corrections, and once all of them will be evaluated and combined in our final result, the ambiguity will disappear.

For the triply–subtracted integral in Eq. (6.25) to converge, the polynomial $p(x)$ has to be at most second order. This additional subtraction—one more than in Eq. (6.6)—is necessary because, in χPT , the discontinuities are valid only at low energy, where they are expanded in powers of momenta and take the form of second–degree polynomials (times the phase space). To achieve a proper matching, we must apply an additional subtraction to the general dispersive expressions in Eq. (6.6), thereby obtaining a sum rule for b_n^{00}. For a_n^{00}, the χPT representation provided here is an essential input to the dispersive approach.

For the T^{++} amplitude, we obtain the following expressions for the single–variable functions at $\mathcal{O}(p^4)$:

$$\begin{aligned}
W_S^{++}(s) =& \frac{s}{4M_\pi^2}\left[a^{++} + \left(b^{++} + c^{++}s\right)\frac{\left(s-4M_\pi^2\right)}{M_\pi^2}\right] + \frac{1}{128\pi F_\pi^4} D\left[(x-2M_\pi^2-2\Delta_\pi)^2\right](s) , \\
W_{c,S}^{+-}(s) =& \frac{s}{4M_\pi^2}\left[a_c^{+-} + \left(b_c^{+-} + c_c^{+-}s\right)\frac{\left(s-4M_\pi^2\right)}{M_\pi^2}\right] + \frac{1}{128\pi F_\pi^4} D\left[(x+4\Delta_\pi)^2\right](s) , \\
W_{c,S}^{00}(s) =& \frac{1}{64\pi F_\pi^4} D_0\left[(x-M_{\pi^0}^2)^2\right](s) , \qquad (6.35) \\
W_{c,P}^{+-}(s) =& -\frac{1}{384\pi F_\pi^4} D\left[(x-4M_\pi^2)^2\right](s) , \qquad (6.36)
\end{aligned}$$

together with the following ones for the expanded constants a, b, and c:

$$
\begin{aligned}
a^{++} =& -\frac{M_\pi^2}{16\pi F_\pi^2}\Bigg\{1-\delta_\pi-\xi\Bigg[\frac{4}{3}\left(\bar\ell_1+2\bar\ell_2\right)-\frac{1}{2}\left(\bar\ell_3+4\bar\ell_4\right)(1-\delta_\pi)^2 \\
&+\frac{1}{2}\left(1+3\delta_\pi+\frac{88}{9}\delta_\pi^2\right)-\delta_\pi(1-\delta_\pi)\left(\frac{\bar k_{31}}{9}-4\bar k_{32}+\frac{62}{9}\bar k_2+5\bar k_4\right)\Bigg]\Bigg\}\,, \\
b^{++} =& \frac{M_\pi^2}{48\pi F_\pi^2}\xi\left(4\bar\ell_2-\frac{23}{9}-4\delta_\pi+\delta_\pi^2\right)\,, \\
c^{++} =& -\frac{\xi}{864\pi F_\pi^2}\,, \\
\mathrm{Re}[a_c^{+-}] =& \frac{M_\pi^2}{16\pi F_\pi^2}\Bigg\{1+\delta_\pi+\xi\Bigg[3+\frac{4}{3}(\bar\ell_1+2\bar\ell_2)-\frac{1}{2}\bar\ell_3+2\bar\ell_4+\delta_\pi\left(2+\bar\ell_3\right)+\delta_\pi^2\left(\frac{62}{9}-\frac{1}{2}\bar\ell_3-2\bar\ell_4\right) \\
&+\delta_\pi\left(\frac{\bar k_{31}}{9}(1+\delta_\pi)+4\bar k_{32}(1-\delta_\pi)-\frac{2}{9}\bar k_2\left(5-31\delta_\pi\right)+\bar k_4(1+5\delta_\pi)\right)\Bigg]\Bigg\}\,, \\
\mathrm{Re}[b_c^{+-}] =& \frac{M_\pi^2}{24\pi F_\pi^2}\xi\left[\frac{73}{72}+\bar\ell_1+\bar\ell_2+4\delta_\pi+\delta_\pi^2\right]\,, \\
c_c^{+-} =& \frac{\xi}{1728\pi F_\pi^2}\,,
\end{aligned}
\tag{6.37}
$$

where k_{32} is the combination,

$$
k_{32}:=k_3+2(k_6+k_8)\;\;\Rightarrow\;\;\bar k_{32}:=-\frac{1}{8Z}\left[3\bar k_3-2\left(1+8Z\right)\bar k_6-\left(1-8Z\right)\bar k_8\right]\,. \tag{6.38}
$$

The renormalization group β function for this combination is $\sigma_{32}=2Z$, ensuring once again that all LECs in Eq. (6.37) only absorb divergences proportional to the pion–mass difference. Note that Eq. (6.37) provides the exact expressions of a^{++}, b^{++}, c^{++}, and c_c^{+-}, while a_c^{+-} and b_c^{+-} are expanded up to $\mathcal{O}(\delta_\pi^2)$, with their exact expressions given in App. D for completeness (the difference between the two expressions is numerically irrelevant).

The amplitude T^x is more complicated because of the presence of particles with unequal masses in the t– and u–channels. However, an expansion in the pion–mass difference significantly simplifies the expressions for the subtraction constants while maintaining numerical accuracy. Below, we present the single–variable functions:

$$
\begin{aligned}
W_{x,S}^{+-}(s) &= \frac{s}{4M_\pi^2}\left[a_1+(b_1+c_1 s)\,\frac{\left(s-4M_\pi^2\right)}{M_\pi^2}\right]-\frac{1}{32\pi F_\pi^2}D\left[\left(\frac{s}{2}+2\delta_\pi\right)\left(s-M_{\pi^0}^2\right)\right](s)\,, \\
W_{x,S}^{00}(s) &= -\frac{1}{64\pi F_\pi^2}D_0\left[M_{\pi^0}^2\left(s-M_{\pi^0}^2\right)\right](s)\,, \\
W_S^{+0}(s) &= \frac{s}{4\bar M_\pi^2}\left[a_2+(b_2+c_2 s)\,\frac{\left(s-4\bar M_\pi^2\right)}{M_\pi^2}\right]-\frac{1}{128F_\pi^4}D_{+0}^{+0}\left[\left(s-2M_\pi^2\right)^2\right](s)\,, \\
W_P^{+0}(s) &= -\frac{\lambda(s,M_{\pi^0}^2,M_\pi^2)}{384F_\pi^4}\tilde J_{+0}^{(2)}(s)\,,
\end{aligned}
\tag{6.39}
$$

where $\tilde J_{+0}^{(2)}(s):=\dfrac{\bar J_{+0}(s)-s\bar J'_{+0}(0)}{s^2}$, which is regular at $s=0$.

The expanded subtraction constants are

$$
\mathrm{Re}[a_1]=-\frac{M_\pi^2}{32\pi F_\pi^2}\Bigg\{3+\frac{\delta_\pi}{4}(2+\delta_\pi)+\xi\Bigg[\frac{11}{2}+\frac{4}{3}(\bar\ell_1+2\bar\ell_2)-\frac{1}{2}\bar\ell_3+6\bar\ell_4
$$

$$
\begin{aligned}
&+\delta_\pi\left(\frac{247}{108}+2\bar{\ell}_1-\frac{4}{3}\bar{\ell}_2+\frac{3}{4}\bar{\ell}_3-5\bar{\ell}_4\right)-\delta_\pi^2\left(\frac{1309}{216}+\frac{\bar{\ell}_1}{3}+\frac{\bar{\ell}_3}{8}+\frac{\bar{\ell}_4}{2}\right)\\
&+\delta_\pi\left(\frac{\bar{k}_{31}}{18}\left(6+\delta_\pi\right)+\bar{k}_{32}(2-\delta_\pi)+\frac{\bar{k}_2}{9}\left(6+13\delta_\pi\right)+\bar{k}_4(2+\delta_\pi)\right)\Bigg]\Bigg\}\,,\\
\mathrm{Re}[b_1]=&-\frac{M_\pi^2}{96\pi F_\pi^2}\xi\left[\frac{119+72\bar{\ell}_1}{18}+\frac{38}{9}\delta_\pi-\frac{\delta_\pi^2}{5}\right]\,,\\
c_1=&-\frac{\xi}{288\pi F_\pi^2}\left(\frac{1}{3}+\frac{\delta_\pi}{6}+\frac{\delta_\pi^2}{10}\right),\\
a_2=&\frac{M_\pi^2}{32\pi F_\pi^2}\Bigg\{1-\delta_\pi\left(1+\frac{\delta_\pi}{16}\right)-\xi\Bigg[\frac{1}{2}+\frac{4}{3}(\bar{\ell}_1+2\bar{\ell}_2)-\frac{1}{2}\bar{\ell}_3-2\bar{\ell}_4\\
&-\delta_\pi\left(3+\frac{4}{3}(\bar{\ell}_1+2\bar{\ell}_2)-\bar{\ell}_3-4\bar{\ell}_4\right)+\frac{\delta_\pi^2}{12}\left(\frac{2669}{72}-\bar{\ell}_1+2\bar{\ell}_2-\frac{45}{8}(\bar{\ell}_3+4\bar{\ell}_4)\right)\\
&-\delta_\pi\left(1-\delta_\pi\right)\left(\frac{\bar{k}_{31}}{9}-2\bar{k}_{32}+\frac{26}{9}\bar{k}_2+2\bar{k}_4\right)\Bigg]\Bigg\}\,,\\
b_2=&\frac{M_\pi^2}{864\pi F_\pi^2}\xi\left[23-36\bar{\ell}_2+\delta_\pi\left(18\bar{\ell}_2+\frac{49}{2}\right)+\delta_\pi^2\frac{3}{16}\left(12\bar{\ell}_2-5\right)\right],\\
c_2=&\frac{\xi}{1728\pi F_\pi^2}\left(1-\frac{\delta_\pi^2}{80}\right)\,.
\end{aligned}
\tag{6.40}
$$

Note that, once again, all LECs in Eq. (6.40) solely renormalize divergences proportional to the pion–mass difference.

Chapter 7

Roy equations for $\Delta M_\pi \neq 0$

In this chapter we will solve the Roy equations including isospin–breaking effects due to the charged–neutral pion mass difference. We will first derive these equation by projecting onto partial waves the amplitudes defined in Sec. 6.2 and then we will give all the necessary ingredients as well as the strategy we adopted to solve them.

7.1 Derivation of the Roy equations for $\Delta M_\pi \neq 0$

Roy equations beyond the isospin limit can be obtained directly by projecting the single–variable decomposition of the pion–pion amplitudes, defined in Sec. 6.2, onto partial waves. This projection is defined by

$$t_J^k(s) = \frac{1}{64\pi}\int_{-1}^{1} \mathrm{d}z\, P_J(z)\, T^k(s,t(s,z),u(s,z))\ , \tag{7.1}$$

where k labels any of the $\pi\pi$ channels in the charge basis defined in Eqs. (5.9) and (5.10), J denotes the angular momentum, P_J stands for the Legendre polynomial of degree J, and z is the cosine of the scattering angle in the corresponding s channel center–of–mass frame.

For example, the S–wave projection of the neutral channel amplitude reads

$$t_S^n(s) = \frac{1}{64\pi}\int_{-1}^{1} \mathrm{d}z\, T^n(s,t(s,z),u(s,z))\ , \tag{7.2}$$

where in this case

$$t(s,z) = \frac{(s-s_{00})(z-1)}{2}\ , \quad u(s,z) = -\frac{(s-s_{00})(z+1)}{2}\ , \quad s_{00} = 4M_{\pi^0}^2\ . \tag{7.3}$$

Including explicitly the single–variable decomposition of the $\pi^0\pi^0 \to \pi^0\pi^0$ amplitude in Eq. (6.5), and performing the angular integration analytically, the neutral–channel S–wave can be recast as

$$t_S^n(s) = a_n^{00} + \int_{s_{00}}^{s_{+-}} \mathrm{d}s' K_n(s,s') \mathrm{Im} t_S^{n,00}(s') + \int_{s_{+-}}^{s_1} \mathrm{d}s' K_n(s,s') \left(\mathrm{Im} t_S^{n,00}(s') + \mathrm{Im} t_S^{n,+-}(s')\right) + d_S^n(s)\ , \tag{7.4}$$

where $s_{+-} = 4M_{\pi^\pm}^2$, $\mathrm{Im} t_S^{n,00}$ and $\mathrm{Im} t_S^{n,+-}$ are defined in Eq. (6.20), and d_S^n denotes the driving–term contribution, i.e., the partial–wave projection of the background integral

$$d_S^n(s) = \frac{1}{64\pi}\int_{-1}^{1} \mathrm{d}z\, T_d^n(s,t(s,z),u(s,z))\ , \tag{7.5}$$

accounting for the contribution of the imaginary part of higher $J > 1$ partial waves as well as of the S– and P–waves above s_1.

The kernel $K_n(s,s')$ is defined as

$$K_n(s,s') = \frac{1}{\pi}\left[\frac{1}{s'-s} - \frac{2}{s'} - \frac{1}{s'-s_{00}} + \frac{2}{s-s_{00}}\log\left(1+\frac{s-s_{00}}{s'}\right)\right] , \tag{7.6}$$

and encodes the whole analytic structure of the $\pi^0\pi^0 \to \pi^0\pi^0$ amplitude. The first term in brackets, $1/(s'-s)$, accounts for the right–hand cut discontinuity generated by both $\pi^0\pi^0$ and $\pi^+\pi^-$ intermediate states, while the log term includes the t and u channel discontinuities. Note that, on the one hand,

$$\lim_{s'\to s_{00}} K(s,s') = \frac{1}{\pi}\frac{1}{s'-s_{00}} + \mathcal{O}\left[(s'-s_{00})^0\right] , \tag{7.7}$$

which, together with the threshold behavior of $\mathrm{Im}t_S^n$, makes the integrand integrable around $s' \sim s_{00}$. On the other hand, in the $\lim s \to s_{00}$ the kernel behaves as $K(s,s') = \mathcal{O}(s-s_{00})$ and hence, the dispersion relation in Eq. (7.4) fulfills $t_S^n(s_{00}) = a_n^{00}$, i.e., the neutral–channel partial–wave amplitude is fixed from the neutral–channel scattering length, which in practice is taken from the χPT expression in Eq. (6.26).

It is also particularly illuminating to discuss the partial–wave projection of the charged–channel amplitude, which can be obtained from Eq. (6.8) using the crossing–symmetry relation in Eq. (5.10):

$$t_J^c(s) = \frac{1}{64\pi}\int_{-1}^{1} \mathrm{d}z\, P_J(z)\, T^{++}(u(s,z),t(s,z),s) , \tag{7.8}$$

where in this case, we have contributions from both S– and P–waves. Performing once again the partial–wave projection analytically, we get, for example, for the S–wave

$$\begin{aligned} t_S^c(s) =& \frac{1}{2}\left(1+\frac{s}{s_{+-}}\right)a_c^{+-} + \frac{1}{2}\left(1-\frac{s}{s_{+-}}\right)a^{++} + \int_{s_{00}}^{s_{+-}} \mathrm{d}s' K_{s,S}^{+-}(s',s)\,\mathrm{Im}t_S^{c,00}(s') \\ &+ \int_{s_{+-}}^{s_1} \mathrm{d}s' \left[K_{s,S}^{+-}(s',s)\left(\mathrm{Im}t_S^{c,00}(s') + \mathrm{Im}t_S^{c,+-}(s')\right) + K_{s,P}^{+-}(s',s)\,\mathrm{Im}t_P^{c,+-}(s')\right. \\ &\left. + K_{s,++}^{+-}(s',s)\,\mathrm{Im}t_S^{++}(s')\right] + d_S^c(s) , \end{aligned} \tag{7.9}$$

where $\mathrm{Im}t_S^{c,00}$, $\mathrm{Im}t_S^{c,+-}$, $\mathrm{Im}t_P^{c,+-}$, and $\mathrm{Im}t_S^{++}$ are defined in Eq. (6.22), $d_S^c(s)$ is the driving–term contribution, and the kernels read

$$\begin{aligned} K_{s,S}^{+-}(s',s) =& \frac{1}{\pi}\left[\frac{1}{s'-s} - \frac{s'+s+3(s'-s_{+-})}{2s'(s'-s_{+-})} + \frac{1}{s-s_{+-}}\ln\left(1+\frac{s-s_{+-}}{s'}\right)\right] , \\ K_{s,P}^{+-}(s',s) =& \frac{3}{\pi}\left[-\frac{3s+2s'-s_{+-}}{2s'(s'-s_{+-})} + \frac{2s+s'-s_{+-}}{(s-s_{+-})(s'-s_{+-})}\ln\left(1+\frac{s-s_{+-}}{s'}\right)\right] , \\ K_{s,++}^{+-}(s',s) =& \frac{1}{\pi}\left[\frac{s-2s'+s_{+-}}{2s'(s'-s_{+-})} + \frac{1}{s-s_{+-}}\ln\left(1+\frac{s-s_{+-}}{s'}\right)\right] . \end{aligned} \tag{7.10}$$

Once again, all kernels are suppressed in the $s \to s_{+-}$ limit and Eq. (7.9) satisfies $t_S^c(s_{+-}) = a_c^{+-}$. Nevertheless, due to the $K_{s,S}^{+-}(s',s)\,\mathrm{Im}t_S^{c,00}(s')$ contribution both in the first and second integrals in Eq. (7.9), the $s' \to s_{+-}$ limit must be studied carefully. On the one hand, close to the charged–pion

threshold the $K^{+-}_{s,S}$ kernel behaves as

$$\lim_{s'\to s_{+-}} K^{+-}_{s,S}(s',s) = -\frac{s+s_{+-}}{2\pi s_{+-}(s'-s_{+-})} + \mathcal{O}\left[(s'-s_{00})^0\right] \ .$$

On the other hand, $\mathrm{Im}t^{c,00}_S$ only vanishes at the neutral–pion threshold, hence leading to an end–point singularity. Although this singularity is integrable by construction, its numerical implementation requires special treatment. First, the $K^{+-}_{s,S}$ can be decomposed in terms of a regular $K^{+-,\,I}_{s,S}$ and singular $K^{+-,\,II}_{s,S}$ part as

$$\begin{aligned} K^{+-}_{s,S}(s',s) &= K^{+-,\,I}_{s,S}(s',s) + K^{+-,\,II}_{s,S}(s',s) \ , \\ K^{+-,\,I}_{s,S}(s',s) &= \frac{1}{\pi}\left[\frac{1}{s'-s} - \frac{2}{s'} + \frac{1}{s-s_{+-}}\ln\left(1+\frac{s-s_{+-}}{s'}\right)\right] \ , \\ K^{+-,\,II}_{s,S}(s',s) &= -\frac{(s+s_{+-})}{2\pi s'(s'-s_{+-})} \ , \end{aligned} \tag{7.11}$$

Second, the singular piece can be recast as

$$\begin{aligned} K^{+-,\,II}_{s,S}(s',s)\,\mathrm{Im}t^{c,00}_S(s') =& \frac{1}{\sigma_0(s_{+-})} K^{+-,\,II}_{s,S}(s',s)\left(\sigma_0(s_{+-})\,\mathrm{Im}t^{c,00}_S(s') - \sigma_0(s')\,\mathrm{Im}t^{c,00}_S(s_{+-})\right) \\ &+ \frac{\sigma_0(s')}{\sigma_0(s_{+-})} K^{+-,\,II}_{s,S}(s',s)\,\mathrm{Im}t^{c,00}_S(s_{+-}), \end{aligned} \tag{7.12}$$

so that the first term in Eq. (7.12) vanishes exactly in the $s' \to s_{+-}$ limit and can be computed using standard integration routines. Third, the second term in Eq. (7.12) can be integrated analytically. Namely,

$$\begin{aligned} &\int_{s_{00}}^{s_1} \mathrm{d}s' K^{+-,II}_{s,S}(s',s)\,\sigma_0(s') = \\ &\qquad \frac{2}{s_{+-}}\left\{\sigma_0(s_1) - \sigma_0(s_{+-})\left[\mathrm{arctanh}\left(\frac{s_{+-}-s_1\,(1-\sigma_0(s_1))}{s_{+-}\sigma_0(s_{+-})}\right) + \frac{1}{2}\log\left(\frac{1-\sigma_0(s_{+-})}{1+\sigma_0(s_{+-})}\right)\right]\right\} \ . \end{aligned} \tag{7.13}$$

Similar end–point singularities appear in the partial–wave projection of the T^{++}, T^x, and T^{+0} amplitudes, for which the very same procedure should be applied. Expressions of the Roy equations, including explicit expressions for all the kernels, for the remaining channels in the charge basis are collected in App. E.

7.2 Scattering lengths, imaginary parts and driving terms

In order to solve Roy equations, we must first fix all input quantities that appear in Eqs. (7.4) and (7.9), and App. E—namely, the values of the scattering lengths, the imaginary parts of S and P waves above s_1 and the driving terms. For the former, we will make use of the $\chi\mathrm{PT}_\gamma$ predictions obtained in Sec. 6.4. For the latter two, as already anticipated, we will use the same phenomenological estimates given in [25, 26] even though those references used these in an isospin–symmetric context. The reason for this strategy is two–fold. First, pion–mass difference effects are expected to be more relevant at low energies, where, on the one hand, the contribution of the $\pi^0\pi^0$, $\pi^+\pi^0$, and $\pi^+\pi^-$ threshold–shift effect is still sizable, and, on the other hand, the impact of the different masses and phase–space factors, entering both the kernels and the imaginary parts, is enhanced. Second, the Roy–equation solutions discussed in [25, 26] were obtained in the isospin limit, but the high–energy and higher partial–wave contributions were fixed from experimental data without attempting to remove isospin–breaking effects. In that context this was

motivated by the expectation that isospin–breaking effects are small at high energy. But all this means that, in the present context, we can just adopt those estimates without the need to apply any correction to them.

7.3 Partial–wave parameterizations for $\Delta M_\pi \neq 0$

The Roy equations beyond the isospin limit derived in Sec. 7.1 relate the real part of the $\pi\pi$ partial waves to an integral over their imaginary parts, which, in turn, are also related through the unitarity relations collected in Sec. 6.3, hence providing a coupled system of integral equations.

Partial waves are customarily expressed in terms of their phase shift and elasticity, i.e., the phase and modulus of the S–matrix element, respectively. In the isospin limit, the unitarity relations for the three isospin amplitudes $I = 0, 1, 2$ are diagonal, and $\pi\pi$ scattering remains elastic below the first inelastic threshold, which formally starts at the 4π threshold. Nevertheless, in practice, inelastic effects become experimentally noticeable only at higher energies [29] and $\pi\pi$ scattering can be considered elastic up to energies around 1 GeV[1]. Hence, in this elastic region, Roy equations translate into a coupled system of integral equations for the phase shifts. Above this energy, one also needs to include the elasticity, which, once again, is obtained from experimental data.

Beyond the isospin limit, one has to switch to the charge basis, which, as discussed in Sec. 6.3, no longer diagonalizes the unitarity relation in the case of the T^n, T^x and T^c S–waves, and requires introducing an additional internal $\pi\pi$ elasticity parameter along with a non–$\pi\pi$ inelasticity contribution. For the latter, we once again rely on the results in [25, 26], which, as extracted directly from data, already account for pion–mass difference effects. For the former, we will perform a coupled–channel analysis.

Thus, following the example in [24–26, 28, 202–204], to solve this system of equations we parameterize the phase shift at low energies in a suitable form, whose free parameters are obtained by minimizing the difference between the left– and right–hand side of Roy equations.

7.3.1 Elastic case

We will start with the $\pi^+\pi^+ \to \pi^+\pi^+$ S–wave, which in terms of its phase shift and elasticity is parameterized as

$$t_S^{++}(s) = \frac{\eta_S^{++}(s)\, \mathrm{e}^{2i\,\delta_S^{++}(s)} - 1}{2i\sigma(s)} \,. \tag{7.14}$$

For the elasticity η_S^{++}, we consider the isospin–limit results in [25, 26] so that $\eta_S^{++}(s) = \eta_0^2(s)$. In the case of the phase shift, we use

$$\delta_S^{++}(s) = \delta_0^2(s) \left(1 + \Delta_\pi \sum_{i=0}^{7} c_i^{++} \left(\frac{s - s_{+-}}{s_{+-}} \right)^i \right) \,, \tag{7.15}$$

i.e., it is parameterized in terms of the isospin–limit phase shift result plus a polynomial correction proportional to the pion–mass difference squared Δ_π.

At the charged–pion threshold s_{+-}, the parametrization in Eq. (7.15) must match the a^{++} scattering length, so that the c_0^{++} coefficient is fully determined by the relation

$$c_0^{++} = \frac{\Delta a^{++}}{a_{\mathrm{IL}}^{++} \Delta_\pi} \,, \tag{7.16}$$

[1] In the isospin limit, the S0–wave is elastic up to the $K\bar{K}$ threshold, the P–wave inelasticity starts quite slowly at the $\pi\omega$ threshold, and the S2–wave remains elastic up to energies around 1 GeV [28].

with $\Delta a^{++} = a^{++} - a^{++}_{\rm IL}$.

Additionally, to ensure a well–defined integrand, the parametrization in Eq. (7.15) and its first derivative at s_1, the maximum energy of validity of Roy equations, must match the isospin–limit results employed in the driving term. This imposes two additional constraints, allowing us to fix the values of the coefficients c_6^{++} and c_7^{++} as follows

$$\begin{aligned} c_6^{++} &= -\left(\frac{s_{+-}}{s_1 - s_{+-}}\right)^6 \sum_{k=0}^{5} (7-k)\, c_k^{++} \left(\frac{s_1 - s_{+-}}{s_{+-}}\right)^k , \\ c_7^{++} &= -\left(\frac{s_{+-}}{s_1 - s_{+-}}\right)^7 \sum_{k=0}^{6} c_k^{++} \left(\frac{s_1 - s_{+-}}{s_{+-}}\right)^k , \end{aligned} \tag{7.17}$$

leaving c_{1-5}^{++} as the only free parameters.

Similar constraints apply to the $\pi^+\pi^- \to \pi^+\pi^-$ P–wave, which we parameterize as

$$t_P^c(s) = \frac{\eta_P^c(s)\, \mathrm{e}^{2i\,\delta_P^c(s)} - 1}{4i\sigma(s)} , \tag{7.18}$$

with $\eta_P^c(s) = \eta_1^1(s)$ and $\delta_P^c(s)$

$$\delta_P^c(s) = \delta_1^1(s) \left(1 + \Delta_\pi \sum_{i=0}^{7} c_i^{c,P} \left(\frac{s - s_{+-}}{s_{+-}}\right)^i\right) , \tag{7.19}$$

where $c_0^{c,P}$ is now a free parameter, and $c_{6-7}^{c,P}$ are fixed by the matching conditions at s_1 analogously to Eq. (7.17).

The $\pi^+\pi^0 \to \pi^+\pi^0$ channel is slightly more involved since, in this case, the threshold opens at $s_{0+} = (M_{\pi^+} + M_{\pi^0})^2$. Starting with the S–wave, its parameterizations in terms of its phase shift and elasticity reads

$$t_S^{+0}(s) = \frac{\eta_S^{+0}(s)\, \mathrm{e}^{2i\,\delta_S^{+0}(s)} - 1}{4i\sigma_{+0}(s)} , \tag{7.20}$$

with $\sigma_{+0}(s) = \lambda^{1/2}(s, M_\pi^2, M_{\pi^0}^2)/s$. Once again, we assume that the elasticity is given by its isospin–limit value in [25, 26], and thus, we assume

$$\eta_S^{+0}(s) = \begin{cases} 1 & s \leq s_{+-}, \\ \eta_0^2(s) & s > s_{+-}. \end{cases} \tag{7.21}$$

The phase shift is parameterized in terms of the isospin–limit phase δ_0^2, which is, however, only defined for energies above the charged–charged threshold s_{+-}. To extend the isospin–limit phase down to the physical $\pi^+\pi^0$ threshold we use the kinematic map (see also [205])

$$\hat{s}(s) = \frac{s_1(s - s_{0+}) - s_{+-}(s - s_1)}{s_1 - s_{0+}} , \tag{7.22}$$

which ensures that $\hat{s}(s_{0+}) = s_{+-}$ and $\hat{s}(s_1) = s_1$.

Thus, in terms of this map, we parameterize the phase shift as

$$\delta_S^{+0}(s) = \delta_0^2(\hat{s}(s)) \left(1 + \Delta_\pi \sum_{i=0}^{7} c_i^{+0,S} \left(\frac{s - s_{0+}}{s_{0+}}\right)^i\right) . \tag{7.23}$$

In order to ensure that at s_{0+}, the parametrization in Eq. (7.23) coincides with the a_c^{+0} scattering length, the coefficient $c_0^{+0,S}$ is fixed to the value

$$c_0^{+0,S} = \frac{1}{\Delta_\pi}\left[\frac{s_{+-}}{s_{0+}}\sqrt{\frac{M_{\pi^0}}{M_\pi}}\sqrt{\frac{s_1-s_{0+}}{s_1-s_{+-}}}\left(1+\frac{\Delta a_c^{+0}}{a_{c,\mathrm{IL}}^{+0}}\right)-1\right], \tag{7.24}$$

with $\Delta a_c^{+0} = a_c^{+0} - a_{c,\mathrm{IL}}^{+0}$. In the same way, the matching conditions with the isospin–limit results in [25,26] impose the $c_6^{+0,S}$ and $c_7^{+0,S}$ to be

$$\begin{aligned}
c_6^{+0,S} =& -\left(\frac{s_{0+}}{s_1-s_{0+}}\right)^6\left[\sum_{k=0}^{5}(7-k)\,c_k^{+0,S}\left(\frac{s_1-s_{0+}}{s_{0+}}\right)^k\right.\\
&+\frac{i}{2\Delta_\pi\delta_0^2(s_1)}\left(7+(s_1-s_{0+})\,\frac{\delta_0^2(s_1)'}{\delta_0^2(s_1)}\right)\log\left(\frac{1+2i\sigma_{+0}(s_1)t_0^2(s_1)}{\eta_0^2(s_1)}\right)\\
&+\frac{(s_1-s_{0+})^2}{\Delta_\pi\delta_0^2(s_1)\,(1+2i\sigma_{+0}(s_1)t_0^2(s_1))}\left(\frac{s_1\Sigma_\pi-\Delta_\pi^2}{s_1^3(s_1-s_{+-})\sigma_{+0}(s_1)}\,t_0^2(s_1)+\frac{\sigma_{+0}(s_1)}{s_1-s_{+-}}t_0^2(s_1)'\right.\\
&\left.\left.+\left(\frac{7\delta_0^2(s_1)}{s_1-s_{0+}}+\frac{i\eta_0^2(s_1)'}{2\eta_0^2(s_1)}\right)\frac{\big(1+2i\sigma_{+0}(s_1)t_0^2(s_1)\big)}{s_1-s_{0+}}\right)\right],\\
c_7^{+0,S} =& -\left(\frac{s_{0+}}{s_1-s_{0+}}\right)^7\left[\sum_{k=0}^{6}c_k^{+0,S}\left(\frac{s_1-s_{0+}}{s_{0+}}\right)^k\right.\\
&\left.+\frac{1}{\Delta_\pi}\left(1+\frac{i}{2\delta_0^2(s_1)}\log\left(\frac{1+2i\sigma_{+0}(s_1)t_0^2(s_1)}{\eta_0^2(s_1)}\right)\right)\right],
\end{aligned} \tag{7.25}$$

where the prime denotes the derivative with respect to s evaluated at s_1. In this way, the new map implies that both coefficients become complex.

The $\pi^+\pi^0 \to \pi^+\pi^0$ P–wave is parameterized similarly. Namely,

$$t_P^{+0}(s) = \frac{\eta_P^{+0}(s)\,\mathrm{e}^{2i\,\delta_P^{+0}(s)}-1}{4i\sigma_{+0}(s)}, \tag{7.26}$$

with

$$\eta_P^{+0}(s) = \begin{cases} 1 & s \le s_{+-}, \\ \eta_1^1(s) & s > s_{+-}, \end{cases} \tag{7.27}$$

and

$$\delta_P^{+0}(s) = \delta_1^1(\hat{s}(s))\left(1+\Delta_\pi\sum_{i=0}^{7}c_i^{+0,P}\left(\frac{s-s_{0+}}{s_{0+}}\right)^i\right), \tag{7.28}$$

where $c_0^{+0,P}=0$ and the coefficients $c_6^{+0,P}$ and $c_7^{+0,P}$ are given by an expression equivalent to Eq. (7.25) but with the opposite log determination:

$$\begin{aligned}
c_6^{+0,P} =& -\left(\frac{s_{0+}}{s_1-s_{0+}}\right)^6\left[\sum_{k=0}^{5}(7-k)\,c_k^{+0,P}\left(\frac{s_1-s_{0+}}{s_{0+}}\right)^k\right.\\
&+\frac{i}{2\Delta_\pi\delta_1^1(s_1)}\left(7+(s_1-s_{0+})\,\frac{\delta_1^1(s_1)'}{\delta_1^1(s_1)}\right)\left\{\log\left(\frac{1+2i\sigma_{+0}(s_1)t_1^1(s_1)}{\eta_1^1(s_1)}\right)-2\pi i\right\}\\
&\left.+\frac{(s_1-s_{0+})^2}{\Delta_\pi\delta_1^1(s_1)\,(1+2i\sigma_{+0}(s_1)t_1^1(s_1))}\left(\frac{s_1\Sigma_\pi-\Delta_\pi^2}{s_1^3(s_1-s_{+-})\sigma_{+0}(s_1)}\,t_1^1(s_1)+\frac{\sigma_{+0}(s_1)}{s_1-s_{+-}}t_1^1(s_1)'\right.\right.
\end{aligned}$$

$$+\left(\frac{7\delta_1^1(s_1)}{s_1-s_{0+}}+\frac{i\eta_1^1(s_1)'}{2\eta_1^1(s_1)}\right)\frac{\left(1+2i\sigma_{+0}(s_1)t_1^1(s_1)\right)}{s_1-s_{0+}}\Bigg)\Bigg]\,,$$

$$c_7^{+0,P}=-\left(\frac{s_{0+}}{s_1-s_{0+}}\right)^7\left\{\sum_{k=0}^{6}c_k^{+0,P}\left(\frac{s_1-s_{0+}}{s_{0+}}\right)^k\right.$$

$$\left.+\frac{1}{\Delta_\pi}\left[1+\frac{i}{2\delta_1^1(s_1)}\left(\log\left(\frac{1+2i\sigma_{+0}(s_1)t_1^1(s_1)}{\eta_1^1(s_1)}\right)-2\pi i\right)\right]\right\}\,. \tag{7.29}$$

7.3.2 Coupled–channel case

As already discussed in Sec. 6.3, in the charge basis, the unitarity relation for the T^n, T^c, and T^x S–waves (see Eq. (6.20)) does not become diagonal. Therefore, these waves must be parameterized through a coupled–channel formalism. Labeling the $\pi^0\pi^0$ state as 1 and the $\pi^+\pi^-$ as 2, we can define a two–by–two inelastic S–matrix as:

$$S=\begin{pmatrix}\eta_S^n(s)\,\eta_S^x(s)\,\mathrm{e}^{2i\delta_S^n(s)} & i\sqrt{1-\eta_S^x(s)^2}\,\mathrm{e}^{i(\delta_S^n(s)+\delta_S^c(s)+\delta_S^x(s))}\\ i\sqrt{1-\eta_S^x(s)^2}\,\mathrm{e}^{i(\delta_S^n(s)+\delta_S^c(s)+\delta_S^x(s))} & \eta_S^c(s)\,\eta_S^x(s)\,\mathrm{e}^{2i\delta_S^c(s)}\end{pmatrix}\,, \tag{7.30}$$

with the T–matrix elements connected to the S–matrix by the standard coupled–channel relations

$$\begin{aligned}S_{11}(s)=S^n(s)=&1+2i\sigma_0(s)t_S^n(s)\,,\\ S_{12}(s)=S^x(s)=&2i\sqrt{2\sigma_0(s)\sigma(s)}t_S^x(s)\,,\\ S_{22}(s)=S^c(s)=&1+4i\sigma(s)t_S^c(s)\,.\end{aligned} \tag{7.31}$$

or, equivalently,

$$\begin{aligned}t_S^n(s)=&\frac{\eta_S^n(s)\,\eta_S^x(s)\,\mathrm{e}^{2i\delta_S^n(s)}-1}{2i\sigma_0(s)}\,,\\ t_S^x(s)=&\frac{\sqrt{1-\eta_S^x(s)^2}\,\mathrm{e}^{i(\delta_S^n(s)+\delta_S^c(s)+\delta_S^x(s))}}{2\sqrt{2\sigma_0(s)\sigma(s)}}\,,\\ t_S^c(s)=&\frac{\eta_S^c(s)\,\eta_S^x(s)\,\mathrm{e}^{2i\delta_S^c(s)}-1}{4i\sigma(s)}\,.\end{aligned} \tag{7.32}$$

Thus, this inelastic S–matrix parametrization is defined via three phase shifts and three inelasticities:

* δ_S^n and δ_S^c are the phase shifts of the neutral and charged channels, respectively.
* η_S^x denotes the $\pi^+\pi^-\to\pi^0\pi^0$ inelasticity, which, below the first non–$\pi\pi$ inelastic threshold, provides the pion–pion inelasticity in the charge basis.
* η_S^n and η_S^c account for the non–$\pi\pi$ inelastic contributions of the neutral and charged channels, respectively.
* δ_S^x provides charge–exchange inelastic phase shift.

The neutral phase shift is parameterized as

$$\delta_S^n(s)=\delta_S^{n,\mathrm{IL}}(\bar{s}(s))\left(1+\Delta_\pi\left[\sum_{i=0}^{7}c_i^n\left(\frac{s-s_{00}}{s_{00}}\right)^i+\sigma(s)\sum_{i=0}^{4}\tilde{c}_i^n\left(\frac{s-s_{00}}{s_{00}}\right)^i\right]\right)\,, \tag{7.33}$$

where, analogously to Eq. (7.22), the map

$$\bar{s}(s) = \frac{s_1(s-s_{00}) - s_{+-}(s-s_1)}{s_1 - s_{00}}\,, \tag{7.34}$$

extends the isospin–limit results below s_{+-}, and the coefficients $\tilde{c}_i^n$ allow the imaginary part of $t_S^n(s)$ to develop also at the charged pion threshold. In addition, as already noted in Sec. 6.3, the phase–space factor $\sigma(s)$ in Eq. (7.33) comes multiplied by $\theta(s-s_{+-})$, so it only contributes to $\delta_S^n(s)$ above s_{+-}.

The coefficient c_0^n is fixed by demanding that the t_n^S partial wave coincides at threshold with the isospin-breaking a_n^{00} scattering length from $\chi\mathrm{PT}_\gamma$. Namely, evaluating t_n^S in Eq. (7.32) at the neutral–pion threshold one gets

$$t_S^n(s_{00}) = a_{n,\mathrm{IL}}^{00}\,(1 + c_0^n\,\Delta_\pi)\,\sqrt{\frac{s_{00}\;(s_1 - s_{+-})}{s_{+-}\,(s_1 - s_{00})}}, \tag{7.35}$$

so that, defining $\Delta a_n^{00} = a_n^{00} - a_{n,\mathrm{IL}}^{00}$, one gets

$$c_0^n = \frac{1}{\Delta_\pi}\left[\sqrt{\frac{s_{+-}\,(s_1 - s_{00})}{s_{00}\;(s_1 - s_{+-})}}\left(1 + \frac{\Delta a_n^{00}}{a_{n,\mathrm{IL}}^{00}}\right) - 1\right]. \tag{7.36}$$

Finally, taking into account that $s_{+-} = s_{00} + 4\Delta_\pi$, at leading order in the pion–mass difference, this reduces to

$$c_0^n \simeq \frac{1}{\Delta_\pi}\frac{\Delta a_n^{00}}{a_{n,\mathrm{IL}}^{00}}. \tag{7.37}$$

Once again, the coefficients c_6^n and c_7^n are fixed by imposing a continuous and differentiable matching at s_1, similarly to Eq. (7.25). Expanding also at leading order in Δ_π, one gets

$$\begin{aligned}
c_6^n =& -\left(\frac{s_{+-}}{s_1 - s_{+-}}\right)^6 \left[\sum_{k=0}^{5}(7-k)\,c_k^n\left(\frac{s_1 - s_{+-}}{s_{+-}}\right)^k\right. \\
&+ \frac{\sigma(s_1)}{2}\sum_{k=0}^{4}\tilde{c}_k^n\left(\frac{s_1 - s_{+-}}{s_{+-}}\right)^k\left(14 - 2k - \frac{s_{+-}}{s_1}\right) \\
&+ \frac{i}{\delta_S^{n,\mathrm{IL}}(s_1)}\left\{\frac{4}{(s_1 - s_{+-})}\left(2 - \frac{1+\tilde{\eta}_S^x(s)^2}{S_n^{\mathrm{IL}}(s_1)}\right) - \left(\frac{1-\tilde{\eta}_S^x(s)^2}{2S_n^{\mathrm{IL}}(s_1)}\right)\frac{\tilde{\eta}_S^x(s)'}{\tilde{\eta}_S^x(s)} - \frac{1+\tilde{\eta}_S^x(s)^2}{2\,S_n^{\mathrm{IL}}(s_1)}\frac{\eta_S^n(s_1)'}{\eta_S^n(s_1)}\right., \\
&\left.\left. + \frac{\delta_S^{n,\mathrm{IL}}(s_1)'}{\delta_S^{n,\mathrm{IL}}(s_1)}\left(\left(1 - \frac{1+\tilde{\eta}_S^x(s)^2}{2\,S_n^{\mathrm{IL}}(s_1)}\right) - 4\,i\,\delta_S^{n,\mathrm{IL}}(s_1)\left(1 + \frac{1+\tilde{\eta}_S^x(s)^2}{4\,S_n^{\mathrm{IL}}(s_1)}\right)\right)\right\}\right], \\
c_7^n =& -\left(\frac{s_{+-}}{s_1 - s_{+-}}\right)^7 \left[\sum_{k=0}^{6}c_k^n\left(\frac{s_1 - s_{+-}}{s_{+-}}\right)^k + \sigma(s_1)\sum_{k=0}^{4}\tilde{c}_k^n\left(\frac{s_1 - s_{+-}}{s_{+-}}\right)^k\right. \\
&\left. + \frac{i}{(s_1 - s_{+-})\;\delta_S^{n,\mathrm{IL}}(s_1)}\left(1 - \frac{1+\tilde{\eta}_S^x(s)^2}{2\,S_n^{\mathrm{IL}}(s_1)}\right)\right],
\end{aligned} \tag{7.38}$$

where

$$\begin{aligned}
S_n^{\mathrm{IL}}(s) =& 1 + 2i\,\sigma(s)\left(t_0^0(s) + 2t_0^2(s)\right)/3\,, \\
\tilde{\eta}_S^x(s) =& \sqrt{1 - 8\,\sigma_0(s)\sigma(s)\;\left|\left(t_0^0(s) - t_0^2(s)\right)/3\right|^2},
\end{aligned} \tag{7.39}$$

and, once again, the prime denotes the derivative with respect to s evaluated at s_1.

In the same way, the charged S–wave phase shift is expressed as

$$\delta_S^c(s) = \delta_S^{c,\mathrm{IL}}(s)\left(1+\Delta_\pi\left[\sum_{i=0}^{7} c_i^{c,S}\left(\frac{s-s_{+-}}{s_{+-}}\right)^i + \sigma_0(s)\sum_{i=0}^{3}\tilde{c}_i^c\left(\frac{s-s_{+-}}{s_{+-}}\right)^i\right]\right)\,, \tag{7.40}$$

whereas, as in the t_S^n case, the coefficients $\tilde{c}_i^c$ allow t_S^c to develop an imaginary part at the neutral–pion thresholds, as demanded by Eq. (6.20).

The coefficient $c_0^{c,S}$ is given by

$$c_0^{c,S} = \frac{\Delta a_c^{+-}}{a_{c,\mathrm{IL}}^{+-}\Delta_\pi} - \tilde{c}_0^c\,\sigma_0(s_{+-})\,, \tag{7.41}$$

with $\Delta a_c^{+-} = a_c^{+-} - a_{c,\mathrm{IL}}^{+-}$, and where the second term in Eq. (7.41) is suppressed in Δ_π.

Finally, the matching conditions at s_1 fix the coefficients $c_6^{c,S}$, $c_7^{c,S}$ to be

$$\begin{aligned}
c_6^c = &-\left(\frac{s_{+-}}{s_1-s_{+-}}\right)^6\left[\sum_{k=0}^{5}(7-k)\,c_k^c\left(\frac{s_1-s_{+-}}{s_{+-}}\right)^k\right.\\
&+\frac{\sigma(s_1)}{2}\sum_{k=0}^{3}\tilde{c}_k^c\left(\frac{s_1-s_{+-}}{s_{+-}}\right)^k\left(14-2k-\frac{s_{+-}}{s_1}\right)\\
&+\frac{i}{\delta_S^{c,\mathrm{IL}}(s_1)}\left\{\left(\frac{4}{s_1-s_{+-}}+\frac{\delta_S^{c,\mathrm{IL}}(s_1)'}{2\delta_S^{c,\mathrm{IL}}(s_1)}+i\delta_S^{n,\mathrm{IL}}(s_1)'+\frac{\eta_S^n(s_1)'}{2\,\eta_S^n(s_1)}\right)\frac{1-\tilde{\eta}_S^x(s)^2}{S_n^{\mathrm{IL}}(s_1)}\right.\\
&\left.\left.+\frac{1+\tilde{\eta}_S^x(s)^2}{2\,S_n^{\mathrm{IL}}(s_1)}\frac{\tilde{\eta}_S^x(s)'}{\tilde{\eta}_S^x(s)}\right\}\right]\,,\\
c_7^c = &-\left(\frac{s_{+-}}{s_1-s_{+-}}\right)^7\left[\sum_{k=0}^{6}c_k^c\left(\frac{s_1-s_{+-}}{s_{+-}}\right)^k+\sigma(s_1)\sum_{k=0}^{3}\tilde{c}_k^c\left(\frac{s_1-s_{+-}}{s_{+-}}\right)^k\right.\\
&\left.+\frac{i}{(s_1-s_{+-})\delta_S^{c,\mathrm{IL}}(s_1)}\frac{1-\tilde{\eta}_S^x(s)^2}{2\,S_n^{\mathrm{IL}}(s_1)}\right]\,.
\end{aligned} \tag{7.42}$$

Below the first inelastic non–$\pi\pi$ threshold s_{in}[2], $\eta_S^n = \eta_S^c = 1$ and $\delta_S^x = 0$, hence recovering the standard two–channel S–matrix parametrization. In this energy region, the elasticity parameter η_S^x provides the $\pi\pi$–inelasticity among the three T^n, T^c and T^x scalar channels, so that

$$\eta_S^x = |S_{11}| = |S_{22}| = \sqrt{1-|S_{12}|^2} \quad \text{for} \quad s < s_{\mathrm{in}}\,. \tag{7.43}$$

Above s_{in}, η_S^x accounts for the whole charge–exchange inelasticity, but we still allow for isospin–breaking corrections up to s_1, where once again we impose the isospin–limit results in [25, 26].

To ensure the correct threshold behavior of the t_S^x partial wave, as well as to describe the cusp effect of its imaginary part at both the charge– and neutral–pion thresholds, we parameterize this elasticity parameter as

$$\eta_S^x(s) = \tilde{\eta}_S^x(s)\left(1+\Delta_\pi\sqrt{(s-s_{+-})(s-s_{00})}\sum_{i=0}^{7}c_i^x\left(\frac{s-s_{+-}}{s_{+-}}\right)^i\right)\,, \tag{7.44}$$

with $\tilde{\eta}_S^x(s)$ defined in Eq. (7.39).

[2] In this case, s_{in} is assumed to correspond to the $\bar{K}K$ threshold, i.e., $s_{\mathrm{in}} = 4M_K^2$.

Once again, the value of the coefficient c_0^x is fixed by the T^x isospin–breaking scattering length value a_x^{+-} as computed in $\chi\mathrm{PT}_\gamma$

$$c_0^x = \frac{4}{s_{+-}\Delta_\pi}\left[(a_x^{+-})^2 - (a_x^{+-}+\Delta a_x^{+-})^2\,\exp\left\{ i\left(1+\sum_{k=0}^{7}\frac{2^{2k}}{s_{00}^k}c_k^x\Delta_\pi^{k+1}\right)\right.\right.$$
$$\left.\left.\times\tan^{-1}\frac{4(a_x^{+-}+a_0^2)\sqrt{(s_1-s_{+-})(s_1(2s_{+-}-s_{00})-s_{+-}^2)\Delta_\pi}}{(s_1-s_{+-})^2-s_1(s_1-s_{00})+8(3a_x^{+-}+2a_x^{+-}a_0^2+2(a_0^2)^2)(s_1-s_{+-})\Delta_\pi}\right\}\right], \quad (7.45)$$

with $\Delta a_x^{+-} = a_x^{+-} - a_{x,\mathrm{IL}}^{+-}$. At leading order in Δ_π this matching condition simplifies to

$$c_0^x = -\frac{8\,a_{x,\mathrm{IL}}^{+-}}{s_{+-}}\left(\frac{\Delta a_x^{+-}}{\Delta_\pi}+\frac{2a_{n,\mathrm{IL}}^{00\,2}a_{x,\mathrm{IL}}^{+-}}{s_{+-}}\right) \quad (7.46)$$

To ensure continuity and differentiability with the isospin–limit solution at s_1, the coefficients c_6^x and c_7^x are fixed by

$$c_6^x = -\left(\frac{s_{+-}}{s_1-s_{+-}}\right)^6\left[\sum_{k=0}^{5}(7-k)\,c_k^x\left(\frac{s_1-s_{+-}}{s_{+-}}\right)^k\right.$$
$$\left.+\frac{1}{s_1-s_{+-}}\left\{\left(\frac{9}{s1-s_{+-}}+2i\delta_S^{n,\mathrm{IL}}(s_1)'+\frac{\eta_S^n(s_1)'}{\eta_S^n(s_1)}\right)\frac{1-\tilde\eta_S^x(s)^2}{S_n^{\mathrm{IL}}(s_1)}+\frac{1+\tilde\eta_S^x(s)^2}{S_n^{\mathrm{IL}}(s_1)}\frac{\tilde\eta_S^x(s)'}{\tilde\eta_S^x(s)}\right\}\right],$$
$$c_7^x = -\left(\frac{s_{+-}}{s_1-s_{+-}}\right)^7\left[\sum_{k=0}^{6}c_k^x\left(\frac{s_1-s_{+-}}{s_{+-}}\right)^k+\frac{1}{(s_1-s_{+-})^2}\frac{1-\tilde\eta_S^x(s)^2}{S_n^{\mathrm{IL}}(s_1)}\right]. \quad (7.47)$$

In the same way, above s_{in} the elasticity parameters η_S^n and η_S^c fulfill $0\le\eta_S^n,\,\eta_S^c\le 1$, and their values are fixed once again from the isospin–limit results in [25,26]. Namely,

$$\eta_S^n(s) = \begin{cases} 1 & s\le s_{+-}\,,\\ \dfrac{\eta_S^{n,\mathrm{IL}}(s)}{\eta_S^{x,\mathrm{IL}}(s)} = \dfrac{|1+2i\sigma(s)\,\left(t_0^0(s)+2t_0^2(s)\right)/3}{\sqrt{1-8\sigma(s)^2\,|(t_20^0(s)-t_0^2(s))/3|^2}} & s>s_{+-}\,,\end{cases}$$
$$\eta_S^c(s) = \frac{\eta_S^{c,\mathrm{IL}}(s)}{\eta_S^{x,\mathrm{IL}}(s)} = \frac{|1+4i\sigma(s)\,\left(2t_0^0(s)+t_0^2(s)\right)/6|}{\sqrt{1-8\sigma(s)^2\,|(t_0^0(s)-t_0^2(s))/3|^2}}\,. \quad (7.48)$$

Finally, δ_S^x is non–vanishing only above s_{in} and provides the charge–exchange phase shift beyond the elastic approximation:

$$\delta_S^x = \arg\left(2\sqrt{2}\,i\,\sigma(s)\left(t_0^0(s)-t_0^2(s)\right)/3\right) - \delta_S^{n,\mathrm{IL}}(s) - \delta_S^{c,\mathrm{IL}}(s)\,. \quad (7.49)$$

7.4 Imaginary parts in the inelastic regime

Below the first non–$\pi\pi$ inelastic threshold, the isospin–breaking parametrizations derived in the previous section, combined with the unitarity relations discussed in Sec. 6.3, provide enough information to compute the imaginary part of the amplitudes in the charge basis. However, the Roy equations beyond the isospin limit, as derived in Sec. 7.1, require these imaginary parts to be defined up to s_1, an energy that lies above s_{in}. Thus, in the kinematic region $s_{\mathrm{in}} < s \le s_1$, the unitarity relations from Sec. 6.3 have to be extended to incorporate inelastic contributions. Namely,

Amplitude T^n:

$$\mathrm{Im}t_S^n(s) = \mathrm{Im}t_S^{n,00}(s) + \mathrm{Im}t_S^{n,+-}(s) = \sigma_0(s)\,|t_S^n(s)|^2 + 2\sigma(s)\,|t_S^x(s)|^2 + \frac{\eta_s^x(s)^2(1-\eta_S^n(s)^2)}{4\sigma_0(s)}. \quad (7.50)$$

Amplitudes T^c and T^{++}:

$$\begin{aligned}
\mathrm{Im}t_S^c(s) =& \mathrm{Im}t_S^{c,00}(s) + \mathrm{Im}t_S^{c,+-}(s) = \sigma_0(s)\,|t_S^x(s)|^2 + 2\sigma(s)\,|t_S^c(s)|^2 + \frac{\eta_s^x(s)^2(1-\eta_S^c(s)^2)}{8\sigma(s)},\\
\mathrm{Im}t_P^{c,+-}(s) =& 2\sigma(s)\,|t_P^c(s)|^2 + \frac{1-\eta_P^c(s)^2}{8\sigma(s)},\\
\mathrm{Im}t_S^{++}(s) =& \sigma(s)\left|t_S^{++}(s)\right|^2 + \frac{1-\eta_S^{++}(s)^2}{4\sigma(s)}.
\end{aligned} \quad (7.51)$$

Amplitudes $\pi^+\pi^- \to \pi^0\pi^0$ and $\pi^+\pi^0 \to \pi^+\pi^0$:

$$\begin{aligned}
\mathrm{Im}t_S^x(s) =& \mathrm{Im}t_S^{x,+-}(s) + \mathrm{Im}t_S^{x,00}(s) = 2\sigma(s)t_S^x(s)t_S^c(s)^* + \sigma_0(s)t_S^n(s)t_S^x(s)^*\\
&+ \frac{i\,\eta_S^x(s)\sqrt{1-\eta_S^x(s)^2}}{4\sqrt{2\sigma_0(s)\sigma(s)}}\mathrm{e}^{i(\delta_S^n(s)-\delta_S^c(s))}\left(\eta_S^n(s)\mathrm{e}^{i\,\delta_S^x(s)} - \eta_S^c(s)\mathrm{e}^{-i\,\delta_S^x(s)}\right),\\
\mathrm{Im}t_S^{+0}(s) =& 2\sigma_{+0}(s)\left|t_S^{+0}(s)\right|^2 + \frac{1-\eta_S^{+0}(s)^2}{8\sigma_{+0}(s)},\\
\mathrm{Im}t_P^{+0}(s) =& 2\sigma_{+0}(s)\left|t_P^{+0}(s)\right|^2 + \frac{1-\eta_P^{+0}(s)^2}{8\sigma_{+0}(s)}.
\end{aligned} \quad (7.52)$$

7.5 Strategy for the numerical solution

The isospin–breaking parameterizations defined in Sec. 7.3 together with their corresponding imaginary parts in Sec. 7.4 provide enough information to check whether Roy equations for $\Delta M_\pi \neq 0$ are satisfied. Specifically, by using the imaginary parts as input, the right–hand side (RHS) of Roy equations in Sec. 7.1 can be computed and then compared with their left–hand sides (LHS), which are directly determined by the real part of the parameterizations.

A numerical solution to Roy equations can be obtained by evaluating and minimizing the least–square difference between the Roy equation LHS and RHS over a mesh of N points in the seven S– and P–wave amplitudes in the charge basis:

$$\Delta^2_{\mathrm{Roy}} = \sum_{k,X}\sum_{j=1}^{N}\left(\mathrm{Re}\,t_X^k(s_j) - F\left[t_X^k\right](s_j)\right)^2, \quad (7.53)$$

where k labels the channels in the charged basis, X denotes the partial wave (S or P), and s_j are squared-energy points taken between the k–channel threshold and $s_{\mathrm{max}} = (0.975\ \mathrm{GeV})^2$ (slightly below the $K\bar{K}$ threshold). Here $F[t_X^k](s)$ denotes the Roy–equation RHS beyond the isospin limit. The numerical Roy solution is then obtained by varying the free parameters to minimize Δ^2_{Roy}.

An exact solution of Eq. (7.53) corresponds to $\Delta_{\mathrm{Roy}} = 0$, meaning Roy equations are perfectly satisfied. In principle, this renders the specific definition of Δ_{Roy} irrelevant. However, in practice, the input quantities—such as scattering lengths and driving terms that influence the matching conditions—are only known within finite precision. This introduces systematic uncertainties in the solutions.

Given this scenario, the precise definition of $\Delta_{\mathrm{Roy}} = 0$ used in the minimization process may influence

the quality of an approximated solution. Ideally, a χ^2–function would be the most suitable choice for minimization algorithms. However, the lack of well–defined statistical errors precludes its direct application. To address this and to ensure that all partial waves are treated uniformly, regardless of their relative magnitude, we adopt the following function:

$$\Delta^2_{\text{Roy}} = \sum_{k,X} \sum_{j=1}^{N} \left(\frac{\operatorname{Re} t^k_X(s_j) - F\left[t^k_X\right](s_j)}{\operatorname{Re} t^k_X(s_j)} \right)^2 , \tag{7.54}$$

where N is varied between 50 to 150 to ensure the stability of the results, and in the end, fixed to 100.

In this way, using the parametrization parameters in Sec. 7.3 as fitting parameters, we look for solutions to Roy equations beyond the isospin limit by minimizing the merit function in Eq. (7.54).

Chapter 8

Results

In this chapter, we will show the results for the dispersive, model–independent analysis of the isospin–breaking effects due to the pion mass difference in the $\pi\pi$ scattering amplitude. We will first list the missing (numerical) pieces to complete the analysis and then we will discuss the solutions of the Roy equations in all the seven physical channels.

8.1 Some important numbers

We start by minimizing the $\Delta_{\rm Roy}$ merit function (see Eq. (7.54)) up to a maximum energy $s_{\rm max} = (0.975\ \text{GeV})^2$, slightly below the $K\bar{K}$ threshold and before the non–$\pi\pi$ inelasticity in the T^n, T^c, and T^x S–waves becomes significant. In addition, we impose the matching conditions with the isospin–limit solution at s_1, the highest energy at which Roy equations are solved. Beyond this point, i.e., $s > s_1$, the $\pi\pi$ input is extracted from experimental data.

The subthreshold parameters, which appear as subtraction constants in the isospin–breaking Roy equation, are derived from the χPT_γ predictions expanded at $\mathcal{O}\left(\delta_\pi^2\right)$, whose expressions are explicitly given in Sec. 6.4. For their numerical evaluation, we use the PDG values [158] for the charged and neutral pion masses,

$$M_{\pi^\pm} = (139.57039 \pm 0.00017)\ \text{MeV}\ , \quad M_{\pi^0} = (134.9768 \pm 0.0005)\ \text{MeV}\ , \tag{8.1}$$

while for the pion–decay constant, we take the FLAG value [206]

$$F_\pi = (92.2 \pm 0.1)\ \text{MeV}\ ,$$

and the renormalization scale μ is set to $\mu = 770$ MeV. For the mesonic low–energy constants (LECs), we use

$$\bar{\ell}_1 = -0.4 \pm 0.6\ , \quad \bar{\ell}_2 = 4.3 \pm 0.1\ , \quad \bar{\ell}_3 = 3.3 \pm 0.3\ , \quad \bar{\ell}_4 = 4.4 \pm 0.2\ , \tag{8.2}$$

where the values of $\bar{\ell}_1$, $\bar{\ell}_2$, and $\bar{\ell}_4$ are taken from [207], and $\bar{\ell}_3$ is obtained as the average between the $N_f = 2+1+1$ and $N_f = 2+1$ FLAG values [206].

Finally, for the electromagnetic LECs (k_i) we use the numerical estimates given in [208],

$$\begin{aligned} \bar{k}_1 =& (1.7 \pm 1.3) \times 10^{-3}\ , \quad \bar{k}_2 = (4.1 \pm 1.2) \times 10^{-3}\ , \quad \bar{k}_3 = (2.3 \pm 2.7) \times 10^{-3}\ , \\ \bar{k}_4 =& (3.8 \pm 1.2) \times 10^{-3}\ , \quad \bar{k}_6 = (4.1 \pm 1.3) \times 10^{-3}\ , \quad \bar{k}_8 = (2.2 \pm 2.9) \times 10^{-3}\ . \end{aligned} \tag{8.3}$$

With these numerical values, we can directly evaluate the χPT_γ expressions for the scattering lengths

given in Sec. 6.4, obtaining the following deviations from their isospin–limit values:

$$\Delta a_n^{00} = -5.375 \times 10^{-3} \,, \quad \Delta a^{++} = 2.918 \times 10^{-3} \,, \quad \Delta a_c^{+-} = 4.076 \times 10^{-3} \,,$$
$$\Delta a_1 = -0.711 \times 10^{-3} \,, \quad \Delta a_2 = -1.467 \times 10^{-3} \,. \tag{8.4}$$

In addition, the values for Δa_x^{+-} and Δa_c^{+0}, which are required for evaluating the parameterizations of the t_S^{+0} and t_S^x partial waves, can be computed from Δa_1 and Δa_2 using the relations in Eqs. (6.13) and (6.14), respectively. Nevertheless, these expressions involve the same parameterizations we aim to compute, leading to an implicit system of equations and significantly complicating the $\Delta_{\rm Roy}$ minimization problem. Instead, since the partial–wave contributions in Eqs. (6.13) and (6.14) are already suppressed by Δ_π and Δ_π^2, respectively, we can initially estimate the parameterization effect using the isospin–limit results and update their values only in a later iteration. In this way, the starting value for the a_x^{+-} and a_c^{+0} scattering length difference reads:

$$\Delta a_x^{+-}\big|_0 = 0.081 \times 10^{-3} \,, \quad \Delta a_c^{+0}\big|_0 = -1.474 \times 10^{-3} \,, \tag{8.5}$$

where the subscript 0 indicates that these are starting values for both quantities. These results show only a small correction relative to Δa_2 for a_c^{+0} but a sizable effect for a_x^{+-} compared to Δa_1.

The scattering lengths in the isospin limit are taken from the Roy–equation analysis in [25,26] and read $a_0^0 = 0.220$ and $a_0^2 = -0.0444$, which in the charge–basis translate to the values

$$a_{n,\,\rm IL}^{00} = 0.0437 \,, \quad a_{\rm IL}^{++} = -0.0444 \,, \quad a_{c,\,\rm IL}^{+-} = 0.0659 \,, \quad a_{x,\,\rm IL}^{+-} = 0.0881 \,, \quad a_{c,\,\rm IL}^{+0} = -0.0222 \,. \tag{8.6}$$

8.2 Roy equations solutions with isospin–breaking effects

Once the scattering length values are fixed, we can begin searching for solutions. To ensure a well–behaved minimum and prevent artificial correlations that might amplify isospin–breaking corrections, we start adiabatically, introducing each parameterization parameter one at a time, stopping when the value of the merit function per number of parameter $\Delta^2_{\rm Roy}/N_{\rm par}$ no longer improves. This procedure yields six free parameters for the P waves and five for most S waves; the partial waves t_S^n and t_S^c require an additional five and four parameters, respectively, to account for the cusp structure. Proceeding in this way, we obtain merit function value of $\Delta^2_{\rm Roy} = 1.4 \cdot 10^{-4}$, achieving a level of consistency between the LHS and RHS of the Roy equations comparable to that in the isospin limit.

While the results for the T^n, T^c, and T^x S–waves, as well as the P–waves, indicate small isospin–breaking corrections—enhanced primarily at the threshold and in the resonance region—the repulsive, non–resonant T^{++} and T^{+0} S–waves exhibit a more uniform effect. Notably, in the T^{+0} case, this effect even increases with energy, leading to an unphysical bending enforced by the matching conditions at s_1, as shown in Fig. 8.1. This result reflects the dominance of the T^{+0} S–wave: in the Roy–equations framework, this wave collects isospin breaking effects from all the other waves, leading to a sizable deviation from the isospin limit solution at s_1. In fact, the T^{+0} S–wave is directly related to the $I = 2$ channel, which in the isospin limit shows rather large uncertainties, as it is shown in Fig. 8.2. To address this issue, we impose the matching conditions only at higher energies, namely $s_2 = 4$ GeV^2, and parameterize the t_S^{+0} input above s_1 using the polynomial,

$$t_S^{+0}(s)\big|_{\rm input} = t_S^{+0,\,\rm IL}(s) + b_S^{+0}\,\frac{s - s_2}{s_1 - s_2}\left(1 - \frac{s - s_2}{s_1 - s_2}\right) \,, \quad \text{for} \quad s_1 \le s \le s_2 \,, \tag{8.7}$$

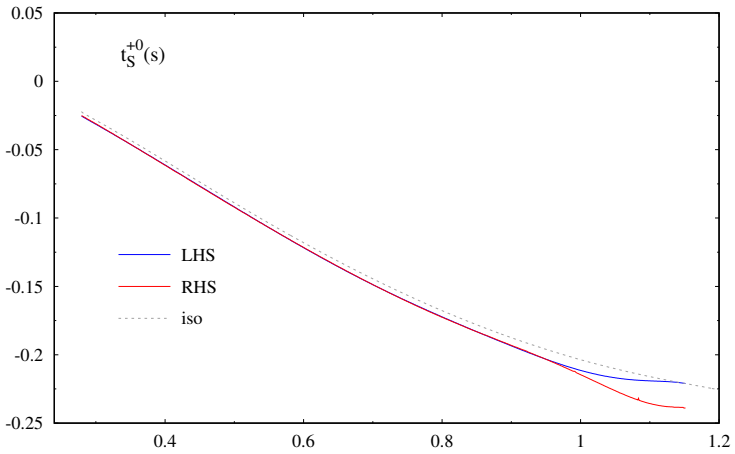

Figure 8.1: Result for the real part of the $t_S^{+0}(s)$ partial wave, with matching conditions imposed at $s_1 = (1.15\ \text{GeV})^2$ to the isospin–limit result (dashed gray line). Roy equations are imposed only in the $\pi\pi$ elastic region so that the LHS (blue) and RHS (red) curves start deviating above $s_{\text{max}} = (0.975\ \text{GeV})^2$.

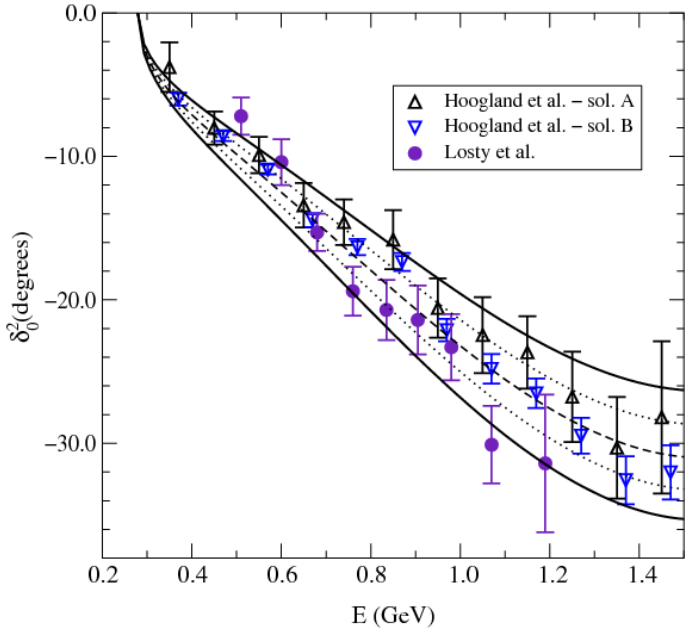

Figure 8.2: Different data sets for the S–wave in the $I = 2$ channel and curves that [24] used as input in the equation analysis. Figure taken from [24].

which ensures a continuous and differentiable matching with the isospin–limit solution at s_2, while allowing for a shift at s_1 given by

$$\Delta t_S^{+0}(s_1) = t_S^{+0}(s_1) - t_S^{+0,\,\mathrm{IL}}(s_1) = b_S^{+0}\,, \tag{8.8}$$

where b_S^{+0} is a complex free parameter determined through the Δ_{Roy} minimization. Note that above s_1, we only need as input $\mathrm{Im}t_S^{+0}$, but below the isospin–breaking parameterization in (7.23) is expressed in terms of its phase shift and elasticity, the latter being fixed from data. Consequently, in order to ensure also a continuous matching at s_1, only the real or imaginary part of the parameter b_s^{+0} can be chosen freely. In practice, we leave $\mathrm{Re}\, b_S^{+0}$ free so that its imaginary part is given by

$$\mathrm{Im}\, b_S^{+0} = -\mathrm{Im}\, t_S^{+0,\,\mathrm{IL}} + \frac{1 - \sqrt{\eta_S^{+0}(s_1)^2 - 16\,\sigma_{+0}(s_1)^2\left(\mathrm{Re}\, t_S^{+0,\,\mathrm{IL}}(s_1) + \mathrm{Re}\, b_S^{+0}\right)^2}}{4\sigma_{+0}(s_1)}\,. \tag{8.9}$$

With this new scheme, we minimize the merit function Δ_{Roy} once again, using both the isospin–breaking parameterization parameters and $\mathrm{Re}\, b_S^{+0}$ as free parameters. As a result, we obtain a value for the merit function $\Delta^2_{\mathrm{Roy}} = 1.2 \times 10^{-4}$, slightly below our previous results when the matching to the isospin–limit was imposed at s_1. The partial waves remain nearly unchanged compared to our previous results, except for t_S^{+0} near s_1, where the unphysical bending observed in Fig. 8.1 now disappears, obtaining at s_1 the difference to the isospin limit,

$$\Delta\mathrm{Re}\, t_S^{+0}(s_1) = \mathrm{Re}\, t_S^{+0}(s_1) - \mathrm{Re}\, t_S^{+0,\,\mathrm{IL}}(s_1) = \mathrm{Re}\, b_S^{+0} = -5.56 \times 10^{-3}\,. \tag{8.10}$$

which amounts to a 2.5% effect. Furthermore, to estimate the effect of the asymptotic matching to the isospin–limit at s_2 for the t_S^{+0} partial wave—and how this affects the value of $\mathrm{Re}\, b_S^{+0}$ and hence, the deviation from the isospin–limit at s_1—we solve the Roy–equations for $\Delta_\pi \neq 0$ once again, varying the asymptotic value of the partial wave $\mathrm{Im}\, t_0^2$ within uncertainties. This variation affects not only the matching conditions but also the value of the driving terms, allowing us to quantify the corresponding changes in the solution.

The resulting coefficient in the isospin–breaking parameterization are given in Table 8.1 and the final values for the corrections to a_x^{+-} and a_c^{+0} read

$$\Delta a_x^{+-} = 0.032 \times 10^{-3}\,, \quad \Delta a_c^{+0} = -1.479 \times 10^{-3}\,, \tag{8.11}$$

which highlights a tiny effect for a_c^{+0}, but makes the correction for a_x^{+-} even smaller in magnitude than the initial estimate.

The results for the real and imaginary parts of each of the seven S and P $\pi\pi$ waves are shown in Figs. 8.3–8.7, where we compare the isospin–breaking parameterizations to the isospin–limit result. The uncertainty band of the isospin–breaking parameterizations reflects the effect of varying the asymptotic value of $\mathrm{Im}\, t_0^2$. For the real part of the partial waves, we plot both the LHS and RHS of Roy equations. In all cases, their difference is almost negligible, reflecting how well Roy equations for $\Delta_\pi \neq 0$ are satisfied.

Moreover, at the bottom of each figure, we include the difference between the isospin–breaking and isospin–limit results, illustrating the size of the pion–mass difference corrections. These corrections should be compared with the difference between the LHS and RHS of the Roy equations and the isospin–breaking uncertainty band, which generally remain smaller across the entire energy region. This ensures that the pion–mass difference corrections lie well above our intrinsic uncertainties.

In more detail, Fig. 8.3 displays the results for the t_S^n partial wave, where one can observe that while

	c_0	c_1	c_2	c_3	$c_4 \times 10$	$c_5 \times 10^2$	$\tilde{c}_0$	$\tilde{c}_1$	$\tilde{c}_2$	$\tilde{c}_3 \times 10$	$\tilde{c}_4 \times 10^2$
t_S^n	—	18.3	−6.85	0.511	0.743	−1.59	112	−7.04	0.574	0.578	−0.320
t_S^c	—	−34.2	9.52	−1.48	1.06	−0.332	−4.90	6.97	0.555	0.641	—
t_P^c	2.45	−13.7	4.19	−0.269	−0.413	0.707	—	—	—	—	—
t_S^x	—	−6.71	−0.913	2.09	−4.52	3.92	—	—	—	—	—
t_S^{++}	—	38.3	−13.4	2.18	−1.52	0.0768	—	—	—	—	—
t_S^{+0}	—	−40.39	15.1	−2.83	2.84	−1.49	—	—	—	—	—
t_P^{+0}	4.06	11.6	−4.11	0.505	−0.251	0.0255	—	—	—	—	—

Table 8.1: Values of the parameter used to describe the isospin–breaking correction in the phase. These values are given in unit of GeV^{-2}, except the one for t_S^x which are in unit of GeV^{-4}.

the physical region starts at the charged–pion threshold for the isospin–limit parameterization, it opens at the neutral–pion threshold in the isospin–breaking case, thereby amplifying the size of the correction. The corrections are also enhanced at the $f_0(500)$ and $f_0(980)$ resonance regions, while remaining small elsewhere, allowing for a smooth matching with the isospin limit at s_1. In more quantitative terms, using the variable $\bar{s}(s)$ in Eq. (7.34) for the evaluation of the isospin–limit result, the pion–mass difference correction for the real part of the $t_S^n(s)$ partial wave is around 12% at the neutral pion–threshold, which by construction coincides with the size of Δa_n^{00} as computed in χPT_γ, below 3% in the $f_0(500)/\sigma$ region ($\sqrt{s} \sim 0.5$ GeV), and around 7.5% near 1 GeV, the $f_0(980)$ region.

Figs. 8.4 and 8.5 show the results for the $t_S^c(s)$ and $t_S^x(s)$ partial waves. In either case, the physical region starts at the charged–pion threshold for both the isospin–limit and isospin–breaking results. Thus, the differences at threshold correspond to the size of the scattering length differences computed in $\chi\ \text{PT}_\gamma$, around 6% for t_S^c and almost negligible for t_S^x. The corrections become small at higher energies, with a moderate increase in the $f_0(980)$ resonance regions of around 5%. Near s_1, the effect is below 1%, ensuring a smooth matching with the isospin–limit results.

Figs. 8.6 and 8.7 depict the results for the P–waves. In both cases, the P–wave centrifugal barrier effect ensures that they vanish at their corresponding threshold, i.e., $t_P^c(s_{+-}) = t_P^{+0}(s_{0+}) = 0$. Nevertheless, while the physical region for the T^c P–wave starts at the charged–pion threshold, making the isospin–breaking results indistinguishable from the isospin–limit at low energies, it begins at s_{0+} for the t_P^{+0}, leading to the pion–mass difference corrections observe in Fig. 8.7. In both cases, pion–mass difference corrections remain small—below 2% over the entire energy range studied—rising to roughly 3% only in the $\rho(770)$ resonance region.

Finally, Figs. 8.8 and 8.9 show the results for the repulsive S–waves. In this case, the uncertainty bands become significantly larger due to the strong dependence of the $t_S^{++}(s)$ and $t_S^{+0}(s)$ partial waves on the asymptotic value of $\text{Im}\, t_0^2(s)$. While the imaginary part of $t_S^{++}(s)$ opens at the charged–pion threshold—so that its difference from the isospin–limit result stems from the χPT_γ correction to the scattering length—the physical region for $t_S^{+0}(s)$ starts at s_{0+}, introducing an additional correction, as seen in Fig. 8.9. In both cases, the pion–mass difference relative corrections reach a maximum at threshold, slightly exceeding 6%. Beyond this maximum, the relative correction decreases until it stabilizes around a plateau at $\sqrt{s} \sim 0.5$ GeV. For the t_S^{++} partial wave, this plateau is around 1%, while for the t_S^{+0}, the relative correction for the real part reaches around 3%. Thus, while the corrections above 1 GeV in the $\pi^+\pi^+ \to \pi^+\pi^+$ channel remain relatively small, allowing for a smooth matching to the isospin–limit value at s_1, the shift with respect to the isospin–limit value required by the fit in the $\pi^+\pi^0 \to \pi^+\pi^0$ S–wave is $\text{Re}\, b_S^{+0} = -5.65 \times 10^{-3}$, and the matching is performed only at s_2.

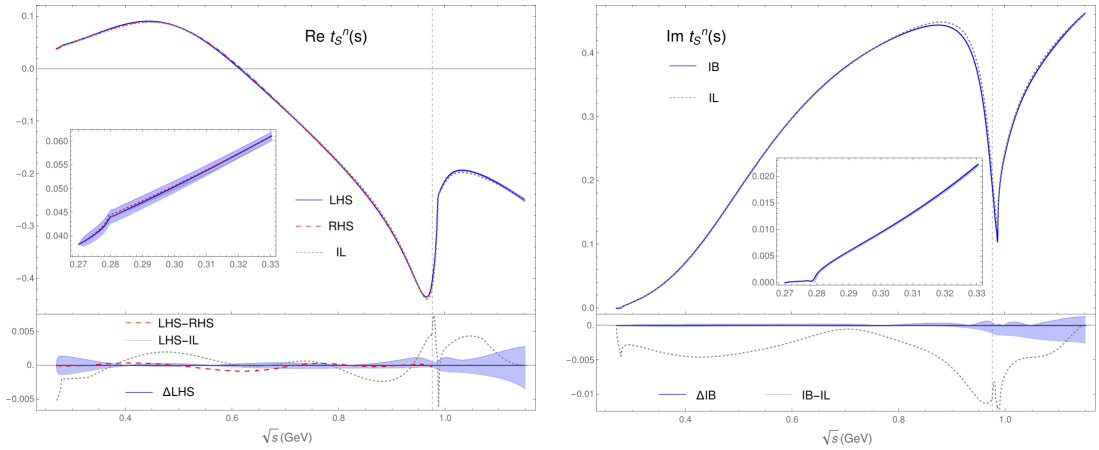

Figure 8.3: Results for the real (left panel) and imaginary (right panel) parts of the $t_S^n(s)$ partial wave. For the real part, we display the isospin–breaking parameterization, i.e., the LHS of Roy equations (solid blue), and the dispersive representation, i.e., the RHS (dashed red), along with the isospin–limit result (gray–dotted line). For the imaginary part, since unitarity is exactly satisfied, we plot only the isospin–breaking parameterization and the isospin–limit result. The blue band represents the uncertainty in the isospin–breaking parameterization due to variations in the asymptotic value of $\mathrm{Im}\, t_0^2$. The inset figures in both panels highlight the low–energy region, where the effect of the neutral–pion threshold becomes visible. At the bottom of both panels, we show the difference between the isospin–breaking and isospin limit parameterizations (gray–dotted line), along with the uncertainty band of the isospin–breaking parameterization. The isospin–limit result is evaluated using the variable $\bar{s}(s)$, defined in Eq. (7.34), which maps the charged–pion threshold into the neutral one, allowing for a direct comparison of both results at the same energies. For the real part, we also plot at the bottom the difference between the LHS and RHS of Roy equations for $\Delta_\pi \neq 0$.

8.3 Resonance pole parameters for $\Delta_\pi \neq 0$

Because our formalism is founded on analyticity, the dispersive representation obtained here provides model–independent access to the physical (first) Riemann sheet, and, by means of the Schwarz reflection principle, can be continued to the unphysical (second) sheet. Consequently, the isospin–breaking amplitudes defined in Sec. 7.1 and App. E permit the extraction of the poles associated with the elastic $\pi\pi$ resonances—$f_0(500)$, $f_0(980)$, $\rho^+(770)$ and $\rho^0(770)$—and, by comparing their pole positions with the isospin–limit values, to quantify the effects of the pion–mass difference.

In the isospin limit, the scalars $f_0(500)$ and $f_0(980)$ are isosinglet ($I = 0$) resonances and therefore appear as a single pole in the three scalar amplitudes T^n, T^c, and T^x:

$$\sqrt{s_{f_0(500)}}\big|_{\mathrm{IL}} = (440 - i\,271)\ \mathrm{MeV}, \qquad \sqrt{s_{f_0(980)}}\big|_{\mathrm{IL}} = (997 - i\,26)\ \mathrm{MeV}\ , \tag{8.12}$$

rounded according to the uncertainties quoted in [209–212].

Within our isospin–breaking formalism, this single–pole structure is also preserved thanks to the coupled–channel formalism described in Sec. 7.3. The continuation of the partial waves t_S^n, t_S^c, and t_S^x to the second sheet yields

$$\sqrt{s_{f_0(500)}}\big|_{\Delta_\pi} = (441 - i\,270)\ \mathrm{MeV}, \qquad \sqrt{s_{f_0(980)}}\big|_{\Delta_\pi} = (997 - i\,26)\ \mathrm{MeV}\ . \tag{8.13}$$

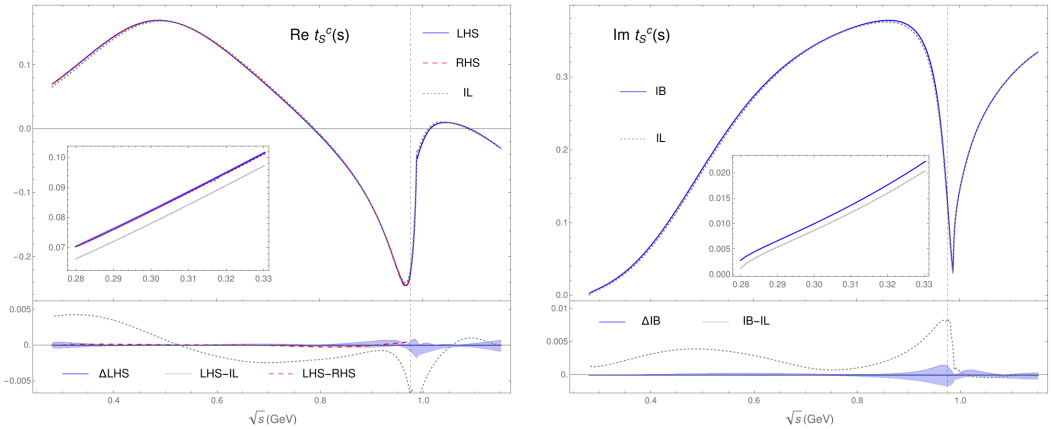

Figure 8.4: We compare the isospin–breaking and isospin–limit results for the real (left panel) and imaginary part (right) of the $t_S^c(s)$ partial wave. The different curves follow the conventions in Fig. 8.3. In this case, the physical region for both the isospin–limit and isospin–breaking parameterizations starts at the charged–pion threshold. Thus, the shift observed at low energies in the inset figures originates from the $\chi\mathrm{PT}_\gamma$ correction to the scattering length.

Comparing Eqs. (8.12) and (8.13) shows that isospin–breaking shifts are negligible at the present level of precision: for the $f_0(500)$ the pole mass increases by ~ 1 MeV and the width decreases by ~ 2 MeV. In contrast, the $f_0(980)$ pole is essentially unchanged within the quoted rounding.

By contrast, the $\rho(770)$ is an isovector ($I = 1$) resonance, so that in the isospin limit the three charge states $\rho^\pm(770)$ and $\rho^0(770)$ are degenerate:

$$\sqrt{s_{\rho(770)}}\big|_{\mathrm{IL}} = (763.29 - i\,71.65)\ \mathrm{MeV}\ . \tag{8.14}$$

Isospin breaking effects lift this degeneracy. Analytically continuing the P–wave amplitudes t_P^c and t_P^{+0} (see App. E) gives

$$\sqrt{s_{\rho^0}}\big|_{\Delta_\pi} = (763.28 - i\,71.66)\ \mathrm{MeV}\ , \qquad \sqrt{s_{\rho^\pm}}\big|_{\Delta_\pi} = (762.29 - i\,71.89)\ \mathrm{MeV}\ . \tag{8.15}$$

These values indicate a mass splitting of order ~ 1 MeV and a width difference of order ~ 0.5 MeV induced by the pion–mass difference. Taking into account the uncertainties reported in [210, 212], the pion–mass–difference effects on the ρ mass and width are therefore minimal and within their error budget.

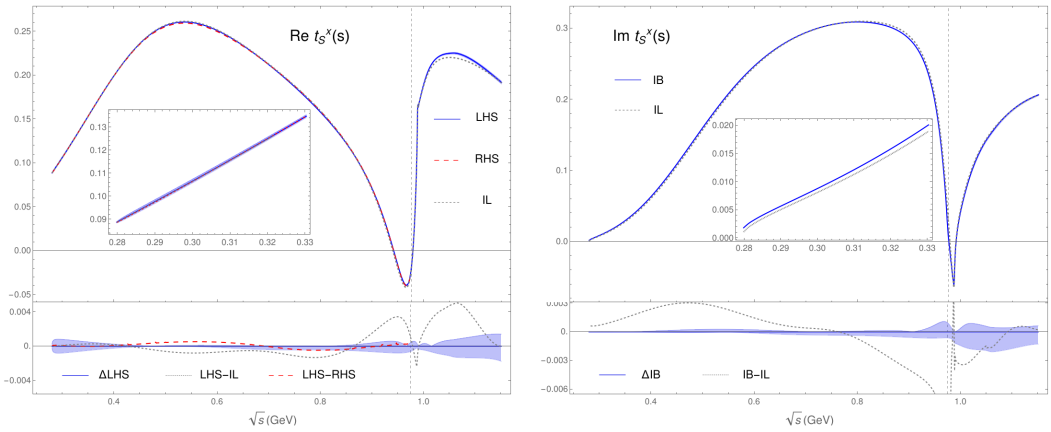

Figure 8.5: Results for the real (left) and imaginary (right) part of the $t_S^x(s)$ partial wave. The curves follow the same conventions as in Fig. 8.3. The imaginary part of both the isospin–breaking and isospin–limit partial waves opens at the charged–pion threshold. At this energy, the pion–mass difference correction is given by Δa_x^{+-}, which value in χPT$_\gamma$leads to the small shift observed in the inset figures.

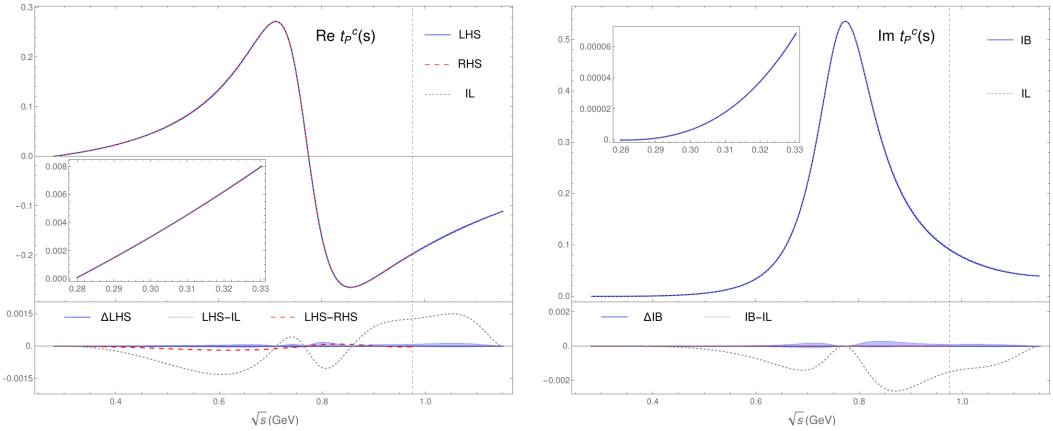

Figure 8.6: We show the isospin–breaking and isospin–limit results for the real (left panel) and imaginary (right panel) of the $t_P^c(s)$ partial wave. The bottom of each figure displays the difference between the isospin–breaking and isospin–limit results, highlighting the minimal impact of pion–mass corrections in this case. For the real part, we also depict the LHS and RHS of Roy equations. Both curves almost coincide in the entire elastic region ($s_{+-} \leq s \leq s_{\rm in}$) with their difference—displayed in the bottom panel—remaining well below the deviation from the isospin–limit result.

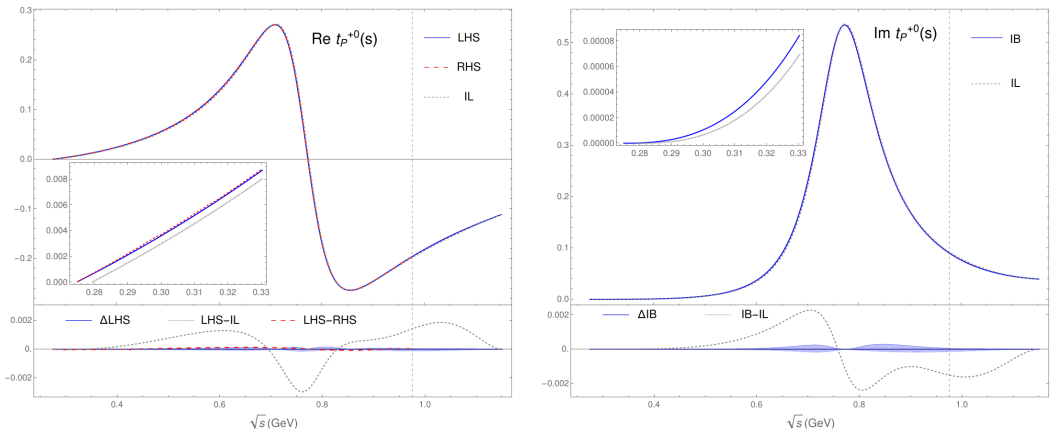

Figure 8.7: Comparison between the isospin–breaking (blue–solid line) and isospin–limit (gray–dotted) results for the real (left panel) and imaginary (right panel) part of the $t_P^{+0}(s)$ partial wave. In the isospin–breaking case, the physical region starts at s_{0+}, whereas in the isospin limit, it opens at the charged–pion threshold s_{+-}. This explains why, despite being a P–wave, a shift appears between the isospin–breaking and isospin–limit results at low energies.

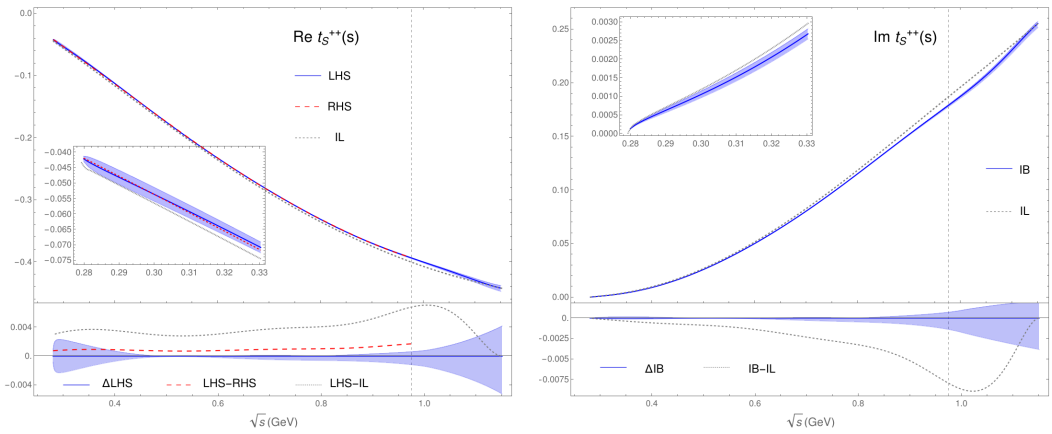

Figure 8.8: Results for the real (left panel) and imaginary (right) part of the $t_S^{++}(s)$ partial wave. The physical region for both the isospin–breaking (solid–blue line and band) and isospin–limit (gray–dotted curve) partial waves starts at the charged–pion threshold. The pion–mass correction at threshold is given by Δa^{++}, whose value is determined in $\chi\mathrm{PT}_\gamma$. For the real part of the partial wave, we also include the RHS of the Roy equation (dashed–red line). The RHS–LHS difference, shown at the bottom, remains consistently smaller than the pion–mass correction.

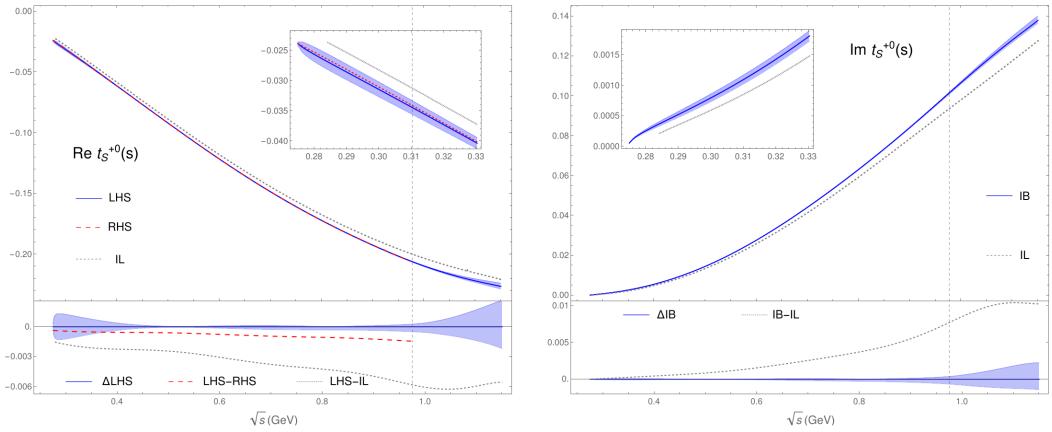

Figure 8.9: Comparison between the isospin–limit and isospin–breaking results for the part (left panel) and imaginary part (right panel) of the $t_S^{+0}(s)$ partial wave. In the isospin–breaking case, the imaginary part opens at s_{0+}, whereas in the isospin limit, it starts at s_{+-}. This shift, together with the χPT$_\gamma$correction to the Δa_c^{+0} scattering length, leads to the significant pion–mass corrections observed in the inset figures at low energies, reaching a maximum of approximately 6% at threshold. At higher energies, these corrections gradually decrease and stabilize around 3% at $\sqrt{s} \sim 0.5$. At s_1, and only for this wave, an additional pion–mass difference correction is required in the fit, encoded in the parameter $\mathrm{Re}\, b_S^{+0} = -5.56 \times 10^{-3}$. The bottom of both panels shows the difference between the isospin–breaking and isospin–limit parameterizations (gray–dotted line), along with the uncertainty band for the isospin–breaking parameterization. For the real part, we also display the difference between the RHS and LHS of the Roy equation (dashed–red line), which remains significantly smaller than the pion–mass correction. The isospin–limit result is evaluated using the variable $\hat{s}(s)$, defined in Eq. (7.22), which maps the charged–pion threshold onto the $\pi^+\pi^0$ threshold, enabling a direct comparison between the isospin–breaking and isospin–limit results at the same energies.

Chapter 9

Isospin–breaking corrections to $\tau \to \pi\pi^0\nu_\tau$: overall strategy

As we pointed out in Ch. 2, the tension between experimental and Standard Model results of the muon anomalous magnetic moment requires new and more precise computations. In this sense, the study of the τ decay provides an alternative and independent way to compute this observable. In the following chapters we will focus on the computation of the long–range corrections to the hadronic τ–decay, usually denoted by $G_{\rm EM}(s)$.

9.1 Why study $\tau \to \pi\pi^0\nu_\tau$

In a data–driven approach, the hadronic contribution to a_μ, $a_\mu^{\rm HVP}$, is determined from the cross section of the reaction $e^+e^- \to \pi^+\pi^-$, which is measured in different experiments, using the initial state radiation (ISR) method (BaBar, KLOE and BESIII) or the energy–scan approach (SND, CMD–2, CMD–3). In particular, a relevant contribution in the error of $a_\mu^{\rm HVP}$ is due to the tension between the high precision experiments BaBar and KLOE. However, this discrepancy increased after the release of the new result from CMD–3 [12]. An overview of the estimations of a_μ for different experiments from $e^+e^- \to \pi^+\pi^-$ can be found in Fig. 2.3. The tensions showed in Fig. 2.3 are the reason why in [14] a data–driven estimate of the $a_\mu^{\rm HVP,\,LO}$ is not provided. In fact, after the CMD–3 measurement of the critical $e^+e^- \to \pi^+\pi^-$ channel, systematic discrepancies had increased to a level that could no longer be taken into account by a meaningful error inflation. There are several ongoing investigations trying to rectify the situation [14,20], including new data as well as improvements of the radiative corrections and Monte Carlo generators [18,21–23,213–215].

In view of this, the study of the hadronic τ decay offers an alternative way to estimate the $e^+e^- \to \pi^+\pi^-$ cross section and ultimately the muon anomalous magnetic moment which can help in clarifying the current situation. As we can see from the diagrams in Fig. (9.1), in the case of the $e^+e^- \to \pi^+\pi^-$ we have an electromagnetic neutral current and a final state with isospin $(I, I_z) = (1, 0)$, while in the τ decay we have a vector–axial vector charged current and a final state with $(I, I_z) = (1, -1)$. Thanks to a conserved–vector–current (CVC) relation between electromagnetic and weak form factors, in the isospin limit, the purely hadronic cross section for $e^+e^- \to \pi^+\pi^-$ (with QED effects removed[3]) can be related to the $\tau^- \to \pi^-\pi^0\nu_\tau$ differential decay width in this limit by Eq. (2.38) where constants and phase–space factors are collected in Eqs. (2.39) and (2.40). Including isospin violation to leading order,

[3] cf. removal of vacuum polarization and initial–state–radiation effects in [102].

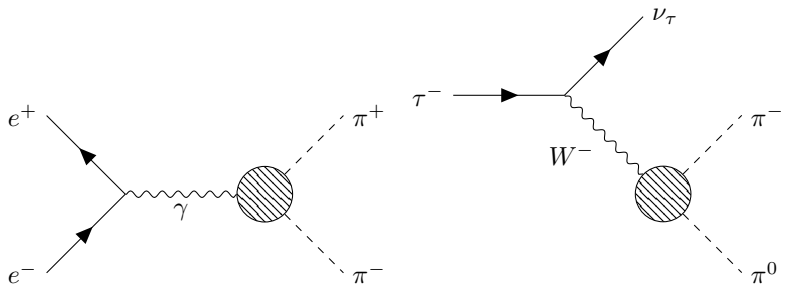

Figure 9.1: Tree level diagrams for the processes $e^+e^- \to \pi^+\pi^-$ and $\tau^- \to \pi^-\pi^0\nu_\tau$.

$\mathcal{O}\left[(m_u - m_d)p^2\right]$ and $\mathcal{O}(e^2p^2)$, the modified CVC relation takes the form

$$\sigma(e^+e^- \to \pi^+\pi^-)(s) = \frac{1}{\mathcal{N}(s)\Gamma_e^{(0)}} \frac{\mathrm{d}\Gamma(\tau^- \to \pi^-\pi^0\nu_\tau)}{\mathrm{d}s} \frac{R_{\mathrm{IB}}(s)}{S_{\mathrm{EW}}^{\pi\pi}} \,, \tag{9.1}$$

where $S_{\mathrm{EW}}^{\pi\pi} = 1 + 2\alpha/\pi \log\left(M_Z/m_\tau\right) + ... = 1.0233(3)(24)$ [216–223] takes into account the dominant short distance electroweak corrections in the convention that the normalization proceeds with respect to the full decay rate $\Gamma_e \equiv \Gamma_e[\tau \to e\nu_\tau\bar{\nu}_e]$, of which Eq. (2.40) represents the LO approximation. The isospin breaking (IB) effects are included in

$$R_{\mathrm{IB}}(s) = \frac{\mathrm{FSR}(s)}{G_{\mathrm{EM}}(s)} \frac{\beta_{\pi\pi}^3(s)}{\beta_{\pi^0\pi}^3(s)} \left|\frac{F_\pi^V(s)}{f_+(s)}\right|^2 \,. \tag{9.2}$$

In particular, $\mathrm{FSR}(s) = 1 + \frac{\alpha}{\pi}\eta(s)$ [137, 224–226] account for final state radiation contributions in $e^+e^- \to \pi^+\pi^-(\gamma)$, $G_{\mathrm{EM}}(s)$ includes the virtual and real photons corrections, $\frac{\beta_{\pi\pi}^3(s)}{\beta_{\pi^0\pi}^3(s)}$ is the phase space correction factor and $\left|\frac{F_\pi^V(s)}{f_+(s)}\right|^2$ accounts for corrections between the different form factors entering the two processes. In this work we will mainly focus on the determination of the $G_{\mathrm{EM}}(s)$ factor which will be computed with a new model–independent dispersive approach. At LO in IB, the τ decay rate can therefore be expressed as

$$\frac{\mathrm{d}\Gamma[\tau \to \pi\pi\nu_\tau(\gamma)]}{\mathrm{d}s} = S_{\mathrm{EW}}^{\pi\pi} K_\Gamma(s) \beta_{\pi\pi^0}^3 |f_+(s)|^2 G_{\mathrm{EM}}(s) \,, \tag{9.3}$$

with

$$K_\Gamma(s) = \frac{\Gamma_e |V_{ud}|^2}{2m_\tau^2} \left(1 - \frac{s}{m_\tau^2}\right)^2 \left(1 + \frac{2s}{m_\tau^2}\right) , \tag{9.4}$$

and where $G_{\mathrm{EM}}(s)$, following [34, 35], can be defined as

$$G_{\mathrm{EM}}(s) = \frac{\int_{t_{\mathrm{min}}(s)}^{t_{\mathrm{max}}(s)} \mathrm{d}t \; D(s,t)\Delta(s,t)}{\int_{t_{\mathrm{min}}(s)}^{t_{\mathrm{max}}(s)} \mathrm{d}t \; D(s,t)} \,, \tag{9.5}$$

where

$$D(s,t) = \frac{m_\tau^2}{2}\left(m_\tau^2 - s\right) + 2M_\pi^2 - 2t\left(m_\tau^2 - s + 2M_\pi^2\right) + 2t^2 \,, \tag{9.6}$$

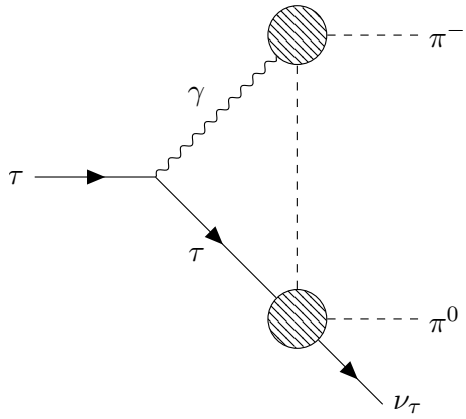

Figure 9.2: Triangle diagram with $\pi\pi\gamma$– and $\tau\nu_\tau\pi\pi$–vertices dressed with the pion vector form factor.

is the tree–level kinematic function, while

$$\Delta(s,t) = 1 + 2f_+^{e^2p^2}(s,t) + g_{\text{Low}}(s,t) + g_{\text{rest}}(s,t)\,. \tag{9.7}$$

includes both real and virtual photons radiative corrections. All the terms in $\Delta(s,t)$ will be explained in detail later in this work. However, we want to stress the fact that, in order to use the hadronic τ decay to compute the $e^+e^- \to \pi^+\pi^-$ cross section, not only radiative corrections have to be understood, but also appropriate IB effects need to be applied to ensure consistency with the standard photon–inclusive definition of the LO HVP contribution as determined from the e^+e^- scattering, $a_\mu^{\text{HVP,LO}}[\pi\pi]$.

For now, we do not aim at a full calculation of second–order isospin breaking effects, which are tiny, and we therefore evaluate $G_{\text{EM}}(s)$ in the isospin limit, $M_{\pi^0} \to M_\pi$ and $F_\pi^V(s) \to f_+(s)$. The only exception where the pion mass differences does matter in the end concerns the a_μ integral, as otherwise fake isospin–breaking effects can be generated if the phase–space boundaries do not match, i.e., the threshold singularity in $G_{\text{EM}}(s)$ sits at $s = 4M_\pi^2$, but the physical threshold of $\tau^\pm \to \pi^\pm\pi^0\nu_\tau$ at $s = (M_\pi + M_{\pi^0})^2$. This mismatch can be avoided by a simple linear mapping [205]

$$G_{\text{EM}}(s) \mapsto G_{\text{EM}}\big[\tilde{s}(s)\big]\,, \tag{9.8}$$

with

$$\tilde{s}(s) = \frac{(m_\tau^2 - 4M_\pi^2)s + \big[4M_\pi^2 - (M_\pi + M_{\pi^0})^2\big]m_\tau^2}{m_\tau^2 - (M_\pi + M_{\pi^0})^2}\,, \tag{9.9}$$

fulfilling $\tilde{s}[(M_\pi + M_{\pi^0})^2] = 4M_\pi^2$ and $\tilde{s}(m_\tau^2) = m_\tau^2$, to ensure that the singularity in $G_{\text{EM}}\big[\tilde{s}(s)\big]$ is shifted to the physical threshold. In fact, this threshold singularity leads to the only second–order IB effects that do need to be included, i.e., the threshold–enhanced terms in $G_{\text{EM}}(s)$ multiplied with the IB corrections from phase space and $S_{\text{EW}}^{\pi\pi}$ lead to non–negligible contributions, so that a linearized form of the corrections in Eqs. (9.1) and (9.2) should be avoided (see Sec. 13.4).

9.2 Our approach

In the literature, IB corrections to the hadronic τ decay are computed with model–dependent methods [34–37]. Here, we developed a new, model–independent dispersive approach for the radiative corrections to $\tau \to \pi\pi\nu_\tau$. In this framework, the only relevant unitary diagram is the one in Fig. 9.2. In a dispersive picture, such a contribution arises by considering the pion–pole singularity in the general ma-

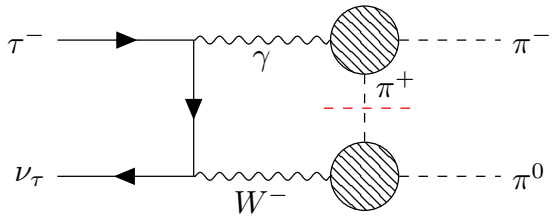

Figure 9.3: Box diagram in a dispersive approach. The gray blobs denote the pion form factor, in the neutral and charged channel, respectively. The short–dashed red line indicates that the intermediate–state pion is taken on–shell

trix element $\langle \pi\pi^0 | j^\mu_{\rm em} j^\nu_W | 0 \rangle$ of weak and electromagnetic currents, which could be generalized in analogy to pion Compton scattering [79–81, 227–229]. However, at low energies the pion–pole contribution gives by far the dominant effect, leading to the picture in Fig. 9.2. Given the short–range weak vertex, the diagram appears as a triangle topology, but actually originates from a box diagram. In fact, keeping in mind that the $\tau\nu_\tau\pi\pi^0$ vertex arises from integrating out the W boson, this topology then takes the form shown in Fig. 9.3. Once the intermediate–state pion is taken on–shell, both the $\pi\pi\gamma$– and the $\tau\nu_\tau\pi\pi$–vertices appearing in the triangle–diagram of Fig. 9.2 are described exactly by the electromagnetic and the weak form factor, respectively. In particular, in our dispersive framework, we employ the unsubtracted dispersive representation

$$f_+(s) = -\frac{1}{\pi}\int_{4M_\pi^2}^{\infty} {\rm d}s' \frac{{\rm Im}\, f_+(s')}{s-s'} \,. \tag{9.10}$$

which satisfies the following sum rule

$$f_+(0) = \frac{1}{\pi}\int_{4M_\pi^2}^{\infty} {\rm d}s' \frac{{\rm Im}\, f_+(s')}{s'} = 1 \,. \tag{9.11}$$

In principle, one would need to differentiate between $F_\pi^V(s)$ and $f_+(s)$ for electromagnetic (Eq. (2.34)) and weak vertices, but since the difference is higher order in isospin–breaking, we use the expression in Eq. (9.10) for both. The unsubtracted form factor in Eq. (9.10) is chosen to ensure that UV divergences already cancel within the triangle diagram itself (in contrast to χPT), at the expense of having to fulfill a posteriori the sum rule in Eq. (9.11) to respect charge conservation.

Our dispersive representation of the triangle diagram (see Fig. 9.2) is sensitive to the high–energy behavior of this unsubtracted form factor. We therefore need to fix the subtraction constants through a matching procedure with the χPT result, in order to guarantee the correct low energy behavior. This step is fundamental not only because our result then display a reduced sensitivity to the high–energy part of the dispersive integrals, but also because it allows us to restore the correct IR singularities, to be canceled from photon real–emissions (see Ch. 12), and the correct chiral logarithms. The detailed procedure is explained in Sec. 11.6.

Chapter 10

Radiative corrections to $\tau \to \pi\pi^0\nu_\tau$ in χPT

As we explained in Ch. 9, radiative corrections to the hadronic τ decay computed in the χPT framework are of fundamental importance in order to restore the correct low–energy behavior in our dispersive computation. In the following sections we detail the χPT computations for the radiative corrections to $\tau \to \pi\pi^0\nu_\tau$, showing explicitly the UV– and IR–divergences cancellation, the latter after considering photon real–emission contribution in the soft–photon approximation.

10.1 χPT representation

At leading order in chiral power counting, the $SU(3)$ χPT Lagrangian including virtual photons and leptons (see Sec. 4.3.5) and relevant for calculating the radiative corrections to $\tau^- \to \pi^-\pi^0\nu_\tau$ includes the terms

$$\begin{aligned}\mathcal{L}_{\text{eff}}^{\text{LO}} \supset\ & \left[(\partial_\mu - ieA_\mu)\,\pi^-\right]\left[(\partial^\mu + ieA^\mu)\,\pi^+\right] + \bar{\tau}\left[i\gamma_\mu\,(\partial^\mu - ieA^\mu) - m_\tau\right]\tau \\ & + i\bar{\nu}_{\tau\text{L}}\partial\!\!\!/\,\nu_{\tau\text{L}} + 2iG_F V_{ud}^*\,\bar{\nu}_{\tau\text{L}}\gamma^\mu\tau\left[\pi^0\,(\partial_\mu + ieA_\mu)\,\pi^+ - \pi^+\partial_\mu\pi^0\right]\ ,\end{aligned} \tag{10.1}$$

where e is the elementary charge, G_F the Fermi constant and V_{ud} a CKM–matrix element. By means of the interactions contained in the LO Lagrangian, the tree–level amplitude for $\tau^-(l_1) \to \pi^-(q_1)\pi^0(q_2)\nu_\tau(l_2)$ is found to be

$$i\mathcal{M}_{\text{tree}} = iG_F V_{ud}^*\bar{u}(l_2,\nu_\tau)(1+\gamma_5)(q\!\!\!/_2 - q\!\!\!/_1)u(l_1,\tau)\ . \tag{10.2}$$

The relevant counterterms of the radiative corrections to the hadronic tau decay originate from terms in the NLO Lagrangians $\mathcal{L}_{e^2p^2}$ and $\mathcal{L}_{\text{lept}}$ listed in Eqs. (4.67) and (4.68) in Sec. 4.3.5.

10.1.1 General Considerations

The decay amplitude of $\tau^-(l_1) \to \pi^-(q_1)\pi^0(q_2)\nu_\tau(l_2)$, once we include radiative corrections, can be written in terms of two form factors by

$$i\mathcal{M} = iG_F V_{ud}^*\bar{u}(l_2,\nu_\tau)\gamma^\mu(1-\gamma_5)u(l_1,\tau)\left[(q_2-q_1)_\mu f_+(s,t) + (q_1+q_2)_\mu f_-(s,t)\right]\ , \tag{10.3}$$

where f_+ represents the contribution due to the $J^P = 1^-$ component of the weak current and f_- vanishes in the isospin limit [34,35].[4] The Mandelstam variables are defined as

$$\begin{aligned} s &= (l_1 - l_2)^2 = (q_1 + q_2)^2 \,, \\ t &= (l_1 - q_1)^2 = (q_2 + l_2)^2 \,, \\ u &= (l_1 - q_2)^2 = (q_1 + l_2)^2 \,. \end{aligned} \tag{10.4}$$

Projecting this expression for the tree–level amplitude onto the form factors, therefore implies

$$f_+^{\text{tree}}(s,t) = 1 \,, \quad f_-^{\text{tree}}(s,t) = 0 \,. \tag{10.5}$$

The spin–averaged squared amplitude can thus be expressed by

$$\begin{aligned} \frac{1}{2}\sum_{\text{spins}} |\mathcal{M}|^2 =& 2G_F^2 |V_{ud}|^2 \Big\{ (m_\tau^4 - m_\tau^2 s)|f_-(s,t)|^2 \\ &- 2m_\tau^2 (2M_{\pi^0}^2 + m_\tau^2 - s - 2t)\,\text{Re}\left[f_+(s,t) f_-^*(s,t)\right] \\ &+ [4M_\pi^2(M_{\pi^0}^2 - t) + 4t(s + t - M_{\pi^0}^2) - m_\tau^2(s + 4t) + m_\tau^4]|f_+(s,t)|^2 \Big\} \,. \end{aligned} \tag{10.6}$$

Furthermore, the differential decay width is given by

$$\mathrm{d}\Gamma = \frac{1}{32 m_\tau^3 (2\pi)^3} \left[\frac{1}{2} \sum_{\text{spins}} |\mathcal{M}|^2 \right] \mathrm{d}s\, \mathrm{d}t \,, \tag{10.7}$$

with the phase space in the $\pi^0\nu_\tau$ invariant mass square limited by $t_{\text{min}} \leq t \leq t_{\text{max}}$ with

$$t_{\text{min}} = (q_2^{0*} + l_2^{0*})^2 - \left[\sqrt{(q_2^{0*})^2 - M_{\pi^0}^2} + l_2^{0*} \right]^2 \,, \tag{10.8}$$

$$t_{\text{max}} = (q_2^{0*} + l_2^{0*})^2 - \left[\sqrt{(q_2^{0*})^2 - M_{\pi^0}^2} - l_2^{0*} \right]^2 \,, \tag{10.9}$$

with particle energies in the $\pi^0\nu_\tau$ center–of–mass frame given by

$$q_2^{0*} = \frac{s - M_\pi^2 + M_{\pi^0}^2}{2\sqrt{s}} \,, \quad l_2^{0*} = \frac{m_\tau^2 - s}{2\sqrt{s}} \,. \tag{10.10}$$

In the $\pi^-\pi^0$ invariant mass squared the phase space is bounded by

$$(M_\pi + M_{\pi^0})^2 \leq s \leq m_\tau^2 \,. \tag{10.11}$$

Ignoring the dependence of $f_\pm(s,t)$ on the second variable, the integral over t reproduces [34]

$$\begin{aligned} \frac{\mathrm{d}\Gamma[\tau \to \pi\pi\nu_\tau]}{\mathrm{d}s} =& \frac{\Gamma_e^{(0)} |V_{ud}|^2}{2m_\tau^2} \beta_{\pi\pi^0}(s) \left(1 - \frac{s}{m_\tau^2}\right)^2 \left[\left(\left[\beta_{\pi\pi^0}(s)\right]^2 \left(1 + \frac{2s}{m_\tau^2}\right) + \frac{3\Delta_\pi^2}{s^2} \right) \left|f_+(s)\right|^2 \right. \\ &\left. - \frac{6\Delta_\pi}{s}\,\text{Re}\left[f_+(s) f_-^*(s)\right] + 3\left|f_-(s)\right|^2 \right] . \end{aligned} \tag{10.12}$$

[4] This is an example of a second–class current [230,231]. As shown in [231], f_- can be traded for a scalar from factor $f_0(s)$, with $f_0(0) = 1$ and $f_-(s) = \frac{\Delta_\pi}{s}\left[f_+(s) - f_0(s)\right]$, which shows that $f_-(s)$ scales with the pion mass difference $\Delta_\pi = M_\pi^2 - M_{\pi^0}^2$.

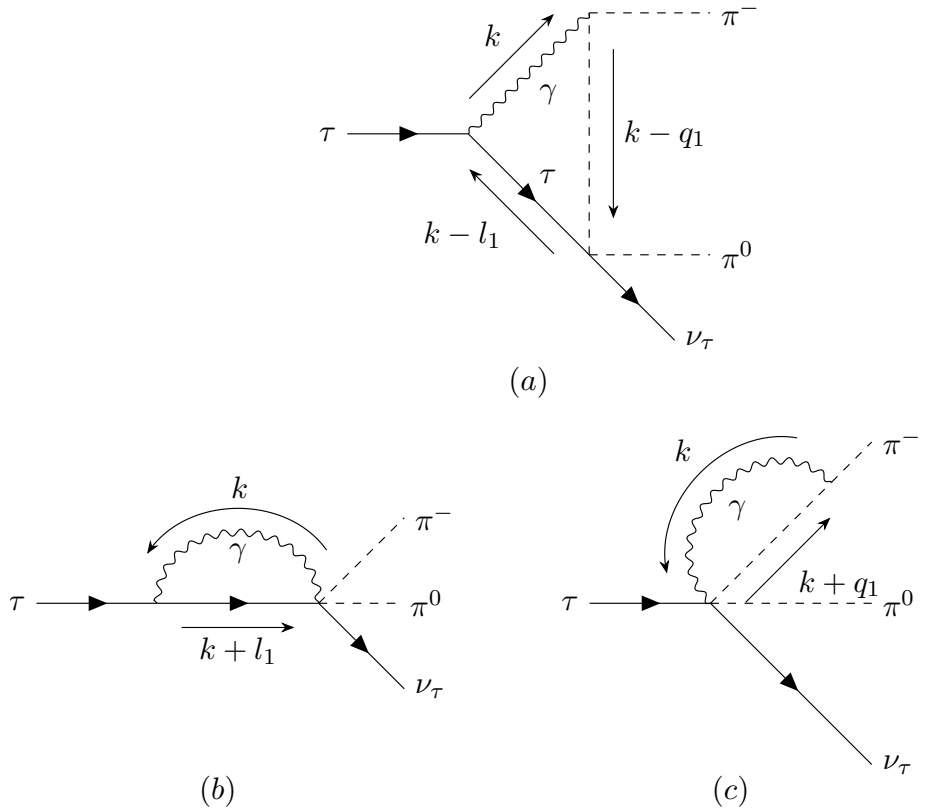

Figure 10.1: Leading diagrams for the radiative corrections to $\tau^-(l_1) \to \pi^-(q_1)\pi^0(q_2)\nu_\tau(l_2)$ excluding wave function renormalization.

10.2 Radiative corrections

At $\mathcal{O}(e^2p^2)$ in χPT, the diagrams arising from the lowest order effective Lagrangian of [190] are shown in Fig. 10.1. In this work, we employ dimensional regularization to deal with both the UV and the IR divergences arising in the computation. Following the definition in Eq. (10.3), the form factors $f_+(s,t)$ for the diagrams in Fig. 10.1 read

$$\begin{aligned} f_+^{(a)}(t) = \frac{e^2}{16\pi^2}\Bigg\{ &- \frac{A_0(M_\pi^2)}{4M_\pi^2} + \frac{1}{m_\tau^4 - 2m_\tau^2(M_\pi^2+t) + (M_\pi^2-t)^2} \\ &\times \Big[2\left(m_\tau^4 - 2tm_\tau^2 + t(t-M_\pi^2)\right) B_0(M_\pi^2, 0, M_\pi^2) \\ &- \left(m_\tau^2(3M_\pi^2+t) + m_\tau^4 - 2(M_\pi^2-t)^2\right) B_0(m_\tau^2, 0, m_\tau^2) \\ &+ \left(m_\tau^2(t-M_\pi^2) + m_\tau^4 + 2t(M_\pi^2-t)\right) B_0(t, M_\pi^2, m_\tau^2) \Big] \\ &+ 2\left(m_\tau^2 + M_\pi^2 - t\right) C_0(M_\pi^2, t, m_\tau^2, 0, M_\pi^2, m_\tau^2) \Bigg\} , \end{aligned} \tag{10.13}$$

$$f_+^{(b)}(t) = 0 , \tag{10.14}$$

$$f_+^{(c)}(t) = \frac{e^2}{16\pi^2 4M_\pi^2}\left[A_0(M_\pi^2) - 4M_\pi^2 B_0(M_\pi^2, 0, M_\pi^2)\right] . \tag{10.15}$$

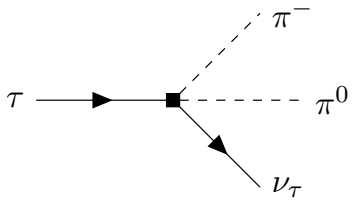

Figure 10.2: Counterterm diagram for the radiative corrections to $\tau^- \to \pi^-\pi^0\nu_\tau$.

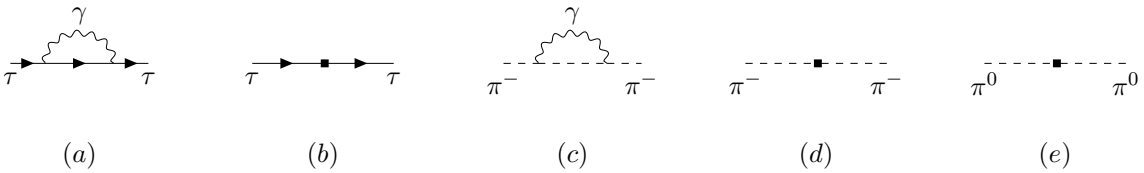

Figure 10.3: Loop and counterterm diagrams of the external leg contributions.

We notice that, in the χPT framework at this order, the form factor $f_+(t)$ depends on the single Mandelstam variable t. The scalar loop integrals used within these expressions are obtained by utilizing Passarino–Veltman reduction techniques [232–238] implemented in FeynCalc [239–242]. Since $f_-(t)$ vanishes in the isospin limit we show from now on only the relevant $f_+(t)$ form factors.

In addition to the one–loop diagrams in Fig. 10.1, a counterterms contribution as in Fig. 10.2 must be included, which gives the following $f_+(t)$

$$f_+^{\rm ct}(t) = \frac{2e^2}{9}\left[12K_1 - 9(K_3 - K_{12}) + 10K_5 - 3X_1\right] \ . \tag{10.16}$$

which is independent on the Mandelstam variable t and where the low–energy constants K_i and X_i contain UV–divergences, which, in dimensional regularization, can be separated from the UV–finite parts accordingly to Eqs. (4.72) and (4.73) with the definition of $\Lambda(\mu)$ in Eq. (4.74).

The $\mathcal{O}(e^2p^2)$ corrections to the τ and π^- 2–point functions in Fig. 10.3 (a) and (c) need to be included and in the case of the τ lepton, this quantity is given by

$$Z_\tau = 1 + \frac{\rm d}{{\rm d}\not{p}}\Sigma_\tau(\not{p})\bigg|_{\not{p}=m_\tau} \ , \tag{10.17}$$

with $\Sigma_\tau(\not{p})$ the associated τ self–energy function. Analogously, for the π^-

$$Z_{\pi^-} = 1 + \frac{\rm d}{{\rm d}p^2}\Sigma_{\pi^-}(p^2)\bigg|_{p^2=M_\pi^2} \ . \tag{10.18}$$

Moreover, the τ and the pions 2–point functions are subject to renormalization by terms from the NLO Lagrangians $\mathcal{L}_{e^2p^2}$ and $\mathcal{L}_{\rm lept}$ (see Fig. 10.3 (b) ,(d) and (e)). The counterterms contribution amounts to [243]

$$\begin{aligned} Z_\tau^{\rm ct} &= -e^2X_6 \ , \\ Z_{\pi^-}^{\rm ct} &= -\frac{4}{9}e^2\left(6K_1 + 5K_5\right) \ , \\ Z_{\pi^0}^{\rm ct} &= -\frac{4}{9}e^2\left(6K_1 - 9K_3 + 5K_5\right) \ . \end{aligned} \tag{10.19}$$

Their contribution to the decay amplitude is obtained through

$$\mathcal{M}_{\text{ext.}} = \left(\sqrt{Z^{\text{ct}}_{\pi^0}\left(Z_{\pi^-}+Z^{\text{ct}}_{\pi^-}\right)\left(Z_\tau+Z^{\text{ct}}_\tau\right)}-1\right) i\mathcal{M}_{\text{tree}}\,. \tag{10.20}$$

Altogether the $\mathcal{O}(e^2p^2)$ amplitude to $\tau^- \to \pi^-\pi^0\nu_\tau$ is given by

$$\begin{aligned} i\mathcal{M}_{\text{virt}} &\coloneqq i\mathcal{M}_a + i\mathcal{M}_b + i\mathcal{M}_c + i\mathcal{M}_{\text{ct}} + \left(\sqrt{Z^{\text{ct}}_{\pi^0}\left(Z_{\pi^-}+Z^{\text{ct}}_{\pi^-}\right)\left(Z_\tau+Z^{\text{ct}}_\tau\right)}-1\right) i\mathcal{M}_{\text{tree}} \\ &= \left[f_+^{(a)}(t) + f_+^{(b)}(t) + f_+^{(c)}(t) + f_+^{\text{ct}}(t) + \left(\sqrt{Z^{\text{ct}}_{\pi^0}\left(Z_{\pi^-}+Z^{\text{ct}}_{\pi^-}\right)\left(Z_\tau+Z^{\text{ct}}_\tau\right)}-1\right)\right] i\mathcal{M}_{\text{tree}}\,. \end{aligned} \tag{10.21}$$

10.2.1 UV–divergences cancellation

The UV–divergent terms arising from the diagram in Fig. 10.1 appear as

$$\begin{aligned} f_+^{(a)}(t)\big|_{\text{UV-div.}} &= -\frac{7e^2}{64\pi^2}32\pi^2\Lambda_{\text{UV}}\,, \\ f_+^{(b)}(t)\big|_{\text{UV-div.}} &= 0\,, \\ f_+^{(c)}(t)\big|_{\text{UV-div.}} &= \frac{3e^2}{64\pi^2}32\pi^2\Lambda_{\text{UV}}\,, \end{aligned} \tag{10.22}$$

where Λ_{UV} is defined in Eq. (4.74) with the subscript indicating that it refers only to the UV–divergent contribution (in the following we will employ Λ_{IR} for the IR–divergent terms in dimensional regularization). For the counterterm Lagrangian we obtain

$$f_+^{\text{ct}}(t)\big|_{\text{UV-div.}} = -\frac{2e^2}{64\pi^2}32\pi^2\Lambda_{\text{UV}}\,. \tag{10.23}$$

The UV–divergent contribution to the τ and pions external legs corrections (Fig. 10.3) are

$$\begin{aligned} &\left(\sqrt{Z_\tau Z_{\pi^-}}-1\right)\Big|_{\text{UV-div.}} = -\frac{2e^2}{64\pi^2}32\pi^2\Lambda_{\text{UV}}, \\ &\left(\sqrt{(1+Z^{\text{ct}}_{\pi^-})(1+Z^{\text{ct}}_{\pi^0})(1+Z^{\text{ct}}_\tau)}-1\right)\Big|_{\text{UV-div.}} = \frac{8e^2}{64\pi^2}32\pi^2\Lambda_{\text{UV}}\,. \end{aligned} \tag{10.24}$$

Altogether the UV divergences therefore cancel: $i\mathcal{M}_{\text{virt}}|_{\text{UV-div}} = 0$.

10.3 IR–divergences in the soft–photon approximation

We will now compute the photon real emission contribution in the soft–photon limit and in sQED and we will explicitly see how these results cancel the IR–divergences present in the virtual contributions in the χPT framework.

By considering the box diagram amplitude in sQED, i.e., Fig. 10.1 (a), the IR–divergent contribution reads

$$f_+^{(a)}(t)\Big|_{\text{IR-div}} = \frac{e^2}{16\pi^2}2\big(M_\pi^2+m_\tau^2-t\big)\Big(-\frac{tB_0^{\pi\tau}(t)}{\lambda_{\pi\tau}(t)}32\pi^2\Lambda_{\text{IR}}\Big) \tag{10.25}$$

where

$$B_0^{\pi\tau}(t) = \frac{\lambda_{\pi\tau}^{1/2}(t)}{t}\log x_t\,, \qquad x_t = -\frac{t-(m_\tau-M_\pi)^2-\lambda_{\pi\tau}^{1/2}(t)}{t-(m_\tau-M_\pi)^2+\lambda_{\pi\tau}^{1/2}(t)}\,, \tag{10.26}$$

and $\lambda_{\pi\tau}(t) = \lambda(t, M_\pi^2, m_\tau^2)$ is the Källén function. This can be written at the amplitude level and explicitly in terms of $\epsilon_{\rm IR} = d-4$ as

$$i\mathcal{M}_a\Big|_{\text{IR-div.}} = \frac{\mathcal{M}_-^{\text{red.}}}{\epsilon_{\rm IR}} 8\frac{m_\tau^2+M_\pi^2-t}{\lambda_{\pi\tau}^{1/2}(t)}\log\left(\frac{m_\tau^2+M_\pi^2-t+\lambda_{\pi\tau}^{1/2}(t)}{2m_\tau M_\pi}\right)\,, \tag{10.27}$$

where

$$\mathcal{M}_-^{\text{red.}} := \frac{ie^2G_FV_{ud}^*}{16\pi^2}\bar{u}(l_2,\nu_\tau)\left[\not{q}_1-\not{q}_2\right]u(p_1,\tau)\,. \tag{10.28}$$

while the amplitudes $\mathcal{M}_b$ and $\mathcal{M}_c$ do not contain any IR–divergent parts. On the other hand, the self–energy (SE) diagrams contribute with

$$f_+^{\rm SE}(t) = \frac{e^2}{16\pi^2}64\pi^2\Lambda_{\rm IR} \tag{10.29}$$

which again can be written in terms of the reduced amplitude as

$$\sqrt{Z_{\pi^-}}\,i\mathcal{M}_{\text{tree}}\Big|_{\text{IR-div.}} = \sqrt{Z_\tau}\,i\mathcal{M}_{\text{tree}}\Big|_{\text{IR-div.}} = -\frac{4}{\epsilon_{\rm IR}}\mathcal{M}_-^{\text{red.}}\,. \tag{10.30}$$

For the purpose of canceling the IR divergences, it is useful to express this contribution in terms of the tree–level differential decay width,

$$\mathrm{d}\Gamma^{\text{tree}} = \frac{1}{(2\pi)^3 32m_\tau^3}\left[\frac{1}{2}\sum_{\text{spins}}|\mathcal{M}^{\text{tree}}|^2\right]\mathrm{d}s\,\mathrm{d}t\,, \tag{10.31}$$

with

$$\frac{1}{2}\sum_{\text{spins}}|\mathcal{M}^{\text{tree}}|^2 = 4G_F^2|V_{ud}|^2\left[4\left(M_\pi^4-2M_\pi^2t+t(s+t)\right)+m_\tau^4-m_\tau^2(s+4t)\right]\,.$$

in the isospin limit, i.e., $M_{\pi^0} = M_\pi$. The IR–divergent contribution to the differential decay width arising from the interference of the triangle diagram with the tree–level amplitude can be expressed by

$$\mathrm{d}\Gamma_a\Big|_{\text{IR-div.}} = -\frac{e^2}{2\pi^2\epsilon_{\rm IR}}\frac{m_\tau^2+M_\pi^2-t}{\lambda_{\pi\tau}^{1/2}(t)}\log\left(\frac{m_\tau^2+M_\pi^2-t+\lambda_{\pi\tau}^{1/2}(t)}{2m_\tau M_\pi}\right)\mathrm{d}\Gamma^{\text{tree}}\,, \tag{10.32}$$

where this specific contribution to the differential decay width is defined as

$$\mathrm{d}\Gamma_a = \frac{(2\pi)^4}{2m_\tau}\sum_{\text{spins}}\{i\mathcal{M}_a(i\mathcal{M}_{\text{tree}})^* + i\mathcal{M}_{\text{tree}}(i\mathcal{M}_a)^*\}\,\mathrm{d}\Phi_3(l_1;l_2,q_1,q_2)\,,$$

with n–body phase space in PDG conventions [244] defined by

$$\mathrm{d}\Phi_n(P;p_1,\ldots,p_n) = \delta^{(4)}\big(P-\sum_{i=1}^n p_i\big)\prod_{i=1}^n\frac{\mathrm{d}^3p_i}{(2\pi)^3 2p_i^0}\,. \tag{10.33}$$

The IR–divergent contribution of the wave function renormalization to the differential decay width can be written as

$$\mathrm{d}\Gamma_{Z_{\pi^-}}\Big|_{\text{IR-div.}} = \mathrm{d}\Gamma_{Z_\tau}\Big|_{\text{IR-div.}} = \frac{e^2}{4\pi^2\epsilon_{\text{IR}}}\mathrm{d}\Gamma^{\text{tree}} \,. \tag{10.34}$$

To obtain an IR–finite result we need to consider also the initial– and final–state radiation contribution which includes the following amplitudes

$i\mathcal{M}^{\text{ISR}} =$ 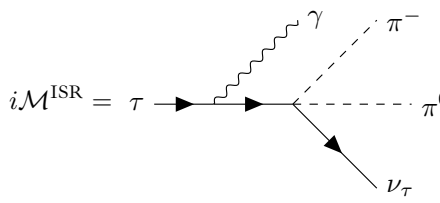

, $i\mathcal{M}^{\text{FSR}} =$ 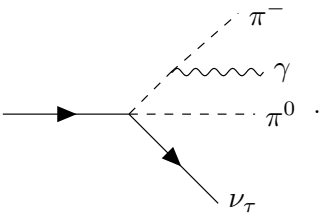

. (10.35)

and for this computation, the soft photon approximation (SPA) can be employed. In the calculation of squared amplitudes, cross sections and decay widths, photon momenta appearing in the numerators are to be neglected in this approximation, in order to extract the leading term in the Low expansion.

The initial–state radiation diagram shown above contributing to $\tau^-(l_1) \to \pi^-(q_1)\pi^0(q_2)\nu_\tau(l_2)\gamma(k)$ evaluates to

$$i\mathcal{M}^{\text{ISR}} = -2iG_F V_{ud}\bar{u}(l_2,\nu_\tau)\left(\not{q}_1 - \not{q}_2\right)\frac{i\left(\not{l}_1 - \not{k} + m_\tau\right)}{(l_1-k)^2 - m_\tau^2}(ie\gamma_\mu)u(l_1,\tau)\left(\epsilon^\mu(k)\right)^* . \tag{10.36}$$

Note that the denominator of this amplitude can be simplified to

$$(l_1-k)^2 - m_\tau^2 = -2l_1\cdot k \,, \tag{10.37}$$

for an on–shell τ. Furthermore, by using Dirac algebra, part of the numerator can be written as

$$\begin{aligned}\left(\not{l}_1 - \not{k} + m_\tau\right)\gamma_\mu u(l_1,\tau) &= \left[2g_{\mu\nu}(l_1-k)^\nu - \gamma_\mu(\not{l}_1 - \not{k} - m_\tau)\right]u(l_1,\tau) \\ &\overset{\text{SPA}}{\approx} \left[2l_{1\mu} - \gamma_\mu(\not{l}_1 - m_\tau)\right]u(l_1,\tau) = 2l_{1\mu}u(l_1,\tau) \,.\end{aligned} \tag{10.38}$$

Therefore, the initial–state radiation amplitude in the SPA appears as

$$i\mathcal{M}^{\text{ISR}} = i\mathcal{M}^{\text{tree}}\left[e\,\frac{l_1\cdot\epsilon^*(k)}{l_1\cdot k}\right] \,. \tag{10.39}$$

Likewise, the final–state radiation amplitude can be expressed as

$$\begin{aligned}i\mathcal{M}^{\text{FSR}} &= 2ieG_F V_{ud}\bar{u}(l_2,\nu_\tau)\left(\not{q}_1 + \not{k} - \not{q}_2\right)u(l_1,\nu_\tau)\frac{(2q_1+k)_\mu}{(q_1+k)^2 - M_\pi^2}\left(\epsilon^\mu(q)\right)^* \\ &\overset{\text{SPA}}{\approx} i\mathcal{M}^{\text{tree}}\left[-e\,\frac{q_1\cdot\epsilon^*(k)}{q_1\cdot k}\right] \,.\end{aligned} \tag{10.40}$$

Note that in SPA the phase–space integration over the soft–photon momentum can be separated

$$\mathrm{d}\Gamma^{\text{brems}} = \frac{(2\pi)^4}{2m_\tau}\left[\frac{1}{2}\sum_{\text{spins}}\left|\mathcal{M}^{\text{ISR}} + \mathcal{M}^{\text{FSR}}\right|^2\right]\mathrm{d}\Phi_4(p_1;p_2,l_1,l_2,q)$$

$$\overset{\text{SPA}}{\approx} \mathrm{d}\Gamma^{\text{tree}} \int' \frac{\mathrm{d}^{d-1}k}{(2\pi)^{d-1}} \frac{1}{2|\mathbf{k}|} \sum_{\text{pol.}} e^2 \left| \frac{l_1 \cdot \epsilon^*}{l_1 \cdot k} - \frac{q_1 \cdot \epsilon^*}{q_1 \cdot k} \right|^2 , \tag{10.41}$$

by neglecting the photon momentum in the argument of the 4–momentum conserving δ–function and where the primed integral only runs over photon momenta $\left|\mathbf{k}\right| < \Delta$, where Δ is a resolution parameter. Performing the polarization sum, the integrand appears as

$$\sum_{\text{pol.}} \left| \frac{l_1 \cdot \epsilon^*}{l_1 \cdot k} - \frac{q_1 \cdot \epsilon^*}{q_1 \cdot k} \right|^2 = \frac{2 l_1 \cdot q_1}{(l_1 \cdot k)(q_1 \cdot k)} - \frac{m_\tau^2}{(l_1 \cdot k)^2} - \frac{M_\pi^2}{(q_1 \cdot k)^2} \, . \tag{10.42}$$

The integrals have been worked out in [236] and earlier in [245–248]. However we are working in dimensional regularization also for the infrared divergences so we recapitulate here our derivation [249]. The terms of the integrand in Eq. (10.41) can be split up

$$\mathrm{d}\Gamma^{\text{brems}} = e^2 \mathrm{d}\Gamma^{\text{tree}} \left[2(l_1 \cdot q_1) I^{\text{int}} - m_\tau^2 I^{\text{ISR}} - M_\pi^2 I^{\text{FSR}} \right] \, . \tag{10.43}$$

and a detailed computation of the different terms is given in App. F. Here we give only the result for the IR divergent contribution:

$$\mathrm{d}\Gamma^{\text{brems}} = \frac{e^2}{2\pi^2 \epsilon_{\text{IR}}} \left[-1 + \frac{m_\tau^2 + M_\pi^2 - t}{\lambda_{\pi\tau}^{1/2}(t)} \log \left(\frac{m_\tau^2 + M_\pi^2 - t + \lambda_{\pi\tau}^{1/2}(t)}{2 m_\tau M_\pi} \right) \right] \mathrm{d}\Gamma^{\text{tree}} \, , \tag{10.44}$$

This term perfectly cancels the IR–divergences coming from virtual corrections in Eqs. (10.32) and (10.34).

Chapter 11

Dispersive analysis of the isospin breaking corrections to $\tau \longrightarrow \pi\pi^0\nu_\tau$

As we saw in Sec. 9.2, the only relevant diagram is the one in Fig. 9.2. In fact, by considering the other loop contributions in the χPT framework, the diagrams (b) and (c) in Fig. 10.1 do not generate analytic singularities in the Mandelstam variables. In order to take into account the strong final–state interactions between τ^- and π^0, since the main purpose of studying this decay concerns a precision measurement of the corresponding πVFF, the tree–level vertex (see Eq. (10.3)) needs to be modified accordingly:

$$i\mathcal{M} \to -iG_F V_{ud}^* \bar{u}(l_2,\nu_\tau)\gamma^\mu(1-\gamma_5)u(l_1,\tau) f_+(s)\left[(q_1-q_2)_\mu(1+\kappa_+(s,t)) + (q_1+q_2)_\mu \kappa_-(s,t)\right] , \tag{11.1}$$

where $f_+(s)$ is the pion vector form factor as defined in the non–radiative process, and by factoring it out, the remaining scalar functions, $\kappa_+(s,t)$ and $\kappa_-(s,t)$, are redefined accordingly. The $\Delta(s,t)$ term in Eq. (9.7) entering the $G_{\rm EM}(s)$ definition therefore read

$$\Delta(s,t) = 1 + 2\ \mathrm{Re}\,\kappa_+(s,t) + g_{\rm Low}(s,t) + g_{\rm rest}(s,t)\ . \tag{11.2}$$

In this chapter, we work out our new model–independent dispersive approach which sets the understanding of the isospin–breaking effects to the hadronic τ decay on a more solid ground.

11.1 Triangle–diagram supplemented by form factors

By considering our dispersive triangle diagram (see Fig. 9.2 and Eq. (9.10)), and projecting it onto the $\kappa_+(s,t)$ form factor, analogously to what was done in Eq. (10.3), the following expression can be obtained

$$\kappa_+^{\rm disp}(s,t) = \frac{e^2}{16\pi^4 f_+(s)} \int_{4M_\pi^2}^\infty \mathrm{d}s'\,\mathrm{d}s''\left[\tilde{\kappa}_B(s,s',s'') + \tilde{\kappa}_C(s,t,s',s'') + \tilde{\kappa}_D(s,t,s',s'')\right] , \tag{11.3}$$

where

$$\begin{aligned}
\tilde{\kappa}_B &= \frac{\mathrm{Im}\, f_+(s')\,\mathrm{Im}\, f_+(s'')}{2s'(s-4M_\pi^2)}\left[\bar{B}_0(M_\pi^2,M_\pi^2,s') - 2\bar{B}_0(s,s',s'')\right] , \\
\tilde{\kappa}_C &= \frac{\mathrm{Im}\, f_+(s')\,\mathrm{Im}\, f_+(s'')}{2s'\left[s((t-M_\pi^2)^2+st) + M_\pi^2 m_\tau^4 - m_\tau^2 s(M_\pi^2+t)\right]} \\
&\quad\times\Big\{ -\left[2st(t-M_\pi^2) + m_\tau^6 + m_\tau^4(2M_\pi^2 - s - 2t) - m_\tau^2(M_\pi^2-t)(M_\pi^2-s+t)\right]
\end{aligned}$$

$$
\begin{aligned}
&\times \bar{C}_0(m_\tau^2, M_\pi^2, t, m_\tau^2, s', M_\pi^2) \\
&+ \big[2s(2M_\pi^4 - 4M_\pi^2 t + t(s+2t)) + m_\tau^6 + m_\tau^4(3M_\pi^2 - 2s - t) + m_\tau^2 s(s - t - 3M_\pi^2)\big] \\
&\quad \times \bar{C}_0(0, m_\tau^2, s, s'', m_\tau^2, s') \\
&- \Big[s\big\{M_\pi^4(s - s'' - 16t) + 2M_\pi^2 t(5s + s'' + 8t) - t(t(3s + s'') + s(s + s''))\big\} \\
&\quad + m_\tau^4\left(8M_\pi^4 + M_\pi^2(3s - s'') - s^2\right) \\
&\quad + m_\tau^2 s\big(4M_\pi^4 + M_\pi^2(s'' - 6s - 20t) + s^2 + 4st + s''t\big)\Big] \frac{\bar{C}_0(M_\pi^2, M_\pi^2, s, s', M_\pi^2, s'')}{s - 4M_\pi^2} \\
&- \frac{s'\big(m_\tau^2 s(M_\pi^2 + t) - m_\tau^4 M_\pi^2 - s((t - M_\pi^2)^2 + st)\big)}{s - 4M_\pi^2} C_0(M_\pi^2, M_\pi^2, s, s', M_\pi^2, s'')\Bigg\}, \\
\tilde{\kappa}_D = &\frac{\operatorname{Im} f_+(s') \operatorname{Im} f_+(s'')}{2s'\big[s((t - M_\pi^2)^2 + st) + M_\pi^2 m_\tau^4 - m_\tau^2 s(M_\pi^2 + t)\big]} \\
&\times \Big\{s'(t - M_\pi^2)\big[m_\tau^2(M_\pi^2 + s + t) - 2st - m_\tau^4\big] D_0(m_\tau^2, M_\pi^2, M_\pi^2, 0, t, s, m_\tau^2, s', M_\pi^2, s'') \\
&+ \Big[m_\tau^6\left(4M_\pi^2 + s - s''\right) + m_\tau^4\left(4M_\pi^4 - 2M_\pi^2(s + s'' + 2t) - s^2 + ss'' - 6st + 2s''t\right) \\
&\quad + m_\tau^2\big(M_\pi^4(s'' - s) + M_\pi^2 s(s - s'' - 8t) + t\big(3s^2 + ss'' + 9st - s''t\big)\big) \\
&\quad + 2s\left(M_\pi^2 - t\right)\left(2M_\pi^4 - 4M_\pi^2 t + t(s + s'' + 2t)\right)\Big] \\
&\quad \times \bar{D}_0(m_\tau^2, M_\pi^2, M_\pi^2, 0, t, s, m_\tau^2, s', M_\pi^2, s'')\Big\},
\end{aligned}
\tag{11.4}
$$

where

$$
\bar{F}_0(..., s', ...) := F_0(..., s', ...) - F_0(..., 0, ...)\,, \qquad F \in B, C, D\,. \tag{11.5}
$$

Differently from the χPT analysis, here the form factor $\kappa_+(s,t)$ indeed depends on both Mandelstam variables s and t. Moreover, thanks to the use of the unsubtracted dispersive representation of $f_+(s)$, the result is now manifestly UV finite, i.e., the suppression of the high–energy modes due to the additional propagators is enough to render the loop integrals finite. Note also that the common prefactor appearing in the denominators of $\tilde{\kappa}_C$ and $\tilde{\kappa}_D$ can be written as

$$
s((t - M_\pi^2)^2 + st) + M_\pi^2 m_\tau^4 - m_\tau^2 s(M_\pi^2 + t) = s(t - t_{\min})(t - t_{\max})\,, \tag{11.6}
$$

for $t_{\min/\max}$ of Eqs. (10.8) and (10.9) in the isospin limit. These divergences at the border of the phase space are canceled by corresponding zeros in the numerator, but the cancellation needs to be made explicit for a stable implementation (see Sec. 11.4).

11.2 Pion vector form factor $f_+(s)$

The pion vector form factor $f_+(s)$ for the $\tau^- \to \pi^-\pi^0\nu_\tau$ decay will be determined by fitting the experimental data (see Sec. 13.1) and the following ansatz is taken

$$
f_+(s) = \left[1 + G_{\text{in}}^N(s) + \sum_{V=\rho',\,\rho''} c_V \mathcal{A}_{\rho'\rho''}(s)\right] \Omega_1^1(s)\,, \tag{11.7}
$$

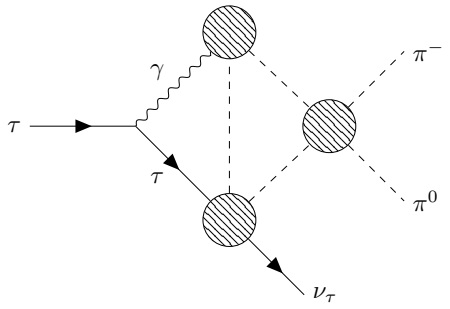

Figure 11.1: $\pi\pi$ rescattering diagram for the decay $\tau^- \to \pi^-\pi^0\nu_\tau$

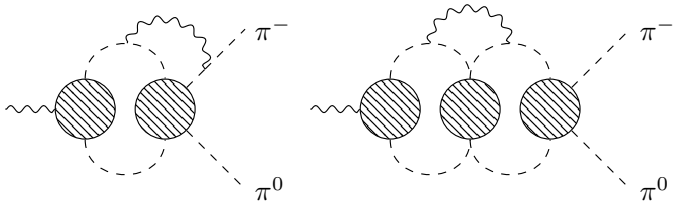

Figure 11.2: Higher order radiative correction to the $\pi\pi$ scattering amplitude.

where the Omnès function [142]

$$\Omega_1^1(s) \equiv \exp\left(\frac{s}{\pi}\int_{4M_\pi^2}^{\infty} \mathrm{d}x \frac{\delta_1^1(x)}{x(x-s-i\epsilon)}\right) , \tag{11.8}$$

is constructed from the $\pi\pi$ P–wave phase shift from solving Roy equations and taking its values at $\delta(s_0)$ and $\delta(s_1)$ with $\sqrt{s_0} = 0.8$ GeV and $\sqrt{s_1} = 1.15$ GeV as fitting parameters [102]. Above $\sqrt{s_c^\delta} = 1.3$ GeV, the phase shift is continued to the value of π with the prescription

$$\delta(s) = \pi - \frac{\left(\pi - \delta(s_c^\delta)\right)^2}{\pi - \delta(s_c^\delta) + \delta'(s_c^\delta)(s - s_c^\delta)} , \tag{11.9}$$

ensuring $\delta(s)$ is continuously differentiable at s_c^δ.

The P–wave phase shift entering Eq. (11.8) is the one in the isospin limit. For a complete analysis on the isospin breaking effects in the hadronic τ decay, this quantity must also include such corrections, which leads to the connection with the isospin breaking corrections in the $\pi\pi$ scattering amplitude, previously described in this work (see Chs. 6–8). Once we include radiative corrections, the isospin limit P–wave phase $\delta_1^1(s)$ is replaced by $\delta^{\mathrm{IB}}(s)$ obtained from $t_P^{+0}(s)$ in Ch. 8, which account for effects due to the charged–neutral pion mass difference. This will allow us to compute rescattering effects as the one in Fig. 11.1. The last step is to include the contribution from further virtual photons in the computation of isospin breaking effects in $\pi\pi$ scattering, i.e., not only effects due to $M_{\pi^0} \neq M_\pi$. This is still a work in progress and will give rise to corrections as the ones in Fig. 11.2, which contribute in the hadronic τ decay through the diagram in Fig. 11.3.

The conformal polynomial

$$G_{\mathrm{in}}^N(s) = \sum_{k=1}^{N} p_k \left(z^k(s) - z^k(0)\right) , \tag{11.10}$$

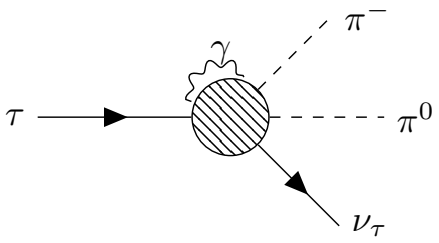

Figure 11.3: Contribution from higher order virtual photons to the hadronic τ decay.

in Eq. (11.7), with conformal variable

$$z(s) = \frac{\sqrt{s_{\rm in} - s_c} - \sqrt{s_{\rm in} - s}}{\sqrt{s_{\rm in} - s_c} + \sqrt{s_{\rm in} - s}} \,, \tag{11.11}$$

should account for inelastic channels, such as 4π. In view of the phenomenological finding that inelasticities below the $\pi\omega$ threshold are negligible, we set $s_{\rm in} = (M_\omega + M_\pi)^2$. Note that for $s > s_{\rm in}$, the square root in $z(s)$ can be analytically continued as $\sqrt{s_{\rm in} - s} \to -i\sqrt{s - s_{\rm in}}$, such that $z(s)$ matches the behavior of $z(s + i\epsilon)$ with infinitesimally small $\epsilon > 0$. Furthermore, the correct threshold behavior of $G_{\rm in}^N(s)$ is enforced letting the term $\propto \sqrt{s_{\rm in} - s}$ vanish by means of the condition [102]

$$p_1 = -\sum_{k=2}^{N} k\, p_k \,, \tag{11.12}$$

amounting to $N - 1$ free parameters in $G_{\rm in}(s)$. The point that is mapped to the origin in the conformal map is identified as s_c, which is set to $s_c = -1\,\text{GeV}^2$ in the following.

Because of the use of unsubtracted dispersion relation in the calculation of virtual corrections, the sum rule in Eq. (9.11) is used as a constrained on the inelastic polynomial $G_{\rm in}^N(s)$, such that the coefficient p_2 is given by

$$p_2 = \frac{\pi + \int_{4M_\pi^2}^\infty {\rm d}x\, C_N(s)}{\int_{4M_\pi^2}^\infty {\rm d}x\, C_D(s)} \tag{11.13}$$

with

$$\begin{aligned} C_N(s) &= \frac{1}{s}{\rm Im}\Bigg\{\Omega_1^1(s)\Bigg[\sum_{k=3}^{N} k\, p_k\,(z(s) - z(0)) - \sum_{k=3}^{N} p_k\left(z^k(s) - z^k(0)\right) \\ &\qquad - \sum_{V=\rho',\,\rho''} c_V \mathcal{A}_{\rho'\rho''}(x) - 1\Bigg]\Bigg\} \,, \\ C_D(s) &= \frac{1}{s}{\rm Im}\left\{\Omega_1^1(s)\left[z^2(s) - z^2(0) - 2\,(z(s) - z(0))\right]\right\} \,. \end{aligned} \tag{11.14}$$

The last term takes into account the contribution of the $\rho' \equiv \rho(1450)$ and $\rho'' \equiv \rho(1700)$ resonances in the $\pi\pi$ spectrum. It is given by

$$\mathcal{A}_{\rho'\rho''}(s) = \frac{s}{\pi}\int_{s_{\rm thr}}^\infty {\rm d}x \frac{{\rm Im}\mathcal{A}(s)}{x(x - s - i\epsilon)} \,, \tag{11.15}$$

where

$$\mathrm{Im}\mathcal{A}(s) = \mathrm{Im}\frac{1}{M_V^2 - s - i\sqrt{s}\Gamma_V(s)} \,, \tag{11.16}$$

where the energy–dependent widths are constructed from the $\omega\pi$ phase space [250]

$$\hat{\Gamma}_V(s) = \Gamma_V \frac{\gamma_{V\to\omega\pi}(s)}{\gamma_{V\to\omega\pi}(M_V^2)}\theta\left(s - s_{\rm in}\right) \,, \quad \gamma_{V\to\omega\pi}(s) = \frac{\lambda^{3/2}(s, M_\omega^2, M_\pi^2)}{s^{3/2}} \tag{11.17}$$

neglecting the $V \to \pi\pi$ and $V \to a_1\pi$ ($a_1 \to 3\pi$) decay channels of ρ' and ρ''. In addition, centrifugal barrier factors according to [251, 252]

$$\Gamma_V(s) = \hat{\Gamma}_V(s)\frac{s}{M_V^2}\frac{\lambda(M_V^2, M_\omega^2, M_\pi^2) + 4M_V^2 p_r^2}{\lambda(s, M_\omega^2, M_\pi^2) + 4s\, p_r^2} \,, \quad p_R = 202.4\,\mathrm{MeV} \,, \tag{11.18}$$

are implemented, altering the asymptotic behavior of the energy–dependent widths.

Regarding the contribution of ρ' and ρ'', we also tried fit variants in which these two resonances are directly implemented via the conformal variable [253], but we observed worse performance especially for the ρ'' resonance due to its location very close to the border of the phase space.

With this ansatz for the πVFF, we end up with two free parameters in $\Omega_1^1(s)$ [102], three for each resonance and $N-2$ free parameters in $G_{\rm in}(s)$, to be determined by fitting to experimental data (see Ch.13).

Finally, we can explicitly list the differences between the $e^+e^- \to \pi^+\pi^-$ and $\tau^- \to \pi^-\pi^0\nu_\tau$. In the $e^+e^- \to \pi^+\pi^-$ case there is a ρ^0 resonance dominance and the $\rho - \omega$ mixing is the most important isospin–breaking effect to include in $F_\pi^V(s)$. In this case the P–wave phase is the one in the $\pi^+\pi^-$ channel (for detailed analysis see [102]). For the $\tau^- \to \pi^-\pi^0\nu_\tau$ process instead, the dominant resonance is the ρ^- and there is a contribution from the ρ' and ρ'' resonances to include (no $\rho - \omega$ mixing). The P–wave phase entering $f_+(s)$ is the one in the $\pi^0\pi^-$ channel.

11.3 Numerical treatment of "special" D_0

The scalar integral $D_0(m_\tau^2, M_\pi^2, M_\pi^2, 0, t, s, m_\tau^2, 0, M_\pi^2, s'')$, appearing in the expression for the $\kappa_+^{\rm disp}(s,t)$ form factor, exhibits a singularity at $s'' = s$ introducing a hurdle to overcome when numerically carrying out the dispersion integrals in Eq. (11.3). In the scalar integral, this divergent part appears as

$$D_0(m_\tau^2, M_\pi^2, M_\pi^2, 0, t, s, m_\tau^2, 0, M_\pi^2, s'') = -\frac{d_0(t)}{s'' - s}\left(32\pi^2\Lambda_{\rm IR} + 1 - \log\frac{\mu_{\rm IR}^2}{M_\pi m_\tau}\right) + D_0^{\pi\tau}(s, t, s'') \,, \tag{11.19}$$

where

$$\begin{aligned} D_0^{\pi\tau}(s,t,s'') =& \frac{2d_0(t)}{s''-s}\log\frac{s''}{s''-s} + D_0^{\rm rest}(t,s'') \,, \qquad d_0(t) = -\frac{t}{\lambda_{\pi\tau}(t)}B_0^{\pi\tau}(t) \,, \\ D_0^{\rm rest}(t,s'') =& \frac{1}{s''-s}\frac{1}{\lambda_{\pi\tau}^{1/2}(t)}\Bigg[-\log x_t \log\frac{M_\pi m_\tau}{s''} + \log^2 x_1 + \log^2 x_2 \\ & - \mathrm{Li}_2\big(1 - x_t^2\big) + \sum_{y\in\left\{x_1x_2, \frac{1}{x_1x_2}, \frac{x_1}{x_2}, \frac{x_2}{x_1}\right\}} \mathrm{Li}_2\big(1 - x_t y\big)\Bigg] \,, \end{aligned} \tag{11.20}$$

where $x_1 = \frac{\sqrt{s''}}{m_\tau}$ and $x_2 = \left(\frac{1-\sigma_\pi(s'')}{1+\sigma_\pi(s'')}\right)^{1/2}$, while $B_0^{\pi\tau}(t)$ and x_t are defined in Eq. (10.26). The dispersion integral over s'' can then be written in the following way

$$\kappa_+^{\rm disp}(s,t) \supset \int_{4M_\pi^2}^{\infty} {\rm d}s''\ {\rm Im}\, f_+(s'') \left(\frac{p_1(s,t)+p_2(s,t)s''}{s''-s}\right)\left[2d_0(t)\log\frac{s''}{s''-s} + D_0^{\rm rest}(t,s'')\right]\,, \quad (11.21)$$

where p_1 and p_2 collect the kinematic prefactors independent of s''. In order to ease the numerical integration, we add and subtract the ${\rm Im}\, f_+(s)$ multiplied with the divergent part of the integrand. By doing so, we get

$$\begin{aligned}
\kappa_+^{\rm disp}(s,t) \supset & \int_{4M_\pi^2}^{\infty} {\rm d}s''\left\{{\rm Im}\, f_+(s'') - {\rm Im}\, f_+(s)\right\}\frac{p_1(s,t)+p_2(s,t)s}{s''-s} \\
& \times\left[2d_0(t)\log\frac{s''}{s''-s} + D_0^{\rm rest}(t,s'')\right] \\
& + p_2(s,t)\int_{4M_\pi^2}^{\infty} {\rm d}s''\left\{{\rm Im}\, f_+(s'') - {\rm Im}\, f_+(s)\theta(\Lambda^2-s'')\right\} \\
& \times\left[2d_0(t)\log\frac{s''}{s''-s} + D_0^{\rm rest}(t,s'')\right] \\
& + {\rm Im}\, f_+(s)\Bigg\{d_0(t)\Big[p_2(s,t)I_{\ell 1}(s,\Lambda^2) + \big(p_1(s,t)+p_2(s,t)s\big)I_{\ell 2}(s)\Big] \\
& + \big(p_1(s,t)+p_2(s,t)s\big)\int_{4M_\pi^2}^{\infty}{\rm d}s''\,\frac{D_0^{\rm rest}(t,s'')}{s''-s} + p_2(s,t)\int_{4M_\pi^2}^{\Lambda^2}{\rm d}s''\,D_0^{\rm rest}(t,s'')\Bigg\}\,,
\end{aligned} \quad (11.22)$$

written in terms of the analytically carried out integrals

$$\begin{aligned}
I_{\ell 1}(s,\Lambda^2) &= 2\int_{4M_\pi^2}^{\Lambda^2}{\rm d}s''\log\frac{s''}{s''-s} \\
&= 2\left\{s\log\frac{\Lambda^2-s}{s-4M_\pi^2} + \Lambda^2\log\frac{\Lambda^2}{\Lambda^2-s} + 4M_\pi^2\log\frac{s-4M_\pi^2}{4M_\pi^2} + i\pi(s-4M_\pi^2)\right\}\,, \\
I_{\ell 2}(s) &= 2\int_{4M_\pi^2}^{\infty}{\rm d}s''\frac{1}{s''-s-i\epsilon}\log\frac{s''}{s''-s-i\epsilon} \\
&= 2\,{\rm Li}_2\left(1-\frac{4M_\pi^2}{s}\right) - \frac{2\pi^2}{3} + \left(2\pi i + \log\frac{s}{s-4M_\pi^2}\right)\log\frac{s}{s-4M_\pi^2}\,.
\end{aligned} \quad (11.23)$$

The dependence on the (high–energy) integral cutoff Λ^2 of $I_{\ell 1}$ will cancel the one introduced by the integral $\int {\rm d}s'' D_0^{\rm rest}(t,s'')$ in Eq. (11.22). The imaginary part that emerges from the Cauchy propagator, see Eq. (11.23), also needs to be kept, as it contributes to ${\rm Re}\,\kappa_+(s,t)$ due to the imaginary part of $f_+(s)$ in Eq. (11.3).

11.4 Endpoint singularities in the phase–space

As pointed out in Sec. 11.1, the common denominator in the expression of the triangle–diagram supplemented with pion VFF can be written as in Eq. (11.6). This gives an endpoint singularity once the phase space integral in t is performed. However, by numerically evaluating these contributions is possible to show that the two infinities cancel and the result is finite. As a first step we can split the triangle form

factor $\kappa_+^{\rm disp}(s,t)$ (see Eq. (11.3)) in the following two contributions

$$\kappa_+^{\rm disp}(s,t) = \frac{e^2}{16\pi^4 f_+(s)} \int_{4M_\pi^2}^{\infty} {\rm d}s' \, {\rm d}s'' \left[\kappa_+^{\rm fin}(s,t,s',s'') + \frac{N(s,t,s',s'')}{s(t-t_{\rm min})(t-t_{\rm max})} \right] , \tag{11.24}$$

where $t_{\rm min/max}$ are defined in Eqs. (10.8) and (10.9), while $\kappa_+^{\rm fin}(s,t,s',s'')$ includes all the terms of $\kappa_+^{\rm disp}(s,t)$ without the divergent denominator and it corresponds to $\tilde{\kappa}_B(s,s',s'')$ in Eq. (11.4). In order to analytically show that the divergences at $t - t_{\rm min/max}$ explicitly cancel we want to rearrange the numerator as $N(s,t,s',s'') = (t-t_{\rm min})(t-t_{\rm max})\bar{N}(s,t,s',s'')$. After checking that $N(s,t_{\rm min},s',s'') = N(s,t_{\rm max},s',s'') = 0$, which can be proved analytically using the algorithm provided in [238] to factorize D_0 at the phase–space boundary into simpler loop functions

$$\begin{aligned}
&D_0(m_\tau^2, M_\pi^2, M_\pi^2, 0, t, s, m_\tau^2, s', M_\pi^2, s'')\big|_{t=t_{\rm min/max}} \\
&= \frac{1}{\mathcal{D}(s,t,s',s'')} \Bigg\{ \Big[m_\tau^4 \, (s''-s) + s \, (s-s'-s'') \, \big(t - M_\pi^2\big) \\
&\qquad + m_\tau^2 \Big(s(s-s'') + (s+s'-s'')(t-M_\pi^2) \Big) \Big] C_0(0, m_\tau^2, s, s'', m_\tau^2, s') \\
&\quad + \Big[2\big(m_\tau^4 M_\pi^2 + s s'' t\big) + (s-s'+s'')(M_\pi^2 - t)^2 - m_\tau^2 (s+s'')(t+M_\pi^2) \Big] \\
&\qquad \times C_0(0, M_\pi^2, t, m_\tau^2, s'', M_\pi^2) \\
&\quad + \Big[m_\tau^4 (s-s'') + (s+s'-s'')(M_\pi^2 - t)^2 + 2 s s' t - m_\tau^2 (2s + s' - 2s'')(t + M_\pi^2) \Big] \\
&\qquad \times C_0(m_\tau^2, M_\pi^2, t, m_\tau^2, s', M_\pi^2) \\
&\quad + \Big[m_\tau^2 \Big(2M_\pi^2 (s + s' - s'') + s(s'' - s) \Big) + s(s - s' - s'')(t + M_\pi^2) \Big] \\
&\qquad \times C_0(M_\pi^2, M_\pi^2, s, s', M_\pi^2, s'') \Bigg\} \Bigg|_{t=t_{\rm min/max}} ,
\end{aligned} \tag{11.25}$$

with

$$\begin{aligned}
\mathcal{D}(s,t,s',s'') &= \lambda_{\pi\tau}(t) \lambda(s,s',s'') \\
&\quad + s' \Big[m_\tau^4 \left(s' - 4M_\pi^2 \right) + 2 m_\tau^2 \left(s - s' + s'' \right) \left(m_\tau^2 - M_\pi^2 - t \right) - 4 s s'' t \Big] ,
\end{aligned} \tag{11.26}$$

and likewise for the second D_0 function with $s' = 0$. Inserting these relations into Eqs. (11.3) and (11.4), indeed the numerators vanish, canceling the zero in the denominator of Eq. (11.6). Accordingly, we can write

$$N(s,t,s',s'') = N(s,t,s',s'') - N(s,t_{\rm max},s',s'') \equiv (t - t_{\rm max}) N_+(s,t,s',s'') , \tag{11.27}$$

such that $N_+(s,t,s',s'') = \frac{N(s,t,s',s'') - N(s,t_{\rm max},s',s'')}{(t-t_{\rm max})}$. Then

$$\begin{aligned}
N(s,t,s',s'') &= (t - t_{\rm max}) N_+(s,t,s',s'') \\
&= (t - t_{\rm max}) [N_+(s,t,s',s'') - N_+(s,t_{\rm min},s',s'')] \\
&= (t - t_{\rm max})(t - t_{\rm min}) \bar{N}(s,t,s',s'') .
\end{aligned} \tag{11.28}$$

After this rearrangement, the $\bar{N}(s,t,s',s'')$ in Eq. (11.28) can be divided into three contributions

$$\bar{N}(s,t,s',s'') = \bar{N}^{\rm fin}(s,t,s',s'') + \bar{N}_+(s,t,s',s'') + \bar{N}_-(s,t,s',s'') \,. \tag{11.29}$$

The first term does not present the endpoint singularities anymore and it can be grouped in $\kappa_+^{\rm fin}(s,t,s',s'')$ such that

$$\begin{aligned}
\kappa_+^{\rm fin} =& \frac{{\rm Im}\, f_+(s')\,{\rm Im}\, f_+(s'')}{s'}\Bigg\{ \frac{\bar{B}_0(M_\pi^2,M_\pi^2,s') - 2\bar{B}_0(s,s',s'')}{2(s-4M_\pi^2)} + 2\bar{C}_0(0,m_\tau^2,s,s'',m_\tau^2,s') \\
&+ \frac{C_0(M_\pi^2,M_\pi^2,s,s',M_\pi^2,s'')}{2(s-4M_\pi^2)} + \frac{3s+s''-16M_\pi^2}{2(s-4M_\pi^2)}\bar{C}_0(M_\pi^2,M_\pi^2,s,s',M_\pi^2,s'') \\
&- \frac{2s+m_\tau^2}{2s}\bar{C}_0(m_\tau^2,M_\pi^2,t,m_\tau^2,s',M_\pi^2) + \frac{m_\tau^2-2s}{2s}D_0(m_\tau^2,M_\pi^2,M_\pi^2,0,t,s,m_\tau^2,s',M_\pi^2,s'') \\
&- \frac{m_\tau^2(s''-9s)+2s\left[s+s''-6M_\pi^2+2(t+t_{\rm min}+t_{\rm max})\right]}{2s} \\
&\times \bar{D}_0(m_\tau^2,M_\pi^2,M_\pi^2,0,t,s,m_\tau^2,s',M_\pi^2,s'')\Bigg\} \,.
\end{aligned} \tag{11.30}$$

The other two terms are

$$\begin{aligned}
\bar{N}_+ =& \frac{{\rm Im}f_+(s'){\rm Im}f_+(s'')}{(t-t_{\rm max})(t_{\rm max}-t_{\rm min})}\Bigg\{ \frac{\bar{C}_0^+(m_\tau^2,M_\pi^2,t,m_\tau^2,s',M_\pi^2)}{2ss'}\Big[2st_{\rm max}(M_\pi^2-t_{\rm max}) \\
&+ m_\tau^2(M_\pi^2-t_{\rm max})(M_\pi^2-s+t_{\rm max}) + m_\tau^4(s+2t_{\rm max}-2M_\pi^2) - m_\tau^6\Big] \\
&- \frac{(M_\pi^2-t_{\rm max})\left[m_\tau^2(M_\pi^2+s+t_{\rm max}) - m_\tau^4 - 2st_{\rm max}\right]}{2s} \\
&\times D_0^+(m_\tau^2,M_\pi^2,M_\pi^2,0,t,s,m_\tau^2,s',M_\pi^2,s'') \\
&+ \frac{\bar{D}_0^+(m_\tau^2,M_\pi^2,M_\pi^2,0,t,s,m_\tau^2,s',M_\pi^2,s'')}{2ss'}\Big[m_\tau^6(4M_\pi^2+s-s'') \\
&+ m_\tau^4\left(4M_\pi^2 - 2M_\pi^2(s+s''+2t_{\rm max}) - s^2 + ss'' - 6st_{\rm max} + 2s''t_{\rm max}\right) \\
&+ m_\tau^2\left(M_\pi^4(s''-s) + M_\pi^2 s(s-s''-8t_{\rm max}) + t_{\rm max}(3s^2+ss''+(9s-s'')t_{\rm max})\right) \\
&+ 2s(M_\pi^2-t_{\rm max})\left(2M_\pi^4 - 4M_\pi^2 t_{\rm max} + t_{\rm max}(s+s''+2t_{\rm max})\right)\Big]\Bigg\} \,,
\end{aligned} \tag{11.31}$$

and

$$\begin{aligned}
\bar{N}_- =& \frac{{\rm Im}f_+(s'){\rm Im}f_+(s'')}{(t-t_{\rm min})(t_{\rm min}-t_{\rm max})}\Bigg\{ \frac{\bar{C}_0^-(m_\tau^2,M_\pi^2,t,m_\tau^2,s',M_\pi^2)}{2ss'}\Big[2st_{\rm min}(M_\pi^2-t_{\rm min}) \\
&+ m_\tau^2(M_\pi^2-t_{\rm min})(M_\pi^2-s+t_{\rm min}) + m_\tau^4(s+2t_{\rm min}-2M_\pi^2) - m_\tau^6\Big] \\
&- \frac{(M_\pi^2-t_{\rm min})\left[m_\tau^2(M_\pi^2+s+t_{\rm min}) - m_\tau^4 - 2st_{\rm min}\right]}{2s} \\
&\times D_0^-(m_\tau^2,M_\pi^2,M_\pi^2,0,t,s,m_\tau^2,s',M_\pi^2,s'') \\
&+ \frac{\bar{D}_0^-(m_\tau^2,M_\pi^2,M_\pi^2,0,t,s,m_\tau^2,s',M_\pi^2,s'')}{2ss'}\Big[m_\tau^6(4M_\pi^2+s-s'') \\
&+ m_\tau^4\left(4M_\pi^2 - 2M_\pi^2(s+s''+2t_{\rm min}) - s^2 + ss'' - 6st_{\rm min} + 2s''t_{\rm min}\right)
\end{aligned}$$

$$+ m_\tau^2 \left(M_\pi^4(s''-s) + M_\pi^2 s(s-s''-8t_{\rm min}) + t_{\rm min}(3s^2+ss''+(9s-s'')t_{\rm min})\right)$$
$$+ 2s(M_\pi^2 - t_{\rm min})\left(2M_\pi^4 - 4M_\pi^2 t_{\rm min} + t_{\rm min}(s+s''+2t_{\rm min})\right)\Big]\Big\}\,, \tag{11.32}$$

where

$$F_0^\pm(...,t,...) := F_0(...,t,...) - F_0(...,t_{\rm max/min},...)\,. \tag{11.33}$$

while the $\bar{F}_0$ functions are defined according to Eq. (11.5) and where we suppressed the arguments of $\kappa_+^{\rm fin}(s,t,s',s'')$ and $\bar{N}_\pm(s,t,s',s'')$ for brevity. We notice that $\bar{N}_\pm(s,t,s',s'')$ still have a divergent denominator at $t_{\rm max/min}$ respectively, but these remaining (removable) singularities can be dealt with by expanding around $t = t_{\rm max/min}$ when the integration in t is close to the boundaries $t_{\rm max/min}$.

11.5 IR singularities and low–energy limit

The D_0 function discussed in Sec. 11.3 gives an example of an IR–divergent loop function in Eq. (11.4). However, a second source of IR–divergences arises in

$$C_0(m_\tau^2, M_\pi^2, t, m_\tau^2, 0, M_\pi^2) = C_0^{\pi\tau}(t) - \frac{tB_0^{\pi\tau}(t)}{\lambda}\Big(32\pi^2\Lambda_{\rm IR} + 1 - \log\frac{\mu_{\rm IR}^2}{M_\pi m_\tau}\Big) \tag{11.34}$$

with

$$C_0^{\pi\tau}(t) = = \frac{1}{\lambda_{\pi\tau}^{1/2}(t)}\Big[\frac{1}{2}\log^2 x_t - \frac{1}{2}\log^2\frac{M_\pi}{m_\tau}$$
$$+ {\rm Li}_2\big(1-x_t^2\big) - {\rm Li}_2\Big(1 - x_t\frac{M_\pi}{m_\tau}\Big) - {\rm Li}_2\Big(1 - x_t\frac{m_\tau}{M_\pi}\Big)\Big]\,, \tag{11.35}$$

and which is the same loop function that defines the bulk of χPT result in Eq. (10.13). For both the D_0 and C_0 terms, the only remaining dependence on s' disappears via the sum rule in Eq. (9.11), and, upon separating $s'' = (s''-s)+s$, the D_0 terms in which s'' appears in the numerator cancel exactly the C_0 contribution, leaving

$$\kappa_+^{\rm disp}(s,t)\Big|_{\rm IR} = -\frac{e^2}{16\pi^2 f_+(s)}\frac{1}{\pi}\int_{4M_\pi^2}^\infty {\rm d}s''\frac{{\rm Im}\, f_+(s'')}{s''-s}\frac{2t(M_\pi^2+m_\tau^2-t)B_0^{\pi\tau}(t)}{\lambda}32\pi^2\Lambda_{\rm IR}$$
$$= -\frac{e^2}{16\pi^2}\frac{2t(M_\pi^2+m_\tau^2-t)B_0^{\pi\tau}(t)}{\lambda}32\pi^2\Lambda_{\rm IR}\,, \tag{11.36}$$

after inserting Eq. (9.10). The resulting IR divergence therefore matches exactly the IR singularity of $f_+^{(a)}(t)$ obtained in χPT (see Eq. (10.25)).

This observation is more general, i.e., by construction our dispersive representation reduces to χPT in the pointlike limit, and, accordingly, the low–energy properties of the representations agree. One key aspect concerns the IR structure, another one the chiral logarithms. To illustrate the latter point, we consider the expansion around $t = 0$

$$f_+^{(a)}(0) = \frac{e^2}{16\pi^2}\Big[\frac{m_\tau^2-2M_\pi^2}{m_\tau^2-M_\pi^2} + \frac{M_\pi^4+2M_\pi^2m_\tau^2-7m_\tau^4}{4(m_\tau^2-M_\pi^2)^2}\log\frac{M_\pi^2}{m_\tau^2} - \frac{7}{4}\Big(32\pi^2\Lambda_{\rm UV} - \log\frac{\mu_{\rm UV}^2}{m_\tau^2}\Big)$$
$$+ \frac{m_\tau^2+M_\pi^2}{m_\tau^2-M_\pi^2}\log\frac{M_\pi^2}{m_\tau^2}\Big(32\pi^2\Lambda_{\rm IR} + 1 - \log\frac{\mu_{\rm IR}^2}{M_\pi m_\tau}\Big)\Big]\,, \tag{11.37}$$

where we have written the UV scale with respect to m_τ to isolate the chiral logarithm. Using a narrow–

width approximation $\text{Im}\, f_+(s) = \pi\delta(s - M_\rho^2)M_\rho^2$, the dispersive result for $s = t = 0$ can be performed in terms of polylogarithms, and the expansion for $M_\rho \to \infty$ gives

$$\kappa_+^{\text{disp}}(0,0) = \frac{e^2}{16\pi^2}\left[\frac{3}{8} - \frac{m_\tau^2}{m_\tau^2 - M_\pi^2} + \frac{M_\pi^4 + 2M_\pi^2 m_\tau^2 - 7m_\tau^4}{4(m_\tau^2 - M_\pi^2)^2}\log\frac{M_\pi^2}{m_\tau^2} + \frac{7}{4}\log\frac{M_\rho^2}{m_\tau^2} + \frac{m_\tau^2 + M_\pi^2}{m_\tau^2 - M_\pi^2}\log\frac{M_\pi^2}{m_\tau^2}\left(32\pi^2\Lambda_{\text{IR}} + 1 - \log\frac{\mu_{\text{IR}}^2}{M_\pi m_\tau}\right)\right] + \mathcal{O}\left(M_\rho^{-2}\right). \tag{11.38}$$

The comparison of Eqs. (11.37) and (11.38) shows again that the IR singularities coincide, but also that the coefficients of the chiral logarithm match exactly. Moreover, the coefficient of the UV divergence is reproduced, upon identifying $\mu_{\text{UV}} = M_\rho$, so that, as expected, the result again becomes UV divergent in the pointlike limit $M_\rho \to \infty$. The only difference then concerns finite contact terms, related to LECs in χPT .

Using the narrow–width limit, one can also study the threshold behavior of the resulting $G_{\text{EM}}(s)$ function analytically. In particular, we showed that the same factorization of D_0 functions based on which the endpoint singularities in Sec. 11.4 disappear also ensures that $G_{\text{EM}}(s)$ derived from the IR–finite parts of $\kappa_+^{\text{disp}}(s,t)$ remains finite at threshold. Accordingly, singularities at threshold only originate from the remainder of the IR cancellation, see Sec. 12.4.1, which behaves as $\log(s - 4M_\pi^2)$, and real–emission diagrams, the latter leading to the dominant $1/(s - 4M_\pi^2)$ threshold divergence.

11.6 Matching with χPT

Our representation of the triangle–diagram supplemented by the pion VFF (see Fig.(9.2)) is sensitive to the high–energy behavior of the unsubtracted form factor $f_+(s)$. In the low energy regime, we need to utilize the very well known chiral perturbation theory (see Sec.10.1). In order to take the best of both worlds, we developed a matching procedure by expanding around $s, t = 0$ both the χPT form factor$f_+^{\chi\text{PT}}(t)$, which from Eq. (10.21) is given by

$$f_+^{\chi\text{PT}}(t) = f_+^{(a)}(t) + f_+^{(b)}(t) + f_+^{(c)}(t) + f_+^{\text{ct}}(t) + \left(\sqrt{Z_{\pi^0}^{\text{ct}}\left(Z_{\pi^-} + Z_{\pi^-}^{\text{ct}}\right)\left(Z_\tau + Z_\tau^{\text{ct}}\right)} - 1\right), \tag{11.39}$$

and the dispersive representation of the triangle–diagram (see Eq.(11.3)). From the perspective of a dispersive analysis, all terms apart from $f_+^{(a)}(t)$ amount to a subtraction constant, as these diagrams do not involve a non–trivial dependence on the Mandelstam variables. We then build the new *matched* form factor:

$$\kappa_+^{\text{match}}(s,t) = \kappa_+^{\text{disp}}(s,t) - \kappa_+^{\text{disp}}(0,0) + f_+^{\chi\text{PT}}(0)\,. \tag{11.40}$$

With this procedure, we suppress the high–energy part of the integral in Eq. (11.3) and thus reduce the sensitivity to the asymptotic form of $\text{Im} f_+(s)$. The new form factor $\kappa_+^{\text{match}}(s,t)$ is still UV finite, since both $\kappa_+^{\text{disp}}(s,t)$ and $f_+^{\chi\text{PT}}(t) = f_+^{\text{loop}}(t) + f_+^{\text{ct}}(t)$ are UV safe, has the right IR singularities and chiral logarithms.

The expanded χPT form factor $f_+^{\chi\text{PT}}(0)$ is then given by

$$f_+^{\chi\text{PT}}(0) = \frac{e^2}{16\pi^2}\left\{\frac{m_\tau^2 - 2M_\pi^2}{m_\tau^2 - M_\pi^2} - \frac{3}{2} - \frac{M_\pi^2 m_\tau^2 \log\frac{M_\pi^2}{m_\tau^2}}{(m_\tau^2 - M_\pi^2)^2} - 8\pi^2 X_\ell(\mu_{\text{UV}}) + \log\frac{\mu_{\text{UV}}^3}{M_\pi^2 m_\tau} - 2\left(1 + \frac{m_\tau^2 + M_\pi^2}{m_\tau^2 - M_\pi^2}\log\frac{M_\pi}{m_\tau}\right)\left(\log\frac{\mu_{\text{IR}}^2}{M_\pi m_\tau} - 32\pi^2\Lambda_{\text{IR}}\right)\right\}, \tag{11.41}$$

where $X_\ell(\mu)$ is defined as the combination

$$X_\ell(\mu) = \frac{4}{3}X_1 + \tilde{X}_6^{\text{phys}}(\mu)\,, \qquad X_\ell(\mu) = X_\ell(M_\rho) + \frac{3}{16\pi^2}\log\frac{\mu^2}{M_\rho^2}\,. \tag{11.42}$$

and $\tilde{X}_6^{\text{phys}}(\mu)$ is the long distance contribution of

$$X_6^{\text{phys}}(\mu) := X_6 - 4K_{12} = X_{6,\text{SD}}^{\text{phys}} + \tilde{X}_6^{\text{phys}}(\mu)\,. \tag{11.43}$$

In particular, the short–distant part is directly related to the S_{EW} term defined in Eq. (9.1) via the relation

$$e^2 X_{6,\text{SD}}^{\text{phys}} = 1 - S_{\text{EW}}^{\pi\pi} + \dots\,, \tag{11.44}$$

For the numerical evaluation we took the value reported in [254], yielding $\bar{X}_\ell(M_\rho) = 14.0(6)\times 10^{-3}$, where exactly the needed combination of LECs is computed in Lattice QCD, thanks to lepton flavor universality, and which differs quite significantly from the resonance–saturation estimate [207, 255, 256]

$$\bar{X}_\ell(M_\rho) \simeq \frac{7}{32\pi^2} - \frac{3}{8\pi^2}\left(\frac{M_\rho}{4\pi F_\pi}\right)^2 \simeq 5\times 10^{-3}\,. \tag{11.45}$$

Moreover, so far we have glossed over the matching to SD contributions, which requires

$$\Delta X_\ell\big|_{\text{SD}} = -\frac{1}{4\pi^2}\log\frac{m_\tau^2}{M_\rho^2} \tag{11.46}$$

to be added to $\bar{X}_\ell(\mu)$. This decomposition follows previous conventions for the SD contribution in the literature [34, 35, 222]. However, we emphasize that only the combination of $S_{\text{EW}}^{\pi\pi}$ and $G_{\text{EM}}(s)$ is scheme independent—at the precision at which the matching calculation is performed (see Sec.11.6.1).[5]

Note that we do not show here the expression for the expanded $\kappa_+^{\text{disp}}(0,0)$ since it involves the expansion of the Passarino–Veltman functions [232–238], performed with the *Package–X* option *LoopRefineSeries* [257, 258], and it turns out to be a rather long and complicated expression.

With this procedure, we obtained an amplitude at $\mathcal{O}(e^2p^2)$ for the $\tau \to \pi\pi^0\nu_\tau$ process which has both the correct low– and high–energy behavior. It also allows us to establish a suitable basis for the connection to short–distance (SD) contributions and lattice QCD [259], most conveniently expressed in terms of the chiral low-energy constant (LEC). However, we still need to cure the IR–divergences present in $\kappa_+^{\text{match}}(s,t)$. This requires the computations of real photon emission contributions, both from initial– and final–states, and it will be explained in details in the next chapter.

11.6.1 Scheme–dependence discussion

In the analysis of the isospin breaking corrections for the hadronic τ decay, only the combination of $S_{\text{EW}}^{\pi\pi}$ and $G_{\text{EM}}(s)$ is scheme independent—at the precision at which the matching calculation is performed. In fact, we just showed that the short–distance part of the LEC $X_{6,\text{SD}}^{\text{phys}}$ can be separated from the rest and that it is directly connected to the S_{EW} correction through Eq. (11.44). The resulting scheme ambiguity amounts to an $\mathcal{O}(\alpha/\pi)$ uncertainty in $S_{\text{EW}}^{\pi\pi}$ [14], which requires a dedicated matching calculation in

[5] The scale μ_{UV} in the χPT result cannot simply be identified with the scale of the low–energy effective (Fermi) theory after the W–boson is integrated out (LEFT), which is already reflected by the fact that the χPT running in Eq. (11.42) and the LEFT running—Eq. (11.46) arises from its naive application between m_τ and M_ρ—do not agree. Instead, the matching between χPT and LEFT is most conveniently formulated at the level of the LECs [223]. For a consistent matching, the dependence on both the χPT scale and the LEFT scale need to cancel in the decay rate at the considered order.

analogy to [223], using input from lattice QCD for the required non–perturbative matrix elements [260, 261].

For future use, we derive a relation between the value of the LEC $\tilde{X}_6^{\text{phys}}(\mu)$ we use in our analysis and any possible value of the same quantity in $G_{\text{EM}}(s)$. As $f_+^{\chi\text{PT}}(t)$, and consequently $\kappa_+^{\text{match}}(s,t)$, depends only linearly on the combination of LECs, the subsequent dependence of $G_{\text{EM}}(s)$, given in Eq. (9.5) with Eqs. (9.6) and (9.7), is also linear,

$$\frac{\partial G_{\text{EM}}}{\partial X_\ell(\mu)} = -e^2 \,, \tag{11.47}$$

and the relation

$$G_{\text{EM}}(s)\big|_{X_\ell(\mu)} = G_{\text{EM}}(s)\big|_{X_\ell(\mu)=\bar{X}_\ell(\mu)} - e^2\big(X_\ell(\mu) - \bar{X}_\ell(\mu)\big) \,, \tag{11.48}$$

is exact at $\mathcal{O}(e^2p^2)$. Our numerical results, presented for $\bar{X}_\ell(M_\rho) = 14 \times 10^{-3}$ from [254], are therefore trivial to adjust once an improved matching analysis becomes available.

Chapter 12

Real–emission contributions

The amplitude computed in Ch. 11 is UV–finite but still IR–divergent. Similarly to the analysis performed in Ch. 10 in the χPT formalism and in the soft–photon approximation, in order to cancel the infrared divergences, the emission of real photons, both from the initial and the final states, must be included. In what follows we compute the real emission contributions from photons, necessary to cancel the IR divergences, and from resonances, in particular ρ, a_1 and ω resonances.

12.1 Real–emission amplitude

The expression for the triangle–diagram (Fig. 9.2), after restoring the correct low–energy behavior through the matching procedure (see Ch. 11.6), shows infrared singularities that cancels once we include initial and final state radiations of Fig.12.1. Notice that also for these diagrams, the $\tau\pi\pi^0\nu_\tau$ vertex is dressed with the pion vector form factor $f_+(s)$ given in Eq. (9.10). Following [35], the matrix element for the

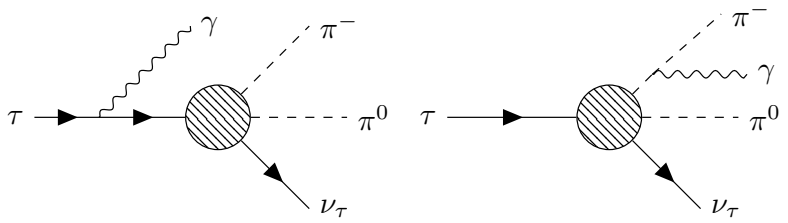

Figure 12.1: Initial and final state radiations diagrams for $\tau^- \to \pi^-\pi^0\nu_\tau$.

decay $\tau^-(l_1) \to \pi^-(q_1)\pi^0(q_2)\nu_\tau(l_2)\gamma(k)$ has the general structure

$$T = eG_F V_{ud}^* \epsilon^\mu(k)^* [F_\nu \bar{u}(l_2)\gamma^\nu(1-\gamma_5)(m_\tau + \not{l}_1 - \not{k})\gamma_\mu u(l_1) + (V_{\mu\nu} - A_{\mu\nu})\bar{u}(l_2)\gamma^\nu(1-\gamma_5)u(l_1)] \,. \tag{12.1}$$

The first part of Eq. (12.1) describes bremsstrahlung off the initial τ lepton with

$$F_\nu = \frac{(q_2 - q_1)_\nu}{2l_1 \cdot k} f_+(s) \,. \tag{12.2}$$

The second part of the matrix element describes the vector and axial–vector components of the transition $W^-(l_1 - l_2) \to \pi^-(q_1)\pi^0(q_2)\gamma(k)$. The hadronic tensor $V_{\mu\nu}$ contains bremsstrahlung off the π^- in the

final state and gauge invariance implies the Ward identities

$$\begin{aligned} k^\mu V_{\mu\nu} &= (q_1 - q_2)_\nu f_+(s) \,, \\ k^\mu A_{\mu\nu} &= 0 \,. \end{aligned} \tag{12.3}$$

For these resonance contributions, $V_{\mu\nu}$ and $A_{\mu\nu}$, we utilize the expressions in [35],

$$\begin{aligned} V_{\mu\nu} = {} & f_+[(l_1-l_2)^2]\frac{q_{1\mu}}{q_1\cdot k}\,(q_1+k-q_2)_\nu - f_+[(l_1-l_2)^2]g_{\mu\nu} \\ & + \frac{f_+[(l_1-l_2)^2]-f_+(s)}{(q_1+q_2)\cdot k}\,(q_1+q_2)_\mu\,(q_2-q_1)_\nu \\ & + v_1\,(g_{\mu\nu}q_1\cdot k - q_{1\mu}k_\nu) + v_2\,(g_{\mu\nu}q_2\cdot k - q_{2\mu}k_\nu) \\ & + v_3\,(q_{1\mu}q_2\cdot k - q_{2\mu}q_1\cdot k)\,q_{1\nu} + v_4\,(q_{1\mu}q_2\cdot k - q_{2\mu}q_1\cdot k)\,(q_1+q_2+k)_\nu \,, \\ A_{\mu\nu} = {} & ia_1\epsilon_{\mu\nu\rho\sigma}\,(q_2-q_1)^\rho\,k^\sigma + ia_2\,(l_1-l_2)_\nu\,\epsilon_{\mu\rho\sigma\tau}k^\rho q_1^\sigma q_2^\tau \,. \end{aligned} \tag{12.4}$$

In particular, the vector corrections $v_1,\ v_2,\ v_3,\ v_4$ come from the resonance Lagrangian of [184] where the contributing diagrams are listed in Fig. 12.2, while the axial–vector ones, a_1 and a_2, come from the leading $\mathcal{O}(p^4)$ contribution of the Wess–Zumino–Witten (WZW) action [262] and the diagrams are the ones in Fig. 12.3. Since the strength of the WZW contribution is determined by the anomaly in terms

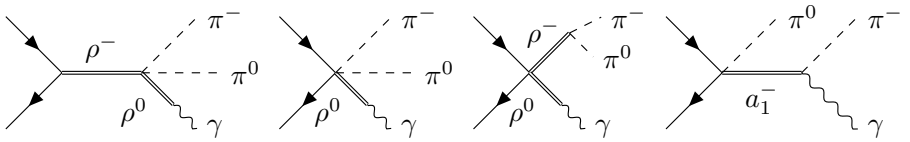

Figure 12.2: ρ and a_1 resonance exchange contribution via resonance chiral theory [184]. In the first diagram, a photon is to be appended wherever possible.

of the pion decay constant, the free parameters in the resonance Lagrangian can be identified with two vector couplings F_V, G_V, one axial–vector coupling F_A and the masses parameters M_V, M_A. By writing $(l_1-l_2)^2 = s + 2(q_1+q_2)\cdot k$, Low's theorem [263] is manifestly satisfied:

$$\begin{aligned} V_{\mu\nu} = {} & f_+(s)\frac{q_{1\mu}}{q_1\cdot k}\,(q_1-q_2)_\nu + f_+(s)\left(\frac{q_{1\mu}k_\nu}{q_1\cdot k} - g_{\mu\nu}\right) \\ & + 2\frac{\mathrm{d}f_+(s)}{\mathrm{d}s}\left(\frac{q_{1\mu}q_2\cdot k}{q_1\cdot k} - q_{2\mu}\right)(q_1-q_2)_\nu + \mathcal{O}(k) \,. \end{aligned} \tag{12.5}$$

Additionally, we take into account the contribution from the resonance diagram containing a radiative $\omega\pi\gamma$ coupling (see Fig. 12.4), since its sizable contribution has been noted before [264, 265]. More explicitly, the algebraic expression for this contribution can be found in Eq. (23) of [264], with values of the

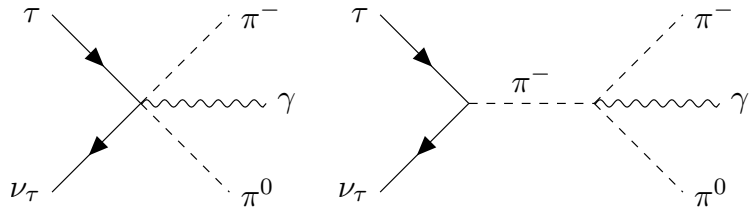

Figure 12.3: Chiral anomaly contribution via Wess–Zumino–Witten action [262].

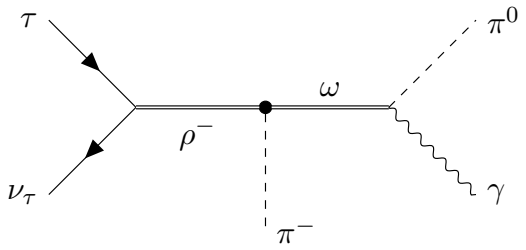

Figure 12.4: Omega resonance contribution containing a radiative $\omega\pi\gamma$ coupling according to [264].

couplings therein given in Eqs. (28), (32) and (33). As in the analysis of $\tau^- \to \pi^-\pi^0\nu_\tau$ performed by the different experiments (Belle, ALEPH, CLEO and OPAL), $\omega \to \pi\gamma$ is considered a background contribution and excluded from the published data, we follow [36, 266, 267] in including only the interference contribution arising from the diagram with the radiative ω coupling.

By following [34, 35], the fully inclusive decay rate, i.e., with photons of all energies included, is given by Eq. (9.3) and in particular we are interested in the computation of the electromagnetic correction function $G_{\rm EM}(s)$. From Eq. (9.7), where after the matching procedure described in Ch. 11.6 the form factor $f_+^{e^2p^2}(s,t)$ is replaced with $\kappa_+^{\rm match}(s,t)$, the terms containing the real (photon and resonances) emission contributions are $g_{\rm Low}(s,t)$ and $g_{\rm rest}(s,t)$. The first term $g_{\rm Low}(s,t)$ accounts for the contribution of (s,t) in the non–radiative Dalitz plot and it can be computed analytically (details in the next section and in [35]), while the second term $g_{\rm rest}(s,t)$, that cannot be accessed by the non–radiative decay, is determined numerically. Moreover, thanks to this separation, the infrared–divergences will be fully contained in $g_{\rm Low}(s,t)$ such that, once this term is added to the equally infrared divergent electromagnetic one–loop correction for the non–radiative decay, i.e., $\kappa_+^{\rm match}(s,t)$, the IR–divergences cancel explicitly. We will see this cancellation explicitly in the following section. However, we must emphasis the fact that, differently for what was done in [35], we are working in dimensional regularization also for IR–divergences.

12.2 Determination of $g_{\rm Low}(s,t)$ and $g_{\rm rest}(s,t)$

Once we consider only the leading Low approximation of $\mathcal{O}(k^{-2})$ to the differential decay rate, we get

$$\mathrm{d}\Gamma = \frac{\alpha G_F^2 |V_{ud}|^2}{32\pi^7 m_\tau} |f_+(s)|^2 D(s,t) \left[\frac{2l_1\cdot q_1}{(l_1\cdot k)(q_1\cdot k)} - \frac{m_\tau^2}{(l_1\cdot k)^2} - \frac{M_\pi^2}{(q_1\cdot k)^2} \right] \mathrm{d}_{\rm LIPS} \,, \tag{12.6}$$

where $\mathrm{d}_{\rm LIPS}$ is the phase space integral given by

$$\mathrm{d}_{\rm LIPS} = \frac{\mathrm{d}^3 l_2}{2E_\nu} \frac{\mathrm{d}^3 q_1}{2E_{\pi^-}} \frac{\mathrm{d}^3 q_2}{2E_{\pi^0}} \frac{\mathrm{d}^3 k}{2k^0} \delta^{(4)}(l_1 - l_2 - q_1 - q_2 - k) \,. \tag{12.7}$$

and the kinematic of the radiative decay can be found in App. G. Integration over neutrino and photon momenta leads to the three–fold differential rate

$$\mathrm{d}\Gamma = \frac{\alpha G_F^2 |V_{ud}|^2}{64\pi^4 m_\tau^3} |f_+(s)|^2 D(s,t) \left[2l_1\cdot q_1 I_{11}(s,t,x) - m_\tau^2 I_{20}(s,t,x) - M_\pi^2 I_{02}(s,t,x) \right] \mathrm{d}s\, \mathrm{d}t\, \mathrm{d}x \,, \tag{12.8}$$

with [268]

$$I_{mn}(s,t,x) = \frac{1}{2\pi} \int \frac{\mathrm{d}^3 l_2}{2E_\nu} \frac{\mathrm{d}^3 k}{2k^0} \frac{\delta^{(4)}(l_1 - l_2 - q_1 - q_2 - k)}{(l_1\cdot k)^m (q_1\cdot k)^n} \,. \tag{12.9}$$

The next step consists in performing the integration over x, the invariant mass squared of photon and neutrino. Here we must distinguish between two different regions in the $s-t$ plane. For (s,t) in the Dalitz plot of the non–radiative decay, the lower limit for the x–integration is 0. This is a consequence of working in dimensional regularization also for IR–divergences, otherwise it would have been $x_{\rm min}(s,t) = M_\gamma^2$, with M_γ a fictitious photon mass. For (s,t) that cannot be accessed in the non–radiative decay the lower limit is given by $x_-(s,t)$ (see App. G). This last contribution is infrared finite and occurs only for

$$s \leq \frac{m_\tau^2 M_\pi}{m_\tau - M_\pi} \, . \tag{12.10}$$

The corresponding contribution to the $G_{\rm EM}$, booked in $g_{\rm rest}(s,t)$, is enhanced in the threshold region and plays an important role in its contribution to a_μ. The upper limit of the x–integration is always given by $x_+(s,t)$ given in App. G.

The double differential decay rate in the leading Low approximation, for (s,t) in the non–radiative Dalitz plot and integrated over all photon momenta, takes the form

$$\mathrm{d}\Gamma = \frac{\alpha G_F^2 |V_{ud}|^2}{64\pi^4 m_\tau^3} |f_+(s)|^2 D(s,t) \left[J_{11}(s,t) + J_{20}(s,t) + J_{02}(s,t) \right] \mathrm{d}s \; \mathrm{d}t \, , \tag{12.11}$$

where

$$\begin{aligned}
J_{11}(s,t) = & \left[32\pi^2 \Lambda_{\rm IR} + 1 - \log \frac{\mu_{\rm IR}^2}{[2x_+(s,t)\bar{\gamma}]^2} \right] \frac{1}{\bar{\beta}} \log\left(\frac{1+\bar{\beta}}{1-\bar{\beta}} \right) + \log(2x_+(s,t)\bar{\gamma}) \frac{1}{\bar{\beta}} \log\left(\frac{1+\bar{\beta}}{1-\bar{\beta}} \right) \\
& + \frac{1}{\bar{\beta}} \left\{ Li_2\left(\frac{1}{Y_2} \right) - Li_2\left(Y_1 \right) + \frac{1}{4} \left[\log^2\left(-\frac{1}{Y_2} \right) - \log^2\left(-\frac{1}{Y_1} \right) \right] \right\} , \\
J_{20}(s,t) = & -\frac{1}{2} \left(32\pi^2 \Lambda_{\rm IR} + 1 - \log \frac{\mu_{\rm IR}^2}{m_\tau^2} \right) + \log\left(\frac{m_\tau^2 - s}{m_\tau x_+(s,t)} \right) , \\
J_{02}(s,t) = & -\frac{1}{2} \left(32\pi^2 \Lambda_{\rm IR} + 1 - \log \frac{\mu_{\rm IR}^2}{m_\tau^2} \right) + \log\left(\frac{m_\tau^2 + M_\pi^2 - s - t}{M_\pi x_+(s,t)} \right) \, .
\end{aligned} \tag{12.12}$$

are the functions in [35] and reported in App. G, but with the IR–divergent parts translated to dimensional regularization. Then $g_{\rm Low}(s,t)$ is given by

$$g_{\rm Low}(s,t) = \frac{\alpha}{\pi} \left[J_{11}(s,t) + J_{20}(s,t) + J_{02}(s,t) \right] \, . \tag{12.13}$$

The remaining part of the radiative decay rate, containing all terms except the leading Low ones, is calculated numerically giving the so called $g_{\rm rest}(s,t)$ term which accounts for the infrared finite remainder of the rate, i.e., all terms except the ones contained in $g_{\rm Low}(s,t)$. Putting everything together, the double differential rate for the photon–inclusive two–pion decay is given by

$$\frac{\mathrm{d}\Gamma_{\pi\pi(\gamma)}}{\mathrm{d}s \; \mathrm{d}t} = \frac{G_F^2 S_{\rm EW} |V_{ud}|^2}{64\pi^3 m_\tau^3} |f_+(s)|^2 D(s,t) \left[1 + 2\kappa_+^{\rm match}(s,t) + g_{\rm Low}(s,t) + g_{\rm rest}(s,t) \right] \, . \tag{12.14}$$

From these result it is possible to explicitly show that the IR–divergences in $2\kappa_+^{\rm match}(s,t) + g_{\rm Low}(s,t)$ cancel. After recalling the expression for the *matched* form factor $\kappa_+^{\rm match}(s,t)$ in Eq. (11.40), the IR–divergences cancellation happens as follows:

$$\left[\kappa_+^{\rm disp}(s,t) + \frac{\alpha}{\pi} J_{11}(s,t) \right] \Bigg|_{\text{IR-div}} = 0 \, ,$$

$$\left[-\kappa_+^{\text{disp}}(0,0) + f_+^{\chi\text{PT}}(0) + \frac{\alpha}{\pi} J_{20}(s,t) + \frac{\alpha}{\pi} J_{02}(s,t) \right] \Bigg|_{\text{IR-div}} = 0 \,. \tag{12.15}$$

This result shows how the matching procedure described in Sec. 11.6 is essential to ensure the IR–divergences cancellation also in the dispersive calculation (Fig. 9.2)

12.3 Soft–photon limit in $g_{\text{rest}}(s,t)$

As remarked earlier, we compute the contribution of $g_{\text{rest}}(s,t)$ purely numerically. This is done by integrating the square of the amplitude T given in Eq. (12.1). However, the piece that gives rise to the IR–divergent $g_{\text{Low}}(s,t)$ needs to be subtracted. Hence, we write $g_{\text{rest}}(s,t)$ as

$$\begin{aligned} g_{\text{rest}}(s,t) = & \frac{1}{128\pi^3 G_F^2 |V_{ud}|^2 D(s,t) |f_+(s)|^2} \\ & \times \int \mathrm{d}x \, \mathrm{d}\cos\theta_k \mathrm{d}\phi_k \, \frac{m_\tau^2 x}{\left(m_\tau^2 - s + x + \cos\theta_k \sqrt{\lambda\left(s,x,m_\tau^2\right)} \right)^2} \left\{ |T|^2 - |T_{\text{Low}}|^2 \right\} , \end{aligned} \tag{12.16}$$

with the measure function of the 4–body phase–space integral spelled out explicitly, see Eq. (G.12) in App. G, and the amplitude square $|T_{\text{Low}}|^2$, giving rise to the expressions in Eq. (12.12), given by

$$|T_{\text{Low}}|^2 = 8e^2 G_F^2 |V_{ud}|^2 |f_+(s)|^2 D(s,t) \left[\frac{2 l_1 \cdot q_1}{(l_1 \cdot k)(q_1 \cdot k)} - \frac{m_\tau^2}{(l_1 \cdot k)^2} - \frac{M_\pi^2}{(q_1 \cdot k)^2} \right] , \tag{12.17}$$

leading to an expression for g_{rest} free of IR singularities.

12.4 Integration at threshold

The numerical integration of $g_{\text{Low}}(s,t)$ in t and g_{rest} in ϕ_k, $\cos\theta_k$, x and t (for details about the phase space integration see App. G) shows a divergence at the threshold $s = 4M_\pi^2$. In order to bypass this end–point singularity we apply a change of variables where we parametrize t and x in terms of angles:

$$x \to \begin{cases} \frac{1}{2} x_+(s,t) \left(z_x - 1 \right) & \text{in } R^{\text{III}} \\ \frac{1}{2} \left[x_+(s,t) - x_-(s,t) \right] z_x + \frac{1}{2} \left[x_+(s,t) + x_-(s,t) \right] & \text{in } R^{\text{IV}} \backslash R^{\text{III}} \end{cases} \tag{12.18}$$

$$t \to \begin{cases} \frac{1}{2} \left[\bar{t}_{\text{max}}(s) - \bar{t}_{\text{min}}(s) \right] z_t + \frac{1}{2} \left[\bar{t}_{\text{max}}(s) + \bar{t}_{\text{min}}(s) \right] & \text{in } R^{\text{III}} \\ \frac{1}{2} \left[(m_\tau - M_\pi)^2 - \bar{t}_{\text{max}}(s) \right] z_t + \frac{1}{2} \left[(m_\tau - M_\pi)^2 + \bar{t}_{\text{max}}(s) \right] & \text{in } R^{\text{IV}} \backslash R^{\text{III}} \end{cases} \tag{12.19}$$

where $-1 \leq z_x \leq 1$ and $-1 \leq z_t \leq 1$ and the expressions for $x_\pm(s,t)$ and $\bar{t}_{\text{min,max}}(s)$ are given in App. G. With this transformation we can isolate the threshold divergence and numerically integrate the amplitude on the full s range, i.e., $s \in [4M_\pi^2, m_\tau^2]$. In particular, it is the product of the radiative amplitude (after the change of variables) times the Jacobian arising from rewriting t in terms of z_t that becomes integrable at threshold. In fact, it is easy to see from Eq. (12.19), that the Jacobian in R^{III}, where the singular behavior arises, reads

$$J_t(s) = \frac{1}{2} \left[\bar{t}_{\text{max}}(s) - \bar{t}_{\text{min}}(s) \right] \,, \tag{12.20}$$

and it vanishes at $s = 4M_\pi^2$ since $\bar{t}_{\rm max}(s) = \bar{t}_{\rm min}(s)$, curing the divergence. The Jacobians in $R^{IV\setminus III}$, instead, do not vanish at threshold and this results in a regular but sizable contribution of the real emission diagrams in this region. Once we checked this approach with the real emission contributions, we apply it to the determination of $\kappa_+^{\rm disp}(s,t)$ such that also in this case the integration exactly at threshold is under control.

12.4.1 Threshold singularity of $g_{\rm Low}(s,t)$

The variable substitution described above turns out to be a good solution for the integration of $\kappa_+^{\rm match}(s,t)$ and $g_{\rm rest}(s,t)$ but it does not work for $g_{\rm Low}(s,t)$ defined in Eq. (12.13). In fact, this result shows a physical divergence at threshold, $s = 4M_\pi^2$, which is not solved by rewriting the variable t in terms of the angle z_t and then multiply for the Jacobian.

In order to solve this problem, we perform the variable substitution also in this case but then we expand the new expression around $s = 4M_\pi^2$. The contribution to $G_{\rm EM}(s)$ from $g_{\rm Low}(s,z_t)$, after the angle integration, i.e.,

$$G_{\rm EM}^J(s) = \frac{\int_{-1}^1 {\rm d}z_t\, J_t(s) D(s,z_t) g_{\rm Low}(s,z_t)}{\int_{-1}^1 {\rm d}z_t\, J_t(s) D(s,z_t)}\,,$$
$$\int_{-1}^1 {\rm d}z_t\, J_t(s) D(s,z_t) = \frac{m^2}{6s}(s-m_\tau^2)^2(2s+m_\tau^2)(s-4M_\pi^2)^{3/2}\,, \tag{12.21}$$

has the following analytical form

$$G_{\rm EM}^J(s) = \left[c_{3/2}^{\rm log}\log\left(\frac{s-4M_\pi^2}{4M_\pi^2}\right) + c_{3/2}^{\rm rest}\right] + c_2^{\rm rest}\sqrt{s-4M_\pi^2}$$
$$+ (s-4M_\pi^2)\left[c_{5/2}^{\rm log}\log\left(\frac{s-4M_\pi^2}{4M_\pi^2}\right) + c_{5/2}^{\rm rest}\right] + \mathcal{O}[(s-4M_\pi^2)^{3/2}]\,, \tag{12.22}$$

where $c_i^{\rm rest}$ include all the terms that are not divergent for $s = 4M_\pi^2$, with $i = 3/2, 2, 5/2, ...$ indicating the degree of the expansion of the numerator in Eq. (12.21). It is then clear that, after the integration in z_t, the contribution of $g_{\rm Low}(s,z_t)$ to $G_{\rm EM}(s)$ is still logarithmically divergent at threshold.

12.5 Determination of resonance couplings

For the numerical evaluation of the resonance contribution to real emission we need to determine the coupling F_V, G_V and F_A. Frequent choices are from the short–distance constraints [35,183]

$$F_V = \sqrt{2}F_\pi \simeq 0.13\,{\rm GeV}\,, \qquad G_V = \frac{F_\pi}{\sqrt{2}} \simeq 0.065\,{\rm GeV}\,, \qquad F_A = F_\pi \simeq 0.092\,{\rm GeV}\,, \tag{12.23}$$

and the phenomenologically motivated one

$$F_V = 0.16\,{\rm GeV}\,, \quad G_V = 0.065\,{\rm GeV}\,, \quad F_A = 0.12\,{\rm GeV}\,, \tag{12.24}$$

where F_V and G_V are extracted from the decay widths of $\rho \to e^+e^-$, $\rho \to \pi\pi$ and $K^* \to K\pi$ [269], while F_A comes from an old measurement [270] of the $a_1 \to \pi\gamma$ partial width via Eq. (4.10) in [183]. The extraction of F_A from $a_1 \to \pi\gamma$ has been challenged in the literature mostly suggesting smaller values of F_A [79,186,271–274], but the situation is far from conclusive. Hoping to shed some light on the issue, we attempted another indirect determination, by assuming that the $a_1 \to \pi\gamma$ decay proceeds via

$a_1 \to \rho\pi \to \pi\gamma$ [87,250]

For the first step of the decay chain $a_1 \to \pi\rho \to \pi\gamma$, one needs the coupling for $a_1 \to \rho\pi$, which could be defined in a hidden–local–symmetry model [275] according to

$$\mathcal{L}_{a_1\pi\rho} = -\frac{i}{\sqrt{2}} g_{a_1\rho\pi}\, \mathrm{Tr}\, \mathcal{A}_\mu [\Phi,\, V^\mu], \tag{12.25}$$

where the relevant fields are collected in

$$\Phi = \begin{pmatrix} \pi^0/\sqrt{2} & \pi^+ \\ \pi^- & -\pi^0/\sqrt{2} \end{pmatrix}, \quad V_\mu = \begin{pmatrix} \rho^0/\sqrt{2} & \rho^+ \\ \rho^- & -\rho^0/\sqrt{2} \end{pmatrix}_\mu, \quad \mathcal{A}_\mu = \begin{pmatrix} a_1^0/\sqrt{2} & a_1^+ \\ a_1^- & -a_1^0/\sqrt{2} \end{pmatrix}_\mu . \tag{12.26}$$

However, in order to ensure gauge invariance, we promote it to

$$\tilde{\mathcal{L}}_{a_1\pi\rho} = -\frac{i}{2\sqrt{2}} \tilde{g}_{a_1\rho\pi}\, \mathrm{Tr}\, \mathcal{A}_{\mu\nu} [\Phi,\, V^{\mu\nu}] \,, \tag{12.27}$$

formulated in terms of the field–strength tensors $V_{\mu\nu} = \partial_\mu V_\nu - \partial_\nu V_\mu$ and $\mathcal{A}_{\mu\nu} = \partial_\mu \mathcal{A}_\nu - \partial_\nu \mathcal{A}_\mu$. Momentum–space Feynman rules extracted from this interaction terms appear as, e.g.,

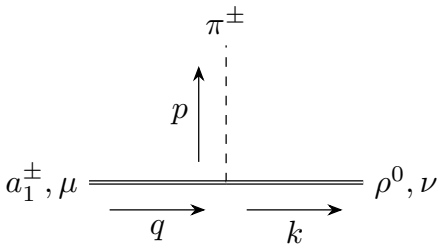

$$= \pm \tilde{g}_{a_1\rho\pi} (g_{\mu\nu}\, k\cdot q - k_\mu q_\nu) \,, \tag{12.28}$$

similar to the $a_1\rho\pi$ interaction term utilized in [264, 265, 276]. Since the interactions for the different channels enabled by the above interaction term differ only by sign, the partial widths appear as

$$\Gamma(a_2^\pm \to \pi^\pm \rho^0) = \Gamma(a_2^\pm \to \pi^0 \rho^\pm) = \Gamma(a_1^0 \to \pi^\pm \rho^\mp) \,. \tag{12.29}$$

We can therefore express

$$\Gamma(a_1 \to \pi\rho) = 2\Gamma(a_2^\pm \to \pi^\pm \rho^0) = \frac{|\tilde{g}_{a_1\rho\pi}|^2}{4\pi} M_\rho^2 |\mathbf{p}_\rho| \left(1 + \frac{2|\mathbf{p}_\rho|^2}{3M_\rho^2}\right), \tag{12.30}$$

with the spatial ρ–momentum $|\mathbf{p}_\rho| = \sqrt{\lambda(m_{a_1}^2, M_\rho^2, M_\pi^2)}/(2m_{a_1})$ in the center–of–mass frame. Further assuming the total experimental width $\Gamma_{a_1} = (0.25, \ldots, 0.6)\,\mathrm{GeV}$ [158], to be dominated by the $\pi\rho$ decay channel $\Gamma_{a_1} = \Gamma(a_1 \to \pi\rho)$, yields

$$|\tilde{g}_{a_1\rho\pi}| = (3.6, \ldots, 5.6)\,\mathrm{GeV}^{-1} \,, \tag{12.31}$$

or $|g_{a_1\rho\pi}| = 5.1\,\mathrm{GeV}^{-1}$ corresponding to $\Gamma_{a_1} = 0.5\,\mathrm{GeV}$ used in the evaluation of the resonance model terms of Eq. (12.4). Utilizing the total width as measured by the COMPASS collaboration $\Gamma_{a_1} = 0.380(80)\,\mathrm{GeV}$ [277], $|g_{a_1\rho\pi}| = 4.5(5)\,\mathrm{GeV}^{-1}$. For comparison, in [264] they cite $g_{\rho a_1\pi} = 4.843\,\mathrm{GeV}^{-1}$ for their coupling strength.

In order to describe the full decay chain, we make further use of the gauge–invariant interaction term

of [278],

$$\mathcal{L}_{\gamma V} = \frac{\sqrt{2}e}{g_{\rho\gamma}} F^{\mu\nu} \,\mathrm{Tr}\, Q V_{\mu\nu} \,, \tag{12.32}$$

with the charge matrix $Q = \mathrm{diag}(2, -1)/3$ and the electromagnetic field–strength tensors $F_{\mu\nu} = \partial_\mu A_\nu - \partial_\nu A_\nu$. Coupling the photon to a neutral ρ with momentum k, the partial decay width can be written as

$$\Gamma(a_1^\pm \to \pi^\pm \gamma) = \frac{e^2 |\tilde{g}_{a_1\rho\pi}|^2}{24\pi g_{\rho\gamma}^2} \left(\frac{k^2}{M_\rho^2 - k^2}\right)^2 |\mathbf{k}| \left(3k^2 + 2|\mathbf{k}|^2\right) , \tag{12.33}$$

where the spatial photon momentum is given by $|\mathbf{k}| = \sqrt{\lambda(m_{a_1}^2, M_\pi^2, k^2)}/(2m_{a_1})$. Taking the limits $M_\rho^2 \to 0$, $k^2 \to 0$, the above expression yields

$$\Gamma(a_1^\pm \to \pi^\pm \gamma) = \frac{e^2 |\tilde{g}_{a_1\rho\pi}|^2 m_{a_1}^3}{96\pi g_{\rho\gamma}^2} \left(1 - \frac{M_\pi^2}{m_{a_1}^2}\right)^3 . \tag{12.34}$$

In contrast, in [184] they obtained

$$\Gamma(a_1^\pm \to \pi^\pm \gamma) = \frac{e^2 F_A^2 m_{a_1}}{96\pi F_\pi^2} \left(1 - \frac{M_\pi^2}{m_{a_1}^2}\right)^3 , \tag{12.35}$$

from resonance chiral theory. Equating the above expressions, yields

$$F_A = \{0.069,\, 0.097,\, 0.11\}\,\mathrm{GeV} \,, \tag{12.36}$$

for $\Gamma_{a_1} = \{0.25,\, 0.5,\, 0.6\}\,\mathrm{GeV}$, where $g_{\rho\gamma} = 5.98$ [91] is employed. With the total width as measured by COMPASS [277], $F_A = 0.085(9)\,\mathrm{GeV}$. However, with $g_{\rho\gamma} = 4.96$ as extracted from $\Gamma(\rho \to e^+e^-)$ [250],

$$F_A = \{0.083,\, 0.12,\, 0.13\}\,\mathrm{GeV} \,, \tag{12.37}$$

or $F_A = 0.10(1)\,\mathrm{GeV}$ using the COMPASS total a_1 width in this case.

These values ought to be compared to the estimate from short–distance constraints in Eq. (12.23) [183] and from the determination by means of the resonance–chiral–theory interaction and the direct experimental measurement of $\Gamma(a_1 \to \pi\gamma)$ given in Eq. (12.24) [279] for which the thesis work of [280] found

$$F_A = 0.12(2)\,\mathrm{GeV}. \tag{12.38}$$

Comparing with the values extracted via $a_1 \to \pi\rho \to \pi\gamma$ and the one due to short–distance constraints that tend to be smaller than the above one, it seems to fit into the picture. Following the remark in [280], the photon production experiments suggest that the branching ratio $\Gamma(a_1 \to \pi\gamma)$ could be smaller than the value obtained by the previous direct measurement [273, 274].

Chapter 13

Results

We now have all the ingredients to compute the contribution of $G_{\rm EM}(s)$, defined in Eq. (9.5), to the hadronic τ–decay, where now the $\Delta(s,t)$ term including the radiative corrections reads

$$\Delta(s,t) = 1 + 2\,\mathrm{Re}\,\kappa_+^{\rm match}(s,t) + g_{\rm Low}(s,t) + g_{\rm rest}(s,t). \tag{13.1}$$

In the following we explain in details our fitting procedure, we show the fit results and, at the end, we give our final estimate of $\Delta a_\mu^{\rm HVP,\,LO}[\pi\pi,\tau]$ in Sec. 13.4.

13.1 Fitting procedure

The pion vector form factor $f_+(s)$ is determined by fitting the experimental data from Belle [281], ALEPH [282], CLEO [283] and OPAL [284]. These experiments measure the spectrum

$$\frac{1}{N}\frac{\mathrm{d}N}{\mathrm{d}s} = \frac{K_\Gamma(s)}{\Gamma_\pi}\beta_{\pi\pi^0}^3(s)|f_+(s)|^2 G_{\rm EM}(s)\,, \tag{13.2}$$

with partial widths $\Gamma_e \equiv \Gamma(\tau^- \to e^-\bar\nu_e\nu_\tau)$ contained in $K_\Gamma(s)$ in Eq. (9.4) and $\Gamma_\pi \equiv \Gamma(\tau^- \to \pi^-\pi^0\nu_\tau)$. For the external inputs we use $S_{\rm EW}^{\pi\pi} = 1.0233(24)$ [14], $\mathrm{Br}[\tau \to e\nu_\tau\bar\nu_e] = 17.82(4)\%$ and $\mathrm{Br}[\tau \to \pi\pi\nu_\tau] = 25.49(9)\%$ from the global fit of [158, 285] (whose errors are correlated with coefficient -0.19), and $V_{ud} = 0.97367(32)$ [158].

Since $G_{\rm EM}(s)$ itself is dependent on the input of $f_+(s)$ but rather expensive to numerically calculate, a self–consistent iterative procedure is followed:

1. Determine $G_{\rm EM}(s)$ from $f_+(s) = \Omega_1^1(s)$, with $\delta(s_0) = 110.4^\circ$ and $\delta(s_1) = 165.7^\circ$, where $s_0 = (0.8\ \mathrm{GeV})^2$ and $s_1 = (1.15\ \mathrm{GeV})^2$, as extracted from fits to $e^+e^- \to \pi^+\pi^-$ (cf. Tab. 10 of [102]).
2. Having fixed $G_{\rm EM}(s)$, we fit the free parameters in $f_+(s)$ of Eq. (11.7) by means of Eq. (13.2) to the experimental data, with the regularization of Eq. (9.9). From the discussion in Sec. 11.2, we have $2 + 2\times 3 + (N-2)$ free fit parameters, with N the degree of the conformal polynomial $G_{\rm in}(s)$.
3. The resulting representation for $f_+(s)$ is then used to calculate $G_{\rm EM}(s)$ in the next step and the fit is repeated with this new input.

The procedure is stopped once there is convergence in the fit parameters, i.e., after a few iterations. In practice, the differences to the starting point $f_+(s) = \Omega_1^1(s)$ are small but certainly not negligible, reflecting the important role of inelastic effects for a precision analysis of $a_\mu^{\rm HVP,\,LO}[\pi\pi]$ [286, 287].

The spectrum provided by the different experiments falls into bins of widths s_b, e.g., in the case of the Belle experiment almost all of the bins are of width $s_b = 0.05\,\mathrm{GeV}^2$. Within the bin, events will not be

distributed equally, but weighted by the distribution, so that the actual observable becomes

$$\left(\frac{1}{N}\frac{\mathrm{d}N}{\mathrm{d}s}(s_i)\right)^{\text{bin}} = \frac{1}{s_i^b}\int_{s_i-s_i^b/2}^{s_i+s_i^b/2}\mathrm{d}s\frac{1}{N}\frac{\mathrm{d}N}{\mathrm{d}s}(s)\,, \tag{13.3}$$

in the bins with center s_i. Alternatively, one can calculate corrected bin centers s_i^{corr} for the pion VFF fit by a null search, and we checked that both approaches lead to identical results. This effect is analogous to the required bin average for hadronic cross–section measurements using initial–state radiation [102,288,289].

Furthermore, we make use of the statistical covariance matrix $\text{Cov}^{\text{stat}}(i,j)$ as well as the full systematic covariance matrix $\text{Cov}^{\text{syst}}(i,j)$ whenever available, i.e., for Belle and ALEPH experiments. While for the CLEO experiment only the systematic covariance matrix is available, the OPAL experiment provides a combined statistical and systematic covariance matrix, without the information to disentangle the two error components. In these two cases we treated the single covariant matrix as purely statistical. In order to avoid the D'Agostini bias [290], the total covariance matrix is constructed via [291]

$$\text{Cov}(i,j) = \text{Cov}^{\text{stat}}(i,j) + \left(\frac{1}{N}\frac{\mathrm{d}N}{\mathrm{d}s}(s_i)\right)^{\text{bin}}\left(\frac{1}{N}\frac{\mathrm{d}N}{\mathrm{d}s}(s_j)\right)^{\text{bin}}\frac{\text{Cov}^{\text{syst}}(i,j)}{y_i y_j}\,, \tag{13.4}$$

where y_i is the central value of the experimental observable in bin i, which is then used in yet another iterative procedure for each fit of the theoretical distribution to the data.

13.2 Sources of uncertainties

The uncertainties we considered in our analysis and that we propagated to $G_{\text{EM}}(s)$ can be divided into the ones coming from the input data and the theoretical ones. For the first group, the uncertainties are given by

- statistical and systematic covariance matrices on $\tau^- \to \pi^-\pi^0\nu_\tau$ data.
- uncertainties on the spectrum due to the branching ratios $\text{Br}(\tau^- \to e^-\bar{\nu}_e\nu_\tau)$ and $\text{Br}(\tau^- \to \pi^-\pi^0\nu_\tau)$.

The errors derived from the covariance matrices give rise to a fit uncertainty on $f_+(s)$, which is then propagated to $G_{\text{EM}}(s)$, including a scale factor if $\chi^2/\text{dof} > 1$. Combined with the uncertainty derived from the branching ratios, this defines the experimental error. On the theory side, the sources of theoretical uncertainties entering in the pion vector form factor $f_+(s)$ are

- the variation of the conformal polynomial degree N,
- the variation of the s_c parameter in the conformal polynomial,

while for uncertainties entering the $G_{\text{EM}}(s)$ directly we have

- the variation of the cutoff of the dispersive integral (from 20 GeV^2 to 9 GeV^2),
- the use of different estimates for the couplings F_V, G_V and F_A that enter once we include the resonances contribution (see Sec. 12.5).

In the latter case, we define the difference between results obtained with the SD couplings (12.23) and the phenomenologically estimated ones (12.24) as 1σ uncertainties, while for the other uncertainties the errors are quoted as the maximal deviation from our central solution. Additionally, for the computation of the uncertainty on the shift Δa_μ (and entering also the spectrum in Eq. (13.2)), the uncertainty due to the scheme dependence of $S_{\text{EM}}^{\pi\pi}$, as reported in [14], is included. The same uncertainty also affects the spectrum (13.2), but only via an overall rescaling. Accordingly, we first present fit results that focus on the uncertainty components listed above, while adding the SD error propagated from $S_{\text{EM}}^{\pi\pi}$ at the end.

13.3 Fit results

We perform fits for different degree of the conformal polynomial ($N = 3, 4, 5$, corresponding to $N-2$ free parameters) to the Belle data only, to Belle+ALEPH and to all the data sets combined (Belle+ALEPH+CLEO+OPAL). The reason behind this choice is as follows: first, the Belle data set provides the most precise spectral function, especially in the ρ', ρ'' region, and we find that individual fits to the other data sets struggle to resolve the detailed resonance structure, which would require using a simplified fit function in these cases, and thus leading to results that are difficult to compare. For this reason, we always include the Belle data in each fit variant. Second, the only other data set for which a full documentation of the statistical and systematic uncertainties is available is ALEPH, while for CLEO and OPAL systematic errors are either not provided or combined with statistical ones, and this motivates a combined fit with Belle. We still quote the global fit as our final result, but it is instructive to compare fits to the more complete data sets only (see Tab. 13.1).

Stable fits are obtained for $N = 3, 4$, with p–values ranging from a few percent if we consider only the Belle data set, over 3.0×10^{-3} for the fit to Belle+ALEPH, to 0.7×10^{-3} for the global fit. Accordingly, it is clear that some tensions are present in the data base, since the fit quality deteriorates considerably in the latter cases. To investigate the fit quality further, we also studied variants allowing for an additional parameter in the conformal polynomial, in which case the p–value increases to over 60% for Belle only and to a few percent for the combined fit, suggesting that the fits with lower N could be too constrained. However, we observe that the gain in the χ^2 values comes at the expense of clear signs of overfitting, i.e., the ρ'' parameters need to be stabilized by imposing penalty functions, as otherwise mass and width parameter would run away to unphysical values. In addition, the asymptotic behavior of Im $f_+(s)$ outside the region constrained by data starts to show unphysical oscillations, indicating that tensions in the physical region are transferred to the high–energy tail. For that reason, we define our central values by $N = 4$, while including the variation to $N = 3, 5$ in the uncertainty estimate. This procedure ensures that both the systematic variation among all fit variants and the error inflation of the statistical error are taken into account. The latter would be minimized or even absent if choosing the $N = 5$ fits as central values, thus hiding the tensions in the data base. We also considered fit variants in which the explicit ρ', ρ'' contributions are replaced by corresponding poles in the conformal variables [253]. In general, the behavior is similar, as fits with smooth high–energy behavior tend to display relatively poor fit quality, which can be overcome by allowing for more fit parameters, but again at the expense of overfitting and even more severe instabilities in the ρ', ρ'' parameters, presumably due to the fact that the sensitivity to the pole parameters is reduced compared to parameterizations better tailored for the real axis. While eventually the former would be preferred, we conclude that with the ρ'' so close to the border of the available phase space, fits to the τ spectral function based on the functional form in Eq. (11.7) are better controlled.

The global fit is shown in Fig. 13.1, while in Figs. 13.2 we show a zoom of our fit result around the ρ resonance peak (left) and close to the threshold $4M_\pi^2$ (right), since it is, in fact, the low energy region that gives the biggest contribution to the muon $g-2$ computation from τ data. Due to the energy weighting in the calculation of $a_\mu^{\mathrm{HVP,\,LO}}[\pi\pi, \tau]$, we find that the threshold region actually plays an integral role, especially, as there appears to be some (compensating) tension between the threshold and ρ–resonance region. That is, while in the central fits with $N = 4$ the VFF in the ρ peak tends to be overestimated, for $N = 5$ the data around the $\rho(770)$ are better reproduced, yet the integrated a_μ value actually increases, due to an enhancement in the threshold region. Within uncertainties all fits are compatible, but the observation remains that the analyticity and unitarity constraints built into our dispersive representation of $f_+(s)$ suggest some tension in the data sets between threshold and resonance region.

The modulus of the pion VFF $f_+(s)$ arising from our global fit to the experimental data is shown in Fig. 13.3, while in Fig. 13.4 we display the real and imaginary parts of $f_+(s)$ separately. It is also instructive

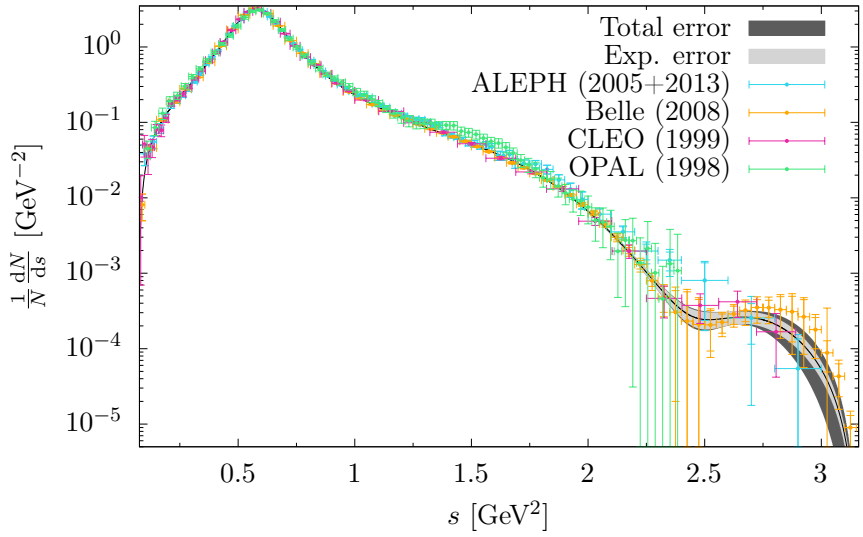

Figure 13.1: Fit to the data sets for the full energy range and considering all the experiments, i.e., Belle+ALEPH+CLEO+OPAL.

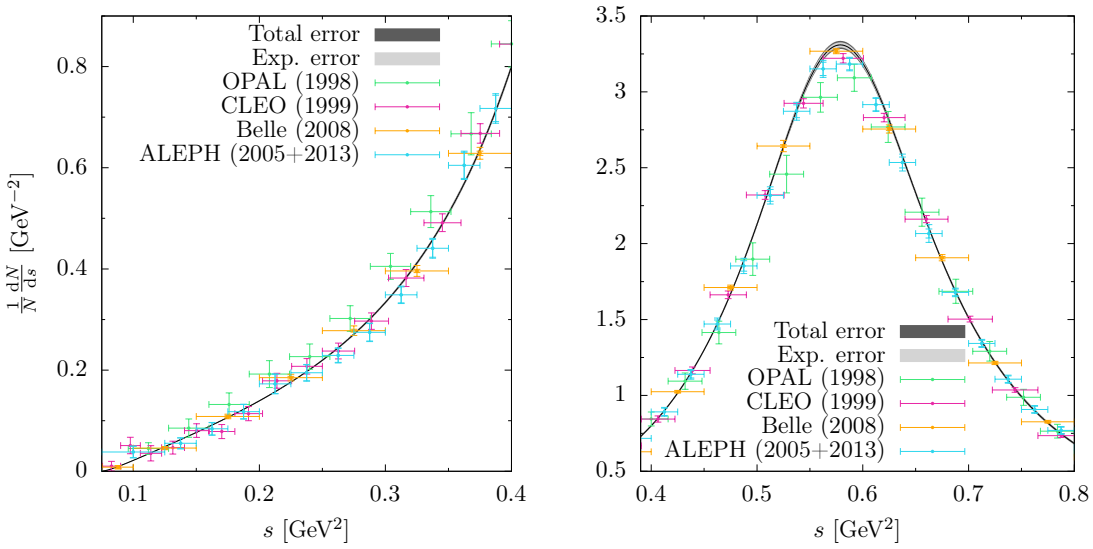

Figure 13.2: Fit result for the energy spectrum in the region close to threshold (left) and around the ρ–resonance peak (right).

χ^2/dof	p-value	$\delta(s_0)$ [°]	$\delta(s_1)$ [°]	$p_3 \times 10^2$	$p_4 \times 10^2$	$p_5 \times 10^2$	$c_{\rho'}$ [GeV^2]	$M_{\rho'}$ [GeV]	$\Gamma_{\rho'}$ [MeV]	$c_{\rho''}$ [GeV^2]	$M_{\rho''}$ [GeV]	$\Gamma_{\rho''}$ [MeV]
Belle ($N_{\rm data} = 62$)												
1.36	0.041	110.05(13)	167.00(10)	3.11(65)			0.47(9)	1.46(2)	443(47)	−0.24(8)	1.67(2)	257(83)
1.30	0.070	109.95(15)	166.93(11)	−3.7(4.4)	3.4(2.2)		0.33(10)	1.44(2)	375(58)	−0.40(14)	1.70(2)	289(76)
0.93	0.62	109.60(16)	166.57(13)	−4.3(4.7)	17.5(3.7)	−6.4(1.4)	0.66(12)	1.49(1)	566(53)	−0.94(20)	1.75(1)	398(58)
1.36	0.043	110.04(14)	167.00(10)	3.13(66)			0.47(10)	1.46(2)	442(51)	−0.24(8)	1.67(2)	257(87)
1.30	0.072	109.94(15)	166.92(11)	−3.6(4.4)	3.3(2.2)		0.33(10)	1.44(2)	376(58)	−0.39(14)	1.70(2)	289(77)
0.93	0.62	109.59(26)	166.57(26)	−4.2(4.9)	17.4(5.5)	−6.4(2.1)	0.66(12)	1.49(1)	565(57)	−0.94(21)	1.75(1)	399(63)
Belle+ALEPH ($N_{\rm data} = 62 + 78 = 140$)												
1.37	0.0029	109.89(13)	166.77(8)	3.11(64)			0.46(8)	1.46(2)	450(47)	−0.21(7)	1.67(2)	262(98)
1.38	0.0028	109.81(13)	166.71(10)	−1.8(3.1)	2.4(1.6)		0.36(6)	1.45(1)	404(35)	−0.32(10)	1.70(2)	297(71)
1.20	0.062	109.41(14)	166.33(10)	−0.77(4.80)	17.7(3.4)	−7.3(1.4)	0.75(13)	1.50(1)	611(52)	−0.82(19)	1.75(1)	400(59)
1.37	0.0030	109.88(12)	166.77(9)	3.13(65)			0.46(9)	1.46(2)	450(47)	−0.21(8)	1.67(2)	260(120)
1.38	0.0030	109.79(14)	166.71(10)	−1.7(4.4)	2.4(2.2)		0.37(10)	1.45(2)	405(57)	−0.32(14)	1.70(3)	297(92)
1.20	0.060	109.41(13)	166.33(9)	−0.7(4.8)	17.5(3.2)	−7.2(1.3)	0.75(13)	1.50(1)	610(51)	−0.81(19)	1.75(1)	401(59)
Belle+ALEPH+CLEO+OPAL ($N_{\rm data} = 62 + 78 + 43 + 72 = 255$)												
1.32	0.0006	109.75(9)	166.59(7)	3.26(69)			0.53(10)	1.47(2)	482(49)	−0.25(8)	1.66(2)	295(69)
1.32	0.0007	109.67(12)	166.54(9)	−1.4(4.2)	2.2(2.1)		0.43(12)	1.46(2)	439(57)	−0.36(14)	1.69(3)	327(90)
1.19	0.021	109.31(12)	166.20(9)	−0.8(5.9)	18.6(3.2)	−7.7(1.4)	0.81(21)	1.50(2)	631(75)	−0.88(19)	1.75(1)	416(57)
1.32	0.0006	109.74(11)	166.59(8)	3.28(67)			0.53(8)	1.47(2)	481(44)	−0.25(5)	1.66(2)	295(52)
1.32	0.0006	109.66(12)	166.54(9)	−1.2(3.8)	2.2(1.9)		0.43(10)	1.46(2)	440(50)	−0.36(13)	1.69(3)	326(85)
1.19	0.020	109.31(15)	166.18(14)	−0.7(5.0)	18.4(4.0)	−7.6(1.7)	0.81(14)	1.50(1)	630(59)	−0.88(20)	1.75(1)	417(68)

Table 13.1: Results of our fits to the (combined) data sets Belle, Belle+ALEPH, and Belle+ALEPH+CLEO+OPAL (in brackets the number of data points). For each (combination of) experimental data set(s), we show the result for $N = 3$ (first line of each set of fits), $N = 4$ (second line of each set of fits), and $N = 5$ (third line of each set of fits). Moreover, the results account for different values of F_V, G_V, and F_A: SD couplings from Eq. (12.23) (upper half of each set of fits) and phenomenological couplings from Eq. (12.24) (lower half of each set of fits). The uncertainties refer to the fits errors, prior to scale–factor inflation (where applicable).

to consider the phase of the pion VFF, see Fig. 13.5, especially in view of the preceding discussion about the asymptotic behavior. In all fit variants, by construction, the phase ultimately tends to π, ensuring the correct asymptotic behavior of the pion VFF $f_+(s) \simeq 1/s$ [292–296], but for $N = 5$ one observes sizable oscillations before the phase returns to its asymptotic value.

13.4 Determination of Δa_μ

From the fit described in the previous section, we obtain the results for $G_{\rm EM}(s)$ in Figs. 13.6 and 13.7. In particular, Fig. 13.6 shows the result for the leading Low contribution to $G_{\rm EM}(s)$, i.e., the one obtained by considering only the effect of $\kappa_+^{\rm match}(s,t)$ and $g_{\rm Low}(s,t)$ in Eq. 13.1. Importantly, the curves labeled by "ChPT" in Figs. 13.6 and 13.7 do not exactly correspond to the numerical results from [34, 35], but are instead constructed replacing $\kappa_+^{\rm match}(s,t)$ in Eq. (13.1) by $f_+^{\chi\rm PT}(t)$, which amounts to replacing the dispersive evaluation of the box diagram by its χPT approximation. In this way, we obtain a more meaningful comparison of χPT and dispersive results, updating other aspects of [34, 35] to the input used in this work, e.g., input for $f_+(s)$ and LECs.

Differently from the previous result (red line), our new model–independent dispersive approach shows a clear structure–dependent correction in the ρ, ρ' and ρ'' regions already in Fig. 13.6. Moreover, we notice that while the χPT $G_{\rm EM}^{\rm Low}(s)$ contribution remains almost constant with values around 1 for most of the energy range, our result becomes greater then 1 around the ρ–resonance region, explaining the difference we observe for the $\Delta a_\mu^{\rm HVP,\,LO}[\pi\pi,\tau]$ estimate due to $G_{\rm EM}^{\rm Low}(s)$ with respect to the result in [35] and leading

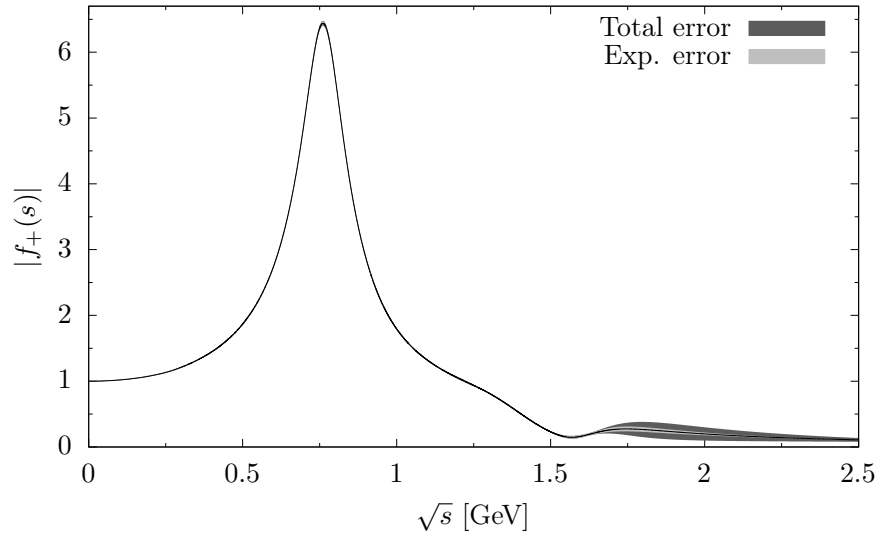

Figure 13.3: Modulus of the pion vector form factor $f_+(s)$ obtained by fitting the full experimental data sets (Belle+ALEPH+CLEO+OPAL).

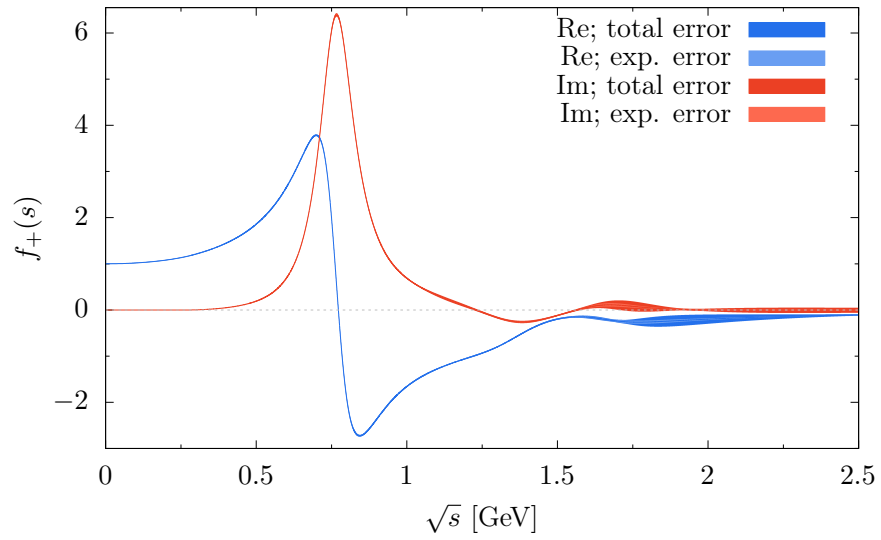

Figure 13.4: Real and imaginary parts of the pion vector form factor $f_+(s)$.

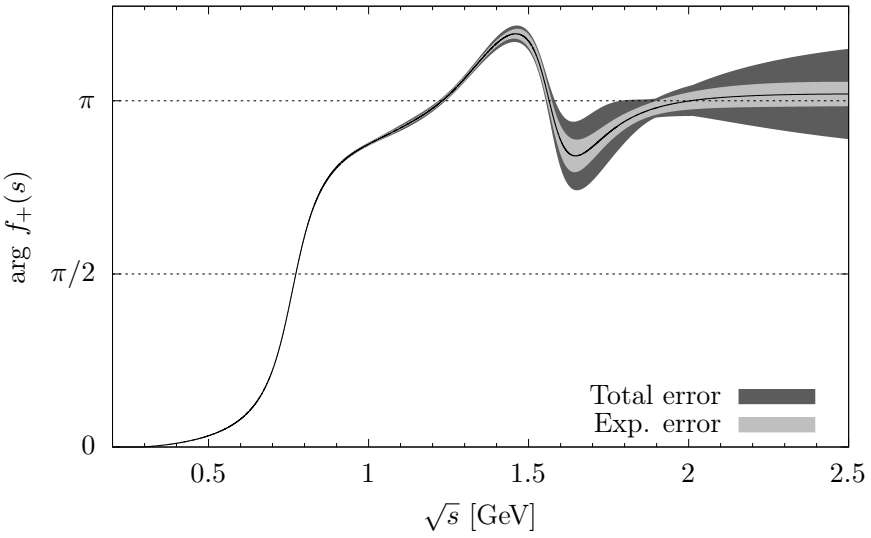

Figure 13.5: Phase of the pion vector form factor $f_+(s)$.

to a substantial decrease by about 2×10^{-10}. Fig. 13.7 shows the full $G_{\rm EM}(s)$, i.e., including also $g_{\rm rest}(s,t)$ with all the resonances terms (v_i, a_i and ω). While the qualitative behavior largely matches previous work, the energy dependence is altered substantially, especially in the vicinity of the ρ resonance. In addition, we observe a constant offset, which traces back to the local term in the χPT contribution, especially the SD logarithm in Eq. (11.46).[6] The large uncertainty band close to the $4M_\pi^2$ threshold is mainly due to the different estimates for the resonance coupling F_V, G_V and F_A we employed, which as a direct consequence will give the largest contribution to the theoretical error in the shift $\Delta a_\mu^{\rm HVP,\,LO}[\pi\pi,\tau]$. We are now in the position to evaluate the shift of the HVP integral caused by IB corrections specific to the hadronic τ decay, $\tau^- \to \pi^-\pi^0\nu_\tau$. By setting $|F_\pi^V(s)/f_+(s)| = 1$ in Eq. (9.2), the shift $\Delta a_\mu^{\rm HVP,LO}$ can be expressed as

$$\Delta a_\mu^{\rm HVP,LO}[\pi\pi,\tau] = \Big(\frac{\alpha m_\mu}{3\pi}\Big)^2 \int_{4M_\pi^2}^{m_\tau^2} {\rm d}s \frac{\hat{K}(s)}{4s^2} \left[\frac{\beta_{\pi\pi}^3(s)}{\beta_{\pi\pi^0}^3(s)} \frac{1}{S_{\rm EW}^{\pi\pi} G_{\rm EM}(\tilde{s}(s))} - 1\right] v_\tau(s)\,, \tag{13.5}$$

with the τ spectral function given by

$$v_\tau(s) = S_{\rm EW}^{\pi\pi} \beta_{\pi\pi^0}^3(s) |f_+(s)|^2 G_{\rm EM}(\tilde{s}(s))\,, \tag{13.6}$$

and charged pion phase space factor $\beta_{\pi\pi}(s) = \sqrt{1 - 4M_\pi^2/s}$. Different contributions to $\Delta a_\mu^{\rm HVP,LO}[\pi\pi,\tau]$ are usually singled out via linearization of the integrand

$$\Delta a_\mu^{\rm HVP,LO}[\pi\pi,\tau]\Big|_{\rm PS} = \Big(\frac{\alpha m_\mu}{3\pi}\Big)^2 \int_{4M_\pi^2}^{m_\tau^2} {\rm d}s \frac{\hat{K}(s)}{4s^2} \left[\frac{\beta_{\pi\pi}^3(s)}{\beta_{\pi\pi^0}^3(s)} - 1\right] v_\tau(s)\,, \tag{13.7}$$

$$\Delta a_\mu^{\rm HVP,LO}[\pi\pi,\tau]\Big|_{S_{\rm EW}} = \Big(\frac{\alpha m_\mu}{3\pi}\Big)^2 \int_{4M_\pi^2}^{m_\tau^2} {\rm d}s \frac{\hat{K}(s)}{4s^2} \left[\frac{1}{S_{\rm EW}^{\pi\pi}} - 1\right] v_\tau(s)\,, \tag{13.8}$$

[6] Part of the local contribution to $f_+^{\chi\rm PT}(t)$, as given in Eqs. (10.16) and (10.19), was absorbed into the definition of the pion VFF $f_+(s)$ in [34, 35]. We avoid this bookkeeping, as it would lead to a more complicated form of $f_+(s)$ in the fit to the τ spectral function, in particular, the normalization would differ from unity, by an amount ultimately controlled by the LEC X_ℓ. Moreover, the analysis of the matching to SD contributions would become more complicated, given that this matching relation is most conveniently derived at the level of the chiral LEC [223].

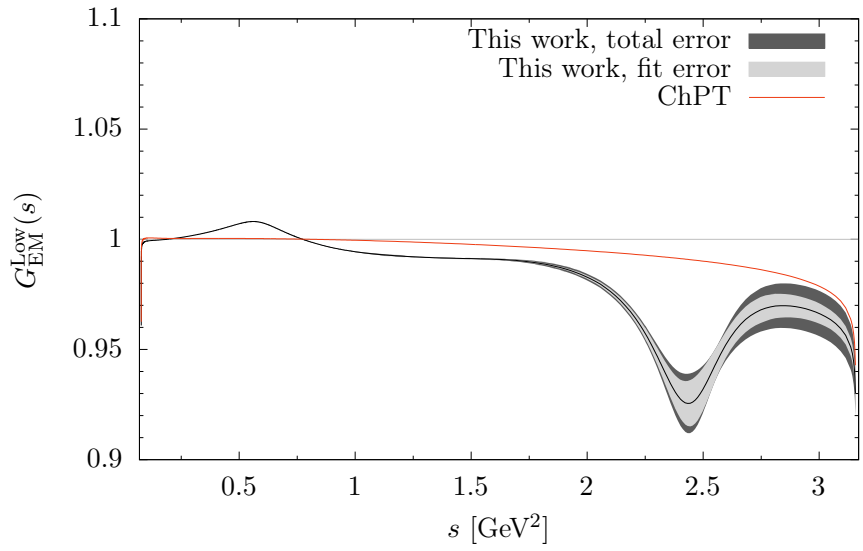

Figure 13.6: Result for the leading Low $G_{\rm EM}(s)$ contribution, i.e., including $\kappa_+^{\rm match}(s,t)$, $g_{\rm Low}(s,t)$ but setting $g_{\rm rest}(s,t)$ to zero.

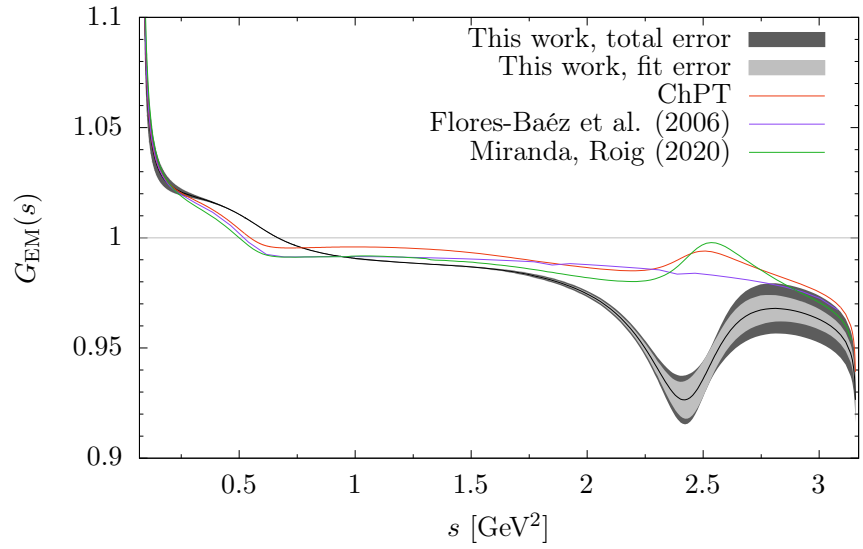

Figure 13.7: Result for the full $G_{\rm EM}(s)$ contribution, i.e., including $\kappa_+^{\rm match}(s,t)$, $g_{\rm Low}(s,t)$ and $g_{\rm rest}(s,t)$. In particular $g_{\rm rest}(s,t)$ include the contributions from the different resonances, i.e., ρ, a_1 and ω.

$$\Delta a_\mu^{\text{HVP,LO}}[\pi\pi,\tau]\Big|_{G_{\text{EM}}} = \left(\frac{\alpha m_\mu}{3\pi}\right)^2 \int_{4M_\pi^2}^{m_\tau^2} \mathrm{d}s \frac{\hat{K}(s)}{4s^2}\left[\frac{1}{G_{\text{EM}}(\tilde{s}(s))} - 1\right] v_\tau(s)\,, \tag{13.9}$$

to represent phase–space, SD, and radiative corrections and such that we can write it in a general form as

$$\Delta a_\mu^{\text{HVP,LO}}[\pi\pi,\tau]\Big|_{r_{\text{IB}}} = \left(\frac{\alpha m_\mu}{3\pi}\right)^2 \int_{4M_\pi^2}^{m_\tau^2} \mathrm{d}s \frac{\hat{K}(s)}{4s^2}\left[r_{\text{IB}}(s) - 1\right] v_\tau(s)\,. \tag{13.10}$$

Explicitly spelling out the effects of $\mathcal{O}(e^2)$ in the integrand as $M_{\pi^0}^2 = M_\pi^2 - e^2\Delta_M$, $S_{\text{EW}}^{\pi\pi} = 1 + e^2\Delta S_{\text{EW}}^{\pi\pi}$ and $G_{\text{EM}} = 1 + \Delta G_{\text{EM}}$, the difference of the linearized integrand and the full one, expanded in e^2, appears as

$$\begin{aligned}&\left[\left(\frac{1}{G_{\text{EM}}} - 1\right) + \left(\frac{\beta_{\pi\pi}^3}{\beta_{\pi\pi^0}^3} - 1\right) + \left(\frac{1}{S_{\text{EW}}^{\pi\pi}} - 1\right) - \left(\frac{\beta_{\pi\pi}^3(s)}{\beta_{\pi\pi^0}^3(s)}\frac{1}{S_{\text{EW}}^{\pi\pi} G_{\text{EM}}(\tilde{s}(s))} - 1\right)\right] v_\tau \\ &\qquad = -e^4 \frac{\sqrt{s-4M_\pi^2}}{s^{3/2}}\left[(s-4M_\pi^2)\Delta G_{\text{EM}}\Delta S_{\text{EM}}^{\pi\pi} + 3\Delta_M(\Delta G_{\text{EM}} + \Delta S_{\text{EM}}^{\pi\pi})\right]|f_+(s)|^2 + \mathcal{O}(e^6)\,,\end{aligned} \tag{13.11}$$

suggesting that since G_{EM} diverges at the $\pi\pi^0$ threshold, the term $\propto \Delta_M \Delta G_{\text{EM}}$ could become relevant due to the resulting threshold enhancement.

The results considering all the three different fit variants for the integrals in Eqs. (13.7), (13.8) and (13.9) as well as the one without factorizing the integral, i.e., Eq. (13.5), are given in Tab. 13.2. In particular, for the contribution to $\Delta a_\mu^{\text{HVP,LO}}[\pi\pi,\tau]$ coming from $G_{\text{EM}}(s)$, we have the following splitting:

- $G_{\text{EM}}^{\text{Low}}(s)$ contribution obtained by setting to zero $g_{\text{rest}}(s,t)$ in Eq. (13.1).
- $G_{\text{EM}}^{\text{no R}\chi\text{PT}}(s)$ contribution that includes $g_{\text{rest}}(s,t)$ but with the resonances terms turned off, i.e., with v_i and a_i in Eq. (12.4) and the ω contributions set to zero.
- $G_{\text{EM}}^{\text{Full}}(s)$ contribution with all the resonances (v_i, a_i and ω) terms restored in $g_{\text{rest}}(s,t)$.

$r_{\text{IB}}(s)$	Belle	Belle+ALEPH	Belle+ALEPH+CLEO+OPAL
$1/G_{\text{EM}}^{\text{Low}}(s)$	$-2.292(15)_{\text{exp}}(14)_{\text{theo}}$	$-2.279(13)_{\text{exp}}(16)_{\text{theo}}$	$-2.267(13)_{\text{exp}}(14)_{\text{theo}}$
$1/G_{\text{EM}}^{\text{no R}\chi\text{PT}}(s)$	$-5.21(3)_{\text{exp}}(2)_{\text{theo}}$	$-5.20(3)_{\text{exp}}(2)_{\text{theo}}$	$-5.19(3)_{\text{exp}}(2)_{\text{theo}}$
$1/G_{\text{EM}}^{\text{Full}}(s)$	$-5.44(3)_{\text{exp}}(40)_{\text{theo}}$	$-5.43(3)_{\text{exp}}(40)_{\text{theo}}$	$-5.41(3)_{\text{exp}}(40)_{\text{theo}}$
$\beta_{\pi\pi}^3(s)/\beta_{\pi\pi^0}^3(s)$	$-7.74(4)_{\text{exp}}(3)_{\text{theo}}$	$-7.73(4)_{\text{exp}}(3)_{\text{theo}}$	$-7.74(4)_{\text{exp}}(3)_{\text{theo}}$
$1/S_{\text{EW}}^{\pi\pi}$	$-12.180(57)_{\text{exp}}(8)_{\text{theo}}$	$-12.177(57)_{\text{exp}}(7)_{\text{theo}}$	$-12.166(56)_{\text{exp}}(8)_{\text{theo}}$
$\sum r_{\text{IB}}$	$-25.36(12)_{\text{exp}}(44)_{\text{theo}}$	$-25.34(12)_{\text{exp}}(44)_{\text{theo}}$	$-25.32(12)_{\text{exp}}(44)_{\text{theo}}$
Full	$-24.84(12)_{\text{exp}}(39)_{\text{theo}}$	$-24.82(12)_{\text{exp}}(39)_{\text{theo}}$	$-24.80(12)_{\text{exp}}(39)_{\text{theo}}$
$\tilde{a}_\mu$	$510.1(2.4)_{\text{exp}}(0.2)_{\text{theo}}$	$510.0(2.4)_{\text{exp}}(0.2)_{\text{theo}}$	$509.5(2.4)_{\text{exp}}(0.2)_{\text{theo}}$

Table 13.2: Result for the correction $\Delta a_\mu^{\text{HVP, LO}}[\pi\pi,\tau]$ (in units of 10^{-10}) due to different $G_{\text{EM}}(s)$ contributions (leading Low, full radiation off τ and π, full real emission including resonances), phase–space factor, and $S_{\text{EW}}^{\pi\pi}$. The results labeled as $\sum r_{\text{IB}}$ are obtained by summing the contributions from $G_{\text{EM}}^{\text{full}}(s)$, phase space, and $S_{\text{EW}}^{\pi\pi}$, while "Full" combines the same effects but without linearization. $\tilde{a}_\mu$ refers to the resulting two–pion contribution $a_\mu^{\text{HVP, LO}}[\pi\pi,\tau]$, but without consideration of IB in the matrix elements and before adding e^+e^-–specific corrections. The theory error do not include yet the uncertainty due to the scheme ambiguity in $S_{\text{EW}}^{\pi\pi}$ nor an estimate of higher intermediate states in the virtual contribution. All results are provided separately for the three fit variants given in Table 13.1.

	Ref. [267]	Ref. [297]	Ref. [14]	This work
Phase space	-7.88	-7.52	$-7.7(2)$	$-7.74(5)$
$S_{\rm EW}^{\pi\pi}$	$-12.21(15)$	$-12.16(15)$	$-12.2(1.3)$	$-12.2(1.3)$
$G_{\rm EM}^{\rm full}$	$-1.92(90)$	$(-1.67)^{+0.60}_{-1.39}$	$-2.0(1.4)$	$-5.4(5)$
Sum	$-22.01(91)$	$(-21.35)^{+0.62}_{-1.40}$	$-21.9(1.9)$	$-25.3(1.4)$
Full	–	–	–	$-24.8(1.4)$
$\tilde{a}_\mu$	$510.3(3.0)$	$510.9^{+2.9}_{-3.1}$	$510.3(3.4)$	$509.5(2.7)$

Table 13.3: Comparison to previous work, following the notation of Table 13.2. Our results have been supplemented by the SD error from [14], which then dominates the final uncertainty, as well as an estimate of higher intermediate states in the virtual contribution.

Finally, Table 13.2 also includes a quantity defined as

$$\tilde{a}_\mu \equiv \left(\frac{\alpha m_\mu}{3\pi}\right)^2 \int_{4M_\pi^2}^{m_\tau^2} \mathrm{d}s \frac{\hat{K}(s)}{4s^2} \frac{\left[\beta_{\pi\pi}(s)\right]^3}{\left[\beta_{\pi\pi^0}(s)\right]^3} \frac{v_\tau(s)}{S_{\rm EW}^{\pi\pi} G_{\rm EM}[\tilde{s}(s)]}\,, \tag{13.12}$$

which can be interpreted as the first step towards $a_\mu^{\rm HVP,\,LO}[\pi\pi,\tau]$, prior to considering corrections in the matrix elements $|F_\pi^V(s)/f_+(s)| = 1 + \mathcal{O}(e^2)$ and adding IB corrections specific for e^+e^-.

First, Table 13.2 shows that the differences for the resulting IB corrections among the different fits are small, which simply reflects the fact that the IB corrections are required with much less relative precision than the full integral. However, even at this level of precision we observe that a linearization of the IB corrections should be avoided, since the threshold–enhanced $\mathcal{O}(e^4)$ terms do become relevant. This observation also emphasizes the importance of a stable numerical implementation down to the two–pion threshold, to fully capture these corrections. Considering the changes among the different $G_{\rm EM}(s)$ variants, the numerically largest contribution arises from the radiation of τ and π, around -3.0×10^{-10}, while the additional contribution due to resonance diagrams only induces an additional shift around -0.2 units. This shift, in fact, is less than half the size of the uncertainty propagated from the resonance couplings, most notably F_A, which dominates the overall uncertainty budget for $G_{\rm EM}(s)$. In view of this substantial uncertainty already of the leading resonance contributions, which are motivated via χPT resonance saturation, together with the overall small impact of resonance contributions on $\Delta a_\mu^{\rm HVP,\,LO}[\pi\pi,\tau]$, we do not see a justification for including yet higher resonance multiplets.

By comparing results for our full dispersive and the χPT version of the triangle diagram, we find that structure–dependent virtual corrections amount to about -2.0×10^{-10}, yielding the second largest contribution after bremsstrahlung off τ and π.[7] Accordingly, one could worry about the possible impact of higher intermediate states in the hadronic matrix element, via resonance left–hand cuts or rescattering corrections. Given the experience from $\gamma^*\gamma^* \to \pi\pi$ [79–81, 227–229], one would expect such effects to be small in the low–energy region, with the first major resonance–enhanced structure related to the $f_2(1270)$ resonance. To account for virtual corrections beyond the pion pole, we assign an additional uncertainty of 0.3×10^{-10} to the $G_{\rm EM}(s)$ contribution, motivated as the same relative uncertainty as resonance diagrams induce in the case of real emission.

[7] The separation of real and virtual contributions is of course scale dependent, but the differences of dispersive and χPT results for the triangle diagram, to quantify structure–dependent virtual contributions, and of $G_{\rm EM}^{\rm rad}$ and $G_{\rm EM}^{\rm Low}$, to quantify radiation off τ and π, are well defined.

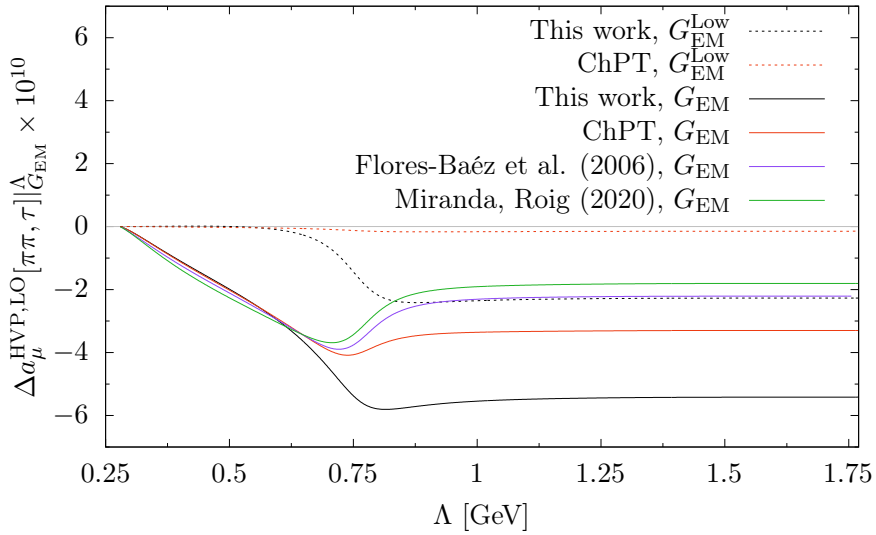

Figure 13.8: $G_{\rm EM}(s)$ contribution to $\Delta a_\mu^{\rm HVP,\,LO}[\pi\pi,\tau]$ as a function of a cutoff Λ in the HVP integral, for our dispersive implementation of the box diagram and its ChPT approximation, in both cases for the leading Low and full evaluation of real emission. Additionally, the results corresponding to using the full $G_{\rm EM}(s)$ of previous works by Flores-Baéz et al. (2006) [265] and Miranda, Roig (2020) [37] are shown.

Our final results are summarized in Table 13.3, with central value defined by the $N = 4$ VFF fits to all data sets and the mean of the strategies in Eqs. (12.23) and (12.24) for the resonance couplings

$$\Delta a_\mu^{\rm HVP,\,LO}[\pi\pi,\tau]\big|_{\rm Full} = -24.8(0.1)_{\rm exp}(0.5)_{\rm th}(1.3)_{\rm SD} \times 10^{-10}\,, \tag{13.13}$$

where the experimental error combines the uncertainties derived from the covariance matrices of the data for the τ spectral function and the τ branching fractions, while the theory error accounts for all contribution listed in Sec. 13.2, i.e., variation of N, s_c, the cutoff of the dispersive integral, and the resonance couplings, with the latter the by far most important effect. Overall, the uncertainty is now dominated by the scheme dependence in $S_{\rm EW}^{\pi\pi}$, that is, the matching between SD contributions contained in $S_{\rm EW}^{\pi\pi}$ and radiative corrections described by $G_{\rm EM}(s)$. As for $G_{\rm EM}(s)$ itself, however, the uncertainty has been reduced by a factor of three compared to the assignment in [14], which mainly reflects the fact that potentially sizable structure–dependent virtual corrections are now explicitly evaluated. In Fig. 13.9, we show the differences $\Delta a_\mu = a_\mu^{\rm SM} - a_\mu^{\rm Exp}$ for different inputs of $a_\mu^{\rm HVP,LO}$. As we can see our result slightly shift the correction closer to the WP20 estimate.

It is also instructive to scrutinize the origin of the changes in central value compared to the previous work listed in Table 13.3, after all, our value for the $G_{\rm EM}(s)$ contribution shifts by about 2.5 σ, part of which is then canceled upon adding the previously neglected $\mathcal{O}(e^4)$ effects. To this end, we first evaluate the $G_{\rm EM}(s)$ contribution as a function of the cutoff in the HVP integral, see Fig. 13.8, and compare the result to the χPT evaluation of the triangle diagram, both for the leading Low and full calculation of the real–emission contributions. The figure shows that there are indeed significant differences in the energy dependence, as expected from Figs. 13.6 and 13.7, leading to the aforementioned decrease by 2.0×10^{-10} due to resonance enhancement of the $\rho(770)$. Apart from this effect, further changes compared to [14,267,297] seem surprising, as one would expect these evaluations to be closer to our "ChPT" result, but a large part of the difference traces back to the local contribution in Eqs. (10.16) and (10.19), for which we use lattice–QCD–based input from [298].[6]

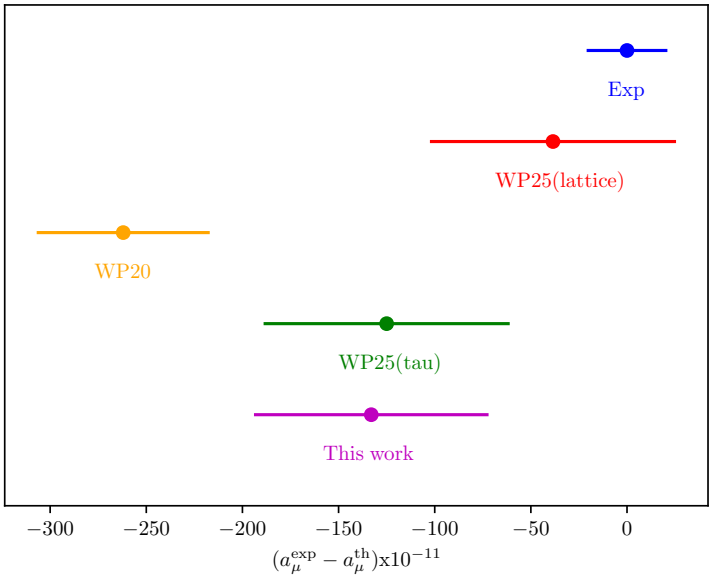

Figure 13.9: Difference between SM and experimental estimates for a_μ considering different $a_\mu^{\rm HVP,LO}$ inputs: lattice (red) as reported in [14], data–driven (orange) as in [9], hadronic τ decay (green) as given in [14] and the one arising from this work (purple).

Chapter 14

Conclusions

The muon anomalous magnetic moment is a very well studied observable and its possible connection with New Physics kept it under close scrutiny in the last decades. In this thesis project we reviewed the state of the art of the Standard Model theoretical prediction of the muon $g-2$, paying particular attention to the hadronic contribution, since it dominates the uncertainty associated to the SM prediction. Moreover, we detailed the current experimental and (data–driven) theoretical discrepancy, trying to highlight the possible fields where an improvement of the theoretical results can help in clarifying the situation.

The goals achieved in this thesis project are mainly two: first, we computed the radiative corrections to the $\pi\pi$ scattering due to the charged–neutral pion mass difference with a model–independent dispersive approach. This is of fundamental importance in order to better and more deeply understand the tension between different experimental results for the $e^+e^- \to \pi^+\pi^-$ cross–section. From this observable one obtains the data–driven SM prediction of the muon anomalous magnetic moment and, therefore, it must be known with great accuracy, requiring the inclusion of rescattering effects such as the $\pi\pi$ scattering. Second, given the current situation concerning the $e^+e^- \to \pi^+\pi^-$ cross–section and the discrepancy between the data–driven and lattice QCD estimate for the muon $g-2$, we applied a model–independent dispersive approach to compute the isospin breaking corrections to the hadronic τ decay, offering, at the end, a completely new estimate of the $e^+e^- \to \pi^+\pi^-$ cross section. The results of this work set the understanding of this isospin–breaking effects, both in the $\pi\pi$–scattering and in the hadronic τ–decay, on a more solid ground.

To analyze the radiative correction in the $\pi\pi$–scattering due to the charged–neutral pion mass difference in a precise and model–independent way, we have generalized Roy equations in order to include these effects. The subtraction constants appearing in Roy equations are obtained by matching the same dispersive representation in χPT_γ. However, differently from what is available in the literature, some significant work was necessary in order to bring our dispersive framework in the correct form, suitable for the matching procedure. We have solved these modified Roy equations for the S– and P–wave partial waves, obtaining the pion–mass difference corrections at low energies, $\sqrt{s} \leq 0.975$.

Our results indicate that the most significant relative corrections occur near the corresponding threshold, reaching up to 12% for the neutral channel, with slightly smaller corrections for other partial waves. For the resonant partial waves, these corrections generally diminish as the energy increases, becoming sizable only in the resonance region. In contrast, for the repulsive S–wave, the pion mass difference effects gradually decrease at higher energies, stabilizing around 3% for the $t_S^{+0}(s)$ partial wave and approximately 1% for $t_S^{++}(s)$ at an energy $\sqrt{s} \sim 0.5$ GeV. These results suggest that, while pion mass difference effects

are most prominent at low energies for most partial waves and gradually fade at higher energies—allowing for a smooth matching to the isospin limit at s_1—they remain small but non–zero for the $t_S^{+0}(s)$ partial wave.

Moreover, we have extracted the pole position of the $f_0(500)$, $f_0(980)$, and $\rho^{\pm,0}(770)$ resonances by analytically continuing the dispersive amplitudes to the second Riemann sheet. We have assessed the impact of the charged–neutral pion–mass difference on these pole parameters and find that isospin breaking produces only very small, charge–dependent shifts in resonance masses and widths, which are well below the current level of precision of these resonances.

Our result provide a rigorous dispersive representation of $\pi\pi$ scattering that can be used for further phenomenological studies. In particular, they are highly relevant for assessing the pion mass difference corrections to the $\pi\pi$ contributions in the hadronic vacuum polarization component of the muon $g-2$.

In the computation of the isospin breaking effects in the hadronic τ–decay, we focused on the long–range corrections, denoted by $G_{\rm EM}(s)$. These are computed in a model–independent way by utilizing a dispersive representation of the pion vector form factor in order to account for the pion internal structure. In particular, we employed an unsubtracted dispersion relation of $f_+(s)$ to ensure the UV finiteness of the amplitude, while the IR divergences are canceled by including photon real emission contributions. We also included the effects due to resonances, in particular ρ, a_1 and ω resonances. The correct low–energy behavior is then restored through a matching procedure with the χPT result for the same radiative corrections.

Besides improving the radiative corrections parameterized by $G_{\rm EM}(s)$, our work also strongly motivates increased efforts in the new measurements of the $\tau^- \to \pi^-\pi^0\nu_\tau$ spectral function, as possible at Belle II [299]. Indeed, our dispersive fits to the spectrum reveal that some tensions among the currently available data sets do exist, and at the same time we observe differences to previous evaluations. Part of the difference might originate from the changes in $G_{\rm EM}(s)$, but we also find that the constraints imposed by analyticity and unitarity result in a moderate tension between the low–energy part of the spectrum and the ρ region, which tends to increase the integral for small values of s.

Our final result of the impact of isospin breaking corrections to a_μ is

$$\Delta a_\mu^{\rm HVP,\,LO}[\pi\pi,\tau]\big|_{\rm Full} = -24.8(0.1)_{\rm exp}(0.5)_{\rm th}(1.3)_{\rm SD}\ . \tag{14.1}$$

Looking at the different contributions, we found good agreement with previous works for phase–space and short–distance corrections, while for $G_{\rm EM}(s)$ a larger negative correction was obtained. We observed that changes due to structure–dependent contributions are indeed sizable in the vicinity of the ρ resonance, leading to a net correction of about -2.0×10^{-10} in the HVP integral, while further changes to previous work trace back to the local χPT contribution.

As main outcome of this work on the hadronic τ–decay, the uncertainty in the $G_{\rm EM}(s)$ contribution is reduced substantially, leaving the matching between the short–distance factor $S_{\rm EW}^{\pi\pi}$ and the radiative corrections described by $G_{\rm EM}(s)$ as the dominant source of uncertainty in the τ–specific IB corrections. This matching can be further improved using input from lattice QCD, and establishing the latter connection could also help to address the remaining, most critical IB correction in the matrix elements. That is, our work allows for a reliable calculation of the long–range radiative corrections, which could be combined with lattice–QCD techniques as well as complementary dispersive calculations of IB in the pion VFF to achieve a complete account of IB corrections to hadronic τ decays, to allow for a robust evaluation of the two–pion HVP contribution to the anomalous magnetic moment of the muon.

Appendix A

Reference formulae

A.1 Feynman rules

A.1.1 QED Lagrangian

Starting from the QED Lagrangian

$$\mathscr{L} = -\frac{1}{4}(F_{\mu\nu})^2 + \bar{\psi}(i\partial\!\!\!/ - m)\psi - e\bar{\psi}\gamma^\mu\psi A_\mu \,, \tag{A.1}$$

the Feynman rules read

Dirac propagator :  $= \dfrac{i(p\!\!\!/ + m)}{p^2 - m^2 + i\epsilon}$, (A.2)

Photon propagator :  $= \dfrac{-ig_{\mu\nu}}{p^2 + i\epsilon}$, (A.3)

QED vertex :  $= -ie\gamma^\mu$, (A.4)

External fermions :  $= u^s(p)$ (initial) , (A.5)

 $= \bar{u}^s(p)$ (final) , (A.6)

External antifermions :  $= \bar{v}^s(p)$ (initial) , (A.7)

 $= v^s(p)$ (final) , (A.8)

External photons : $= \epsilon_\mu(p)$ (initial) , (A.9)

 $= \epsilon^*_\mu(p)$ (final) , (A.10)

A.1.2 χPT with virtual photons and leptons

At lowest order in chiral power counting, the $SU(3)$ χPT Lagrangian including virtual photons and leptons, introduced in Eq. (4.62), includes the terms

$$\begin{aligned}\mathcal{L}_{\text{eff}}^{\text{LO}} \supset\ & \left[(\partial_\mu - ieA_\mu)\,\pi^-\right]\left[(\partial^\mu + ieA^\mu)\,\pi^+\right] + \bar{\tau}\left[i\gamma_\mu\,(\partial^\mu - ieA^\mu) - m_\tau\right]\tau \\ & + i\bar{\nu}_{\tau\text{L}}\partial\!\!\!/\,\nu_{\tau\text{L}} + 2iG_F V_{ud}^*\,\bar{\nu}_{\tau\text{L}}\gamma^\mu\tau\left[\pi^0\,(\partial_\mu + ieA_\mu)\,\pi^+ - \pi^+\partial_\mu\pi^0\right]\ ,\end{aligned} \tag{A.11}$$

relevant for calculating the radiative corrections to $\tau^- \to \pi^-\pi^0\nu_\tau$. The following Feynman rules can be extracted:

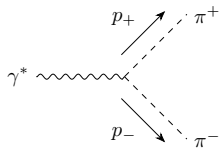

$$= ie(p_- - p_+)^\mu\ , \tag{A.12}$$

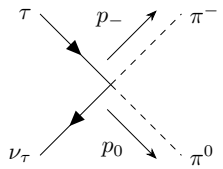

$$= -2iG_F V_{ud}^*(p\!\!\!/_- - p\!\!\!/_0)\ , \tag{A.13}$$

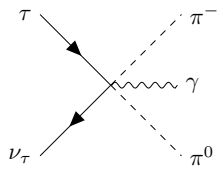

$$= -2ieG_F V_{ud}^*\gamma^\mu\ , \tag{A.14}$$

where e is the elementary charge, G_F the Fermi constant and V_{ud} a CKM–Matrix element. Note that in the conventions of Ref. [190] the QED vertex appears as

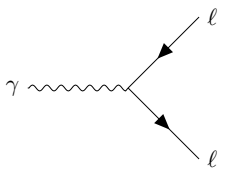

$$= ie\gamma^\mu\ . \tag{A.15}$$

Appendix B

$SU(3)$ group

The $SU(3)$ group is of fundamental importance in the study of strong interactions because on one hand it is the gauge group of QCD and, on the other hand, flavor $SU(3)$ is approximately realized as a global symmetry of the hadron spectrum [300–302], so that the observed (low–mass) hadrons can be organized in approximately degenerate multiplets fitting the dimensionalities of irreducible representations of $SU(3)$. Moreover, the direct product $SU(3)_L \times SU(3)_R$ is the chiral–symmetry group of QCD for vanishing u–, d– and s–quark masses. In this section we will review few basic properties of this group and its Lie algebra su(3) [303–305].

The group $SU(3)$ is defined as the set of all unitary, unimodular, 3×3 matrices U, i.e., $U^\dagger U = 1$ and $\det(U) = 1$. So any group element can be parametrized by a set of eight independent real parameters $\Theta = (\Theta_1, ..., \Theta_8)$ varying over a continuous range. Elements of $SU(3)$ are conveniently written in terms of the exponential representation

$$U(\Theta) = \exp\left(-i\sum_{a=1}^{8}\Theta_a\frac{\lambda_a}{2}\right) , \tag{B.1}$$

where λ_a are the eight linearly independent Gell–Mann matrices:

$$\lambda_1 = \begin{pmatrix} 0 & 1 & 0 \\ 1 & 0 & 0 \\ 0 & 0 & 0 \end{pmatrix} , \quad \lambda_2 = \begin{pmatrix} 0 & -i & 0 \\ i & 0 & 0 \\ 0 & 0 & 0 \end{pmatrix} , \quad \lambda_3 = \begin{pmatrix} 1 & 0 & 0 \\ 0 & -1 & 0 \\ 0 & 0 & 0 \end{pmatrix} , \quad \lambda_4 = \begin{pmatrix} 0 & 0 & 1 \\ 0 & 0 & 0 \\ 1 & 0 & 0 \end{pmatrix} , \tag{B.2}$$
$$\lambda_5 = \begin{pmatrix} 0 & 0 & -i \\ 0 & 0 & 0 \\ i & 0 & 0 \end{pmatrix} , \quad \lambda_6 = \begin{pmatrix} 0 & 0 & 0 \\ 0 & 0 & 1 \\ 0 & 1 & 0 \end{pmatrix} , \quad \lambda_7 = \begin{pmatrix} 0 & 0 & 0 \\ 0 & 0 & -i \\ 0 & i & 0 \end{pmatrix} , \quad \lambda_8 = \frac{1}{\sqrt{3}}\begin{pmatrix} 1 & 0 & 0 \\ 0 & 1 & 0 \\ 0 & 0 & 2 \end{pmatrix} .$$

The structure of the Lie group is encoded in the commutation relations of the Gell–Mann matrices

$$\left[\frac{\lambda_a}{2}, \frac{\lambda_b}{2}\right] = if_{abc}\frac{\lambda_c}{2} , \tag{B.3}$$

where $f_{abc} = \frac{1}{4i}\langle[\lambda_a, \lambda_b]\lambda_c\rangle$. The anticommutator relations read

$$\{\lambda_a, \lambda_b\} = \frac{4}{3}\delta_{ab} + 2d_{abc}\lambda_c , \tag{B.4}$$

where $d_{abc} = \frac{1}{4}\langle\{\lambda_a, \lambda_b\}\lambda_c\rangle$. Moreover, it is convenient to introduce a ninth matrix $\lambda_0 = \sqrt{\frac{2}{3}}\mathrm{diag}(1, 1, 1)$.

Finally, an arbitrary 3×3 matrix M can be written as

$$M = \sum_{a=0}^{8} \lambda_a M_a \ , \tag{B.5}$$

where M_a are complex numbers given by $M_a = \frac{1}{2}\langle \lambda_a M \rangle$.

Appendix C

Loop integrals

In this section we show the explicit expression of the loop integrals defined in the $\pi\pi$–scattering amplitude, following [198, 236]:

$$\begin{aligned} A(M^2) &= -i\mu^{2\epsilon}\int \frac{\mathrm{d}^d k}{(2\pi)^d}\frac{1}{k^2-M^2+i\epsilon}\,, \\ J_{PQ}(s) &= -i\mu^{2\epsilon}\int \frac{\mathrm{d}^d k}{(2\pi)^d}\frac{1}{(k^2-M_P^2+i\epsilon)[(k-p)^2-M_Q^2+i\epsilon]}\,, \\ G_{\pm\gamma}(s) &= -i\mu^{2\epsilon}\int \frac{\mathrm{d}^d k}{(2\pi)^d}\frac{1}{(k^2-m_\gamma^2+i\epsilon)[k^2-2k\cdot p_1+i\epsilon][k^2+2k\cdot p_2+i\epsilon]}, \end{aligned} \tag{C.1}$$

where $s=p^2$, μ is a scale introduced to preserve the natural dimensions of the integrals and the masses in the propagator are considered reals.

The simplest case is the one–point function for which the explicit expression reads

$$A(M^2) = \frac{M^2}{16\pi^2}\left(\Delta_\epsilon - \ln\frac{M^2}{\mu^2}+1\right)\,, \tag{C.2}$$

where Δ_ϵ is the divergent contribution of the loop function and it reads

$$\Delta_\epsilon = \frac{1}{\epsilon} - \gamma_E + \ln 4\pi\,, \tag{C.3}$$

where ϵ is defined starting from the number of space–time dimensions, $d=4-2\epsilon$, and γ_E is the Euler–Mascheroni constant.

For the two point function we recall the definition

$$J_{PQ}(s) \equiv \bar{J}_{PQ}(s) + J_{PQ}(0)\,, \tag{C.4}$$

where for $s>(M_P+M_Q)^2$ and $d=4$, one finds

$$\begin{aligned} \bar{J}_{PQ}(s) = \frac{1}{32\pi^2}\Bigg\{ & 2 + \frac{\Delta_{PQ}}{s}\ln\frac{M_Q^2}{M_P^2} - \frac{\Sigma_{PQ}}{\Delta_{PQ}}\ln\frac{M_Q^2}{M_P^2} \\ & + \frac{\lambda_{PQ}^{\frac{1}{2}}(s)}{s}\ln\left[\frac{\left(s-\lambda_{PQ}^{\frac{1}{2}}(s)\right)^2-\Delta_{PQ}^2}{\left(s+\lambda_{PQ}^{\frac{1}{2}}(s)\right)^2-\Delta_{PQ}^2}\right] + 2i\pi\frac{\lambda_{PQ}^{\frac{1}{2}}(s)}{s}\Bigg\}\,, \end{aligned} \tag{C.5}$$

and

$$J_{PQ}(0) = \frac{1}{16\pi^2}\left\{\Delta_\epsilon - \frac{M_P^2}{M_P^2 - M_Q^2}\ln\frac{M_P^2}{M_Q^2} + \ln\frac{\mu^2}{M_Q^2} + 1\right\}, \tag{C.6}$$

with $\Sigma_{PQ} = M_P^2 + M_Q^2$, $\Delta_{PQ} = M_P^2 - M_Q^2$ and $\lambda_{PQ}(s) = \lambda(s, M_P^2, M_Q^2)$.

The last loop integral that we worked with is the three–point function $G_{\pm\gamma}(s)$. Introducing two Feynman parameters and performing standard manipulations leads to the following integral representation

$$G_{\pm\gamma}(s) = -\frac{1}{32\pi^2}\int_0^1 \mathrm{d}x \int_0^1 \mathrm{d}y \frac{1}{f(x)} \cdot \frac{\mathrm{d}}{\mathrm{d}y}\ln\left[y^2 f(x) + (1-y)m_\gamma^2\right] + \mathcal{O}(m_\gamma^2)\,, \tag{C.7}$$

where $f(x) = M_{\pi^\pm}^2 - x(1-x)s - i\epsilon$. For $s < 0$, the roots of $f(x)$ are real and lie outside of the interval $[0, 1]$, so that the integration is straightforward

$$\begin{aligned} G_{\pm\gamma}(s) = -\frac{1}{32\pi^2 s\sigma}\Bigg\{ & 4\mathrm{Li}_2\left(\frac{1-\sigma}{1+\sigma}\right) + \frac{\pi^2}{3} + \ln^2\left(\frac{1-\sigma}{1+\sigma}\right) \\ & + 2\left[\ln\left(\frac{-s}{M_{\pi^\pm}^2}\right) - \ln\left(\frac{m_\gamma^2}{M_{\pi^\pm}^2}\right) + 2\ln(\sigma)\right]\ln\left(\frac{1-\sigma}{1+\sigma}\right)\Bigg\}, \end{aligned} \tag{C.8}$$

The dilogarithm or Spence function is defined as usual,

$$\mathrm{Li}_2(x) = -\int_1^x \frac{\ln t}{1-t}dt\,. \tag{C.9}$$

Appendix D

Explicit expressions for the subtraction constants

D.1 Neutral channel

For the T^n, the exact, explicit expressions of the subtraction constants a_n^{00} and b_n^{00} read

$$\begin{aligned} a_n^{00} =& \frac{M_{\pi^0}^2}{32\pi F_\pi^2}\left\{1+\xi_0\left[4\bar{\ell}_1+8\bar{\ell}_2-\frac{3}{2}\bar{\ell}_3+2\bar{\ell}_4-\frac{23}{2}-\frac{9-11\delta_\pi}{(1-\delta_\pi)}L_\pi+9j_0\left(4M_{\pi^0}^2\right)\right]\right. \\ &\left.+\xi\delta_\pi\left(\frac{\bar{k}_{31}}{9}-\frac{10}{9}\bar{k}_2-\bar{k}_4\right)\right\}, \\ b_n^{00} =& \frac{M_{\pi^0}^2}{384\pi F_\pi^2}\xi\left[16\left(\bar{\ell}_1+2\bar{\ell}_2-3\right)+2\delta_\pi(1-24\lambda_\pi)+27j_0\left(4M_{\pi^0}^2\right)\right], \end{aligned} \tag{D.1}$$

where $\xi_0 := M_{\pi^0}^2/(16\pi^2F_\pi^2) = \xi(1-\delta_\pi)$, $L_\pi := -\ln(1-\delta_\pi) = \delta_\pi + \mathcal{O}(\delta_\pi^2)$ and $\lambda_\pi := L_\pi/\delta_\pi = 1+\mathcal{O}(\delta_\pi)$.

D.2 $\pi^+\pi^-$ channel

For the T^c amplitude, we get

$$\begin{aligned} a^{++} =& -\frac{M_\pi^2}{16\pi F_\pi^2}\left\{1-\delta_\pi-\xi\left[\frac{4}{3}\left(\bar{\ell}_1+2\bar{\ell}_2\right)-\frac{1}{2}\left(\bar{\ell}_3+4\bar{\ell}_4\right)(1-\delta_\pi)^2-\frac{1}{2}\left(1+3\delta_\pi+\frac{88}{9}\delta_\pi^2\right)\right.\right. \\ &\left.\left.-\delta_\pi(1-\delta_\pi)\left(\frac{\bar{k}_{31}}{9}-4\bar{k}_{32}+\frac{62}{9}\bar{k}_2+5\bar{k}_4\right)\right]\right\}, \\ b^{++} =& \frac{M_\pi^2}{48\pi F_\pi^2}\xi\left(4\bar{\ell}_2-\frac{23}{9}-4\delta_\pi+\delta_\pi^2\right), \\ c^{++} =& -\frac{\xi}{864\pi F_\pi^2}, \\ a_c^{+-} =& \frac{M_\pi^2}{16\pi F_\pi^2}\left\{1+\delta_\pi+\xi\left[\frac{4}{3}\left(\bar{\ell}_1+2\bar{\ell}_2\right)-\frac{1}{2}\bar{\ell}_3(1-\delta_\pi)^2+2\bar{\ell}_4\left(1-\delta_\pi^2\right)\right.\right. \\ &\left.\left.-\frac{27-90\delta_\pi-133\delta_\pi^2+124\delta_\pi^3}{18(1-\delta_\pi)}+\frac{(3+\delta_\pi)^2}{4}j_0\left(4M_\pi^2\right)\right.\right. \end{aligned}$$

$$
\begin{aligned}
&\quad + \delta_\pi \left(\frac{\bar{k}_{31}}{9}(1+\delta_\pi) + 4\bar{k}_{32}(1-\delta_\pi) - \frac{2}{9}\bar{k}_2\,(5-31\delta_\pi) + \bar{k}_4(1+5\delta_\pi) \right) \Bigg] \Bigg\} \,, \\
b_c^{+-} =& \frac{M_\pi^2}{24\pi F_\pi^2}\xi \left[\bar{\ell}_1 + \bar{\ell}_2 - \frac{97 - 754\delta_\pi + 297\delta_\pi^2 + 144\delta_\pi^3}{144\,(1-\delta_\pi)} + \frac{3}{32}\,(3+\delta_\pi)^2\, j_0\left(4M_\pi^2\right) \right] \,, \\
c_c^{+-} =& \frac{\xi}{1728\pi F_\pi^2} \,.
\end{aligned} \tag{D.2}
$$

D.3 $\pi^+\pi^- \to \pi^0\pi^0$ channel

For the amplitude T^x

$$
\begin{aligned}
a_1 =& -\frac{M_\pi^2}{32\pi F_\pi^2\,(2-\delta_\pi)} \Bigg\{ 2\,(3-\delta_\pi) + \frac{\xi}{3} \Bigg[\frac{33 + 158\delta_\pi - 29\delta_\pi^2 - 36\delta_\pi^3}{3} + 8\bar{\ell}_1\left(1 + \delta_\pi - \delta_\pi^2\right) \\
&+ 4\bar{\ell}_2\,(2-\delta_\pi)^2 - 3\bar{\ell}_3\,(1-\delta_\pi)^2 + 12\bar{\ell}_4\left(3 - 4\delta_\pi + \delta_\pi^2\right) + \frac{3}{2}\left(6 - 7\delta_\pi + \delta_\pi^3\right) j_0\left(4M_\pi^2\right) \\
&+ 2\left(2 - 11\delta_\pi - 18\delta_\pi^2 + 9\delta_\pi^3\right)\lambda_\pi + \frac{4}{3}\delta_\pi\left(16 - 21\delta_\pi + 2\delta_\pi^2\right)\bar{j}_{+0}^{(1)} + \frac{3}{2}\delta_\pi^4\bar{j}_{+0}^{(2)} \\
&+ \delta_\pi\left(\frac{2}{3}\bar{k}_{31}(3-\delta_\pi) + 12\bar{k}_{32}(1-\delta_\pi) + \frac{4}{3}\bar{k}_2(3+5\delta_\pi) + 12\bar{k}_4 \right) \Bigg] \Bigg\} \,, \\
b_1 =& -\frac{M_\pi^2}{96\pi F_\pi^2}\xi \left[4\bar{\ell}_1 + \frac{23}{12} + \frac{51}{4}\delta_\pi + 2\delta_\pi^2 + 2\,(1-3\delta_\pi)\,\lambda_\pi + \frac{3}{8}(1-\delta_\pi)(3+\delta_\pi) j_0\left(4M_\pi^2\right) + \frac{8}{3}\bar{j}_{+0}^{(1)} \right] \,, \\
c_1 =& -\frac{\xi}{144\pi F_\pi^2}\bar{j}_{+0}^{(1)} \,, \\
a_2 =& \frac{M_\pi^2}{32\pi F_\pi^2}\frac{1}{\eta\,(2-\delta_\pi)} \Bigg\{ 2\,(1-\delta_\pi) - \xi \Bigg[\frac{1}{3}\Bigg(\frac{\left(17 + 10\delta_\pi - 23\delta_\pi^2\right) + 8\eta\,(2-\delta_\pi)}{3} + 8\,(1-\delta_\pi)\,\bar{\ell}_1 \\
&- 4\,(2-\delta_\pi)\,(2-\delta_\pi-4\eta)\,\bar{\ell}_2 - 3\,(1-\delta_\pi)^2\left(\bar{\ell}_3 + 4\bar{\ell}_4\right) \Bigg) \\
&+ \frac{2}{3}\left[6 - 8\eta\,(2-\delta_\pi) - \delta_\pi\left(7 - 9\delta_\pi + 6\delta_\pi^2\right)\right]\lambda_\pi - \frac{\eta^2\delta_\pi^2}{4}\,(2-\delta_\pi)\left(1 - 2\eta^{-1}\right)\bar{\bar{j}}_{+0}\left(4\bar{M}_\pi^2\right) \\
&+ (2-\delta_\pi)\eta\left((1-2\eta^{-1})^2 + \frac{\eta^2\delta_\pi^4}{64} \right)\bar{j}_{+0}\left(4\bar{M}_\pi^2\right) + \frac{\delta_\pi^4}{8}\left(4 - \eta\,(2-\delta_\pi)\right) j_{+0}^{(2)} \\
&- \left((2-\delta_\pi)\left(\frac{16}{9\eta^2} + \frac{\delta_\pi^4\eta^2}{16} \right) - \frac{4}{9}\left(8 - 12\delta_\pi + 3\delta_\pi^2 - 4\delta_\pi^3\right) \right) j_{+0}^{(1)} \\
&- \delta_\pi\,(1-\delta_\pi)\left(\frac{2}{9}\bar{k}_{31} - 4\bar{k}_{32} + \frac{52}{9}\bar{k}_2 + 4\bar{k}_4 \right) \Bigg] \Bigg\} \,, \\
b_2 =& -\frac{M_\pi^2}{96\pi F_\pi^2}\frac{\xi}{\eta} \Bigg[2\left(2\bar{\ell}_2 - 2\lambda_\pi + \frac{1}{3} \right) + 3\left(1 - \eta + \frac{\eta^2}{4} + \frac{\eta^4\delta_\pi^4}{256} \right)\bar{j}_{+0}\left(4\bar{M}_\pi^2\right) \\
&+ \frac{3\eta^2\delta_\pi^2}{16}\,(2-\eta)\,\bar{\bar{j}}_{+0}\left(4\bar{M}_\pi^2\right) - \left(\frac{4}{3\eta} + 3\eta + \frac{3\eta^3\delta_\pi^4}{64} \right)\bar{j}_{+0}^{(1)} - \frac{3\eta\delta_\pi^2}{32}\left(\eta\delta_\pi^2 - 16\right)\bar{j}_{+0}^{(2)} - \frac{\eta\delta_\pi^4}{8}\bar{j}_{+0}^{(3)} \Bigg] \,, \\
c_2 =& \frac{\xi}{288\pi F_\pi^2\eta}\bar{j}_{+0}^{(1)} \,,
\end{aligned} \tag{D.3}
$$

where we have defined $\eta := M_\pi^2/\bar{M}_\pi^2$ and $\bar{\bar{j}}_{+0}(s) := \bar{j}_{+0}(s) - s\bar{j}'_{+0}(0)$, and $\bar{j}^{(i)}_{+0} := M_\pi^{2i}\partial_s^i \bar{j}_{+0}(s)_{|_{s=0}}$.

$$
\begin{aligned}
j_0\left(4M_{\pi^0}^2\right) &= 2 + \sqrt{\frac{\delta_\pi}{1-\delta_\pi}}\left(-\pi + 2\arctan\sqrt{\frac{\delta_\pi}{1-\delta_\pi}}\right) \,, \\
\bar{j}_0(4M_\pi^2) &= 2 - \sqrt{\delta_\pi}\left[\ln\frac{1+\sqrt{\delta_\pi}}{1-\sqrt{\delta_\pi}} + i\pi\right] \,, \\
\bar{j}_{+0}(4\bar{M}_\pi^2) &= 1 + \left(1 - \frac{\delta_\pi}{2} - \frac{\eta\delta_\pi^2}{8}\right)\lambda_\pi + \frac{\rho}{2}\ln\frac{4-\eta(2-\delta_\pi)-4\rho}{4-\eta(2-\delta_\pi)+4\rho} \,, \\
\bar{\bar{j}}_{+0}(4\bar{M}_\pi^2) &= 1 - \frac{2(2-\delta_\pi)}{\eta\delta_\pi^2} + \left(\frac{4}{\eta\delta_\pi^2}(1-\delta_\pi) + 1 - \frac{\delta_\pi}{2} - \frac{\eta\delta_\pi^2}{8}\right)\lambda_\pi + \frac{\rho}{2}\ln\frac{4-\eta(2-\delta_\pi)-4\rho}{4-\eta(2-\delta_\pi)+4\rho} \,, \\
\bar{\bar{j}}^{(1)}_{+0} &= \frac{1}{2\delta_\pi^3}\left[\delta_\pi(2-\delta_\pi) - 2(1-\delta_\pi)L_\pi\right] \,, \\
\bar{\bar{j}}^{(2)}_{+0} &= \frac{1}{3\delta_\pi^5}\left[\delta_\pi(12 - 12\delta_\pi + \delta_\pi^2) - 6(2-\delta_\pi)(1-\delta_\pi)L_\pi\right] \,, \\
\bar{\bar{j}}^{(3)}_{+0} &= \frac{1}{2\delta_\pi^7}\left[\delta_\pi(2-\delta_\pi)(30 - 30\delta_\pi + \delta_\pi^2) - 12(1-\delta_\pi)(5 - 5\delta_\pi + \delta_\pi^2)L_\pi\right] \,,
\end{aligned}
\tag{D.4}
$$

with

$$
\rho := \sqrt{1 - \eta(1-\delta_\pi/2) + \eta^2\delta_\pi^2/16} \,, \tag{D.5}
$$

and with $j(s) := 16\pi^2\bar{J}(s)$, $\Sigma_\pi = M_\pi^2(2-\delta_\pi)$ and $\bar{M}_\pi = \frac{M_\pi}{2}(1+\sqrt{1-\delta_\pi})$.

Appendix E

Explicit expressions for the kernels

E.1 $\pi^+\pi^+$ channel

The S-wave projection of the $\pi^+\pi^+$ channel reads

$$\begin{aligned} t_S^{++}(s) =& \frac{a^{++}s}{s_{+-}} - \frac{a_c^{+-}(s-s_{+-})}{s_{+-}} + \int_{s_{00}}^{s_{+-}} \mathrm{d}s' \Bigg[K_{c,S}^{++}(s',s)\mathrm{Im}t_S^{c,00}(s') \\ &+ \int_{s_{+-}}^{s_1} \mathrm{d}s' \Bigg[K_S^{++}(s',s)\mathrm{Im}t_S^{++}(s') + K_{c,S}^{++}(s',s)\left(\mathrm{Im}t_S^{c,00}(s') + \mathrm{Im}t_S^{c,+-}(s')\right) \\ &+ K_{c,P}^{++}(s',s)\mathrm{Im}t_P^{c,+-}(s') \Bigg] + d_S^{++}(s) \,, \end{aligned} \tag{E.1}$$

where the kernels are

$$\begin{aligned} K_S^{++}(s',s) =& \frac{1}{\pi}\frac{s(s-s_{+-})}{s'(s'-s_{+-})(s'-s)} \,, \\ K_{c,S}^{++}(s',s) =& \frac{1}{\pi}\left[\frac{s-2s'+s_{+-}}{s'(s'-s_{+-})} + \frac{2}{s-s_{+-}}\ln\left(\frac{s'+s-s_{+-}}{s'}\right)\right] \,, \\ K_{c,P}^{++}(s',s) =& \frac{3}{\pi}\left[\frac{3s+2s'-s_{+-}}{s'(s'-s_{+-})} - \frac{2(2s+s'-s_{+-})}{(s-s_{+-})(s'-s_{+-})}\ln\left(\frac{s'+s-s_{+-}}{s'}\right)\right] \,. \end{aligned} \tag{E.2}$$

E.2 $\pi^+\pi^-$ channel

In this case, both an S- and P-wave partial decomposition is present. For the S-wave, we obtain

$$\begin{aligned} t_S^c(s) =& -\frac{a^{++}(s-s_{+-})}{2s_{+-}} + \frac{a_c^{+-}(s+s_{+-})}{2s_{+-}} + \int_{s_{00}}^{s_{+-}} \mathrm{d}s' K_{s,S}^{+-}(s',s)\mathrm{Im}t_S^{c,00}(s') \\ &+ \int_{s_{+-}}^{s_1} \mathrm{d}s' \Bigg[K_{s,S}^{+-}(s',s)\left(\mathrm{Im}t_S^{c,00}(s') + \mathrm{Im}t_S^{c,+-}(s')\right) + K_{s,P}^{+-}(s',s)\mathrm{Im}t_P^{c,+-}(s') \\ &+ K_{+-,S}^{++}(s',s)\mathrm{Im}t_S^{++}(s') \Bigg] + d_S^c(s) \,, \end{aligned} \tag{E.3}$$

with

$$K_{s,S}^{+-}(s',s) = \frac{1}{\pi}\left[\frac{1}{s'-s} - \frac{s'+s+3(s'-s_{+-})}{2s'(s'-s_{+-})} + \frac{1}{s-s_{+-}}\ln\left(\frac{s'+s-s_{+-}}{s'}\right)\right] \,,$$

$$
\begin{aligned}
K^{+-}_{s,P}(s',s) =& \frac{3}{\pi}\left[-\frac{3s+2s'-s_{+-}}{2s'(s'-s_{+-})}+\frac{2s+s'-s_{+-}}{(s-s_{+-})(s'-s_{+-})}\ln\left(\frac{s'+s-s_{+-}}{s'}\right)\right] ,\\
K^{+-}_{+-,S}(s',s) =& \frac{1}{\pi}\left[\frac{s-2s'+s_{+-}}{2s'(s'-s_{+-})}+\frac{1}{s-s_{+-}}\ln\left(\frac{s'+s-s_{+-}}{s'}\right)\right] ,
\end{aligned}
\tag{E.4}
$$

while for the P-wave we have

$$
\begin{aligned}
t^c_P(s) =& \frac{a^{+-}_c-a^{++}}{6s_{+-}}(s-s_{+-})+\int_{s_{00}}^{s_{+-}}\mathrm{d}s' K^{+-}_{s,P}(s',s)\mathrm{Im}t^{c,00}_S(s')\\
&+\int_{s_{+-}}^{s_1}\mathrm{d}s'\Big[K^{+-}_{s,P}(s',s)\left(\mathrm{Im}t^{c,00}_S(s')+\mathrm{Im}t^{c,+-}_S(s')-\mathrm{Im}t^{++}_S(s')\right)\\
&\qquad +K^{+-}_{p,P}(s',s)\mathrm{Im}t^{c,+-}_P(s')\Big]+d^c_P(s) ,
\end{aligned}
\tag{E.5}
$$

where the kernels are

$$
\begin{aligned}
K^{+-}_{p,S}(s',s) =& \frac{1}{\pi}\left[-\frac{s-s_{+-}}{6s'(s'-s_{+-})}-\frac{2}{s-s_{+-}}+\frac{s+2s'-s_{+-}}{(s-s_{+-})^2}\ln\left(\frac{s'+s-s_{+-}}{s'}\right)\right] ,\\
K^{+-}_{p,P}(s',s) =& \frac{1}{\pi}\Bigg[\frac{s(s-s_{+-})}{s'(s'-s_{+-})(s'-s)}-\frac{s-s_{+-}}{2s'(s'-s_{+-})}-\frac{6(2s+s'-s_{+-})}{(s-s_{+-})(s'-s_{+-})}\\
&+\frac{3(s+2s'-s_{+-})(2s+s'-s_{+-})}{(s-s_{+-})^2(s'-s_{+-})}\ln\left(\frac{s'+s-s_{+-}}{s'}\right)\Bigg] .
\end{aligned}
\tag{E.6}
$$

E.3 $\pi^+\pi^- \to \pi^0\pi^0$ channel

The S-wave projection for the $\pi^+\pi^- \to \pi^0\pi^0$ scattering reads

$$
\begin{aligned}
t^x_S(s) =& \frac{a^{+-}_x s}{s_{+-}}-\frac{a^{+0}_c\left[s-2\Sigma_\pi\right]}{s_{\pi^\pm 0}}+\int_{s_{00}}^{s_{+-}}\mathrm{d}s' K_{x,S}(s',s)\mathrm{Im}t^{x,00}_S(s')\\
&+\int_{s_{+-}}^{s_1}\mathrm{d}s' K_{x,S}(s',s)\left(\mathrm{Im}t^{x,00}_S(s')+\mathrm{Im}t^{x,+-}_S(s')\right)\\
&+\int_{s_{0+}}^{s_1}\mathrm{d}s'\left[K^{0+}_{x,S}(s',s)\mathrm{Im}t^{0+}_S(s')+K^{0+}_{x,P}(s',s)\mathrm{Im}t^{0+}_P(s')\right]\Bigg\}+d^x_S(s) ,
\end{aligned}
\tag{E.7}
$$

where the kernels read

$$
\begin{aligned}
K_{x,S}(s',s) =& \frac{1}{\pi}\frac{s(s-s_{+-})}{s'(s'-s_{+-})(s'-s)} ,\\
K^{0+}_{x,S}(s',s) =& \frac{1}{\pi}\Bigg\{\frac{s-2s'+4M_\pi M_{\pi^0}}{s'(s'-s_{0+})}+\frac{1}{2q(s,s_{+-})q(s,s_{00})}\times\\
&\left[\ln\left(1+\frac{4q(s,s_{+-})q(s,s_{00})}{s+2s'-2\Sigma_\pi}\right)-\ln\left(1-\frac{4q(s,s_{+-})q(s,s_{00})}{s+2s'-2\Sigma_\pi}\right)\right]\Bigg\} ,\\
K^{0+}_{x,P}(s',s) =& \frac{-3}{\pi\lambda_{\pm 0}(s')}\Bigg\{3s+2s'-2\Sigma_\pi-\frac{s'\left(s'+2s-2\Sigma_\pi\right)+\Delta^2_\pi}{2q(s,s_{+-})q(s,s_{00})}\times\\
&\left[\ln\left(1+\frac{4q(s,s_{+-})q(s,s_{00})}{s+2s'-2\Sigma_\pi}\right)-\ln\left(1-\frac{4q(s,s_{+-})q(s,s_{00})}{s+2s'-2\Sigma_\pi}\right)\right]\Bigg\} ,
\end{aligned}
\tag{E.8}
$$

where $q(x,y)=\frac{1}{2}\sqrt{x-y}$ and $\lambda_{\pm 0}(s)=\lambda(s,M_\pi,M_{\pi^0})=\left[s-(M_\pi+M_{\pi^0})^2\right]\left[s-(M_\pi-M_{\pi^0})^2\right]$.

E.4 $\pi^+\pi^0 \to \pi^+\pi^0$ channel

The last $\pi^+\pi^0 \to \pi^+\pi^0$ channel can be decomposed in both an S- and P-wave. For the S-wave, we get

$$\begin{aligned} t_S^+(s) =& \frac{a_c^{+0}\left(s+(M_\pi-M_{\pi^0})^2\right)(s+s_{0+})}{2ss_{0+}} - \frac{a_x^{+-}\lambda_{\pm0}(s)}{2ss_{+-}} \\ &+ \int_{s_{00}}^{s_{+-}} \mathrm{d}s' K_{x,S}^{0+}(s',s)\mathrm{Im}t_S^{x,00}(s') + \int_{s_{+-}}^{s_1} \mathrm{d}s' K_{x,S}^{0+}(s',s)\left(\mathrm{Im}t_S^{x,00}(s') + \mathrm{Im}t_S^{x,+-}(s')\right) \\ &+ \int_{s_{0+}}^{s_1} \mathrm{d}s' \left[K_{s,S}^{0+}(s',s)\mathrm{Im}t_S^{0+}(s') + K_{s,P}^{0+}(s',s)\mathrm{Im}t_P^{0+}(s')\right] \Bigg\} + d_S^+(s)\,, \end{aligned} \tag{E.9}$$

with

$$\begin{aligned} K_{x,S}^{0+}(s',s) =& \frac{1}{\pi}\left[\frac{\lambda_{\pm0}(s)}{2ss'(s'-s_{+-})} - \frac{1}{s'} + \frac{s}{\lambda_{\pm0}(s)}\ln\left(\frac{ss'+\lambda_{\pm0}(s)}{ss'}\right)\right], \\ K_{s,S}^{0+}(s',s) =& \frac{1}{\pi}\Bigg\{\frac{1}{s'-s} - \frac{2}{s'} - \frac{1}{2ss'}\frac{(s+s_{0+})\left(s+(M_\pi-M_{\pi^0})^2\right)}{s'-s_{0+}} \\ &+ \frac{s}{\lambda_{\pm0}(s)}\ln\left(\frac{s\left(s+s'-2\Sigma_\pi\right)}{ss'-\Delta_\pi^2}\right)\Bigg\}, \\ K_{p,P}^{0+}(s',s) =& \frac{3}{\pi\lambda_{\pm0}(s')}\left\{s+s'+\frac{\lambda_{\pm0}(s)}{2s} - \frac{s\left(\lambda_{\pm0}(s')+2ss'-2\Delta_\pi^2\right)}{\lambda_{\pm0}(s)}\ln\left(\frac{s\left(s+s'-2\Sigma_\pi\right)}{ss'-\Delta_\pi^2}\right)\right\}, \end{aligned} \tag{E.10}$$

while the P-wave decomposition reads

$$\begin{aligned} t_P^+(s) =& -\frac{a_c^{+0}\lambda_{\pm0}(s)}{6ss_{0+}} + \frac{a_x^{+-}\lambda_{\pm0}(s)}{6ss_{+-}} + \int_{s_{00}}^{s_{+-}} \mathrm{d}s' K_{x,P}^{0+}(s',s)\mathrm{Im}t_S^{x,00}(s') \\ &+ \int_{s_{+-}}^{s_1} \mathrm{d}s' K_{x,P}^{0+}(s',s)\left(\mathrm{Im}t_S^{x,00}(s') + \mathrm{Im}t_S^{x,+-}(s')\right) \\ &+ \int_{s_{0+}}^{s_1} \mathrm{d}s' \left[K_{p,S}^{0+}(s',s)\mathrm{Im}t_S^{0+}(s') + K_{p,P}^{0+}(s',s)\mathrm{Im}t_P^{0+}(s')\right] \Bigg\} + d_P^+(s)\,, \end{aligned} \tag{E.11}$$

where the kernels are

$$\begin{aligned} K_{x,P}^{0+}(s',s) =& \frac{1}{\pi}\left[-\frac{\lambda_{\pm0}(s)}{6ss'(s'-s_{+-})} - \frac{2s}{\lambda_{\pm0}(s)} + \frac{s}{\lambda_{\pm0}(s)}\left(1+\frac{2ss'}{\lambda_{\pm0}(s)}\right)\ln\left(\frac{ss'+\lambda_{\pm0}(s)}{ss'}\right)\right], \\ K_{p,S}^{0+}(s',s) =& \frac{1}{\pi}\Bigg\{\frac{2s}{\lambda_{\pm0}(s)} + \frac{\lambda_{\pm0}(s)}{6ss'\left(s'-s_{0+}\right)} \\ &+ \frac{s}{\lambda_{\pm0}(s)}\left[1-\frac{2s\left(s+s'-2\Sigma_\pi\right)}{\lambda_{\pm0}(s)}\right]\ln\left(\frac{s\left(s+s'-2\Sigma_\pi\right)}{ss'-\Delta_\pi^2}\right)\Bigg\}, \\ K_{p,P}^{0+}(s',s) =& \frac{1}{\pi\lambda_{\pm0}(s')}\Bigg\{\left(\frac{1}{s'-s}-\frac{1}{2s}\right)\lambda_{\pm0}(s) + \frac{6s\left[\Delta_\pi^2 - s'\left(s'+2s-2\Sigma_\pi\right)\right]}{\lambda_{\pm0}(s)} \\ &+ \frac{3s\left[\Delta_\pi^2 - 2s'\left(s-\Sigma_\pi\right)\right) - s'^2\right]\left[\lambda_{\pm0}(s) - 2s\left(s+s'-2\Sigma_\pi\right)\right]}{\lambda_{\pm0}(s)^2} \end{aligned}$$

$$\times \ln\left(\frac{s\,(s+s'-2\Sigma_\pi)}{ss'-\Delta_\pi^2}\right)\Bigg\}\,. \tag{E.12}$$

Appendix F

Soft Bremsstrahlung

The first (phase space) integral we need to compute is

$$I^{\text{int}} = \mu^{2\epsilon}\rho \int' \frac{\mathrm{d}^{d-1}k}{(2\pi)^{d-1}} \frac{1}{2|\mathbf{k}|} \frac{1}{(l\cdot k)(q_1\cdot k)}, \tag{F.1}$$

where $\epsilon = \frac{4-d}{2}$ and $l = \rho l_1$. The parameter ρ is defined in such a way that $(l-q_1)^2 = 0$ and such that $(l^0 - q_1^0)$ has the same sign as q_1^0. After performing the integrals over the polar angles (that the integrand does not depend on) except for θ, we obtain

$$\mu^{2\epsilon}\int' \frac{\mathrm{d}^{3-2\epsilon}k}{(2\pi)^{3-2\epsilon}} = \frac{\mu^{2\epsilon}}{4\pi^2}\Gamma(1-2\epsilon)(4\pi)^{\epsilon}4^{\epsilon}\int_0^{\Delta}\mathrm{d}|\mathbf{k}|\,|\mathbf{k}|^{2-2\epsilon}\int_0^{\pi}\mathrm{d}\theta\,(\sin\theta)^{1-2\epsilon}\,. \tag{F.2}$$

Now we introduce a Feynman parameterization and define $p_\alpha^\mu = \alpha l^\mu + (1-\alpha)q_1^\mu$ such that

$$\frac{1}{(l_1\cdot k)(q_1\cdot k)} \to \int_0^1 \mathrm{d}\alpha \frac{1}{(p_\alpha\cdot k)^2}. \tag{F.3}$$

Then the integral in Eq. (F.1) can be written in the form

$$I^{\text{int}} = \frac{\mu^{2\epsilon}\rho}{8\pi^2}\Gamma(1-2\epsilon)(4\pi)^{\epsilon}4^{\epsilon}\int_0^{\Delta}\mathrm{d}|\mathbf{k}|\,|\mathbf{k}|^{-1-2\epsilon}\int_0^1\mathrm{d}\alpha\int_0^{\pi}\mathrm{d}\theta\,(\sin\theta)^{1-2\epsilon}\,\frac{1}{(p_\alpha^0 - |\mathbf{p}_\alpha|\cos\theta)^2}\,. \tag{F.4}$$

The integrals over momentum $|\mathbf{k}|$ and angle θ give

$$\int_0^{\Delta}|\mathbf{k}|^{-1-2\epsilon}\mathrm{d}|\mathbf{k}| = -\frac{\Delta^{-2\epsilon}}{2\epsilon} \tag{F.5}$$

$$4^{\epsilon}\int_0^{\pi}\mathrm{d}\theta\,\frac{(\sin\theta)^{1-2\epsilon}}{(p_\alpha^0 - |\mathbf{p}_\alpha|\cos\theta)^2} = \frac{2}{p_\alpha^2}\left[1 - \epsilon\frac{p_\alpha^0}{|\mathbf{p}_\alpha|}\log\frac{p_\alpha^0 - |\mathbf{p}_\alpha|}{p_\alpha^0 + |\mathbf{p}_\alpha|} + \mathcal{O}(\epsilon^2)\right]\,.$$

By expanding in ϵ we get

$$I^{\text{int}} = \frac{1}{4\pi^2}\int_0^1\mathrm{d}\alpha\frac{1}{p_\alpha^2}\left[\frac{1}{\epsilon_{\text{IR}}} + \frac{1}{2}\gamma_E - \frac{1}{2}\log(4\pi) + \frac{1}{2}\log\frac{\Delta^2}{\mu^2} + \frac{p_\alpha^0}{2|\mathbf{p}_\alpha|}\log\frac{p_\alpha^0 - |\mathbf{p}_\alpha|}{p_\alpha^0 + |\mathbf{p}_\alpha|}\right] \tag{F.6}$$

where, in analogy with the UV–divergences, we have $\epsilon_{\rm IR} = -2\epsilon$. The last step is to compute the two different integrals in α. Due to the way the parameter ρ is defined,

$$p_\alpha^2 = 2\alpha(\rho\, l_1 \cdot q_1 - q_1^2) + q_1^2 = \alpha(\rho^2 m_\tau^2 - M_\pi^2) + M_\pi^2 \,. \tag{F.7}$$

The integral multiplying the IR–divergent term can then be written as

$$\int_0^1 \mathrm{d}\alpha\, \frac{1}{p_\alpha^2} = \frac{2}{\rho \lambda_{\pi\tau}^{1/2}(t)} \log\left(\frac{m_\tau^2 + M_\pi^2 - t + \lambda_{\pi\tau}^{1/2}(t)}{2 m_\tau M_\pi}\right) \,. \tag{F.8}$$

Furthermore, the more complicated integral associated to the finite bremsstrahlung contribution, is given by [236]

$$\begin{aligned}\int_0^1 \mathrm{d}\alpha\, \frac{1}{p_\alpha^2}\frac{p_\alpha^0}{|\mathbf{p}_\alpha|} \log\frac{p_\alpha^0 - |\mathbf{p}_\alpha|}{p_\alpha^0 + |\mathbf{p}_\alpha|} = &\left\{ \frac{1}{4\ell v}\log^2\left(\frac{m(m+v)}{2vq_1^0 - q_1^2 - mv}\right) - \frac{1}{2\ell v}\log^2\left(-\frac{v(m+v)}{2vq_1^0 - q_1^2 + v^2}\right)\right. \\ &\left. - \frac{1}{\ell v}\left[-\mathrm{Sp}\left(\frac{m+v}{v}\right) + \mathrm{Sp}\left(\frac{v(m+v)}{2vq_1^0 - q_1^2 + v^2}\right)\right]\right\}_{m=q_1^0 - |\mathbf{q_1}|}^{m=\rho(l_1^0 - |\mathbf{l_1}|)} \,.\end{aligned} \tag{F.9}$$

where $\ell = \rho l_1^0 - q_1^0 = \pm|\rho \mathbf{l}_1 - \mathbf{q}_1|$, $v = \frac{\rho^2 l_1^2 - q_1^2}{2\ell}$ and ρ is defined such that $(\rho l_1 - q_1)^2 = 0$ and such that $(\rho l_1^0 - q_1^0)$ has the same sign of q_1^0:

$$\rho = \frac{l_1 \cdot q_1}{l_1^2} \pm \sqrt{\frac{(l_1 \cdot q_1)^2}{l_1^4} - \frac{q_1^2}{l_1^2}} \,. \tag{F.10}$$

The Spence function is defined by

$$\mathrm{Sp}(z) = -\int_0^z \mathrm{d}u\, \frac{\log(1-u)}{u} \,, \tag{F.11}$$

and the Källèn function is referred to with suppressed arguments $\lambda = \lambda(t, m_\tau^2, M_\pi^2)$. Simplifying this result and applying identities relating $\mathrm{Sp}(z)$ to $\mathrm{Sp}(1/z)$, the Feynman-parameter integral can be expressed by [236]

$$\int_0^1 \mathrm{d}\alpha\, \frac{1}{p_\alpha^2}\frac{p_\alpha^0}{|\mathbf{p}_\alpha|} \log\frac{p_\alpha^0 - |\mathbf{p}_\alpha|}{p_\alpha^0 + |\mathbf{p}_\alpha|} = \tag{F.12}$$

$$\frac{1}{\ell v}\left\{\frac{1}{4}\log^2\frac{u^0 - |\mathbf{u}|}{u^0 + |\mathbf{u}|} + \mathrm{Sp}\left(\frac{v - u^0 - |\mathbf{u}|}{v}\right) + \mathrm{Sp}\left(\frac{v - u^0 + |\mathbf{u}|}{v}\right)\right\}_{u=q_1}^{u=\rho l_1} \,. \tag{F.13}$$

In the τ rest frame, the auxiliary quantities involved in the expression above appear as

$$\begin{aligned}\rho &= \frac{m_\tau^2 + M_\pi^2 - t + \lambda_{\pi\tau}^{1/2}(t)}{2m_\tau^2} \,, \quad v = m_\tau \rho \,, \\ \ell &= \frac{\lambda_{\pi\tau}^{1/2}(t)}{2m_\tau}, \quad q_1^0 = \frac{m_\tau^2 + M_\pi^2 - t}{2m_\tau}.\end{aligned} \tag{F.14}$$

Similarly we have

$$
\begin{aligned}
I^{\mathrm{ISR,FSR}} &= \mu^{2\epsilon} \int' \frac{\mathrm{d}^{d-1}k}{(2\pi)^{d-1}} \frac{1}{2|\mathbf{k}|} \frac{1}{(p_i \cdot k)^2} \\
&= \frac{1}{4\pi^2} \frac{1}{p_i^2} \left[\frac{1}{\epsilon_{\mathrm{IR}}} + \frac{1}{2}\gamma_E - \frac{1}{2}\log(4\pi) + \frac{1}{2}\log\frac{\Delta^2}{\mu^2} + \frac{p_i^0}{2|\mathbf{p}_i|} \log\frac{p_i^0 - |\mathbf{p}_i|}{p_i^0 + |\mathbf{p}_i|} \right]
\end{aligned}
\tag{F.15}
$$

where $p_i = l_1, q_1$.

Appendix G

Phase–space integration for $\tau^{\pm} \to \pi^{\pm}\pi^0\nu_\tau\gamma$

G.1 Kinematics

We will now compute the phase–space integration for a process with 4 particles in the final state, such as the radiative τ decay and then we will discuss the physical regions to consider in order to compute the differential decay rate and spectrum.

The kinematic of the process $\tau^-(l_1) \to \pi^-(q_1)\pi^0(q_2)\nu_\tau(l_2)\gamma(k)$ is described by the following invariants:

$$s = (q_1 + q_2)^2 = (l_1 - l_2 - k)^2, \tag{G.1}$$
$$t = (l_1 - q_1)^2 = (l_2 + q_2 + k)^2, \tag{G.2}$$
$$u = (l_1 - q_2)^2 = (q_1 + l_2 + k)^2, \tag{G.3}$$
$$x = (q_2 + k)^2 = (l_1 - q_1 - q_2)^2, \tag{G.4}$$

with $s + t + u + x = m_\tau^2 + 2M_\pi^2$, $l_1^2 = m_\tau^2$ and $q_1^2 = q_2^2 = M_\pi^2$. Note that, since we are interested in $\mathcal{O}(e^2p^2)$ corrections to the hadronic τ decay, we set $M_{\pi^0} = M_\pi$ everywhere in our analysis. After the integration over neutrino and photon 4–momenta the remaining integrals that need to be computed are $I_{mn}(s,t,x)$ given in Eq. (12.9). By writing the δ–function in different components we get

$$I_{mn}(s,t,x) = \frac{1}{2\pi}\int \frac{\mathrm{d}^3 l_2}{2l_2^0}\frac{\mathrm{d}^3 k}{2k^0}\delta^{(0)}(l_1^0 - l_2^0 - q_1^0 - q_2^0 - k^0)\frac{\delta^{(3)}(\mathbf{l_1} - \mathbf{l_2} - \mathbf{q_1} - \mathbf{q_2} - \mathbf{k})}{(l_1\cdot k)^m (q_1\cdot k)^n}. \tag{G.5}$$

In the τ center–of–mass frame, the four momenta read

$$\begin{aligned} l_1 &= (m_\tau, \mathbf{0}), \qquad l_2 = (|\mathbf{l}_2|, \mathbf{l}_2), \qquad k = (|\mathbf{k}|, \mathbf{k}), \\ q_1 &= \left(\sqrt{M_\pi^2 + |\mathbf{q}_1|^2}, \mathbf{q}_1\right), \qquad q_2 = \left(\sqrt{M_\pi^2 + |\mathbf{q}_2|^2}, \mathbf{q}_2\right). \end{aligned} \tag{G.6}$$

By imposing the three momentum conservation in this reference frame, i.e., $\mathbf{l}_2 = -\mathbf{q_1} - \mathbf{q_2} - \mathbf{k}$, and from the definition of the invariant x in Eq. (G.4), we get

$$|\mathbf{l}_2| = \frac{1}{|\mathbf{k}|}\left(\frac{x}{2} - |\mathbf{k}|^2 - |\mathbf{k}||\mathbf{q}_1 + \mathbf{q}_2|\cos\theta_k\right), \tag{G.7}$$

with θ_k the angle between $\mathbf{k}$ and $|\mathbf{q}_1 + \mathbf{q}_2|$. We can now use the energy conservation by considering the

argument of the $\delta^{(0)}$–function in the τ–rest frame, which reads

$$f(|\mathbf{k}|) = m_\tau - |\mathbf{l}_2| - \sqrt{M_\pi^2 + |\mathbf{q}_1|^2} - \sqrt{M_\pi^2 + |\mathbf{q}_2|^2} - |\mathbf{k}|. \tag{G.8}$$

By imposing $f(|\mathbf{k}|) = 0$, we get

$$|\mathbf{k}|_0 = \frac{m_\tau x}{m_\tau^2 - s + x + \cos\theta_k \sqrt{\lambda\left(s, x, m_\tau^2\right)}} \,. \tag{G.9}$$

With these results we can write $|\mathbf{k}|_0$ in terms of Mandelstam variables, masses and one angle while $\delta^{(0)}(l_1^0 - l_2^0 - q_1^0 - q_2^0 - k^0)$ can be written as

$$\delta^{(0)}(l_1^0 - l_2^0 - q_1^0 - q_2^0 - k^0) = \frac{\delta\left(|\mathbf{k}| - |\mathbf{k}|_0\right)}{\left|f'\left(|\mathbf{k}|_0\right)\right|} \,, \tag{G.10}$$

such that the integral in Eq. (G.5) is now given by

$$I_{mn} = \frac{1}{2\pi} \int \mathrm{d}\cos\theta_k \; \mathrm{d}\phi_k \; \mathrm{d}|\mathbf{k}| \frac{|\mathbf{k}|^2}{4|\mathbf{l}_2||\mathbf{k}|} \frac{\delta\left(|\mathbf{k}| - |\mathbf{k}|_0\right)}{\left|f'\left(|\mathbf{k}|_0\right)\right|} \frac{1}{\left(l_1 \cdot k\right)^m \left(q_1 \cdot k\right)^n}. \tag{G.11}$$

where

$$\frac{|\mathbf{k}|^2}{4|\mathbf{l}_2||\mathbf{k}|} \frac{1}{\left|f'\left(|\mathbf{k}|_0\right)\right|} = \frac{m_\tau^2 x}{2\left(m_\tau^2 - s + x + \cos\theta_k \sqrt{\lambda\left(s, x, m_\tau^2\right)}\right)^2} \,. \tag{G.12}$$

We now need to find an expression for $|\mathbf{q}_1|$, $|\mathbf{q}_2|$ and $|\mathbf{q}_1 + \mathbf{q}_2|$ in terms of masses and Mandelstam variables:

* from $l_1 \cdot q_1 = m_\tau \sqrt{M_\pi^2 + |\mathbf{q}_1|^2} = \frac{1}{2}(m_\tau^2 + M_\pi^2 - t)$ we get

$$|\mathbf{q}_1| = \frac{\lambda_{\pi\tau}^{1/2}(t)}{2m_\tau} \,, \tag{G.13}$$

* from $l_1 \cdot q_2 = m_\tau \sqrt{M_\pi^2 + |\mathbf{q}_2|^2} = \frac{1}{2}(s + t - x - M_\pi^2)$ we get

$$|\mathbf{q}_2| = \frac{\sqrt{\left(M_\pi^2 - s - t + x\right)^2 - 4M_\pi^2 m_\tau^2}}{2m_\tau} \,, \tag{G.14}$$

* $|\mathbf{q}_1 + \mathbf{q}_2| = \sqrt{(\mathbf{q}_1 + \mathbf{q}_2)^2} = \sqrt{|\mathbf{q}_1|^2 + |\mathbf{q}_2|^2 + 2|\mathbf{q}_1||\mathbf{q}_2|\cos\theta_q}$, where θ_q is the angle between $\mathbf{q}_1$ and $\mathbf{q}_2$ and can be determined from

$$q_1 \cdot q_2 = \frac{s - 2M_\pi^2}{2} = \sqrt{M_\pi^2 + |\mathbf{q}_1|^2}\sqrt{M_\pi^2 + |\mathbf{q}_2|^2} - |\mathbf{q}_1||\mathbf{q}_2|\cos\theta_q \,. \tag{G.15}$$

The last step consists in rewriting the scalar products $l_1 \cdot k$ and $q_1 \cdot k$ in terms of the quantities just determined. In the τ–rest frame we have

$$\begin{aligned} l_1 \cdot k &= m_\tau |\mathbf{k}|_0 \,, \\ q_1 \cdot k &= |\mathbf{k}|_0 \left(\sqrt{M_\pi^2 + |\mathbf{q}_1|^2} - |\mathbf{q}_1|\cos\theta_{kq_1}\right) \,, \end{aligned} \tag{G.16}$$

with θ_{kq_1} the angle between $\mathbf{k}$ and $\mathbf{q}_1$. This angle can be determined by looking at Fig. (G.1) and by choosing the coordinate axes such that

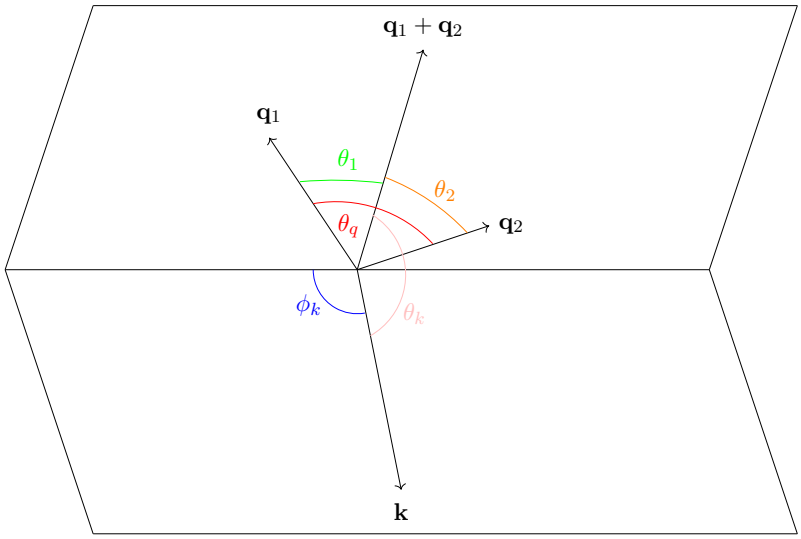

Figure G.1: The $\tau \to \pi\pi^0\nu\gamma$ decay in the τ–rest frame

$$\mathbf{q}_1 + \mathbf{q}_2 = \begin{pmatrix} 0 \\ 0 \\ |\mathbf{q}_1 + \mathbf{q}_2| \end{pmatrix} \quad \text{and} \quad \mathbf{k} = \begin{pmatrix} \sin\theta_k \cos\phi_k \\ \sin\theta_k \sin\phi_k \\ \cos\theta_k \end{pmatrix} |\mathbf{k}| \,, \tag{G.17}$$

and

$$\mathbf{q}_1 = \begin{pmatrix} \sin\theta_1 \\ 0 \\ \cos\theta_1 \end{pmatrix} |\mathbf{q}_1| \quad \text{and} \quad \mathbf{q}_2 = \begin{pmatrix} -\sin\theta_2 \\ 0 \\ \cos\theta_2 \end{pmatrix} |\mathbf{q}_2| \,, \tag{G.18}$$

with constraint

$$\mathbf{q}_1 + \mathbf{q}_2 = \begin{pmatrix} |\mathbf{q}_1| \sin\theta_1 - |\mathbf{q}_2| \sin\theta_2 \\ 0 \\ |\mathbf{q}_1| \cos\theta_1 + |\mathbf{q}_2| \cos\theta_2 \end{pmatrix} \stackrel{!}{=} \begin{pmatrix} 0 \\ 0 \\ |\mathbf{q}_1 + \mathbf{q}_2| \end{pmatrix} . \tag{G.19}$$

We then find

$$\cos\theta_1 = \frac{|\mathbf{q}_1| + |\mathbf{q}_2| \cos\theta_q}{\sqrt{|\mathbf{q}_1|^2 + |\mathbf{q}_2|^2 + 2|\mathbf{q}_1||\mathbf{q}_2| \cos\theta_q}} \,, \tag{G.20}$$

where $\cos\theta_q$ is determined in Eq. (G.15). Finally, from

$$\mathbf{q}_1 \cdot \mathbf{k} = |\mathbf{k}||\mathbf{q}_1| \cos\theta_{kq_1} = |\mathbf{k}||\mathbf{q}_1| \left(\sin\theta_k \cos\phi_k \sin\theta_1 + \cos\theta_k \cos\theta_1\right) \,, \tag{G.21}$$

we get

$$\cos\theta_{kq_1} = \sqrt{1 - \cos^2\theta_k}\sqrt{1 - \cos^2\theta_1} \cos\phi_k + \cos\theta_k \cos\theta_1 \,, \tag{G.22}$$

and we can write the integral I_{mn} in terms of masses, Mandelstam variables and only one angle.

G.2 Integration region and boundaries

In order to calculate differential rates and spectra, we need the physical region $\mathcal{D}$ in the form of a normal domain:

$$\mathcal{D} = \{s_{\min} \le s \le s_{\max},\ t_{\min}(s) \le t \le t_{\max}(s),\ x_{\min}(s,t) \le x \le x_{\max}(s,t)\} \,, \tag{G.23}$$

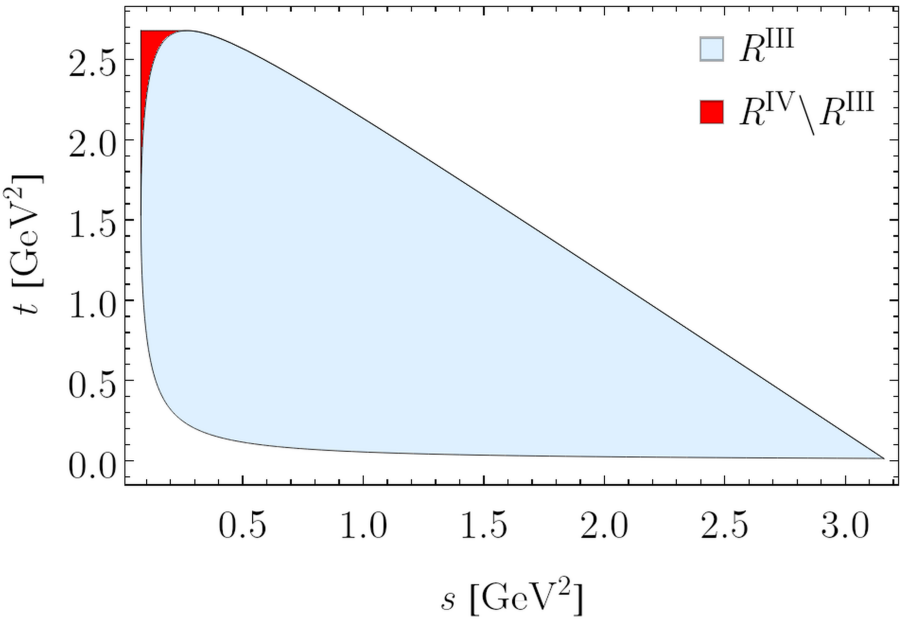

Figure G.2: (s,t) Dalitz plot where R^{IV} represent the full radiative phase space while R^{III} is accessible to the non-radiative decay. The contribution in $R^{\mathrm{IV}} \setminus R^{\mathrm{III}}$ is important for the threshold behavior.

where $s_{\mathrm{min}} = 4M_\pi^2$ and $s_{\mathrm{max}} = m_\tau^2$. In order to give the explicit form of $t_{\mathrm{min/max}}(s)$ and $x_{\mathrm{min/max}}(s,t)$ we introduce the functions

$$t_\pm(s,x) = \frac{1}{2s}\left[2s\left(m_\tau^2 + M_\pi^2\right) - s\left(m_\tau^2 + s - x\right) \pm \sqrt{\lambda\left(s, M_\pi^2, M_\pi^2\right)\lambda\left(m_\tau^2, s, x\right)}\right],$$
$$x_\pm(s,t) = \frac{1}{2M_\pi^2}\left[2M_\pi^2\left(m_\tau^2 + s\right) - s\left(m_\tau^2 + M_\pi^2 - t\right) \pm \sqrt{\lambda\left(s, M_\pi^2, M_\pi^2\right)\lambda_{\pi\tau}(t)}\right]. \qquad \text{(G.24)}$$

In the following, let us call R^{III} the region in the $s-t$ plane accessible in the non–radiative three–body decay, and R^{IV} the region accessible in the radiative decay. A plot representing the two different regions can be found in Fig. G.2. R^{III} is given by

$$\bar{t}_{\mathrm{min}}(s) = t_-(s,0) \qquad \text{for} \quad s_{\mathrm{min}} \le s \le s_{\mathrm{max}}\ ,$$
$$\bar{t}_{\mathrm{max}}(s) = t_+(s,0) \qquad \text{for} \quad s_{\mathrm{min}} \le s \le s_{\mathrm{max}}\ , \qquad \text{(G.25)}$$

while R^{IV} corresponds to

$$t_{\mathrm{min}}(s) = t_-(s,0) \qquad \text{for} \quad s_{\mathrm{min}} \le s \le s_{\mathrm{max}}\ ,$$

$$t_{\mathrm{max}}(s) = \begin{cases} t_+(s,0) & \text{for} \quad s_* \le s \le s_{\mathrm{max}} \\ (m_\tau - M_\pi)^2 & \text{for} \quad s_{\mathrm{min}} \le s \le s_* \end{cases}, \qquad \text{(G.26)}$$

with

$$s_* = \frac{m_\tau^2 M_\pi}{m_\tau - M_\pi}\ . \qquad \text{(G.27)}$$

Finally, for given (s,t) the limits for x are

$$x_{\mathrm{max}}(s,t) = x_+(s,t)\ ,$$

$$x_{\min}(s,t) = \begin{cases} 0 & \text{for } (s,t) \in R^{\mathrm{III}} \\ x_-(s,t) & \text{for } (s,t) \in R^{\mathrm{IV}} \backslash R^{\mathrm{III}} \end{cases} , \tag{G.28}$$

where the value $x_{\min}(s,t) = 0$ is a consequence of working in dimensional regularization also for IR–divergences, otherwise it would have been $x_{\min}(s,t) = M_\gamma^2$, with M_γ a fictitious photon mass. Moreover, the following combinations of invariants appear in Eq. (12.12):

$$Y_{1,2} = \frac{1 - 2\bar{\alpha} \pm \sqrt{(1-2\bar{\alpha})^2 - \left(1 - \bar{\beta}^2\right)}}{1 + \bar{\beta}} , \tag{G.29}$$

with

$$\begin{aligned} \bar{\alpha} &= \frac{\left(m_\tau^2 - s\right)\left(m_\tau^2 + M_\pi^2 - s - t\right)}{M_\pi^2 + m_\tau^2 - t} \cdot \frac{\lambda_{\pi\tau}(t)}{2\bar{\delta}} , \quad \bar{\beta} = -\frac{\lambda_{\pi\tau}^{1/2}(t)}{M_\pi^2 + m_\tau^2 - t} , \quad \bar{\gamma} = \frac{\lambda_{\pi\tau}^{1/2}(t)}{2\sqrt{\bar{\delta}}} , \\ \bar{\delta} &= M_\pi^2 \left(m_\tau^2 - s\right)\left(M_\pi^2 - t\right) - st\left(s + t - m_\tau^2\right) + M_\pi^2\left(st - m_\tau^4 + m_\tau^2 s + m_\tau^2 t\right) - M_\pi^4 m_\tau^2 , \end{aligned} \tag{G.30}$$

Bibliography

[1] G. Colangelo, M. Cottini, M. Hoferichter and S. Holz, *Improved calculation of radiative corrections to $\tau \to \pi\pi\nu_\tau$ decays*, 2510.26871.

[2] G. Colangelo, M. Cottini, M. Hoferichter and S. Holz, *Radiative corrections to $\tau \to \pi\pi\nu_\tau$*, 2511.07507.

[3] G. Colangelo, M. Cottini and J.R. de Elvira, *Isospin-breaking in the $\pi\pi$ scattering amplitude I: Effects due to the pion mass difference*, 2511.08680.

[4] MUON $g-2$ collaboration, *Precise measurement of the positive muon anomalous magnetic moment*, *Phys. Rev. Lett.* **86** (2001) 2227 [hep-ex/0102017].

[5] MUON $g-2$ collaboration, *Measurement of the positive muon anomalous magnetic moment to 0.7 ppm*, *Phys. Rev. Lett.* **89** (2002) 101804 [hep-ex/0208001].

[6] MUON $g-2$ collaboration, *Measurement of the negative muon anomalous magnetic moment to 0.7 ppm*, *Phys. Rev. Lett.* **92** (2004) 161802 [hep-ex/0401008].

[7] MUON $g-2$ collaboration, *Final Report of the Muon E821 Anomalous Magnetic Moment Measurement at BNL*, *Phys. Rev. D* **73** (2006) 072003 [hep-ex/0602035].

[8] MUON $g-2$ collaboration, *Measurement of the Positive Muon Anomalous Magnetic Moment to 0.46 ppm*, *Phys. Rev. Lett.* **126** (2021) 141801 [2104.03281].

[9] T. Aoyama et al., *The anomalous magnetic moment of the muon in the Standard Model*, *Phys. Rept.* **887** (2020) 1 [2006.04822].

[10] MUON $g-2$ collaboration, *Measurement of the Positive Muon Anomalous Magnetic Moment to 0.20 ppm*, *Phys. Rev. Lett.* **131** (2023) 161802 [2308.06230].

[11] S. Borsanyi et al., *Leading hadronic contribution to the muon magnetic moment from lattice QCD*, *Nature* **593** (2021) 51 [2002.12347].

[12] CMD-3 collaboration, *Measurement of the $e^+e^- \to \pi^+\pi^-$ cross section from threshold to 1.2 GeV with the CMD-3 detector*, *Phys. Rev. D* **109** (2024) 112002 [2302.08834].

[13] MUON $g-2$ collaboration, *Measurement of the Positive Muon Anomalous Magnetic Moment to 127 ppb*, 2506.03069.

[14] R. Aliberti et al., *The anomalous magnetic moment of the muon in the Standard Model: an update*, 2505.21476.

[15] J-PARC $g-2$/EDM collaboration, *A novel precision measurement of muon $g-2$ and EDM at J-PARC*, *AIP Conf. Proc.* **1467** (2012) 45.

[16] T. Mibe, *Measurement of muon $g-2$ and edm with an ultra-cold muon beam at J-PARC*, *Nucl. Phys. B - Proc. Suppl.* **218** (2011) 242.

[17] M. Abe et al., *A New Approach for Measuring the Muon Anomalous Magnetic Moment and Electric Dipole Moment*, *PTEP* **2019** (2019) 053C02 [1901.03047].

[18] G. Abbiendi et al., *Mini-Proceedings of the STRONG2020 Virtual Workshop on "Space-like and*

Time-like determination of the Hadronic Leading Order contribution to the Muon g − 2", in *STRONG2020 Virtual Workshop "Space-like and Time-like determination of the Hadronic Leading Order contribution to the Muon g − 2"*, 1, 2022 [2201.12102].

[19] Working Group on Radiative Corrections, Monte Carlo Generators for Low Energies collaboration, *Quest for precision in hadronic cross sections at low energy: Monte Carlo tools vs. experimental data*, *Eur. Phys. J. C* **66** (2010) 585 [0912.0749].

[20] G. Colangelo et al., *Prospects for precise predictions of a_μ in the Standard Model*, 2203.15810.

[21] F. Campanario, H. Czyż, J. Gluza, T. Jeliński, G. Rodrigo, S. Tracz et al., *Standard model radiative corrections in the pion form factor measurements do not explain the a_μ anomaly*, *Phys. Rev. D* **100** (2019) 076004 [1903.10197].

[22] F. Ignatov and R.N. Lee, *Charge asymmetry in $e^+e^- \to \pi^+\pi^-$ process*, *Phys. Lett. B* **833** (2022) 137283 [2204.12235].

[23] G. Colangelo, M. Hoferichter, J. Monnard and J.R. de Elvira, *Radiative corrections to the forward-backward asymmetry in $e^+e^- \to \pi^+\pi^-$*, *JHEP* **08** (2022) 295 [2207.03495].

[24] B. Ananthanarayan, G. Colangelo, J. Gasser and H. Leutwyler, *Roy equation analysis of $\pi\pi$ scattering*, *Phys. Rept.* **353** (2001) 207 [hep-ph/0005297].

[25] G. Colangelo, J. Gasser and H. Leutwyler, *$\pi\pi$ scattering*, *Nucl. Phys. B* **603** (2001) 125 [hep-ph/0103088].

[26] I. Caprini, G. Colangelo and H. Leutwyler, *Regge analysis of the $\pi\pi$ scattering amplitude*, *Eur. Phys. J. C* **72** (2012) 1860 [1111.7160].

[27] R. Garcia-Martin, R. Kaminski, J.R. Pelaez, J. Ruiz de Elvira and F.J. Yndurain, *The Pion-pion scattering amplitude. IV: Improved analysis with once subtracted Roy-like equations up to 1100 MeV*, *Phys. Rev. D* **83** (2011) 074004 [1102.2183].

[28] J.R. Peláez, P. Rabán and J.R. de Elvira, *Global parametrizations of $\pi\pi$ scattering with dispersive constraints: Beyond the S_0 wave*, *Phys. Rev. D* **111** (2025) 074003 [2412.15327].

[29] B. Hyams et al., *$\pi\pi$ Phase Shift Analysis from 600-MeV to 1900-MeV*, *Nucl. Phys. B* **64** (1973) 134.

[30] BNL-E865 collaboration, *A New measurement of K^+_{e4} decay and the S wave $\pi\pi$ scattering length $a_0(0)$*, *Phys. Rev. Lett.* **87** (2001) 221801 [hep-ex/0106071].

[31] NA48/2 collaboration, *Observation of a cusp-like structure in the $\pi_0\pi_0$ invariant mass distribution from $K\pm \to \pi^\pm\pi^0\pi^0$ decay and determination of the $\pi\pi$ scattering lengths*, *Phys. Lett. B* **633** (2006) 173 [hep-ex/0511056].

[32] NA48/2 collaboration, *New high statistics measurement of K_{e4} decay form factors and $\pi\pi$ scattering phase shifts*, *Eur. Phys. J. C* **54** (2008) 411.

[33] B. Adeva et al., *Determination of $\pi\pi$ scattering lengths from measurement of $\pi^+\pi^-$ atom lifetime*, *Phys. Lett. B* **704** (2011) 24 [1109.0569].

[34] V. Cirigliano, G. Ecker and H. Neufeld, *Isospin violation and the magnetic moment of the muon*, *Phys. Lett. B* **513** (2001) 361 [hep-ph/0104267].

[35] V. Cirigliano, G. Ecker and H. Neufeld, *Radiative tau decay and the magnetic moment of the muon*, *JHEP* **08** (2002) 002 [hep-ph/0207310].

[36] M. Davier, A. Hoecker, G. Lopez Castro, B. Malaescu, X.H. Mo, G. Toledo Sanchez et al., *The Discrepancy Between tau and e^+e^- Spectral Functions Revisited and the Consequences for the Muon Magnetic Anomaly*, *Eur. Phys. J. C* **66** (2010) 127 [0906.5443].

[37] J.A. Miranda and P. Roig, *New τ-based evaluation of the hadronic contribution to the vacuum polarization piece of the muon anomalous magnetic moment*, *Phys. Rev. D* **102** (2020) 114017

[2007.11019].

[38] G.E. Uhlenbeck and S. Goudsmit, *Ersetzung der Hypothese vom unmechanischen Zwang durch eine Forderung bezüglich des inneren Verhaltens jedes einzelnen Elektrons*, *Naturwissenschaften* **13** (1925) 953.

[39] G.E. Uhlenbeck and S. Goudsmit, *Spinning Electrons and the Structure of Spectra*, *Nature* **117** (1926) 264.

[40] E. Back and A. Landé, *Zeemaneffekt und Multiplettstruktur der Spektrallinien*, J. Springer (1925).

[41] W. Pauli, *Zur Quantenmechanik des magnetischen Elektrons*, *Zeitschrift für Physik* **43** (1927) 601.

[42] P.A.M. Dirac, *The quantum theory of the electron*, *Proc. Roy. Soc. Lond. A* **117** (1928) 610.

[43] P.A.M. Dirac, *The Quantum theory of electron. 2.*, *Proc. Roy. Soc. Lond. A* **118** (1928) 351.

[44] J.E. Nafe, E.B. Nelson and I.I. Rabi, *The Hyperfine Structure of Atomic Hydrogen and Deuterium*, *Phys. Rev.* **71** (1947) 914.

[45] P. Kusch and H.M. Foley, *The Magnetic Moment of the Electron*, *Phys. Rev.* **74** (1948) 250.

[46] J.S. Schwinger, *On Quantum electrodynamics and the magnetic moment of the electron*, *Phys. Rev.* **73** (1948) 416.

[47] T. Aoyama, T. Kinoshita and M. Nio, *Theory of the Anomalous Magnetic Moment of the Electron*, *Atoms* **7** (2019) 28.

[48] G.F. Giudice, P. Paradisi and M. Passera, *Testing new physics with the electron $g-2$*, *JHEP* **11** (2012) 113 [1208.6583].

[49] V.B. Berestetskii, O.N. Krokhin and A.K. Khlebnikov, *Concerning the Radiative Correction to the μ-Meson Magnetic Moment*, *Sov. Phys. JETP* **3** (1956) 761.

[50] M. Passera, *The Standard model prediction of the muon anomalous magnetic moment*, *J. Phys. G* **31** (2005) R75 [hep-ph/0411168].

[51] K. Melnikov and A. Vainshtein, *Theory of the muon anomalous magnetic moment*, vol. 216, Springer (2006), 10.1007/3-540-32807-6.

[52] F. Jegerlehner, *The Anomalous Magnetic Moment of the Muon*, vol. 274, Springer, Cham (2017), 10.1007/978-3-319-63577-4.

[53] T. Kinoshita, B. Nizic and Y. Okamoto, *Eighth order QED contribution to the anomalous magnetic moment of the muon*, *Phys. Rev. D* **41** (1990) 593.

[54] T. Kinoshita and W.J. Marciano, *Quantum Electrodynamics* (1990), 10.1007/978-1-4613-1147-8-2.

[55] S.J. Brodsky and J.D. Sullivan, *W boson contribution to the anomalous magnetic moment of the muon*, *Phys. Rev.* **156** (1967) 1644.

[56] R.H. Parker, C. Yu, W. Zhong, B. Estey and H. Müller, *Measurement of the fine-structure constant as a test of the standard model*, *Science* **360** (2018) 191–195.

[57] T. Aoyama, M. Hayakawa, T. Kinoshita and M. Nio, *Complete Tenth-Order QED Contribution to the Muon $g-2$*, *Phys. Rev. Lett.* **109** (2012) 111808 [1205.5370].

[58] A. Czarnecki, B. Krause and W.J. Marciano, *Electroweak Fermion loop contributions to the muon anomalous magnetic moment*, *Phys. Rev. D* **52** (1995) R2619 [hep-ph/9506256].

[59] A. Czarnecki, B. Krause and W.J. Marciano, *Electroweak corrections to the muon anomalous magnetic moment*, *Phys. Rev. Lett.* **76** (1996) 3267 [hep-ph/9512369].

[60] T.V. Kukhto, E.A. Kuraev, Z.K. Silagadze and A. Schiller, *The Dominant two loop electroweak contributions to the anomalous magnetic moment of the muon*, *Nucl. Phys. B* **371** (1992) 567.

[61] M. Hoferichter, J. Lüdtke, L. Naterop, M. Procura and P. Stoffer, *Improved Evaluation of the Electroweak Contribution to Muon $g-2$*, *Phys. Rev. Lett.* **134** (2025) 201801 [2503.04883].

[62] F. Jegerlehner and A. Nyffeler, *The Muon $g-2$*, *Phys. Rept.* **477** (2009) 1 [0902.3360].

[63] J. Prades, E. de Rafael and A. Vainshtein, *The Hadronic Light-by-Light Scattering Contribution to the Muon and Electron Anomalous Magnetic Moments*, *Adv. Ser. Direct. High Energy Phys.* **20** (2009) 303 [0901.0306].

[64] T. Blum, ed., *Hadronic contributions to the muon anomalous magnetic moment Workshop. $(g-2)_\mu$: Quo vadis? Workshop. Mini proceedings*, 7, 2014.

[65] J.F. De Troconiz and F.J. Yndurain, *Precision determination of the pion form-factor and calculation of the muon $g-2$*, *Phys. Rev. D* **65** (2002) 093001 [hep-ph/0106025].

[66] H. Leutwyler, *Electromagnetic form-factor of the pion*, in *Continuous Advances in QCD 2002 / ARKADYFEST (honoring the 60th birthday of Prof. Arkady Vainshtein)*, pp. 23–40, 12, 2002, DOI [hep-ph/0212324].

[67] G. Colangelo, *Hadronic contributions to a_μ below one-GeV*, *Nucl. Phys. B Proc. Suppl.* **131** (2004) 185 [hep-ph/0312017].

[68] J.F. de Troconiz and F.J. Yndurain, *The Hadronic contributions to the anomalous magnetic moment of the muon*, *Phys. Rev. D* **71** (2005) 073008 [hep-ph/0402285].

[69] B. Ananthanarayan, I. Caprini, D. Das and I. Sentitemsu Imsong, *Two-pion low-energy contribution to the muon $g-2$ with improved precision from analyticity and unitarity*, *Phys. Rev. D* **89** (2014) 036007 [1312.5849].

[70] B. Ananthanarayan, I. Caprini, D. Das and I. Sentitemsu Imsong, *Precise determination of the low-energy hadronic contribution to the muon $g-2$ from analyticity and unitarity: An improved analysis*, *Phys. Rev. D* **93** (2016) 116007 [Ananthanarayan:2016mns].

[71] M. Hoferichter, B. Kubis, J. Ruiz de Elvira, H.W. Hammer and U.G. Meißner, *On the $\pi\pi$ continuum in the nucleon form factors and the proton radius puzzle*, *Eur. Phys. J. A* **52** (2016) 331 [1609.06722].

[72] C. Hanhart, S. Holz, B. Kubis, A. Kupść, A. Wirzba and C.W. Xiao, *The branching ratio $\omega \to \pi^+\pi^-$ revisited*, *Eur. Phys. J. C* **77** (2017) 98 [1611.09359].

[73] M. Hoferichter, G. Colangelo, M. Procura and P. Stoffer, *Virtual photon-photon scattering*, *Int. J. Mod. Phys. Conf. Ser.* **35** (2014) 1460400 [1309.6877].

[74] G. Colangelo, M. Hoferichter, M. Procura and P. Stoffer, *Dispersive approach to hadronic light-by-light scattering*, *JHEP* **09** (2014) 091 [1402.7081].

[75] G. Colangelo, M. Hoferichter, B. Kubis, M. Procura and P. Stoffer, *Towards a data-driven analysis of hadronic light-by-light scattering*, *Phys. Lett. B* **738** (2014) 6 [1408.2517].

[76] G. Colangelo, M. Hoferichter, M. Procura and P. Stoffer, *Dispersion relation for hadronic light-by-light scattering: theoretical foundations*, *JHEP* **09** (2015) 074 [1506.01386].

[77] G. Colangelo, M. Hoferichter, M. Procura and P. Stoffer, *Rescattering effects in the hadronic light-by-light contribution to the anomalous magnetic moment of the muon*, *Phys. Rev. Lett.* **118** (2017) 232001 [1701.06554].

[78] G. Colangelo, M. Hoferichter, M. Procura and P. Stoffer, *Dispersion relation for hadronic light-by-light scattering: two-pion contributions*, *JHEP* **04** (2017) 161 [1702.07347].

[79] R. Garcia-Martin and B. Moussallam, *MO analysis of the high statistics Belle results on $\gamma\gamma \to \pi^+\pi^-, \pi^0\pi^0$ with chiral constraints*, *Eur. Phys. J. C* **70** (2010) 155 [1006.5373].

[80] M. Hoferichter, D.R. Phillips and C. Schat, *Roy-Steiner equations for $\gamma\gamma \to \pi\pi$*, *Eur. Phys. J. C* **71** (2011) 1743 [1106.4147].

[81] B. Moussallam, *Unified dispersive approach to real and virtual photon-photon scattering at low energy*, *Eur. Phys. J. C* **73** (2013) 2539 [1305.3143].

[82] L.-Y. Dai and M.R. Pennington, *Comprehensive amplitude analysis of $\gamma\gamma \to \pi^+\pi^-, \pi^0\pi^0$ and $\overline{K}K$ below 1.5 GeV*, *Phys. Rev. D* **90** (2014) 036004 [1404.7524].

[83] F. Niecknig, B. Kubis and S.P. Schneider, *Dispersive analysis of $\omega \to 3\pi$ and $\phi \to 3\pi$ decays*, *Eur. Phys. J. C* **72** (2012) 2014 [1203.2501].

[84] S.P. Schneider, B. Kubis and F. Niecknig, *The $\omega \to \pi^0\gamma^*$ and $\phi \to \pi^0\gamma^*$ transition form factors in dispersion theory*, *Phys. Rev. D* **86** (2012) 054013 [1206.3098].

[85] M. Hoferichter, B. Kubis and D. Sakkas, *Extracting the chiral anomaly from $\gamma\pi \to \pi\pi$*, *Phys. Rev. D* **86** (2012) 116009 [1210.6793].

[86] M. Hoferichter, B. Kubis, S. Leupold, F. Niecknig and S.P. Schneider, *Dispersive analysis of the pion transition form factor*, *Eur. Phys. J. C* **74** (2014) 3180 [1410.4691].

[87] M. Hoferichter, B. Kubis and M. Zanke, *Radiative resonance couplings in $\gamma\pi \to \pi\pi$*, *Phys. Rev. D* **96** (2017) 114016 [1710.00824].

[88] M. Hoferichter, B.-L. Hoid, B. Kubis, S. Leupold and S.P. Schneider, *Pion-pole contribution to hadronic light-by-light scattering in the anomalous magnetic moment of the muon*, *Phys. Rev. Lett.* **121** (2018) 112002 [1805.01471].

[89] M. Hoferichter, B.-L. Hoid, B. Kubis, S. Leupold and S.P. Schneider, *Dispersion relation for hadronic light-by-light scattering: pion pole*, *JHEP* **10** (2018) 141 [1808.04823].

[90] S. Holz, M. Hoferichter, B.-L. Hoid and B. Kubis, *Precision Evaluation of the η- and η'-Pole Contributions to Hadronic Light-by-Light Scattering in the Anomalous Magnetic Moment of the Muon*, *Phys. Rev. Lett.* **134** (2025) 171902 [2411.08098].

[91] S. Holz, M. Hoferichter, B.-L. Hoid and B. Kubis, *Dispersion relation for hadronic light-by-light scattering: η and η' poles*, *JHEP* **04** (2025) 147 [2412.16281].

[92] F. Stollenwerk, C. Hanhart, A. Kupsc, U.G. Meissner and A. Wirzba, *Model-independent approach to $\eta \to \pi^+\pi^-\gamma$ and $\eta' \to \pi^+\pi^-\gamma$*, *Phys. Lett. B* **707** (2012) 184 [1108.2419].

[93] C. Hanhart, A. Kupść, U.G. Meißner, F. Stollenwerk and A. Wirzba, *Dispersive analysis for $\eta \to \gamma\gamma^*$*, *Eur. Phys. J. C* **73** (2013) 2668 [1307.5654].

[94] B. Kubis and J. Plenter, *Anomalous decay and scattering processes of the η meson*, *Eur. Phys. J. C* **75** (2015) 283 [1504.02588].

[95] S. Holz, J. Plenter, C.W. Xiao, T. Dato, C. Hanhart, B. Kubis et al., *Towards an improved understanding of $\eta \to \gamma^*\gamma^*$*, *Eur. Phys. J. C* **81** (2021) 1002 [1509.02194].

[96] M. Albaladejo and B. Moussallam, *Form factors of the isovector scalar current and the $\eta\pi$ scattering phase shifts*, *Eur. Phys. J. C* **75** (2015) 488 [1507.04526].

[97] I. Danilkin, O. Deineka and M. Vanderhaeghen, *Theoretical analysis of the $\gamma\gamma \to \pi^0\eta$ process*, *Phys. Rev. D* **96** (2017) 114018 [1709.08595].

[98] C. Bouchiat and L. Michel, *La résonance dans la diffusion méson π— méson π et le moment magnétique anormal du méson μ*, *J. Phys. Radium* **22** (1961) 121.

[99] L. Durand, *Pionic Contributions to the Magnetic Moment of the Muon*, *Phys. Rev.* **128** (1962) 441.

[100] S.J. Brodsky and E. De Rafael, *Suggested Boson–Lepton Pair Couplings and the Anomalous Magnetic Moment of the Muon*, *Phys. Rev.* **168** (1968) 1620.

[101] M. Gourdin and E. De Rafael, *Hadronic contributions to the muon g-factor*, *Nucl. Phys. B* **10** (1969) 667.

[102] G. Colangelo, M. Hoferichter and P. Stoffer, *Two-pion contribution to hadronic vacuum polarization*, *JHEP* **02** (2019) 006 [1810.00007].

[103] A. Keshavarzi, D. Nomura and T. Teubner, *Muon $g-2$ and $\alpha(M_Z^2)$: a new data-based analysis*,

Phys. Rev. D **97** (2018) 114025 [1802.02995].

[104] A. Keshavarzi, D. Nomura and T. Teubner, *$g-2$ of charged leptons, $\alpha(M_Z^2)$, and the hyperfine splitting of muonium*, *Phys. Rev. D* **101** (2020) 014029 [1911.00367].

[105] T. Blum, *Lattice calculation of the lowest order hadronic contribution to the muon anomalous magnetic moment*, *Phys. Rev. Lett.* **91** (2003) 052001 [hep-lat/0212018].

[106] C. Aubin and T. Blum, *Calculating the hadronic vacuum polarization and leading hadronic contribution to the muon anomalous magnetic moment with improved staggered quarks*, *Phys. Rev. D* **75** (2007) 114502 [hep-lat/0608011].

[107] X. Feng, K. Jansen, M. Petschlies and D.B. Renner, *Two-flavor QCD correction to lepton magnetic moments at leading-order in the electromagnetic coupling*, *Phys. Rev. Lett.* **107** (2011) 081802 [1103.4818].

[108] RBC, UKQCD collaboration, *Calculation of the hadronic vacuum polarization contribution to the muon anomalous magnetic moment*, *Phys. Rev. Lett.* **121** (2018) 022003 [1801.07224].

[109] C. Aubin, T. Blum, M. Golterman and S. Peris, *Muon anomalous magnetic moment with staggered fermions: Is the lattice spacing small enough?*, *Phys. Rev. D* **106** (2022) 054503 [2204.12256].

[110] RBC, UKQCD collaboration, *Update of Euclidean windows of the hadronic vacuum polarization*, *Phys. Rev. D* **108** (2023) 054507 [2301.08696].

[111] A. Boccaletti et al., *High precision calculation of the hadronic vacuum polarisation contribution to the muon anomaly*, 2407.10913.

[112] RBC, UKQCD collaboration, *Long-Distance Window of the Hadronic Vacuum Polarization for the Muon $g-2$*, *Phys. Rev. Lett.* **134** (2025) 201901 [2410.20590].

[113] D. Djukanovic, G. von Hippel, S. Kuberski, H.B. Meyer, N. Miller, K. Ottnad et al., *The hadronic vacuum polarization contribution to the muon $g-2$ at long distances*, *JHEP* **04** (2025) 098 [2411.07969].

[114] B. Chakraborty, C.T.H. Davies, P.G. de Oliviera, J. Koponen, G.P. Lepage and R.S. Van de Water, *The hadronic vacuum polarization contribution to a_μ from full lattice QCD*, *Phys. Rev. D* **96** (2017) 034516 [1601.03071].

[115] M. Della Morte, A. Francis, V. Gülpers, G. Herdoíza, G. von Hippel, H. Horch et al., *The hadronic vacuum polarization contribution to the muon $g-2$ from lattice QCD*, *JHEP* **10** (2017) 020 [1705.01775].

[116] D. Giusti, F. Sanfilippo and S. Simula, *Light-quark contribution to the leading hadronic vacuum polarization term of the muon $g-2$ from twisted-mass fermions*, *Phys. Rev. D* **98** (2018) 114504 [1808.00887].

[117] D. Giusti and S. Simula, *Lepton anomalous magnetic moments in Lattice QCD+QED*, *PoS* **LATTICE2019** (2019) 104 [1910.03874].

[118] A. Gérardin, M. Cè, G. von Hippel, B. Hörz, H.B. Meyer, D. Mohler et al., *The leading hadronic contribution to $(g-2)_\mu$ from lattice QCD with $N_{\rm f}=2+1$ flavours of O(a) improved Wilson quarks*, *Phys. Rev. D* **100** (2019) 014510 [1904.03120].

[119] PACS collaboration, *Hadronic vacuum polarization contribution to the muon $g-2$ with 2+1 flavor lattice QCD on a larger than (10 fm)^4 lattice at the physical point*, *Phys. Rev. D* **100** (2019) 034517 [1902.00885].

[120] Budapest-Marseille-Wuppertal collaboration, *Hadronic vacuum polarization contribution to the anomalous magnetic moments of leptons from first principles*, *Phys. Rev. Lett.* **121** (2018) 022002 [1711.04980].

[121] ETM collaboration, *Four-Flavour Leading-Order Hadronic Contribution To The Muon*

Anomalous Magnetic Moment, *JHEP* **02** (2014) 099 [1308.4327].

[122] Fermilab Lattice, LATTICE-HPQCD, MILC collaboration, *Hadronic-vacuum-polarization contribution to the muon's anomalous magnetic moment from four-flavor lattice QCD*, *Phys. Rev. D* **101** (2020) 034512 [1902.04223].

[123] C. Lehner and A.S. Meyer, *Consistency of hadronic vacuum polarization between lattice QCD and the R-ratio*, *Phys. Rev. D* **101** (2020) 074515 [2003.04177].

[124] chiQCD collaboration, *Muon $g-2$ with overlap valence fermions*, *Phys. Rev. D* **107** (2023) 034513 [2204.01280].

[125] M. Cè et al., *Window observable for the hadronic vacuum polarization contribution to the muon $g-2$ from lattice QCD*, *Phys. Rev. D* **106** (2022) 114502 [2206.06582].

[126] Extended Twisted Mass collaboration, *Lattice calculation of the short and intermediate time-distance hadronic vacuum polarization contributions to the muon magnetic moment using twisted-mass fermions*, *Phys. Rev. D* **107** (2023) 074506 [2206.15084].

[127] S. Kuberski, M. Cè, G. von Hippel, H.B. Meyer, K. Ottnad, A. Risch et al., *Hadronic vacuum polarization in the muon $g-2$: the short-distance contribution from lattice QCD*, *JHEP* **03** (2024) 172 [2401.11895].

[128] S. Spiegel and C. Lehner, *High-precision continuum limit study of the HVP short-distance window*, *Phys. Rev. D* **111** (2025) 114517 [2410.17053].

[129] Extended Twisted Mass collaboration, *Strange and charm quark contributions to the muon anomalous magnetic moment in lattice QCD with twisted-mass fermions*, *Phys. Rev. D* **111** (2025) 054502 [2411.08852].

[130] MILC, Fermilab Lattice, HPQCD collaboration, *Hadronic vacuum polarization for the muon $g-2$ from lattice QCD: Complete short and intermediate windows*, *Phys. Rev. D* **111** (2025) 094508 [2411.09656].

[131] Fermilab Lattice, HPQCD, MILC collaboration, *Hadronic Vacuum Polarization for the Muon $g-2$ from Lattice QCD: Long-Distance and Full Light-Quark Connected Contribution*, *Phys. Rev. Lett.* **135** (2025) 011901 [2412.18491].

[132] C.M. Carloni Calame, M. Passera, L. Trentadue and G. Venanzoni, *A new approach to evaluate the leading hadronic corrections to the muon $g-2$*, *Phys. Lett. B* **746** (2015) 325 [1504.02228].

[133] B.E. Lautrup and E. De Rafael, *Calculation of the sixth-order contribution from the fourth-order vacuum polarization to the difference of the anomalous magnetic moments of muon and electron*, *Phys. Rev.* **174** (1968) 1835.

[134] G. Rodrigo, H. Czyz, J.H. Kuhn and M. Szopa, *Radiative return at NLO and the measurement of the hadronic cross-section in electron positron annihilation*, *Eur. Phys. J. C* **24** (2002) 71 [hep-ph/0112184].

[135] H. Czyz, A. Grzelinska, J.H. Kuhn and G. Rodrigo, *The Radiative return at Φ and B factories: Small angle photon emission at next-to-leading order*, *Eur. Phys. J. C* **27** (2003) 563 [hep-ph/0212225].

[136] H. Czyz, A. Grzelinska, J.H. Kuhn and G. Rodrigo, *The Radiative return at Φ and B factories: FSR at next-to-leading order*, *Eur. Phys. J. C* **33** (2004) 333 [hep-ph/0308312].

[137] H. Czyz, A. Grzelinska, J.H. Kuhn and G. Rodrigo, *The Radiative return at Φ and B factories: FSR for muon pair production at next-to-leading order*, *Eur. Phys. J. C* **39** (2005) 411 [hep-ph/0404078].

[138] Muon $g-2$ collaboration, *Improved measurement of the positive muon anomalous magnetic moment*, *Phys. Rev. D* **62** (2000) 091101 [hep-ex/0009029].

[139] M.E. Peskin and D.V. Schroeder, *An Introduction to quantum field theory*, Addison-Wesley, Reading, USA (1995), 10.1201/9780429503559.

[140] R.E. Cutkosky, *Singularities and discontinuities of Feynman amplitudes*, *J. Math. Phys.* **1** (1960) 429.

[141] A.D. Martin and T.D. Spearman, *Elementary Particle Theory*, North-Holland Publishing Co., Amsterdam (1970).

[142] R. Omnes, *On the Solution of certain singular integral equations of quantum field theory*, *Nuovo Cim.* **8** (1958) 316.

[143] N.I. Muskhelishvili, *Singular Integral Equations*, Noordhoff (1953).

[144] J.A. Oller, *A Brief Introduction to Dispersion Relations*, SpringerBriefs in Physics, Springer (2019), 10.1007/978-3-030-13582-9.

[145] F.J. Yndurain, *Low-energy pion physics*, `hep-ph/0212282`.

[146] S. Weinberg, *Phenomenological Lagrangians*, *Physica A* **96** (1979) 327.

[147] J. Gasser and H. Leutwyler, *Chiral Perturbation Theory to One Loop*, *Annals Phys.* **158** (1984) 142.

[148] J. Gasser and H. Leutwyler, *Chiral Perturbation Theory: Expansions in the Mass of the Strange Quark*, *Nucl. Phys. B* **250** (1985) 465.

[149] D.J. Gross and F. Wilczek, *Ultraviolet Behavior of Nonabelian Gauge Theories*, *Phys. Rev. Lett.* **30** (1973) 1343.

[150] S. Weinberg, *Nonabelian Gauge Theories of the Strong Interactions*, *Phys. Rev. Lett.* **31** (1973) 494.

[151] H. Fritzsch, M. Gell-Mann and H. Leutwyler, *Advantages of the Color Octet Gluon Picture*, *Phys. Lett. B* **47** (1973) 365.

[152] F. Scheck, *Electroweak and Strong Interactions. An Introduction to Theoretical Particle Physics*, Graduate Texts in Physics, Springer (1996), 10.1007/978-3-662-03245-9.

[153] G. 't Hooft, *Symmetry Breaking Through Bell-Jackiw Anomalies*, *Phys. Rev. Lett.* **37** (1976) 8.

[154] C.G. Callan, Jr., R.F. Dashen and D.J. Gross, *The Structure of the Gauge Theory Vacuum*, *Phys. Lett. B* **63** (1976) 334.

[155] R.J. Crewther, *Chirality Selection Rules and the U(1) Problem*, *Phys. Lett. B* **70** (1977) 349.

[156] W.J. Marciano and H. Pagels, *Quantum Chromodynamics: A Review*, *Phys. Rept.* **36** (1978) 137.

[157] G. Altarelli, *Partons in Quantum Chromodynamics*, *Phys. Rept.* **81** (1982) 1.

[158] Particle Data Group collaboration, *Review of particle physics*, *Phys. Rev. D* **110** (2024) 030001.

[159] H. Pagels, *Departures from Chiral Symmetry: A Review*, *Phys. Rept.* **16** (1975) 219.

[160] A. Manohar and H. Georgi, *Chiral Quarks and the Nonrelativistic Quark Model*, *Nucl. Phys. B* **234** (1984) 189.

[161] H. Georgi, *Weak Interactions and Modern Particle Theory* (1984).

[162] M. Gell-Mann and M. Levy, *The axial vector current in β decay*, *Nuovo Cim.* **16** (1960) 705.

[163] G. Ecker, *Chiral symmetry*, *Lect. Notes Phys.* **521** (1999) 83 [`hep-ph/9805500`].

[164] G. 't Hooft, C. Itzykson, A. Jaffe, H. Lehmann, P.K. Mitter, I.M. Singer et al., eds., *Recent Developments in Gauge Theories. Proceedings, Nato Advanced Study Institute, Cargese, France, August 26 - September 8, 1979*, vol. 59, 1980. 10.1007/978-1-4684-7571-5.

[165] Y. Frishman, A. Schwimmer, T. Banks and S. Yankielowicz, *The Axial Anomaly and the Bound State Spectrum in Confining Theories*, *Nucl. Phys. B* **177** (1981) 157.

[166] S.R. Coleman and B. Grossman, *'t Hooft's Consistency Condition as a Consequence of Analyticity and Unitarity*, *Nucl. Phys. B* **203** (1982) 205.

[167] C. Vafa and E. Witten, *Restrictions on Symmetry Breaking in Vector-Like Gauge Theories*, *Nucl. Phys. B* **234** (1984) 173.

[168] C. Vafa and E. Witten, *Eigenvalue Inequalities for Fermions in Gauge Theories*, *Commun. Math. Phys.* **95** (1984) 257.

[169] Y. Nambu, *Axial vector current conservation in weak interactions*, *Phys. Rev. Lett.* **4** (1960) 380.

[170] Y. Nambu and G. Jona-Lasinio, *Dynamical Model of Elementary Particles Based on an Analogy with Superconductivity. I.*, *Phys. Rev.* **122** (1961) 345.

[171] Y. Nambu and G. Jona-Lasinio, *Dynamical model of elementary particles based on an analogy with superconductivity. II.*, *Phys. Rev.* **124** (1961) 246.

[172] J. Goldstone, *Field Theories with Superconductor Solutions*, *Nuovo Cim.* **19** (1961) 154.

[173] J. Goldstone, A. Salam and S. Weinberg, *Broken Symmetries*, *Phys. Rev.* **127** (1962) 965.

[174] S. Scherer, *Introduction to chiral perturbation theory*, *Adv. Nucl. Phys.* **27** (2003) 277 [hep-ph/0210398].

[175] S.R. Coleman, J. Wess and B. Zumino, *Structure of phenomenological Lagrangians. 1.*, *Phys. Rev.* **177** (1969) 2239.

[176] C.G. Callan, Jr., S.R. Coleman, J. Wess and B. Zumino, *Structure of phenomenological Lagrangians. 2.*, *Phys. Rev.* **177** (1969) 2247.

[177] M. Gell-Mann, R.J. Oakes and B. Renner, *Behavior of current divergences under* $SU(3) \times SU(3)$, *Phys. Rev.* **175** (1968) 2195.

[178] L. Maiani, G. Pancheri and N. Paver, eds., *The DAΦNE physics handbook. Vol. 1, 2* (1992).

[179] D. Ebert and H. Reinhardt, *Effective Chiral Hadron Lagrangian with anomalies and skyrme terms from quark flavour dynamics*, *Nucl. Phys. B* **271** (1986) 188.

[180] D. Espriu, E. de Rafael and J. Taron, *The QCD Effective Action at Long Distances*, *Nucl. Phys. B* **345** (1990) 22.

[181] D. Ebert, A.A. Belkov, A.V. Lanyov and A. Schaale, *Effective chiral Lagrangians for strong, weak and electromagnetic weak interactions of mesons from quark flavor dynamics*, *Int. J. Mod. Phys. A* **8** (1993) 1313.

[182] J. Bijnens, C. Bruno and E. de Rafael, *Nambu-Jona-Lasinio like models and the low-energy effective action of QCD*, *Nucl. Phys. B* **390** (1993) 501 [hep-ph/9206236].

[183] G. Ecker, J. Gasser, H. Leutwyler, A. Pich and E. de Rafael, *Chiral Lagrangians for Massive Spin–1 Fields*, *Phys. Lett. B* **223** (1989) 425.

[184] G. Ecker, J. Gasser, A. Pich and E. de Rafael, *The Role of Resonances in Chiral Perturbation Theory*, *Nucl. Phys. B* **321** (1989) 311.

[185] J.F. Donoghue, C. Ramirez and G. Valencia, *The Spectrum of QCD and Chiral Lagrangians of the Strong and Weak Interactions*, *Phys. Rev. D* **39** (1989) 1947.

[186] M. Knecht and A. Nyffeler, *Resonance estimates of* $\mathcal{O}(p^6)$ *low-energy constants and QCD short distance constraints*, *Eur. Phys. J. C* **21** (2001) 659 [hep-ph/0106034].

[187] S. Leupold, *Vector meson properties from matching resonance saturation to a constituent quark model*, hep-ph/0111204.

[188] S. Myint and C. Rebbi, *Derivation of chiral Lagrangians from lattice QCD*, *Nucl. Phys. B Proc. Suppl.* **34** (1994) 213.

[189] M. Golterman, *Chiral perturbation theory, nonleptonic kaon decays, and the lattice*, in *3rd*

Workshop on Chiral Dynamics - Chiral Dynamics 2000: Theory and Experiment, pp. 33–45, 7, 2000, DOI [hep-ph/0011084].

[190] M. Knecht, H. Neufeld, H. Rupertsberger and P. Talavera, *Chiral perturbation theory with virtual photons and leptons*, *Eur. Phys. J. C* **12** (2000) 469 [hep-ph/9909284].

[191] R. Urech, *Virtual photons in chiral perturbation theory*, *Nucl. Phys. B* **433** (1995) 234 [hep-ph/9405341].

[192] S. Weinberg, *Pion scattering lengths*, *Phys. Rev. Lett.* **17** (1966) 616.

[193] J. Bijnens, G. Colangelo, G. Ecker, J. Gasser and M.E. Sainio, *Elastic $\pi\pi$ scattering to two loops*, *Phys. Lett. B* **374** (1996) 210 [hep-ph/9511397].

[194] S.M. Roy, *Exact integral equation for pion pion scattering involving only physical region partial waves*, *Phys. Lett. B* **36** (1971) 353.

[195] A. Martin, *Extension of the axiomatic analyticity domain of scattering amplitudes by unitarity.—II*, *Il Nuovo Cimento A Series 10* **44** (1966) 1219.

[196] S.M. Roy, *Pion pion scattering*, *Helv. Phys. Acta* **63** (1990) 627.

[197] C. Pomponiu and G. Wanders, *On the Manifold of Solutions of Roy's Equations for Pion Pion Scattering: The Neighborhood of the Physical P Wave*, *Nucl. Phys. B* **103** (1976) 172.

[198] M. Knecht and R. Urech, *Virtual photons in low-energy $\pi\pi$ scattering*, *Nucl. Phys. B* **519** (1998) 329 [hep-ph/9709348].

[199] M. Knecht and A. Nehme, *Electromagnetic corrections to charged pion scattering at low-energies*, *Phys. Lett. B* **532** (2002) 55 [hep-ph/0201033].

[200] G. Colangelo, J. Gasser and A. Rusetsky, *Isospin breaking in K(l4) decays*, *Eur. Phys. J. C* **59** (2009) 777 [0811.0775].

[201] J. Gasser and H. Leutwyler, *Quark Masses*, *Phys. Rept.* **87** (1982) 77.

[202] R. Garcia-Martin, R. Kaminski, J.R. Pelaez, J. Ruiz de Elvira and F.J. Yndurain, *The Pion-pion scattering amplitude. IV: Improved analysis with once subtracted Roy-like equations up to 1100 MeV*, *Phys. Rev.* **D83** (2011) 074004 [1102.2183].

[203] P. Buettiker, S. Descotes-Genon and B. Moussallam, *A new analysis of πK scattering from Roy and Steiner type equations*, *Eur. Phys. J. C* **33** (2004) 409 [hep-ph/0310283].

[204] M. Hoferichter, J. Ruiz de Elvira, B. Kubis and U.-G. Meißner, *Roy–Steiner-equation analysis of pion–nucleon scattering*, *Phys. Rept.* **625** (2016) 1 [1510.06039].

[205] G. Colangelo, S. Lanz, H. Leutwyler and E. Passemar, *Dispersive analysis of $\eta \to 3\pi$*, *Eur. Phys. J. C* **78** (2018) 947 [1807.11937].

[206] Flavour Lattice Averaging Group (FLAG) collaboration, *FLAG Review 2024*, 2411.04268.

[207] J. Bijnens and G. Ecker, *Mesonic low-energy constants*, *Ann. Rev. Nucl. Part. Sci.* **64** (2014) 149 [1405.6488].

[208] C. Haefeli, M.A. Ivanov and M. Schmid, *Electromagnetic low-energy constants in χPT*, *Eur. Phys. J. C* **53** (2008) 549 [0710.5432].

[209] I. Caprini, G. Colangelo and H. Leutwyler, *Mass and width of the lowest resonance in QCD*, *Phys. Rev. Lett.* **96** (2006) 132001 [hep-ph/0512364].

[210] R. Garcia-Martin, R. Kaminski, J.R. Pelaez and J. Ruiz de Elvira, *Precise determination of the $f_0(600)$ and $f_0(980)$ pole parameters from a dispersive data analysis*, *Phys. Rev. Lett.* **107** (2011) 072001 [1107.1635].

[211] J.R. Pelaez, A. Rodas and J.R. de Elvira, *$f_0(1370)$ Controversy from Dispersive Meson-Meson*

Scattering Data Analyses, *Phys. Rev. Lett.* **130** (2023) 051902 [2206.14822].

[212] M. Hoferichter, J.R. de Elvira, B. Kubis and U.-G. Meißner, *Nucleon resonance parameters from Roy–Steiner equations*, *Phys. Lett. B* **853** (2024) 138698 [2312.15015].

[213] BABAR collaboration, *Measurement of additional radiation in the initial-state-radiation processes $e^+e^- \to \mu^+\mu^-\gamma$ and $e^+e^- \to \pi^+\pi^-\gamma$ at BABAR*, *Phys. Rev. D* **108** (2023) L111103 [2308.05233].

[214] E. Budassi, C.M. Carloni Calame, M. Ghilardi, A. Gurgone, G. Montagna, M. Moretti et al., *Pion pair production in e^+e^- annihilation at next-to-leading order matched to Parton Shower*, *JHEP* **05** (2025) 196 [2409.03469].

[215] R. Aliberti et al., *Radiative corrections and Monte Carlo tools for low-energy hadronic cross sections in e^+e^- collisions*, 2410.22882.

[216] A. Sirlin, *Large M_W, M_Z Behavior of the $\mathcal{O}(\alpha)$ Corrections to Semileptonic Processes Mediated by W*, *Nucl. Phys. B* **196** (1982) 83.

[217] W.J. Marciano and A. Sirlin, *Radiative Corrections to beta Decay and the Possibility of a Fourth Generation*, *Phys. Rev. Lett.* **56** (1986) 22.

[218] W.J. Marciano and A. Sirlin, *Electroweak Radiative Corrections to tau Decay*, *Phys. Rev. Lett.* **61** (1988) 1815.

[219] W.J. Marciano and A. Sirlin, *Radiative corrections to π_{l2} decays*, *Phys. Rev. Lett.* **71** (1993) 3629.

[220] E. Braaten and C.-S. Li, *Electroweak radiative corrections to the semihadronic decay rate of the tau lepton*, *Phys. Rev. D* **42** (1990) 3888.

[221] J. Erler, *Electroweak radiative corrections to semileptonic tau decays*, *Rev. Mex. Fis.* **50** (2004) 200 [hep-ph/0211345].

[222] M. Davier, S. Eidelman, A. Hocker and Z. Zhang, *Confronting spectral functions from e^+e^- annihilation and tau decays: Consequences for the muon magnetic moment*, *Eur. Phys. J. C* **27** (2003) 497 [hep-ph/0208177].

[223] V. Cirigliano, W. Dekens, E. Mereghetti and O. Tomalak, *Effective field theory for radiative corrections to charged-current processes: Vector coupling*, *Phys. Rev. D* **108** (2023) 053003 [2306.03138].

[224] A. Hoefer, J. Gluza and F. Jegerlehner, *Pion pair production with higher order radiative corrections in low energy e+ e- collisions*, *Eur. Phys. J. C* **24** (2002) 51 [hep-ph/0107154].

[225] J. Gluza, A. Hoefer, S. Jadach and F. Jegerlehner, *Measuring the FSR inclusive pi+ pi- cross-section*, *Eur. Phys. J. C* **28** (2003) 261 [hep-ph/0212386].

[226] Y.M. Bystritskiy, E.A. Kuraev, G.V. Fedotovich and F.V. Ignatov, *The Cross sections of the muons and charged pions pairs production at electron-positron annihilation near the threshold*, *Phys. Rev. D* **72** (2005) 114019 [hep-ph/0505236].

[227] I. Danilkin and M. Vanderhaeghen, *Dispersive analysis of the $\gamma\gamma^* \to \pi\pi$ process*, *Phys. Lett. B* **789** (2019) 366 [1810.03669].

[228] M. Hoferichter and P. Stoffer, *Dispersion relations for $\gamma^*\gamma^* \to \pi\pi$: helicity amplitudes, subtractions, and anomalous thresholds*, *JHEP* **07** (2019) 073 [1905.13198].

[229] I. Danilkin, O. Deineka and M. Vanderhaeghen, *Dispersive analysis of the $\gamma^*\gamma^* \to \pi\pi$ process*, *Phys. Rev. D* **101** (2020) 054008 [1909.04158].

[230] S. Weinberg, *Charge symmetry of weak interactions*, *Phys. Rev.* **112** (1958) 1375.

[231] S. Descotes-Genon and B. Moussallam, *Analyticity of $\eta\pi$ isospin-violating form factors and the $\tau \to \eta\pi\nu$ second-class decay*, *Eur. Phys. J. C* **74** (2014) 2946 [1404.0251].

[232] G. Passarino and M.J.G. Veltman, *One Loop Corrections for e^+e^- Annihilation Into $\mu^+\mu^-$ in the Weinberg Model*, *Nucl. Phys. B* **160** (1979) 151.

[233] M. Consoli, *One Loop Corrections to $e^+e^- \to e^+e^-$ in the Weinberg Model*, *Nucl. Phys. B* **160** (1979) 208.

[234] M.J.G. Veltman, *Radiative Corrections to Vector Boson Masses*, *Phys. Lett. B* **91** (1980) 95.

[235] M. Green and M.J.G. Veltman, *Weak and Electromagnetic Radiative Corrections to Low-Energy Processes*, *Nucl. Phys. B* **169** (1980) 137.

[236] G. 't Hooft and M.J.G. Veltman, *Scalar One Loop Integrals*, *Nucl. Phys. B* **153** (1979) 365.

[237] D.B. Melrose, *Reduction of Feynman diagrams*, *Nuovo Cim.* **40** (1965) 181.

[238] A. Denner, *Techniques for calculation of electroweak radiative corrections at the one loop level and results for W physics at LEP-200*, *Fortsch. Phys.* **41** (1993) 307 [0709.1075].

[239] R. Mertig, M. Bohm and A. Denner, *FEYN CALC: Computer algebraic calculation of Feynman amplitudes*, *Comput. Phys. Commun.* **64** (1991) 345.

[240] V. Shtabovenko, R. Mertig and F. Orellana, *New Developments in FeynCalc 9.0*, *Comput. Phys. Commun.* **207** (2016) 432 [1601.01167].

[241] V. Shtabovenko, R. Mertig and F. Orellana, *FeynCalc 9.3: New features and improvements*, *Comput. Phys. Commun.* **256** (2020) 107478 [2001.04407].

[242] V. Shtabovenko, R. Mertig and F. Orellana, *FeynCalc 10: Do multiloop integrals dream of computer codes?*, 2312.14089.

[243] P. Stoffer, *Isospin breaking effects in $K_{\ell 4}$ decays*, *Eur. Phys. J. C* **74** (2014) 2749 [1312.2066].

[244] Particle Data Group collaboration, *Review of Particle Physics*, *PTEP* **2022** (2022) 083C01.

[245] P. Van Nieuwenhuizen, *Muon-electron scattering cross-section to order α^3*, *Nucl. Phys. B* **28** (1971) 429.

[246] F.A. Berends, K.J.F. Gaemers and R. Gastmans, *α^3 Contribution to the angular asymmetry in $e^+e^- \to \mu^+\mu^-$*, *Nucl. Phys. B* **63** (1973) 381.

[247] F.A. Berends, K.J.F. Gaemer and R. Gastmans, *Hard photon corrections for the process $e^+e^- \to \mu^\pm\mu^\mp$*, *Nucl. Phys. B* **57** (1973) 381.

[248] F.A. Berends, K.J.F. Gaemers and R. Gastmans, *Hard photon corrections for Bhabha scattering*, *Nucl. Phys. B* **68** (1974) 541.

[249] W.J. Marciano and A. Sirlin, *Dimensional Regularization of Infrared Divergences*, *Nucl. Phys. B* **88** (1975) 86.

[250] M. Zanke, M. Hoferichter and B. Kubis, *On the transition form factors of the axial-vector resonance $f_1(1285)$ and its decay into e^+e^-*, *JHEP* **07** (2021) 106 [2103.09829].

[251] COMPASS collaboration, *Resonance Production and $\pi\pi$ S-wave in $\pi^- + p \to \pi^-\pi^-\pi^+ + p_{recoil}$ at 190 GeV/c*, *Phys. Rev. D* **95** (2017) 032004 [1509.00992].

[252] F. Von Hippel and C. Quigg, *Centrifugal-barrier effects in resonance partial decay widths, shapes, and production amplitudes*, *Phys. Rev. D* **5** (1972) 624.

[253] M. Kirk, B. Kubis, M. Reboud and D. van Dyk, *A simple parametrisation of the pion form factor*, *Phys. Lett. B* **861** (2025) 139266 [2410.13764].

[254] M. Peng-Xiang, F. Xu, G. Mikhail, J. Lu-Chang and S. Chien-Yeah, *Lattice QCD calculation of the electroweak box diagrams for the kaon semileptonic decays*, *Phys. Rev. D* **103** (2021) 114503 [2102.12048].

[255] B. Ananthanarayan and B. Moussallam, *Four-point correlator constraints on electromagnetic chiral*

parameters and resonance effective Lagrangians, *JHEP* **06** (2004) 047 [hep-ph/0405206].

[256] S. Descotes-Genon and B. Moussallam, *Radiative corrections in weak semi-leptonic processes at low energy: A Two-step matching determination*, *Eur. Phys. J. C* **42** (2005) 403 [hep-ph/0505077].

[257] H.H. Patel, *Package-X: A Mathematica package for the analytic calculation of one-loop integrals*, *Comput. Phys. Commun.* **197** (2015) 276 [1503.01469].

[258] H.H. Patel, *Package-X 2.0: A Mathematica package for the analytic calculation of one-loop integrals*, *Comput. Phys. Commun.* **218** (2017) 66 [1612.00009].

[259] M. Bruno, T. Izubuchi, C. Lehner and A. Meyer, *On isospin breaking in τ decays for $(g-2)_\mu$ from Lattice QCD*, *PoS* **LATTICE2018** (2018) 135 [1811.00508].

[260] X. Feng, M. Gorchtein, L.-C. Jin, P.-X. Ma and C.-Y. Seng, *First-principles calculation of electroweak box diagrams from lattice QCD*, *Phys. Rev. Lett.* **124** (2020) 192002 [2003.09798].

[261] J.-S. Yoo, T. Bhattacharya, R. Gupta, S. Mondal and B. Yoon, *Electroweak box diagram contribution for pion and kaon decay from lattice QCD*, *Phys. Rev. D* **108** (2023) 034508 [2305.03198].

[262] J. Wess and B. Zumino, *Consequences of anomalous Ward identities*, *Phys. Lett. B* **37** (1971) 95.

[263] F.E. Low, *Bremsstrahlung of very low-energy quanta in elementary particle collsion*, *Phys. Rev.* **110** (1958) 974.

[264] A. Flores-Tlalpa, G. Lopez Castro and G. Sanchez Toledo, *Radiative two-pion decay of the tau lepton*, *Phys. Rev. D* **72** (2005) 113003 [hep-ph/0511315].

[265] F. Flores-Baez, A. Flores-Tlalpa, G. Lopez Castro and G. Toledo Sanchez, *Long-distance radiative corrections to the di-pion tau lepton decay*, *Phys. Rev. D* **74** (2006) 071301 [hep-ph/0608084].

[266] M. Davier, A. Höcker, B. Malaescu, C.-Z. Yuan and Z. Zhang, *Update of the ALEPH non-strange spectral functions from hadronic τ decays*, *Eur. Phys. J. C* **74** (2014) 2803 [1312.1501].

[267] M. Davier, A. Hoecker, A.-M. Lutz, B. Malaescu and Z. Zhang, *Tensions in $e^+e^- \to \pi^+\pi^-(\gamma)$ measurements: the new landscape of data-driven hadronic vacuum polarization predictions for the muon $g-2$*, *Eur. Phys. J. C* **84** (2024) 721 [2312.02053].

[268] E.S. Ginsberg, *Radiative corrections to the $K_{e3}^{\pm}$ Dalitz Plot*, *Phys. Rev.* **162** (1967) 1570.

[269] G. Colangelo, M. Hoferichter, B. Kubis, M. Niehus and J.R. de Elvira, *Chiral extrapolation of hadronic vacuum polarization*, *Phys. Lett. B* **825** (2022) 136852 [2110.05493].

[270] M. Zielinski, D. Berg, C. Chandlee, S. Cihangir, T. Ferbel, J. Huston et al., *Evidence for the electromagnetic production of the A_1*, *Phys. Rev. Lett.* **52** (1984) 1195.

[271] B. Moussallam, *A Sum rule approach to the violation of Dashen's theorem*, *Nucl. Phys. B* **504** (1997) 381 [hep-ph/9701400].

[272] V. Cirigliano, G. Ecker, M. Eidemüller, A. Pich and J. Portolés, *The $< VAP >$ Green function in the resonance region*, *Phys. Lett. B* **596** (2004) 96 [hep-ph/0404004].

[273] G.T. Condo, T. Handler, W.M. Bugg, G.R. Blackett, M. Pisharody and K.A. Danyo, *Further results from charge exchange photoproduction*, *Phys. Rev. D* **48** (1993) 3045.

[274] CLAS collaboration, *Search for the photo-excitation of exotic mesons in the $\pi^+\pi^+\pi^-$ system*, *Phys. Rev. Lett.* **102** (2009) 102002 [0805.4438].

[275] M. Bando, T. Kugo and K. Yamawaki, *Nonlinear Realization and Hidden Local Symmetries*, *Phys. Rept.* **164** (1988) 217.

[276] G. López Castro and G. Toledo Sánchez, *Gauge invariance and finite width effects in radiative two pion tau lepton decay*, *Phys. Rev. D* **61** (2000) 033007 [hep-ph/9909405].

[277] COMPASS collaboration, *Light isovector resonances in $\pi^- p \to \pi^-\pi^-\pi^+ p$ at 190 GeV/c*, *Phys. Rev. D* **98** (2018) 092003 [1802.05913].

[278] F. Klingl, N. Kaiser and W. Weise, *Effective Lagrangian approach to vector mesons, their structure and decays*, *Z. Phys. A* **356** (1996) 193 [hep-ph/9607431].

[279] M. Zielinski et al., *Evidence for the Electromagnetic Production of the A1*, *Phys. Rev. Lett.* **52** (1984) 1195.

[280] P. Lüghausen, *The Charged-to-Neutral Rho-Meson Mass Difference*, Master's thesis, University of Bonn, 2019.

[281] BELLE collaboration, *High-Statistics Study of the $\tau^- \to \pi^-\pi^0\nu_\tau$ Decay*, *Phys. Rev. D* **78** (2008) 072006 [0805.3773].

[282] ALEPH collaboration, *Branching ratios and spectral functions of tau decays: Final ALEPH measurements and physics implications*, *Phys. Rept.* **421** (2005) 191 [hep-ex/0506072].

[283] CLEO collaboration, *Hadronic structure in the decay $\tau^- \to \pi^-\pi^0\nu_\tau$*, *Phys. Rev. D* **61** (2000) 112002 [hep-ex/9910046].

[284] OPAL collaboration, *Measurement of the strong coupling constant $\alpha(s)$ and the vector and axial vector spectral functions in hadronic tau decays*, *Eur. Phys. J. C* **7** (1999) 571 [hep-ex/9808019].

[285] HEAVY FLAVOR AVERAGING GROUP collaboration, *Averages of b-hadron, c-hadron, and τ-lepton properties as of 2023*, 2411.18639.

[286] G. Chanturia, *A two-potential formalism for the pion vector form factor*, *PoS* **Regio2021** (2022) 030.

[287] L.A. Heuser, G. Chanturia, F.K. Guo, C. Hanhart, M. Hoferichter and B. Kubis, *From pole parameters to line shapes and branching ratios*, *Eur. Phys. J. C* **84** (2024) 599 [2403.15539].

[288] D. Stamen, D. Hariharan, M. Hoferichter, B. Kubis and P. Stoffer, *Kaon electromagnetic form factors in dispersion theory*, *Eur. Phys. J. C* **82** (2022) 432 [2202.11106].

[289] M. Hoferichter, B.-L. Hoid, B. Kubis and D. Schuh, *Isospin-breaking effects in the three-pion contribution to hadronic vacuum polarization*, *JHEP* **08** (2023) 208 [2307.02546].

[290] G. D'Agostini, *On the use of the covariance matrix to fit correlated data*, *Nucl. Instrum. Meth. A* **346** (1994) 306.

[291] NNPDF collaboration, *Fitting Parton Distribution Data with Multiplicative Normalization Uncertainties*, *JHEP* **05** (2010) 075 [0912.2276].

[292] V.L. Chernyak and A.R. Zhitnitsky, *Asymptotic Behavior of Hadron Form-Factors in Quark Model. (In Russian)*, *JETP Lett.* **25** (1977) 510.

[293] G.R. Farrar and D.R. Jackson, *The Pion Form-Factor*, *Phys. Rev. Lett.* **43** (1979) 246.

[294] A.V. Efremov and A.V. Radyushkin, *Factorization and Asymptotical Behavior of Pion Form-Factor in QCD*, *Phys. Lett. B* **94** (1980) 245.

[295] G.P. Lepage and S.J. Brodsky, *Exclusive Processes in Quantum Chromodynamics: Evolution Equations for Hadronic Wave Functions and the Form-Factors of Mesons*, *Phys. Lett. B* **87** (1979) 359.

[296] G.P. Lepage and S.J. Brodsky, *Exclusive Processes in Perturbative Quantum Chromodynamics*, *Phys. Rev. D* **22** (1980) 2157.

[297] G.L. Castro, A. Miranda and P. Roig, *Isospin breaking corrections in 2π production in tau decays and e^+e^- annihilation: Consequences for the muon $g-2$ and conserved vector current tests*, *Phys. Rev. D* **111** (2025) 073004 [2411.07696].

[298] P.-X. Ma, X. Feng, M. Gorchtein, L.-C. Jin and C.-Y. Seng, *Lattice QCD calculation of the*

electroweak box diagrams for the kaon semileptonic decays, *Phys. Rev. D* **103** (2021) 114503 [2102.12048].

[299] BELLE-II collaboration, *The Belle II Physics Book*, *PTEP* **2019** (2019) 123C01 [1808.10567].

[300] Y. Ne'eman, *Derivation of strong interactions from a gauge invariance*, *Nucl. Phys.* **26** (1961) 222.

[301] M. Gell-Mann, *Symmetries of baryons and mesons*, *Phys. Rev.* **125** (1962) 1067.

[302] M. Gell-Mann and Y. Ne'eman, *The Eightfold way: a review with a collection of reprints*, .

[303] A.P. Balachandran and C.G. Trahern, *Lectures on Group Theory for Physicists* (1986).

[304] L. O'Raifeartaigh, *Group Structure of Gauge Theories*, Cambridge Monographs on Mathematical Physics, Cambridge University Press (1988), 10.1017/CBO9780511564031.

[305] H.F. Jones, *Groups, representations and physics* (1990).

Declaration of consent

on the basis of Article 18 of the PromR Phil.-nat. 19

Name/First Name:	Martina Cottini
Registration Number:	21-142-500
Study program:	Theoretical Physics, PhD Bachelor ☐ Master ☐ Dissertation ☒
Title of the thesis:	Dispersive approach to the calculation of isospin–breaking corrections to $\pi\pi$–scattering and $\tau^{\pm} \to \pi^{\pm}\pi^{0}\nu$
Supervisor:	Prof. Dr. Gilberto Colangelo

I declare herewith that this thesis is my own work and that I have not used any sources other than those stated. I have indicated the adoption of quotations as well as thoughts taken from other authors as such in the thesis. I am aware that the Senate pursuant to Article 36 paragraph 1 litera r of the University Act of September 5th, 1996 and Article 69 of the University Statute of June 7th, 2011 is authorized to revoke the doctoral degree awarded on the basis of this thesis.
For the purposes of evaluation and verification of compliance with the declaration of originality and the regulations governing plagiarism, I hereby grant the University of Bern the right to process my personal data and to perform the acts of use this requires, in particular, to reproduce the written thesis and to store it permanently in a database, and to use said database, or to make said database available, to enable comparison with theses submitted by others.

Place/Date: Bern, 17.11.2025 Signature

Martina Cottini